TECHNISCHE UNIVERSITÄT MÜNCHEN
Fakultät für Maschinenwesen
Lehrstuhl für Luftfahrtsysteme

Multidisciplinary Design of Aeronautical Composite Cycle Engines

Sascha Kaiser

Vollständiger Abdruck der von der Fakultät für Maschinenwesen der Technischen Universität München zur Erlangung des akademischen Grades eines

Doktor-Ingenieurs (Dr.-Ing.)

genehmigten Dissertation.

Vorsitzender:	Prof. Dr.-Ing. Volker Gümmer
Prüfer der Dissertation:	1. Prof. Dr.-Ing. Mirko Hornung
	2. Adjunct Prof. Dr. Anders Lundbladh Chalmers University of Technology, Gothenburg, Sweden

Die Dissertation wurde am 28.02.2019 bei der Technischen Universität München eingereicht und durch die Fakultät für Maschinenwesen am 28.10.2019 angenommen.

Acknowledgement

> We set out to achieve the lowest sfc in the world, regardless of weight and bulk; so far we've achieved the weight and the bulk.
>
> – *Frank Owner about the Bristol Proteus turboprop engine*

This thesis is the result of six years of work. It would not have been possible without the support from many people, who cannot be counted or named individually. To some of them I want to convey my gratitude on this page. First, I want to thank my thesis supervisor Prof. Mirko Hornung and my second examiner Prof. Anders Lundbladh for their continuous support throughout the thesis in guiding the research topics into the right direction and asking the right questions at the right time.

Most of the work has been conducted at the research institute Bauhaus Luftfahrt e.V., where a motivating and liberal working environment allowed me to explore many different perspectives of my work before converging on the research question. I want to thank my dear colleagues, who held up the good spirit at all times, and fostered a supportive research environment. In particular, I want to thank Oliver Schmitz and Clement Pornet, who accompanied my early years in research, Patrick Vratny, Michael Schmidt, Ulrich Kling, Philipp Heinemann and Anne Schuster, who became outstanding friends, and the core propulsion group around Arne Seitz and Markus Nickl.

During my work, I could rely on profound and thought provoking feedback from colleagues in industry. Stefan Donnerhack was a strong promoter of my work, and enabled research partnerships that will most likely persist beyond this thesis. Hermann Klingels is the ingenious inventor behind the concept with a matchless intuition for engineering solutions. Jens Trübenbach and Alyssa Butler accompanied the finishing.

Last but not least, I could not have accomplished such an enduring task without a solid basis. My family and my parents gave me their absolute support and backing, and never missed to put a smile on my face, when I needed it. Thank you Sonja, Sophie and Alexander.

Sascha Kaiser

Munich, 29th January 2020

The method development for this thesis was partially conducted in the projects LEMCOTEC (Low Emissions Core-Engine Technologies) and ULTIMATE (Ultra Low emission Technology Innovations for Mid-century Aircraft Turbine Engines). LEMCOTEC was co-funded by the European Commission within the Seventh Framework Programme (2007-2013) under the Grant Agreement n° 283216. ULTIMATE received funding from the European Union's Horizon 2020 research and innovation programme under grant agreement n° 633436.

Abstract

The efficiency of aero engines improved with every new generation. Improvements of turbo components, as well as increase of overall pressure ratio and combustor temperatures raised thermal efficiency, while higher bypass ratio fans raised propulsive efficiency. With the newest generation of turbofans, the improvement potential of the Joule-/Brayton-cycle and the propulsive efficiency approach technically viable limits. At the same time, ambitious emission reduction targets require further leaps in engine efficiency. The *Composite Cycle Engine* concept introduced in this thesis is a candidate for a step change in core engine architectures.

The concept introduces a piston engine to the high-pressure part of a turbofan core engine, where it drives a high pressure compressor. Piston engines burn fuel at constant volume, which brings along a free pressure rise. They enable higher cycle temperatures and pressures due to instationary operation. The created efficiency improvement comes at the price of higher weight, size and pressure oscillations. This thesis answers the question, if the resulting fuel burn improvement can achieve future emission reduction targets with detailed multidisciplinary component modelling. The piston engine is simulated with a 0D time-resolved model. Engine weight and size are estimated on component-level to generate physically adequate results for comparison with a turbofan. A sophisticated 2-zone NO_x emissions model was developed to evaluate compliance with projected certification targets.

The appraisal of the technical viability was supported by detailed preliminary, conceptual design of the core engine. Particularly piston engine features were specified such as operating mode, layout, lubrication, cooling and coupling to turbo components. The choice of component limits was supported by data from production piston engines from all fields of applications.

The concept was evaluated on a short-to-medium range aircraft platform with a year 2035 technological level. The engine was evaluated against a projected geared turbofan. With a four-stroke piston engine, overall efficiency can be increased by 12.3 %. Mission fuel burn reduces only by 5.7 % as engine mass increases significantly from 3 502 kg to 5 962 kg. NO_x emissions triple. Using a two-stroke piston engine almost allows to meet fuel burn reduction targets for the year 2035 with a further 1.1 % improvement due to lower engine weight, although efficiency is worse. The additional use of an intercooler can alleviate thermal and NO_x problems, but does not provide better efficiency or engine mass. A more advanced free-piston engine concept could considerably improve engine efficiency and mass. The main challenges identified are high mechanical and thermal loads on the piston engines.

Contents

Vorwort **i**

Abstract **iii**

List of Figures **xii**

List of Tables **xiv**

Nomenclature **xv**

1 Introduction **1**

2 The Composite Cycle Engine Concept **3**

2.1 Thermodynamic Benefits of Composite Cycle Engines 3

2.2 Piston Engines in Aviation 6

2.3 Experience and Research on the Composite Cycle Engine Architecture 11

2.4 Alternative Cycles and Closed Volume Combustion Concepts 15

3 Methods **19**

3.1 Fluid Properties 19

3.2 Propulsion System Simulation 23

3.3 Piston System Simulation 29

3.3.1 Heat Losses 34

3.3.2 Numerical Integration 36

3.3.3 Implementation into Engine Simulation Environment 37

3.3.4 Validation 39

3.3.5 Mechanical Losses 42

3.4 Heat Exchanger Modelling 45

3.5 Flow Path Generation . . . 47
3.6 Mass Estimation . . . 48
3.7 Aircraft Level Assessment . . . 53
3.8 Instationary Operation . . . 54
3.8.1 Impact of Pulsating Flow on Turbo Components . . . 54
3.8.2 Mechanical Oscillation . . . 56
3.9 Emissions . . . 57
3.9.1 CO_2 Emissions . . . 57
3.9.2 NO_x Emissions . . . 58
3.9.3 Noise Emissions . . . 67
3.9.4 Other Emissions and Interference between Emission Targets . . . 68

4 Conceptual Design of Composite Cycle Engines 71
4.1 Evaluation Platform . . . 71
4.2 Overall Engine Design . . . 77
4.3 Piston Engine Design . . . 81
4.4 Synergistic Technologies . . . 87

5 Results of Selected Composite Cycle Engine Concepts 91
5.1 Baseline Four-Stroke Engine Concept . . . 91
5.1.1 Flow Path and Mass . . . 95
5.1.2 Fuel Burn . . . 98
5.1.3 Part-Load Behaviour . . . 99
5.1.4 NO_x Emissions . . . 100
5.1.5 Technology Sensitivity Study . . . 101
5.2 Alternative Piston Engine Concepts . . . 102
5.2.1 Two-Stroke Piston Engine . . . 102
5.2.2 Intercooled Composite Cycle Engine . . . 105
5.2.3 Free-Piston Engine . . . 108
5.2.4 Summary . . . 111
5.3 Technology Road Mapping . . . 116

6 Conclusion and Outlook 119

Bibliography 123

A Appendix **143**

A.1 Turbo Component Setup 143

A.2 Validation 2-Stroke Engine Neural Network 144

A.3 Supplementary figures 145

A.4 Supplementary Data 147

List of Figures

1.1 Engine fuel burn reduction targets by engine manufacturers in the context of SRIA and NASA N+3 targets. 1

2.1 Temperature T over specific entropy s diagram of the Composite Cycle in contrast to the Joule-/Brayton-cycle at ToC conditions (adapted from [17]). Station nomenclature according to Figure 3.2. Station 41 after addition of turbine stator cooling air, station 44 after turbine work extraction. 4

2.2 Options for CCE turbofan architectures with fan shaft driven by (a) the piston engine, (b) the turbine, and (c) a compound of both. 5

2.3 IFSD rates of piston engines in contrast to large commercial aircraft regulations and turbo engines. 8

2.4 Inflation-adjusted fuel price over time [40]. 10

2.5 Brake specific fuel consumption BSFC of piston engines over time. 11

2.6 General arrangements of (a) the Wright R-3350 TC [50], and (b,c) the Napier Nomad E.145 [24]. 13

2.7 Wankel-type rotary engine (a) rotor and (b) casing [62], and (c) cross-sectional schematic drawing [63]. 15

2.8 Schematic illustration of (a) a pulsed detonation engine [75], and (b) a wave rotor engine [76]. 17

3.1 Combustion temperature in dependence of FAR and pressure p for combustor entry temperature $T_3 = 1\,000\,\mathrm{K}$. 21

3.2 CCE schematic general arrangement with station nomenclature (top), and with respective simulation sequence within APSS (bottom). 24

3.3 Component map of a low pressure ratio outer fan with efficiency iso-contours and typical design and off-design operating points. 28

3.4 Single-zone cylinder control volume with relevant mass, energy and enthalpy flows. 29

3.5 Synthetic valve lift characteristic over non-dimensional opening time. 31

3.6 Comparison between scavenging efficiency η_s over delivery ratio of different scavenging models against uni-flow, loop and cross scavenging [106]. 32

3.7 Normalised rates of heat release $\mathrm{d}Q_{\mathrm{fuel}}$ (top) and their cumulative rates (bottom) for variations of the Wiebe parameters w_a (left) and w_m (right). 33

3.8 Compressibility factor Z for various pressures and temperatures for FAR = 0 as provided in literature and interpolation used here. 34

3.9 Impact of real gas correction for typical CCE piston engine TO conditions. . 35

3.10 (a) Simplified piston geometry used here in contrast to (b) a real high-performance piston [118]. 36

3.11 Cylinder pressure p over relative volume V diagram contrasting cycles with surrogate solution and adapted valve timing and combustion parameters for TO conditions. 39

3.12 Cylinder pressure p over relative volume V diagram contrasting cycles with surrogate solution and adapted valve timing and combustion parameters for cruise conditions. 40

3.13 Crank-angle resolved temperature T and pressure p of published data [123] against the piston engine simulation program. 42

3.14 Stacked contributions to FMEP by various components over engine speed for typical TO conditions. 44

3.15 (a) Schematic of an intercooled recuperated engine, and (b) MTU profile tube heat exchanger [130]. 45

3.16 Important geometric ratios on (a) turbo components, and (b) ducts. 47

3.17 Flow path visualisation (blue solid lines) over a PW1100G general arrangement drawing [132]. 48

3.18 Cross-section of a high-performance piston [134] with derived basic geometric relations for other piston components. 49

3.19 Fan mass estimates [138] and regression (solid line). 49

3.20 Iso-contours of change in fuel burn depending on TSFC and total engine mass m_{PPS} on a year 2035 short-to-mid range aircraft. Red lines indicate engine-related emission reduction targets. 54

3.21 Schematic illustration of the two engine mountings [155]. 56

3.22 Limits of $\mathrm{NO_x}$ emissions in the LTO cycle with future SRIA reduction targets, and some current in-service and projected aircraft engines. 58

3.23 Schematic illustration of the relations of the zones of the 2-zone model [105]. 60

3.24 Qualitative scope of (a) temperature and (b) mass in both zones of the 2-zone-model in contrast to mean values. 63

3.25 Creation of NO over crank angle in contrast to equilibrium NO concentration. 64

3.26 Simulated NO_x emissions in contrast to published data from piston engines. . 65

3.27 Plot of combustion temperature over fuel-air-ratio for assessment of equivalent combustor inlet temperature T_3^*. 67

4.1 Turbine cooling air distribution on cascades for given material temperatures for the year 2015 engine. 73

4.2 Evaluation logic for assessing the year 2035 GTF. 75

4.3 Changes in fuel burn and sizing thrust F_N for a year 2015 and year 2035 GTFs. 75

4.4 Comparison between engine general arrangement drawings for (bottom) a present and (top) a year 2035 technological standard. 76

4.5 Schematic of the investigated CCE engine architecture. 78

4.6 Schematics of gearing options with (a-c) planetary gearbox, and (d) a two-stage spur gear transmission. 80

4.7 (a) Parametric study of gearbox geometric properties, and (b) gearing nomenclature. 80

4.8 Geometric compression ratio CR over mean piston velocity v_{mean} categorised by engine fuel. 82

4.9 Pressure over volume diagram for a four-stroke engine with no pressure rise (left), a pressure ratio of 1.5 (middle), and operating as a gas generator (right). 83

4.10 (a) Options for valve drive trains, and (b) comparison of wet and dry cylinder liner cooling. 84

4.11 Free double piston arrangement with the engine on the centre line and piston compressors around the piston using the engine power [241]. 87

4.12 (a) Options for including intercoolers into the CCE baseline (top left). Options for recuperators (b) with different working fluids, and in (c) different locations. 88

4.13 Temperature T over specific entropy s diagram of the baseline CCE cycle [81]. Station nomenclature according to Figure 3.2. Stations 31-34 piston engine internal, instationary states. Station 41 after addition of turbine stator cooling air, station 44 after turbine work extraction in equivalent single stage turbine model [102]. 89

5.1 Temperature T over specific entropy s diagram of CCE against GTF at ToC conditions. Station nomenclature according to Figure 3.2. Station 41 after addition of turbine stator cooling air, station 43 after turbine work extraction, and station 44 after addition of rotor cooling air in equivalent single stage turbine model [102]. 94

5.2 Power and heat balance for the core engine under TO conditions. 96

5.3 (a) General arrangement of the baseline CCE (top) drawn against the reference GTF (bottom). (b) Cross-sectional view through the piston engine (top) with piston engine gearbox (bottom). 97

5.4 Changes in fuel burn and sizing thrust F_N for baseline CCE. 98

5.5 CCE part power characteristics (a) TSFC, and (b) change in TSFC against GTF and fuel ratio burned in the piston engine. 99

5.6 Comparison between four-stroke and two-stroke CCE in a temperature T over specific entropy s diagram at ToC conditions. 104

5.7 General arrangement of the baseline four-stroke CCE (top) drawn against two-stroke CCE (bottom). 104

5.8 General arrangement of the intercooled two-stroke CCE (top) drawn against a two-stroke CCE (bottom). 107

5.9 Temperature T over specific entropy s diagram of CCE with and without intercooler at ToC conditions. 107

5.10 General arrangement of the free-piston CCE (top) drawn against two-stroke CCE (bottom). 110

5.11 Power and heat balance of the high pressure spool of the free-piston engine. . 110

5.12 Changes in fuel burn and sizing thrust F_N for the CCE concepts and GTF engines. 112

5.13 Changes in fuel burn FB, TSFC (left), PPS mass m_{PPS} and bore (right) of the investigated CCE concepts when varying number of cylinders. 112

5.14 CCE NO_x emission levels in LTO cycle with respect to emission reduction targets. 113

5.15 Displacement volume specific power over mean effective pressure p_{mean} categorised by engine application. 114

5.16 Displacement volume specific engine mass over power specific engine mass categorised by engine application. 115

5.17 CCE TRL maturation road map. 117

A.1 Verifications of the calculation of the equilibrium constant K_c exemplary for Reaction (3.116). 145

A.2 Verifications of the equilibrium concentrations of the species of the OHC-System over temperature against published data [172]. 145

A.3 Power per volume flow over power per area. 146

List of Tables

3.1 Thermodynamic properties tables specifying inputs with ranges. 21

3.2 Standard design iteration scheme for a GTF. 26

3.3 Standard off-design iteration scheme for a GTF. 28

3.4 Input parameters for the four-stroke piston engine surrogate artificial neural network with ranges and output parameters. 37

3.5 Adaptation of valve timings and combustion parameters for TO conditions to meet piston engine specified performance. 40

3.6 Adaptation of valve timings and combustion parameters for cruise conditions to meet piston engine specified performance. 41

3.7 Input parameters for the piston engine validation and comparison between outputs in reference and simulation. 41

3.8 Pressure losses in heat exchanger. 45

3.9 Summary of geometric properties of turbo components. 47

3.10 Structure of engine masses and validation values. 52

3.11 Diesel engines and references used for the validation of the NO_x simulation model, completeness of simulation data, and simulation error. 65

4.1 Assumptions for reference GTF ToC design point with a year 2035 technological standard. 74

4.2 Specifications for main operating points for reference GTF design with a year 2035 technological standard on a year 2035 airframe. 76

4.3 NO_x emission estimates for LTO cycle and cruise. 77

5.1 Assumptions for CCE design point performance. 92

5.2 Efficiency corrections for CCE simulation. 93

5.3 Baseline CCE cycle properties. 94

5.4 Piston engine limit properties. Operating point TO if not specified otherwise. 95

5.5 Mass breakdown of CCE against GTF. 96
5.6 Aircraft level metrics with baseline CCE. 98
5.7 CCE NO_x emission estimates in LTO cycle and cruise. 100
5.8 CCE sensitivities of technology assumptions on TSFC, power plant system mass m_{PPS} and fuel burn FB in order of highest fuel burn improvement potential. 102
5.9 Two-stroke CCE cycle properties. 103
5.10 CCE two-stroke NO_x emission estimates in LTO cycle and cruise. 105
5.11 Main cycle characteristics of a CCE with intercooler. 106
5.12 Intercooled CCE NO_x emission estimates in LTO cycle and cruise. 108
5.13 Parameter assumptions for FP engine. 108
5.14 Main cycle characteristics of a CCE with free piston. 109
5.15 Free-piston CCE NO_x emission estimates in LTO cycle and cruise. 111

A.1 Input parameters for the two-stroke piston engine surrogate artificial neural network with ranges and output parameters. 144
A.2 Structure of engine weights and validation values for 2-stroke CCE. 147
A.3 Structure of engine weights and validation values for intercooled 2-stroke CCE. 148
A.4 Structure of engine weights and validation values for free-piston CCE. 148
A.5 Station report for four-stroke CCE. 149
A.6 Station report for two-stroke CCE. 150
A.7 Station report for intercooled two-stroke CCE. 151
A.8 Station report for free-piston CCE. 152
A.9 Comparison of results of piston engine surrogate artificial neural network with simulation model of four-stroke CCE. 153
A.10 Comparison of results of piston engine surrogate artificial neural network with simulation model of two-stroke CCE. 154
A.11 Comparison of results of piston engine surrogate artificial neural network with simulation model of intercooled two-stroke CCE. 155
A.12 Comparison of results of piston engine surrogate artificial neural network with simulation model of free-piston CCE. 156

Nomenclature

List of Latin Symbols

A	m^2	Area
a_i	–	NASA CEA polynomial coefficients
A^*	K	Initial temperature difference in the two-zone model
AR	–	Aspect Ratio
b_i	–	NASA CEA polynomial coefficients
BMEP	Pa	Brake Mean Effective Pressure
BPR	–	Bypass Ratio
BSFC	g/kW h	Brake Specific Fuel Consumption
c	–	Correction or calibration factor
C	W/K	Heat capacity rate
c_A	–	Calibration factor for initial temperature difference A^*
c_D	–	Nozzle discharge coefficient
c_{FG}	–	Nozzle thrust coefficient
c_p	J/(kg K)	Specific heat at constant pressure
C_p°	J/(mol K)	Specific molar heat at constant pressure
CR	–	Geometric Compression Ratio
c_s	–	NO_x proportionality factor
d	m	Diameter
D_p	g	Pollutant emitted in LTO cycle
EINOx	g_{NOx}/kg_{fuel}	Emission Index NO_x
EOC	°	End of Combustion
EVC	°	Exhaust Valve Closing
EVO	°	Exhaust Valve Opening
f	Hz	Pulsation frequency
F	N	Thrust (force)
FAR	–	Fuel-Air-Ratio
FB	kg	Mission fuel burn
FF	–	Flow Function
FHV	J/kg	Fuel Heating Value (lower)
FL	100 ft	Flight Level (pressure altitude)

FMEP	Pa	Friction Mean Effective Pressure
G	J/kg	Gibbs energy
GR	–	Gap Ratio
h	J/kg	Specific enthalpy
$\Delta_f H^\circ_{298}$	J/mol	Molar enthalpy at 298 K
H°	J/mol	Specific molar enthalpy
HTR	–	Hub-to-Tip Ratio
IMEP	Pa	Indicated Mean Effective Pressure
IVC	°	Intake Valve Closing
IVO	°	Intake Valve Opening
k	W/(m^2 K)	Thermal conductivity
K_c	–	Equilibrium constant
k_f	$(\mathrm{m}^3/(\mathrm{mol\,s}))^n$	Forward reaction coefficient
k_r	$(\mathrm{m}^3/(\mathrm{mol\,s}))^n$	Reverse reaction coefficient
l	m	Length
M	–	Mach number
m	kg	Mass
M	kg/mol	Molar mass
$\dot{m}$	kg/s	Mass flow rate
MTOW	kg	Maximum Take-Off Weight
n	Hz	Spool speed
n	–	Number
NTU	–	Number of Transfer Units
OEW	kg	Operating Empty Weight
OPR	–	Overall Pressure Ratio
P	W	Power
p	Pa	Total pressure
p_{peak}	Pa	Piston engine peak pressure
PPR	–	Peak Pressure Ratio
$\dot{Q}$	W	Heat flow rate
q	–	Ratio
Q	J	Heat
R	J/(kg K)	Specific gas constant
r	m	Radius
R_m	J/(mol K)	Universal gas constant
RNI	–	Reynolds Number Index
s	J/(kg K)	Specific entropy
s	m	Stroke
$\Delta_f S^\circ_{298}$	J/(mol K)	Molar entropy at 298 K
S°	J/(mol K)	Specific molar entropy
SM	–	Surge Margin
s_{NOx}	$\mathrm{g_{NOx}/kg_{fuel}}$	NO_x severity parameter
SOC	°	Start of Combustion

t	s	Time
T	K	Total temperature
TR	–	Taper Ratio
TSFC	kg/(N s)	Thrust Specific Fuel Consumption
U	J	Inner energy
u	J/kg	Specific inner energy
v	m/s	Velocity
V	m^3	Volume
v_{mean}	m/s	Mean piston velocity
v_{tip}	m/s	Fan tip speed
W	J	Work
w_a	–	Wiebe parameter
w_m	–	Wiebe parameter
WAR	–	Water-Air-Ratio
WP	J/kg	Work Potential
y	–	Non-dimensional time of heat release
Z	–	Compressibility factor

List of Greek Symbols

α	W/(m^2 K)	Heat transfer coefficient
β	–	Auxiliary parameter in component maps
ϵ	–	Heat exchanger effectiveness
η	–	Efficiency
η_{air}	–	Air efficiency
η_{core}	–	Core efficiency
η_{is}	–	Isentropic efficiency
η_o	–	Overall efficiency
η_p	–	Propulsive efficiency
η_{pol}	–	Polytropic efficiency
η_s	–	Scavenging efficiency
η_{th}	–	Thermal efficiency
η_{tr}	–	Transmission efficiency
γ	–	Heat capacity ratio
λ	–	Delivery ratio
λ_0	–	Initial air ratio in combustion zone of the two-zone model
λ_s	–	Connecting rod ratio
μ	Pa s	Dynamic viscosity
ν	–	Mole number
ϕ	°	Crankshaft angle
ϕ	–	Air number
Π	–	Pressure ratio

ψ	–	Load coefficient
Ψ	–	Entropy function
ρ	kg/m^3	Density

List of Subscripts

0	Ambient Conditions	**is**	Isentropic
1	Component inlet	**i**	Inner (fan)
2	Component exit	**M**	Material
cold	Heat exchanger cold side	**m**	Mean
c	Combustion	**N**	Net
cool	Cooling air	**o**	Outer (fan)
corr	Corrected	**s**	Static
des	Design mode	**st**	Stream Tube
d	Displacement	**0–9**	Station nomenclature (see
G	Gross		Figure 3.2)
hot	Heat exchanger hot side	**std**	Standard
id	Ideal	**c**	Cooling

List of Acronyms

ACC	Active Clearance Control
AE	All-Electric
CCE	Composite Cycle Engine
CEA	Chemical Equilibrium with Applications
CLAIRE	CLean AIR Engine
CO	Carbon Monoxide
CO_2	Carbon Dioxide
CR	Cruise
EGR	Exhaust Gas Recirculation
ETOPS	Extended Operations
FDGS	Fan Drive Gear System
FP	Free Piston
GTF	Geared Turbofan
HALE	High Altitude Long Endurance
HPC	High-Pressure Compressor
HPT	High-Pressure Turbine
IC	Intercooler
IFSD	In-flight Shutdown
IPC	Intermediate-Pressure Compressor
IRA	Intercooled Recuperated Aero engine

ISA	International Standard Atmosphere
LDI	Lean Direct Injection
LPS	Low-Pressure Spool
LPT	Low-Pressure Turbine
LTO	Landing and Take-off
NO	Nitrogen oxide
NO_x	Nitrogen oxides, mainly nitric oxide (NO) and nitrogen dioxide (NO_2)
OH	Hydroxide
PC	Piston Compressor
PE	Piston Engine
PPS	Power Plant System
SCR	Selective Catalytic Reduction
SLS	Sea Level Static
SoA	State of the Art
SRIA	Strategic Research & Innovation Agenda
TBC	Thermal Barrier Coating
TBO	Time Between Overhaul
TCDS	Type-Certificate Data Sheet
TDC	Top Dead Centre
TiAl	Titanium Aluminide
TO	Take-Off
ToC	Top of Climb
TRL	Technology Readiness Level
UDF	Unducted Fan
UHC	Unburned Hydrocarbons

List of Organisations and Software

ACARE	Advisory Council for Aviation Research and Innovation in Europe
APD	Pacelab APD, PACE GmbH
APSS	Aircraft Propulsion System Synthesis
ATAG	Air Transport Action Group
BHL	Bauhaus Luftfahrt e.V.
CAEP	Committee on Aviation Environmental Protection
CLEEN	Continuous Lower Energy, Emissions and Noise
EASA	European Aviation Safety Agency
EC	European Commission
ENOVAL	Engine Module Validators
ERAST	Environmental Research Aircraft and Sensor Technology
GasTurb	GasTurb®, GasTurb GmbH
IATA	International Air Transport Association
ICAO	International Civil Aviation Organization

LEMCOTEC	Low-Emissions Core-Engine Technologies
MATLAB	MATLAB® R2017b, The MathWorks inc.
NASA	National Aeronautics Space Administration
ULTIMATE	Ultra Low emission Technology Innovations for Mid- century Aircraft Turbine Engines

Chapter 1

Introduction

Environmental protection targets dictate the pace of improvement of aero engines. Emissions of carbon dioxide (CO_2) have received increasing awareness in past years, and ambitious reduction targets have been specified. Based on standards in 2000, the Strategic Research & Innovation Agenda (SRIA) targets reduction per passenger and kilometre at the engine level of 20 % by 2020, 30 % by 2035, and 43 %[1] by 2050 [1]. The National Aeronautics Space Administration (NASA) specifies stricter targets N+1 to N+3 of 18 % by 2015, 29 % by 2020 and 37 % by 2025 [2][2]. However, these require the target technologies to be only in development on a technology readiness level (TRL) of four to six but not in service. Fuel efficiency targets are not yet part of aircraft certification but are foreseen for the near future [3][3]. Both SRIA and NASA targets are indicated as shaded regions in Figure 1.1.

[1]The target assumes that reduction of emissions of CO_2 by aircraft and engine by 68 % is evenly divided on both.

[2]Again assuming that targets for aircraft and engine are evenly divided on both.

[3]Please note that the document is only in a draft state at the time of writing.

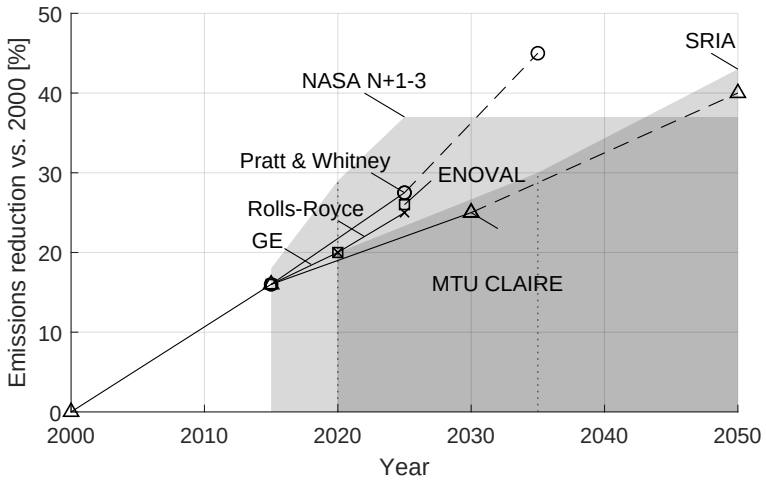

Figure 1.1: Engine fuel burn reduction targets by engine manufacturers in the context of SRIA and NASA N+3 targets.

Comparing the afore-mentioned targets to the goals of aero engine concepts foreseen by important manufacturers shows a discrepancy. An improvement of 15 % was achieved by modern turbofan engines [4, 5]. Beyond that point, e.g. MTU's CLean AIR Engine (CLAIRE) agenda foresees a next-generation geared turbofan (GTF) by the year 2030 with a further 10 % improvement [6–8]. A third CLAIRE concept aims to feature an advanced cycle beyond the Joule-/Brayton-cycle. Pratt & Whitney foresees a further, more ambitious 10 % to 15 % improvement by 2025 [2, 9]. For a third generation GTF, a generic cost improvement by 45 % is envisaged, which embraces fuel burn, maintenance and manufacturing cost. Rolls-Royce foresees the three-spool turbofan ADVANCE with an improvement of 20 % by 2020, and the geared UltraFan with variable pitch fan with 25 % improvement by 2025 [10, 11]. From GE Aviation, no engine agenda goes beyond the GE9X [12]. The European research programme ENOVAL found a similar mid-term improvement target of 26 % by 2025 [13, 14].

The projected improvements are on a good trajectory to achieve SRIA 2020 targets, but no improvements beyond 25 % to 30 % are foreseen on a Joule-/Brayton-cycle based engine. Therefore, a novel cycle is required in the mid future. The Composite Cycle Engine (CCE) is presented in this thesis as a candidate concept, which combines advantages of turbofan and piston engines. The concept introduces a piston engine on the high-pressure part of a turbofan core. The combustion in piston engines is partially isochoric, and thereby provides pressure rise without the cost of shaft power. Due to an instationary operating principle, much higher combustion temperatures and pressures can be sustained. Thus, the CCE has significant thermal efficiency improvement potential over turbofan engines. This thesis seeks to answers the question:

> Can the Composite Cycle Engine achieve future emission reduction targets under consideration of weight penalties and conceptual design constraints on a short-to-medium range aircraft?

The target of this thesis is to identify the true fuel burn improvement of the concept as optimising thermal efficiency only is misleading. An application-oriented conceptual design identifies the key technologies, which are required to implement the cycle. Multidisciplinary methods for meaningful benchmarking of novel engine concepts and detailed evaluation are developed. Engine weight is estimated from the bottom up to capture relevant design and sizing effects. Efficiency and weight are used to evaluate mission fuel burn. This translates into fuel cost and CO_2 emissions as a metric for environmental footprint. Flow path layout and engine sizing determine the mechanical feasibility of the concept. Detailed conceptual design of the CCE, and in particular its piston engine are presented. Multiple operating points are used to size the engine and evaluate performance. The impact at the aircraft level is quantified. A sophisticated model for estimation of NO_x emissions in piston engine and combustor is used to assess applicability to certification scenarios. In addition to these quantitative measures, further disciplines – such as mechanical oscillations or emissions of noise, soot and water vapour – are discussed qualitatively. The presented methods are applied to designs with four-stroke and two-stroke engines, as well as in combination with intercoolers, and with an advanced free-piston engine.

Chapter 2

The Composite Cycle Engine Concept

The integrated assembly of at least two heat engine cycles featuring independent compression, heat source and expansion operating on the same working fluid is denoted as *Composite Cycle Engine*[1] [16]. The first complete cycle is the Joule-/Brayton-cycle, which is conventionally used in turbofan engines. It consists of turbo compression, isobaric combustion and turbo expansion. In the concept investigated in this thesis, the second cycle entirely takes place in a piston engine. The term was established in the scope of the LEMCOTEC project [16]. It was sought in distinction to the well-established term *Compound Engine*, which denotes an engine that uses at least two different principles of power extraction – usually a piston engine followed by a turbine – that contribute to shaft power working on the same fluid.

In this chapter, the benefits of a CCE over the turbofan are discussed for application in a civil transport category aircraft mission. The challenges introduced by the piston engine are discussed by means of built engines. Related studies with composite and compound engine designs are then reviewed to summarize previous findings in the field.

2.1 Thermodynamic Benefits of Composite Cycle Engines

The CCE concept allows for increased thermal efficiency. It improves the thermodynamic cycle by putting a topping cycle upon the Joule-/Brayton-cycle as shown in the temperature T over specific entropy s diagram in Figure 2.1 (p. 4). The higher peak pressure and temperature is the first main thermodynamic benefit of the Composite Cycle. This is enabled by the instationary operation of the piston engine, which reduces the mean thermal load of the material to a technically feasible level. The second main benefit is the (partially) isochoric combustion. This leads to a pressure rise that is achieved by heat addition rather than shaft power as in a turbo compressor. This effectively reduces the required compression power for

[1] Note that the term *Composite Cycle* was rarely used before in the context of *variable cycle* engines (also *augmented cycle* and *convertible cycle*). These engines can alter the cycle during operation to achieve optimal behaviour under highly varied operating conditions. It is often used to switch from turbofan characteristics in subsonic operation to turbojet characteristics during supersonic operation. One example is GE's *Composite Cycle Engine* [15, p. 13-7, Fig-2], which was designed for supersonic operation up to and above Mach numbers of 3.0, and could switch to a pure turbojet mode above $M = 2.0$.

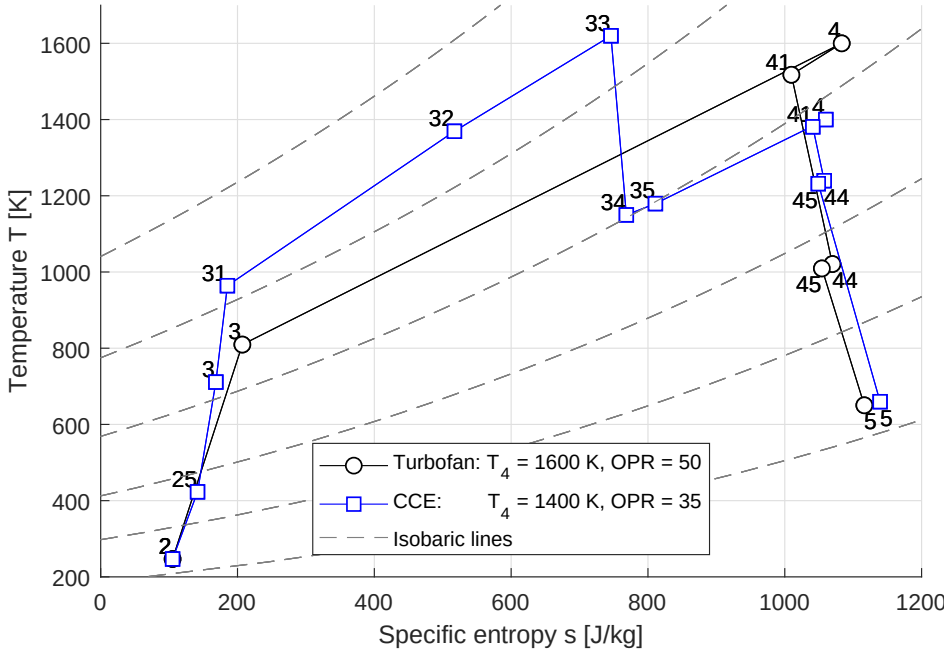

Figure 2.1: Temperature T over specific entropy s diagram of the Composite Cycle in contrast to the Joule-/Brayton-cycle at ToC conditions (adapted from [17]). Station nomenclature according to Figure 3.2. Station 41 after addition of turbine stator cooling air, station 44 after turbine work extraction.

a given target pressure at the beginning of the expansion process. A minor benefit comes from the more efficient compression and expansion process within the piston engine. The reasons are avoidance of tip losses, lower fluidic frictional losses due to much less required wetted area for achieving high pressure, and partially intercooled compression through wall heat losses.

The thermal efficiency in the modern turbofans based on the Joule-/Brayton-cycle approaches technologically viable limits. Further improvements of the cycle are increasingly difficult to achieve and the required leaps in efficiency to achieve emission reduction targets appear unlikely. Current engines can achieve 15 % to 16 % mission fuel burn reductions compared to the year 2000 technological standards [4, 5]. Turbofan engines for the near-to-mid future are projected to achieve 19 % to 26 % shown in Chapter 1 [13, 14, 18]. No significant further improvement potential beyond that point is foreseen.

The SRIA CO_2 reduction target on the propulsion system level is −30 % [1] by 2035 and −43 % CO_2 by 2050. To achieve these targets while ignoring aircraft level cascading effects, overall engine efficiency η_o in an engine for a short-to-medium range aircraft would need to increase from 31 % in 2000 [19] to 44 % and 54 %, respectively. Assuming a long-term improvement of propulsive efficiency η_p to 85 %, thermal efficiency of 52 % and 64 %, respectively, would be required.

Modern aero engines achieve a thermal efficiency of approximately 46 % [17]. A study covering changes in OPR and combustor exit temperature T_4 for generic top of climb conditions (M0.80, FL350, ISA) shows that with further optimisation of the main cycle parameters, an

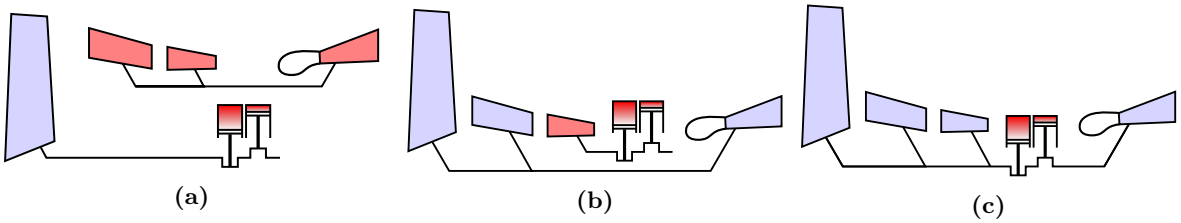

Figure 2.2: Options for CCE turbofan architectures with fan shaft driven by (a) the piston engine, (b) the turbine, and (c) a compound of both.

improvement to 48 % is possible by 2035 at higher OPR and slightly lower T_4 [17]. To reach the efficiency improvement targets, turbo component losses would need to reduce further by 40 % and OPR to increase to 60 to reach 2035 targets. To achieve 2050 targets with the Joule-/Brayton-cycle, turbo components need 100 % component efficiency and an OPR of 120. These numbers assume that engine mass and relative turbine cooling air do not increase.

Several physical limitations impede the achievement of these improvements: first, higher OPR results in smaller volume flow at the high-pressure compressor (HPC) exit, leading to reduced blade height. As the gap between blade and casing cannot be reduced arbitrarily to maintain a margin for transient operation, tip leakage grows, and compressor efficiency reduces [20]. Second, the combustor exit temperature T_3 increases with OPR, which requires heavier and more expensive materials in the last HPC stages. It incurs higher engine cost due to added turbo component stages and more complex component technology. Raising T_3 and T_4 leads to a considerable increase in turbine cooling flow and required cooling effectiveness for a given permissible blade material temperature. Piston engines in the high-pressure part of the core are a solution to the OPR ceiling of turbo engines.

The power provided by the piston engine can be either used for core compression or for the fan. The resulting fundamental architectural options are shown in Figure 2.2. In option (a), the piston engine drives the fan, while a turbine runs the core compression. In Option (b), the piston power is used for compression of the core flow. Option (c) is a combination of both, where the piston engine provides a share of the total shaft power. The number of turboshafts is arbitrary.

Thermodynamically, none of the options is inherently better than another. As long as gross power provided by piston engine and turbine are unchanged, their assignment to individual shafts does not alter the overall balance of fuel flows and net shaft power. Therefore, other criteria may favour one of the concepts. In a previous qualitative assessment of these architectures, the turbine driven shaft in option (b) was shown to be most suitable for a turbofan arrangement [16]. Geometric restrictions in connecting the piston engine to a power sink are low. Mechanical loads are smallest by avoiding couplings between turbo and piston shafts. If the piston engine drives the fan alone as in option (a), it needs to be considerably larger to provide enough power than in the other two options. Therefore, only option (b) is further investigated in this thesis.

Compared to turbo engines, piston engines have several drawbacks. They have high mechanical losses, if they are connected to a crankshaft. These can be of the order of 5 % to 10 %. The operation is intermittent, which leads to lower utilisation of the displacement volume it occupies, higher bulk size, and engine mass. The practical implications are discussed in the next section.

2.2 Piston Engines in Aviation

The history of controlled, powered, heavier-than-air flight started in 1901 with piston engines [21]. Two years later, the Wright brothers performed their first flight tests with a 4-cylinder water-cooled piston engine with a power of 12 kW [22]. Langley experimented with unpiloted aeroplanes with a five-cylinder radial engine that had a power of 2.4 kW and a mass of 3.2 kg [22]. It had one of the lowest ever achieved displacement volume-specific masses of 4.2 kg/L. Even earlier applications of piston engines in aeronautics go back to 1872 in dirigible balloon flights [22]. From that point on, piston engines grew larger in size, power, and number of pistons.

The technological zenith of piston engines was in the 1940s. The highest number of pistons was in the Wright R-2160 Tornado with 42 cylinders and six rows of radial engines in seven banks. The engine had to be cooled by water, as cooling air in the first rows would have heated up to such a degree that cooling was insufficient in the rear rows. It had a shaft power of 1 750 kW. The most powerful planned aeronautical piston engine was the Rolls-Royce Crecy. The Crecy's twelve cylinders delivered a shaft power of 3 100 kW [23]. It used super-charging and an exhaust power turbine for power augmentation. Its specific mass was 0.40 kg/kW based on take-off power. It was developed over five years until 1945 but was never flight tested. The Napier Sabre with 24 cylinders in an H-arrangement had a shaft power of 2 240 kW, the most powerful non-radial aeronautical piston engine to date [24]. The largest single piston displacement volume was achieved on the Charomskiy ACh-30 with a bore of 0.18 m and a stroke of 0.20 m [25]. It was a turbocharged V-12 engine for long-range aircraft.

With the advent of reliable and powerful turbo engines, large aeronautical piston engines abruptly ceased to persist in development. The de Havilland Ghost turbojet entered service on the Comet in 1949, the Rolls-Royce Dart turboprop on the Vickers Viscount in 1953, and the Allison T-56 turboprop engine in 1955. The first turboprop engines had a specific consumption of 320 g/kW h (0.52 lb/hp h), which was 40 % higher than comparable piston engines at the time such as the Wright R-3350 turbo-compound [26]. Thermal efficiency levels similar to the last large piston-based aero engines were reached only recently in 2009 with the Europrop TP400 engine [27]. The reasons why turbo engines were commercially more viable at the time are important for understanding the main drawbacks of piston engines. If these issues are solved, piston engines can be a competitive alternative in the future.

Size and Weight: The Allison T-56 turboprop specific mass of 0.25 kg/kW – three times lower than that of comparable in-service piston engines such as the Wright R-3350 turbo-compound with 0.74 kg/kW, or the non-compounded Wright R-3350 R-18 with

0.80 kg/kW. The bulk volume of the Wright was 32 % larger than the Allison's, and the diameter was more than double with 1.42 m.

To make a like-for-like comparison, the Piper PA-46 aircraft will be featured on the next pages. It entered service in 1983 and can be equipped with either the Lycoming TIO-540 piston engine (aircraft sales name Piper Malibu or Piper M350, [28]) or the PT6A turboprop engine (aircraft sales name Piper Meridian or Piper M500, [29]). Both engines were developed in the late 1950s. While the Lycoming has a specific mass of 1.0 kg/kW, the PT6A denotes 0.30 kg/kW at maximum power[2]. Despite lower engine mass and larger tank capacity, the PT6A equipped Piper has a 340 nmi shorter mission range due to 35 % higher specific fuel consumption. The aircraft with piston engine would have further saving potential when sizing the aircraft for the same mission range. Despite higher maximum take-off weight (MTOW) of the piston-powered aircraft, the payload with full fuel is 5 % smaller. Therefore, a novel engine concept with piston engines must achieve lower engine mass and bulk size. Otherwise, the engine could be too heavy or large for under-wing installation and lead to cuts in payload.

Reliability and Maintenance: A common perception about piston engines is that they have relatively low reliability and short maintenance intervals. An important measure to quantify reliability is the in-flight shutdown (IFSD) rate, expressing the number of in-flight shutdowns per flight hour. A low IFSD on an aircraft-engine combination is required to receive extended operations (ETOPS) certification. This permits an airline to fly for extended time spans with one engine on a twin-engine aircraft in case of an IFSD [30, 31]. For example, ETOPS 120 allows an aircraft to fly for two hours on one engine to the closest airport at any given time during a mission. To get ETOPS 120 certification, an IFSD rate of less than 5×10^{-5}/h must be proven on an engine type in operation. For ETOPS 180, less than 2×10^{-5}/h is required. This was later translated into a dual engine failure probability of less than 0.3×10^{-8}/h [32]. For more than 180 minutes, a rate lower than 1×10^{-5}/h is required. Achieving ETOPS is necessary to cross oceans on a shorter or direct route.

Some reference numbers comparing IFSD rates are shown in Figure 2.3 (p. 8). The ICAO fleet average of piston engines in 1953 was 35×10^{-5}/h. The Wright R-1820, which was used on the DC-3, had already achieved 9×10^{-5}/h [33]. General aviation piston engines of the 1960s were still more reliable with rates of 4.6×10^{-5}/h on single-engine aircraft and 2.3×10^{-5}/h on twin-engine aircraft [34]. The latter were almost reliable enough to achieve ETOPS 180. Of the engine-related accidents, 51 % could be attributed to pilot error, for example inadequate pre-flight planning or the mismanagement of fuel. In 10 % of the cases, improper maintenance, servicing and inspection could be attributed to the accident. These errors can be avoided in commercial aviation, meaning that ETOPS certifiable reliability levels appear feasible. Early large turbofans demonstrated similar IFSD rates of 40×10^{-5}/h [35]. Modern large turbofan engines averaged a rate of 1×10^{-5}/h in 2003 [31], and can be as low as 0.1×10^{-5}/h for individual engine models.

[2]The engine has a rated power of 630 kW, but it is derated to 370 kW in the Piper PA-46.

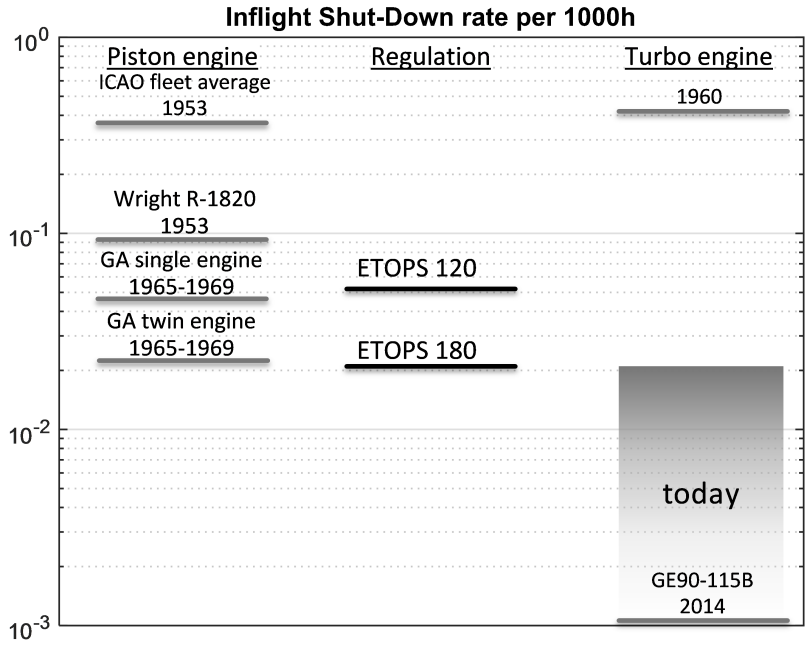

Figure 2.3: IFSD rates of piston engines in contrast to large commercial aircraft regulations and turbo engines.

A study investigating accidents on rotorcraft over three decades showed similar probability for engine-related accidents on piston and turbine single-engine vehicles around 30 % [36]. The rate of engine-related accidents was also similar with about 20 accidents per 1 000 registered rotorcraft. They highlighted, however, that helicopters with a single-turbine engine are safer than with a single-piston engine, when considering higher utilisation rates for single-turbine rotorcraft. The comparability was limited as typical usage and pilot experience differed significantly between both categories, and as most accidents could be attributed to human error.

Comparing the Piper PA-46 aircraft engines, time between overhaul (TBO) of the Lycoming engine is 2 000 h, and that of the PT6A is 3 600 h. The difference between the two is less than a factor of two. Moreover, the aircraft with PT6A engine is 900 000 $ (73 %) more expensive, partially due to a considerably higher engine price tag. If piston engines were built with the same level of manufacturing cost and thus technical sophistication, the TBOs can be expected to converge. Engine overhaul cost per flight hour for the PT6A is three times higher than that of the Lycoming piston engine, despite higher TBO.

Low flight altitude and speed: Naturally aspirated piston engines have a significant power lapse in altitude. Power decreases with air density, as engine speed cannot be increased due to mechanical constraints. Transport category aircraft with piston engines from the 1940s and 1950s had a cruise altitude of 15 000 ft (5 000 m). This is insufficient to ensure over-the-weather flight. So, piston engine powered aircraft were susceptible to bad weather, leading to diverted and cancelled flights. Only over-sizing of the piston

engine could have alleviated the problem for naturally aspirated piston engines. One way to cope with the restricted power supply at altitude was a reduction of airspeed. With turboprop engines in connection with pressurised cabins, cruise altitude could be increased to over 20 000 ft (6 000 m) with the Rolls-Royce Dart powered Vickers Viscount [37] as turbo engines can process higher volume flows. Later with turbojets like the de Havilland Ghost, altitudes over 30 000 ft (9 000 m) were feasible.

Turbocharged piston engines alleviate the problem of the constant displacement volume by increasing air density before induction [38]. The turbo-supercharged Wright R-3350 TC for the Lockheed Super Constellation, and the turbo-supercharged Wright R-2800 Double Wasp for the DC-6 both reached a flight altitude of 23 000 ft (7 000 m). The super-charged Junkers Jumo 207 with a charging pressure of 3 bar was operated at altitudes over 40 000 ft (12 200 m) [23].

Looking at the Piper PA-46, the turbocharged Lycoming powered M350 has a cruise altitude of 25 000 ft (7 600 m) and an airspeed of 213 kts (110 m/s). In contrast, the PT6A powered M500 has a cruise altitude of 30 000 ft (9 100 m) and an airspeed of 260 kts (134 m/s). The Lycoming is charged with a boost of 1.2 bar, which almost remedies the differences in flight speed and altitude. Turbocharging therefore removes the lack of power in altitude.

Fuel price: The fuel price was at an inflation-adjusted all-time low in the 1950s and -60s as shown in Figure 2.4 (p. 10). Consequently, the incentive for operators to use fuel-efficient engines was relatively low. While it is hardly conceivable that operators today would use an engine with 40 % higher specific consumption, it was viable at that time. The advantages of turbo engines mentioned above could outshine their lower efficiency. Today, fuel price has a large share of the operating cost of an aircraft. It is about a third of the direct operating cost on a short-to-medium range aircraft and more than 40 % on a long-range aircraft [39].

The advancement of progressive engine technology is subject to many unknowns and very costly. Market boundary conditions dictate the likelihood of success for novel technologies. A famous example is the open rotor research conducted mainly during the 1980s. The open rotor engines GE Unducted Fan (UDF) [41] and PW/Allison 578-DX were flight-tested in 1987 and 1989. Thus, they reached TRL 6. At the same time, the inflation-adjusted fuel price declined to a 15-year low. The open rotor concept development was consequently cancelled in 1989 [41], when McDonnell Douglas decided to equip the MD-90 with V2500 turbofans rather than open rotor engines. The low fuel price was one of the reasons for this decision [42]. In the 2000s, research and development recommenced with the Clean Sky research engines SAGE 1 by Rolls-Royce and SAGE 2 by SNECMA [43], or by GE in the CLEEN program [41]. Coincidentally, the fuel price increased considerably during that time. The current fuel price is lower than in the 2000s but still at a relatively high level, which may incentivise the development and use of fuel-efficient engines.

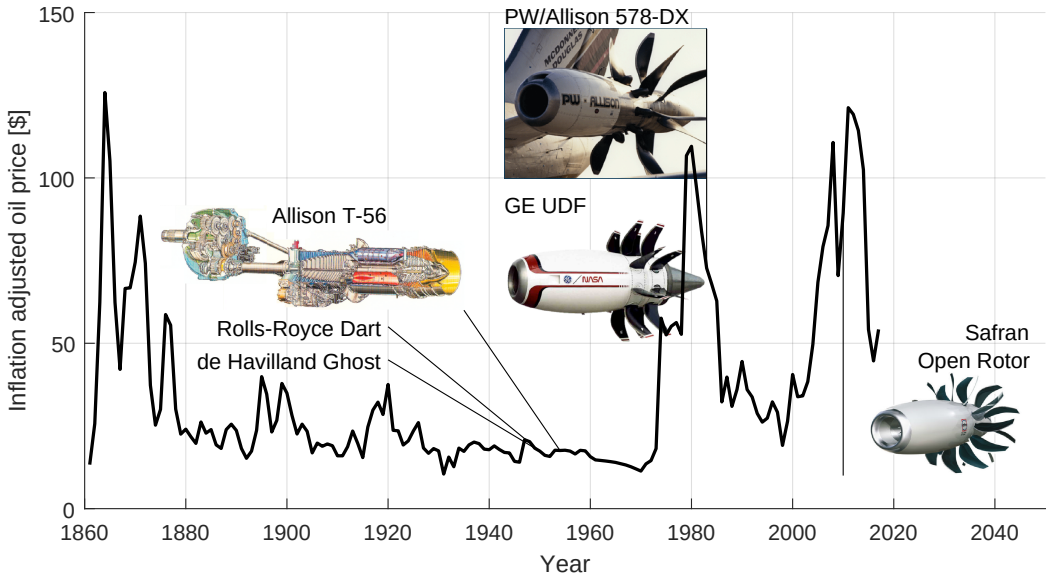

Figure 2.4: Inflation-adjusted fuel price over time [40].

After piston engines were supplanted by turbo engines in large aeronautical applications, the development of aeronautical piston engines came to a halt. Piston engines that were further used in general aviation were designs from the 1960s such as the afore-mentioned Lycoming TIO-540-AE2A. Only in recent years, the development of novel small-scale designs commenced. Thielert developed the TAE 125 engine, now under the names CD135 and CD155 by Technify Motors, running on kerosene with a specific consumption as low as 214 g/kW h (0.352 lb/hp h). Austro Engines also develops new aeronautical piston engines running on kerosene. In the European Commission (EC) funded Clean Sky programme, Austro Engines developed the AE440 V-8 diesel engine for helicopter application with a specific dry mass of only 0.6 kg/kW [44].

Piston engine efficiency has clearly improved over the past century. The trend of brake specific fuel consumption (BSFC), i.e. referring to shaft power, over time is illustrated in Figure 2.5 (p. 11). Modern marine piston engines achieve a specific consumption of about 180 g/kW h (0.296 lb/hp h) and down to 166 g/kW h (0.273 lb/hp h) at full power in the MAN S90ME-C9 two-stroke diesel engine [45]. Still, it is difficult to predict what efficiencies large aeronautical piston engines could achieve with technological progress since engines in other applications are subject to different design goals. The lowest BSFC from all engines reviewed in this thesis is achieved by the projected turbo-compound high altitude long endurance (HALE) engine ERAST TE95-627 [46] with 148 g/kW h (0.243 lb/hp h). In comparison, the CCE technological target for the pure piston engine appears rather modest with about 350 g/kW h. However, this figure only refers to the piston engine itself. Since it is highly charged, the cycle starts at a high temperature and pressure level. The pressure ratio over the piston engine is, therefore, small and the isolated cycle efficiency relatively low, while overall core engine

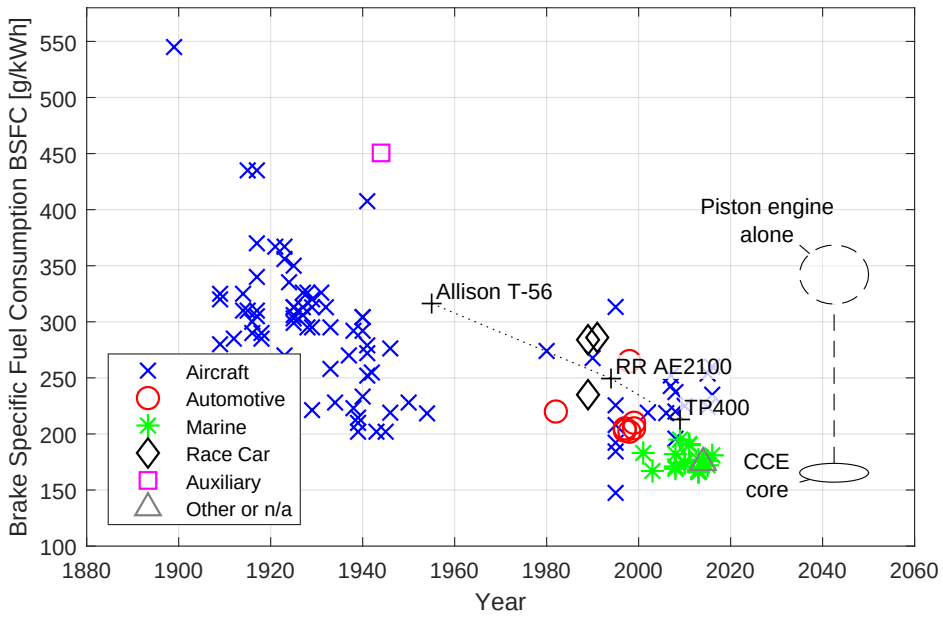

Figure 2.5: Brake specific fuel consumption BSFC of piston engines over time.

efficiency is better than in a naturally aspirated piston engine. The entire CCE core engine would achieve a BSFC[3] around 175 g/kW h.

With current technological advances in motor engineering and research, the past flaws of piston engines can be overcome. Lower reliability and higher maintenance efforts have been shown to be manageable. The inflation-adjusted fuel price is on a high level today. The findings from this section highlight that a CCE should deviate from past aeronautical piston engines in two main points: First, a turbine should serve as the main power source to leverage its outstanding power-to-mass ratio and to reduce the required shaft power from the piston engine. Second, the piston engine should be highly turbocharged to reduce its size and mass for a given power. This also eliminates limitation of flight altitude and speed.

2.3 Experience and Research on the Composite Cycle Engine Architecture

Examples of research and application of the CCE and the turbo-compound principle showcase the benefits of the combination of piston and turbomachinery. Per definition, the CCE and turbo-compound architectures only differ in the existence of a second combustor. In practical applications, however, most turbo-compounds used the piston engine as the main power provider, while the CCE uses the piston engine only to put the highly efficient topping cycle into effect.

[3]This is a synthetic number for a turbofan as a fraction of the fan power is used to pressurise the core. This fraction has been deducted from the shaft power here.

In a turbo-compound, a turbine is added to the piston engine for power augmentation. It operates on the piston exhaust pressure and remaining heat. This leads to lower fuel consumption and higher specific power [47]. Turbo-compounding famously appeared in operation in the 1950s with the Wright R-3350 TC [48] and as a concept in the Napier Nomad E.145 [24, 49]. Their general arrangements are depicted in Figure 2.6 (p. 13). In both engines, the piston engine provides the main share of the shaft power, and is only supported by a turbine driven by the exhaust gas from the piston engine. Both engines feature a turbo compressor that charges the piston engine. In the Wright R-3350 TC, the turbo compressor is coupled with the piston shaft and works as a supercharger. The compressor achieves a manifold pressure of 1.3 bar. The blow-down turbine recovers the kinetic energy of the exhaust flow and contributes about 15 % of the shaft power.

In case of the Napier Nomad E.145, the compressor is coupled to the turbine. Only the net power of both is transmitted to the piston shaft via an infinitely variable gear displayed in the top right of Figure 2.6 (p. 13)(b). The gear moderates speeds between the turbine-compressor assembly and the piston engine. The speed on the turbo shaft can then be chosen freely during operation in part load. The turbo shaft contributes about 13 % of the net shaft power after deduction of compressor power. The turbine alone provides about the same amount of power as the piston engine. The Napier Nomad E.145 boosts the pressure before the piston engine to 6 bar. The pressure ratio increases in altitude to obtain enough engine power. Its efficiency is unmatched by turboprop engines until today. Both engines improve efficiency over pure piston engines considerably.

The term *composite engine* appeared in advertisements for the previously mentioned Napier Nomad E.145 engine [51]. It was then used to promote its composition of “half diesel” and “half gas turbine”. Its architecture is a typical turbo-compound. Its predecessor, the Napier Nomad E.125 prototype, was developed in 1945 and is a CCE according to the definition used here [49]. The E.125 features an axial compressor driven by a turbine followed by a radial compressor driven by a piston engine. It has two separate shafts. On the first, the piston engine drives a radial compressor. On the second, the turbine drives the axial compressor. Both shafts contribute their excess power to independent, counter-rotating propellers. An auxiliary constant pressure combustor after the piston engine is used for power augmentation in high power conditions, such as take-off. The peak pressure of 138 bar achieved by the piston engine exceeds the pressures achieved by any turbo engine.

An application area of highly charged piston engines are HALE platforms. These use piston engines because they make better use of the available oxygen in the air [52, 53]. A turbo engine requires four times as much air mass flow rate as a spark ignition engine for a given power. Moreover, the low BSFC of turbocharged piston engines is almost independent from altitude. When the piston engine inlet conditions are kept constant to sea level ambient pressure, the charging pressure ratio can be increased to 125 at a flight altitude of 100 kft [52]. The extremely high pressure ratio raises the thermal efficiency potential by 25 % to 40 %, which is counteracted by increasing losses in the compression and intercooling system. Projected BSFC in such a turbo-compound application can be as low as 175 g/kW h (0.29 lb/hp h)[52].

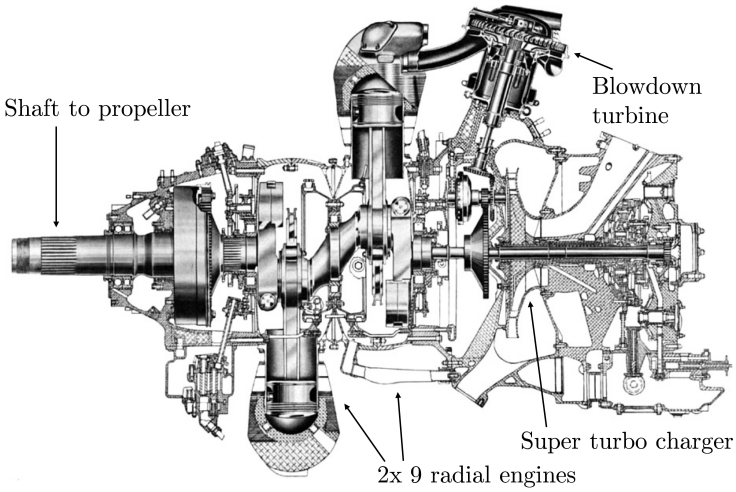

(a)

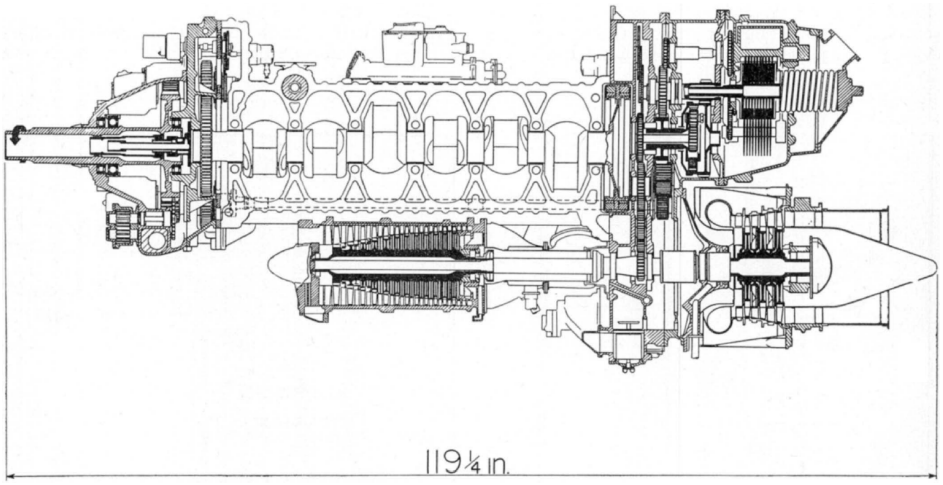

(b)

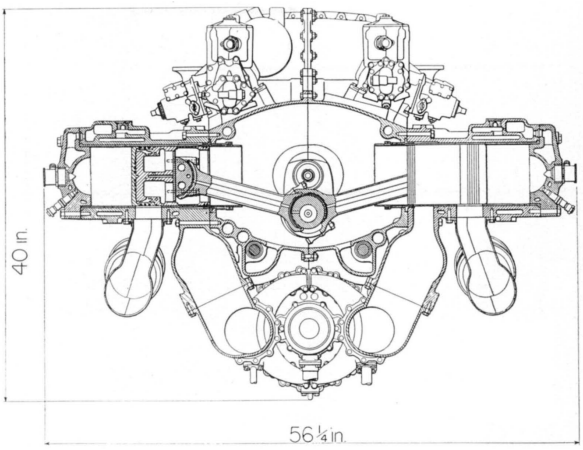

(c)

Figure 2.6: General arrangements of (a) the Wright R-3350 TC [50], and (b,c) the Napier Nomad E.145 [24].

The Grob G 850 Strato 2C high altitude platform used an off-the-shelf Continental piston engine as its core and sole power provider. It was charged with a three-spool turbo compression system. Thus, it flew up to 60 kft, the highest altitude ever flown by a piston engine. It was capable of flying up to 78 kft [54]. In the NASA research programme Environmental Research Aircraft and Sensor Technology (ERAST), many propulsion options for a HALE platform for flight altitudes up to 100 kft were investigated on paper [46, 55]. At peak altitude, the turbo pressure ratio is between 85 and 95. Similar to the Strato 2C engine, they envisaged a three-spool turbocharger system with three intercoolers. They also investigated turbo-compound arrangements with turbine contributions up to 24 % of the shaft power. The lowest projected BSFC of 157 g/kW h (0.26 lb/hp h) was estimated on a turbo-compound two-stroke diesel engine.

Compound and CCE concepts were also subject in many research publications, which investigated the viability under various operating scenarios or for special applications. In the 1980s, NASA investigated concepts for turbo-compound and highly turbocharged piston engines for helicopter application with a power of 750 kW [23]. They drew the conclusion that turbocharged piston engines would not be competitive with respect to mass. Thus, turbo-compounding would be required. Two-stroke engines were found to be favourable over four-stroke engines due to lower mass, despite slightly lower efficiency. A pressure ratio before the piston engine above 10.0 could help to reduce piston engine mass. A cooler before the piston engine was suggested to reduce the thermal load on the piston engine and increase engine life at the cost of 6 % BSFC. A specific mass of 0.26 kg/kW was projected. The turbine would provide a net contribution of 24 % of the total shaft power at full load. Fuel consumption would reduce by 31 % at 20 % higher engine mass compared to a gas turbine.

A turbo-compound concept for utility vehicles was designed and tested by the Cummins Engine Company in the 1970s and early 1980s [56, 57]. They achieved a fuel burn improvement of 20 % over a conventional utility diesel engine. Like the NASA concept, a power turbine was used to augment piston engine power, and a separate turbocharger was employed. After extensive testing, normal wear was observed on the piston engine.

Another study with a turbo-compound engine concept raised mean effective pressure p_{mean} of a marine diesel from 22 bar to up to 80 bar to increase power from a given displacement volume [58]. Power quadrupled with small improvements in efficiency. Heat losses tripled, and peak pressure increased to 720 bar. When restricting peak pressure to 250 bar, power could still be 2.5 times higher. The approach was then transferred to an aeronautical one-shaft CCE concept [59]. A charge pressure ratio of 9.1 and a pressure ratio across the four-stroke piston engine of about 2.0 was specified. Depending on piston engine mass, a fuel burn improvement of 8 % to 12 % could be achieved on a short-to-medium range aircraft. A different study for an aeronautical CCE in the 500 kN thrust class found a potentially very high mass up to 30 t. However, mass could reduce considerably, if small trades in efficiency were made [60].

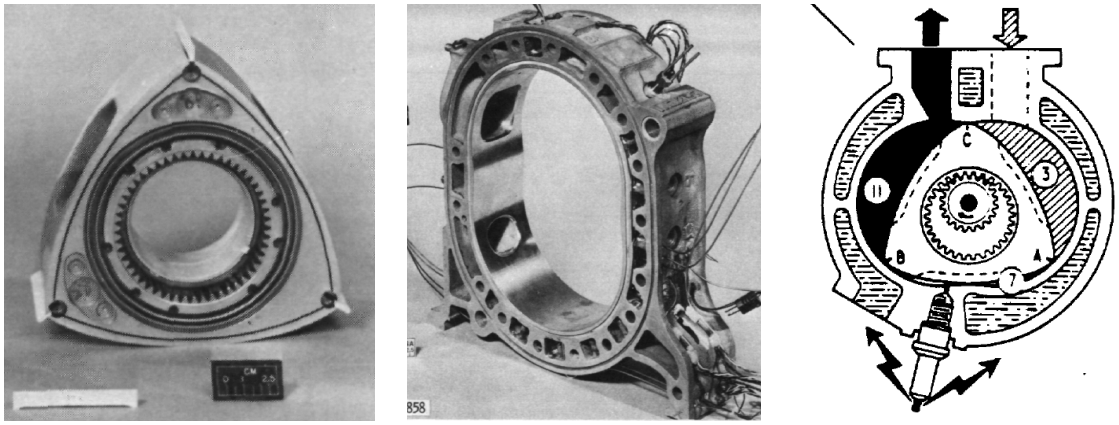

(a) (b) (c)

Figure 2.7: Wankel-type rotary engine (a) rotor and (b) casing [62], and (c) cross-sectional schematic drawing [63].

2.4 Alternative Cycles and Closed Volume Combustion Concepts

Other approaches were pursued to achieve higher power densities with closed volume combustion. The rotary engine is a closed volume combustion engine that directly produces torque along the engine axis. Thus, no conversion of linear into revolutionary motion is needed. The Wankel-type rotary engine is the most popular concept of this engine class. It is constituted by a disk that rotates eccentrically around the engine shaft. The most renowned configuration with three chambers is depicted in Figure 2.7. The volume covered by the movement of the rotor constitutes the engine displacement volume, and the perimeter is enclosed by the casing. This type of engine can rotate around another shaft. Therefore, it can be built around the low-pressure spool of a two-spool turbofan and be placed co-axially to the turbo components. This allows for a very compact flow path layout [61].

As a further benefit, rotary engine concepts typically feature lower specific mass of 0.4 kg/kW to 0.5 kg/kW [64, 65] than crankshaft bound piston engines that typically have a mass that is higher than 1 kg/kW. This is a result of the engine layout, which features three chambers and, hence, performs three cycles simultaneously. The engine has a four-stroke characteristic with all connected benefits. Particularly, the scavenging behaviour of such an engine is superior to that of a two-stroke engine [66]. Mean and peak cycle temperatures are lower, and inlet and outlet pressure are decoupled since both valves are opened separately. Thus, it is possible to provide a pressure boost at the cost of reduced shaft power. Mechanical engine oscillations are much lower than in piston engines and only of second order.

The rotary engine has some drawbacks. The feasible geometric compression ratio of the engine is limited by the envelope covered by the rotor and typically lower than in piston engines. The chamber geometry results in a very slim volume during combustion [65], as can be seen at the bottom of Figure 2.7(c). This leads to delayed, and sometimes incomplete combustion, as well as high soot production. The rate of heat release can be expected to be

lower than in piston engines. The rotor or casing geometry can be compromised to achieve a more suitable geometry for combustion, such as a pocket in the rotor or a pilot combustion chamber. These measures result in an even lower geometric compression ratio.

The heat release always occurs at the same location of the casing, exposing it to high thermal load. In contrast, hot surfaces in piston engines are exposed to cool air during the scavenging stroke. Another technical challenge is the sealing of the engine since the edges separating the chambers move relative to the steady casing. This leads to leakage between the chambers and restricts the permissible peak pressure in the cycle. Current research projects have achieved up to 100 bar [64, 65], which is still comparably low. Both leakage and the low peak pressure are the main sources for inferior performance compared to piston engines [67, 68].

The rotary engine concept will not be investigated further in this thesis. It may be viable in cases where small packaging is required, flow path layout with piston engines would be too complicated, piston engine oscillations are excessive, or to make use of the four-stroke engine characteristics, such as in gas generator operation. Former examinations of this concept showed a thrust specific fuel consumption (TSFC) improvement of 14 % with an increase in mass of 5 % [69] against a turbofan of similar technological level. A different study predicted 4.5 % improvement with an increase in mass of 31 % [70]. The configuration that leads a turboshaft through the rotary engine axis is geometrically challenging and may lead to large and heavy disks [70]. Studies comparing rotary engines with piston engines in aeronautical applications show a competitive BSFC with 20 % lower specific mass [62]. The company LiquidPiston investigates an inverted rotary engine design with improved combustion chamber geometry and static seals. They have only presented a 2.4 kW demonstrator so far, but predict a relative increase in efficiency of the order of 10 % over conventional piston engines [71].

Many other concepts with isochoric combustion have been proposed. Pulsed detonation as shown in Figure 2.8 (p. 17)(a) is achieved by detonating a fuel-air mixture in tubes [72]. The detonation wave then travels downstream with high pressure spikes to a turbine. This leads to highly unsteady operating conditions in the high-pressure turbine (HPT) with an order of magnitude pressure oscillation. This results in highly varying incidence angles on the turbine rotor blades and severe penalties on HPT efficiency. Equivalent steady state values can be as low as 27 % [73], or at best 70 % at low utilisation of the combustor tubes [74]. The improvements through isochoric combustion could be vitiated by the degradation of turbine efficiency [75]. Turbine film cooling is difficult to achieve as the cooling flow could reverse during pressure spikes. To avoid this, cooling air pressure could be increased to the pressure spike level, or internal blade cooling could be used.

The wave rotor as shown in Figure 2.8 (p. 17)(b) uses complex shock systems to achieve isochoric combustion [76, 77]. It delivers a comparatively steady mass flow, but wall cooling, and particularly off-design performance are critical issues when the finely concerted shock system falls out of synchronisation. Moreover, thermal expansion of the rotor and sealing of the rotor surfaces is technically not mastered [78]. Therefore, only special purpose concepts envisage a wave rotor for future applications.

In conclusion, other isochoric combustion technologies currently fall behind the maturity of piston engines and suffer from major challenges that have not been solved to date. Therefore,

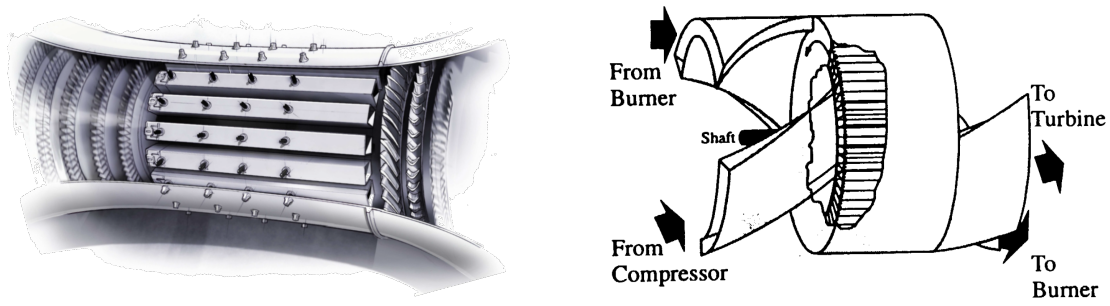

(a) (b)

Figure 2.8: Schematic illustration of (a) a pulsed detonation engine [75], and (b) a wave rotor engine [76].

they will not be considered in this thesis. As an option, the secondary combustion chamber in the CCE concept could be either of these technologies. This promises only small improvement as most of the fuel is burnt in the piston engine during the mission fuel burn relevant cruise phase. The additional complexity does not appear to be justified.

Many other candidate technologies for future aero engines are being investigated, and no clear favourite has emerged, yet. For example, electrification of the propulsive drive train has received increasing attention. The first major variants are parallel-hybrid electric architectures that provide a part of the source energy as electrical energy stored in batteries aboard the aircraft. Battery energy density limits the achievement of significant reductions in fuel and energy consumption. For applicability in passenger aircraft, a minimum a system energy density of 1 000 W h/kg has been identified in past studies for beneficial application in short-to-medium range passenger aircraft [19, 79–81]. Benefits can be realised on design ranges up to 1 000 nmi [19]. The introduction of 50 % electrification could potentially reduce fuel burn by 14 %, while total energy consumption would increase by 7 % [80]. Current battery technology achieves system energy density of 200 to 250 W h/kg on cell level [82], and it is not clear whether the required improvements can be achieved in batteries fulfilling the safety and reusability requirements for commercial aviation. Including overall CO_2 emissions with electricity production and a projected energy mix, viable mission ranges with net savings are further reduced [19]. Also, hybrid-electric concepts require major changes in the airport infrastructure. In conclusion, this technology is not a competitor for civil passenger transport class aircraft.

In contrast, the CCE concept uses drop-in fuels. It is compatible with a potential future shift to biofuels or hydrogen. The outer engine mould line remains the same, and the concept does not require additional components outside of the engine, such as electrical systems. The interface between aircraft and engine does not alter except for the required adaption to increased engine weight. Thus, the aircraft architecture can be retained, just like the traditional aircraft and engine design process. No complicated interactions between aircraft and engine manufacturers are required. Lastly, the components foreseen in the CCE are well known and at respectively high TRL. Hence, the technology and development risk is lower than with unproven technologies.

Chapter 3

Methods

This chapter introduces methods for multidisciplinary design of CCEs. First, methods for performance simulation of turbo and piston engines are presented. Their outcomes are used for the estimation of flow path and mass. Then, metrics for impact at the aircraft level will be shown. Next, effects due to instationary operation of the piston engine are assessed. Finally, emissions of CO_2, NO_x, noise and others are discussed. In this chapter, representative operating conditions from the CCE simulations presented later in this thesis (Chapter 5) are used to illustrate the impact of assumptions made.

3.1 Fluid Properties

The simulation of thermodynamic cycles requires the knowledge of fluid properties every time changes to the fluid state occur. In gas turbine engines, wide ranges of pressures and temperatures are covered. Consequently, the assumption of ideal gas properties, i.e. constant specific heat capacity c_p, and heat capacity ratio γ causes errors, which are too large for accurate calculation of central performance metrics such as thermal efficiency η_{th} [83]. Therefore, half-ideal gas properties are used within the scope of this thesis, where the gas properties are dependent on temperature T but not pressure p. The introduced error by neglecting the impact of pressure is small for the range of pressures observed in a gas turbine engine[1]. The additional computational effort was avoided in this manner.

The fluid properties were obtained with the NASA Chemical Equilibrium with Applications (CEA) database [84, 85]. It contains coefficients a_i for polynomial representation of the fluid properties for all relevant species, e.g. N_2 and O_2, as shown for specific molar heat capacity C_p° in Eq. (3.1) [86]. The polynomials are specified for ranges from 200 K to 1 000 K, and from 1 000 K to 6 000 K. The polynomials for the enthalpy are obtained by integration according to Eq. (3.2) and Eq. (3.3), with the molar enthalpy $\Delta_f H_{298}^\circ$ and the molar entropy $\Delta_f S_{298}^\circ$ of the formation at 298.15 K. For each temperature range, seven coefficients a_i and two integration constants b_i are provided in tables.

[1] The difference in specific heat capacity c_p between 1 bar and 100 bar is 0.3 % at 1 800 K, and 0.01 % at 1 500 K. The integral error in a Joule-/Brayton-cycle is negligible.

$$\frac{C_p^\circ}{R_m} = \frac{a_1}{T^2} + \frac{a_2}{T} + a_3 + a_4 T + a_5 T^2 + a_6 T^3 + a_7 T^4 \tag{3.1}$$

$$\begin{aligned}\frac{H^\circ}{R_m} &= \frac{\Delta_f H_{298}^\circ}{R_m} + \int_{298.15\,\mathrm{K}}^{T} \frac{C_p^\circ}{R_m} \mathrm{d}T \\ &= -\frac{a_1}{T} + a_2 \ln T + a_3 T + \frac{a_4 T^2}{2} + \frac{a_5 T^3}{3} + \frac{a_6 T^4}{4} + \frac{a_7 T^5}{5} + b_1\end{aligned} \tag{3.2}$$

$$\begin{aligned}\frac{S^\circ}{R_m} &= \frac{\Delta_f S_{298}^\circ}{R_m} + \int_{298.15\,\mathrm{K}}^{T} \frac{C_p^\circ}{R_m T} \mathrm{d}T \\ &= -\frac{a_1}{2T^2} - \frac{a_2}{T} + a_3 \ln T + a_4 T + \frac{a_5 T^2}{2} + \frac{a_6 T^3}{3} + \frac{a_7 T^4}{4} + b_2\end{aligned} \tag{3.3}$$

The properties of mixtures of species are calculated by summation of the individual properties weighted by their molar fraction. Air is modelled as a composition of 78.0840 % of nitrogen (N_2), 20.9476 % of oxygen (O_2), 0.9365 % of argon (Ar), and 0.0319 % of CO_2. Further species are neglected. The (mass) specific properties are then obtained by division through the molar mass M of the species, e.g. $c_p = C_p^\circ / M$. Since pressure dependency is not considered, all properties were evaluated at a pressure of 100 bar in accordance with the commercial gas turbine simulation environment GasTurb®. High pressure turns down the amount of dissociation and, thus, reduces non-linearity at high temperatures. Neglecting dissociation may result in a slight over-prediction of engine performance as molecules may not recombine during expansion in a real engine. The effect of excitation of vibrational modes in molecules at high temperatures is retained.

Combustion is modelled for kerosene, specifically Jet-A1 fuel, at a fuel temperature of 298 K [87]. In the NASA CEA, Jet-A1 fuel is chemically represented as hydrocarbon with the molecular formula $C_{12}H_{23}$. The ideal reaction with air (neglecting Ar and CO_2) in dependence of the air number ϕ is given in Reaction (3.4). The resulting stoichiometric fuel-air-ratio is $\mathrm{FAR_{st}} = 0.0682$ ($\phi = 1$, air-fuel-ratio = 14.67). In the CEA database, a fuel heating value FHV of 43.031 MJ/kg is specified. The value used in this thesis is the Jet-A1 certification minimum FHV of 42.80 MJ/kg [88]. FAR is corrected accordingly in the engine simulation.

$$\begin{aligned}&\phi\ \mathrm{C_{12}H_{23}} + 17.75\ \mathrm{O_2} + 3.7738 \cdot 17.75\ \mathrm{N_2} \\ &\qquad \longrightarrow 12\phi\ \mathrm{CO_2} + 11.5\phi\ \mathrm{H_2O} + 17.75(1-\phi)\ \mathrm{O_2} + 66.9852\ \mathrm{N_2}\end{aligned} \tag{3.4}$$

The combustion of kerosene adds an additional dimension to the fluid properties. The products of combustion in the gas, H_2O and CO_2 need to be considered. Particularly at high temperatures, by-products such as carbon monoxide (CO) and hydroxide (OH) form due to incomplete combustion and dissociation. Here, equilibrium composition is assumed at all conditions. This assumption neglects the incomplete recombination of combustion products such as CO and OH, after they were created at high temperatures. This simplification is accepted to reduce computational effort. Otherwise, the chemical composition of the

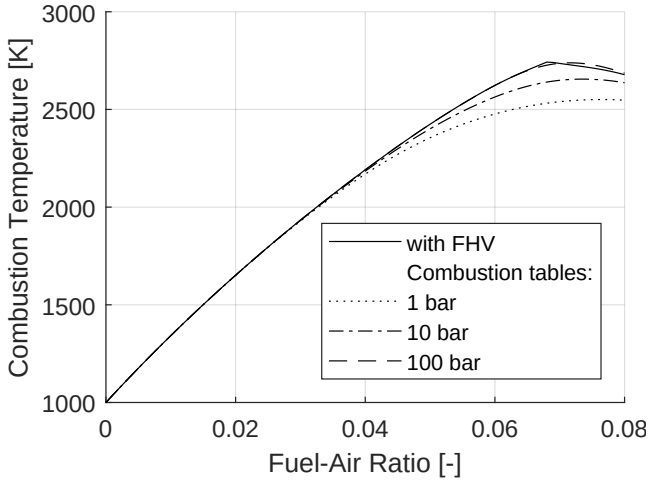

Figure 3.1: Combustion temperature in dependence of FAR and pressure p for combustor entry temperature $T_3 = 1\,000\,\mathrm{K}$.

gas would need to be modelled and traced throughout the engine, and their properties would need to be recalculated at each station. During combustion, dissociation of molecules plays an important role. Therefore, the combustion pressure p is an additional parameter that is used for calculating combustion composition and its final temperature. Combustion temperature deviates at high FAR as illustrated in Figure 3.1. Lower pressure leads to more dissociation, and consequently lower combustion temperatures. In contrast, the ideal calculation without dissociation is indicated as a solid line. Beyond stoichiometric FAR, the calculation without dissociation becomes erroneous.

The gas properties are pre-calculated and implemented in the engine simulation as gridded tabulated data. The input ranges are summarised in Table 3.1. The properties are obtained with a multidimensional spline interpolation function, which is computationally efficient on gridded data. Entropy is interpolated logarithmically in temperature, because the physical relation between both is logarithmic.

Table 3.1: Thermodynamic properties tables specifying inputs with ranges.

Input	**Unit**	**Range**	**Step size**
Temperature	K	200 - 4 000	100*
FAR	–	0.00 - 0.10	0.01
Pressure (combustion only)	bar	0.1 - 1 000	$\cdot\sqrt{10}$
Output	**Unit**		
Specific entropy s	J/(kg K)		
Specific enthalpy h	J/(kg K)		
Heat capacity ratio γ	–		
Specific heat capacity c_p	J/(kg K)		
Molar mass M	kg/mol		

* 50 K between 200 K and 400 K.

Other gas properties are calculated from the tabulated ones according to Equations (3.5)-(3.8). The specific gas constant R is obtained via the molar mass M and the universal gas constant R_m [84]. The entropy function Ψ is useful for numerical computation of compression and expansion processes. Other important properties – such as the heat capacity ratio γ or inner energy u – are calculated in dependence of these properties according to the fundamental thermodynamic relations [89]. The work potential WP is the extractable specific work when expanding a fluid from a given state with temperature T_1 and pressure p_1 to ambient conditions p_0.

$$R = \frac{R_m}{M} \quad \text{with} \quad R_m = 8.31451\,\frac{\mathrm{J}}{\mathrm{mol\,K}} \tag{3.5}$$

$$\Psi = \frac{s}{R} - \ln\left(\frac{p}{p_{\mathrm{std}}}\right) \tag{3.6}$$

$$\mathrm{WP} = h_1 - h_{0,\mathrm{is}} = h(T_1) - h(T(\Psi_{0,\mathrm{is}})) \tag{3.7}$$

$$\text{with} \quad \Psi_{0,\mathrm{is}} = \Psi_1 - \ln\left(\frac{p_1}{p_0}\right) \tag{3.8}$$

The corrected mass flow rate $\dot{m}_{\mathrm{corr}}$ given in Eq. (3.9) is used in component maps for off-design (see Section 3.2), and for flow path generation. Most importantly, the cross-sectional area A scales linearly with $\dot{m}_{\mathrm{corr}}$ for a given Mach number M [83]. The standard corrected mass flow rate $\dot{m}_{\mathrm{corr,std}}$ given in Eq. (3.11) fulfils the same purpose with the benefit of having the unit kg/s. The standard corrected spool speed $n_{\mathrm{corr,std}}$, and the Reynolds number index RNI with the dynamic viscosity μ are used for loss-scaling in off-design, which will be described in the following section.

$$\dot{m}_{\mathrm{corr}} = \dot{m}\frac{\sqrt{T \cdot R}}{p} \tag{3.9}$$

$$A = \dot{m}_{\mathrm{corr}} \cdot f(M) \tag{3.10}$$

$$\dot{m}_{\mathrm{corr,std}} = \dot{m}\frac{\sqrt{\frac{T}{T_{\mathrm{std}}}\frac{R}{R_{\mathrm{std}}}}}{\frac{p}{p_{\mathrm{std}}}} \tag{3.11}$$

$$n_{\mathrm{corr,std}} = \frac{n}{\sqrt{\frac{T}{T_{\mathrm{std}}}\frac{R}{R_{\mathrm{std}}}}} \tag{3.12}$$

$$\mathrm{RNI} = \frac{\frac{p}{p_{\mathrm{std}}}\frac{\mu}{\mu(T_{\mathrm{std}})}}{\sqrt{\frac{T}{T_{\mathrm{std}}}\frac{R}{R_{\mathrm{std}}}}} \tag{3.13}$$

The standard conditions are specified as:

$$p_{\mathrm{std}} = 101\,325\,\mathrm{Pa} \qquad T_{\mathrm{std}} = 288.15\,\mathrm{K} \qquad R_{\mathrm{std}} = 287.05\,\frac{\mathrm{J}}{\mathrm{kg\,K}} \tag{3.14}$$

All properties displayed in this thesis are total states, if not denoted otherwise. Static conditions are indicated by a lower case "s" subscript. Static states are obtained in dependence of the flow Mach number M. Since the initial static temperature T_s in Eq. (3.15) is unknown, the static state needs to be found by iteration until the condition in Eq. (3.18) is satisfied. The other static parameters can be calculated directly henceforth.

$$a = \sqrt{\gamma R T_\mathrm{s}} \tag{3.15}$$

$$v = M \cdot a \tag{3.16}$$

$$h_\mathrm{s} = h - v^2 \tag{3.17}$$

$$h(T_\mathrm{s}) = h_\mathrm{s} \tag{3.18}$$

3.2 Propulsion System Simulation

The propulsion system was simulated using the Bauhaus Luftfahrt (BHL) in-house simulation environment Aircraft Propulsion System Synthesis (APSS) [90]. It is a component-based, modular program written in MATLAB® [91]. Its detail level and fidelity are similar to GasTurb® [92, 93]. APSS allows to set up and modify arbitrary engine architectures, which is necessary for the appropriate implementation of piston components into the engine. The principal structure of the engine simulation environment has been described in numerous theses [94–98] and books [83, 99, 100]. Therefore, only the fundamental architecture of APSS is described here. Generally, components are described with subscript "1" for inlet conditions and subscript "2" for outlet conditions in deviation to the station nomenclature of an aero engine, which is introduced later.

The engine is simulated in the sequence the air passes through the engine as illustrated in Figure 3.2 (p. 24). The atmosphere is the international standard atmosphere (ISA) with respective temperature deviations ΔT_ISA [101]. The intake features an intake pressure loss. The fan is the first compressor stage. A compression process with a given pressure ratio Π is expressed by means of the entropy functions Ψ according to equation Eq. (3.19) with polytropic efficiency η_pol. The temperature after compression T_2 needs to satisfy Eq. (3.20). The solution can be found by iteration. The required power P for a given mass flow rate $\dot{m}$ is a result. The fan additionally splits the flow into bypass and core stream based on the bypass ratio (BPR). The following intermediate-pressure compressor (IPC) and HPC are simulated accordingly.

$$\Psi_2 = \Psi_1 + \frac{\ln(\Pi)}{\eta_\mathrm{pol}} \tag{3.19}$$

$$\Psi(T_2) = \Psi_2 \tag{3.20}$$

$$P = \dot{m}_1 \cdot (h(T_2) - h(T_1)) \tag{3.21}$$

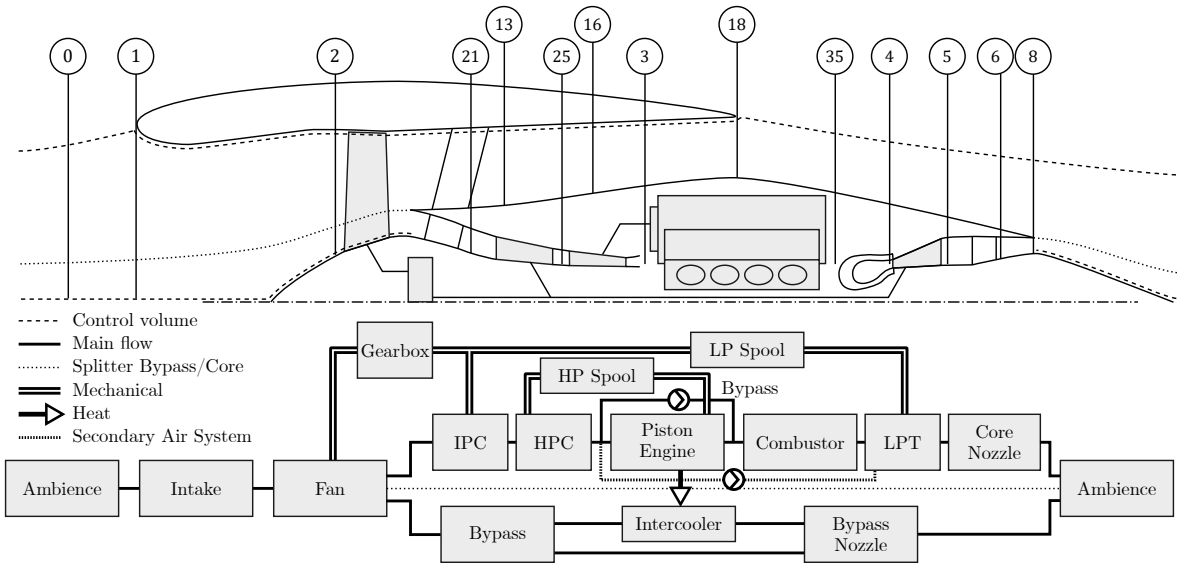

Figure 3.2: CCE schematic general arrangement with station nomenclature (top), and with respective simulation sequence within APSS (bottom).

In the combustor, the required FAR is calculated to match the prescribed exit temperature. The turbine satisfies the power requirement P_{req} of compressors and potential power off-takes with given isentropic efficiency η_{is}. The turbine pressure ratio $\mathit{\Pi}$ is an outcome of the resulting temperature T_2 according to Eq. (3.23). An equivalent single-stage turbine cooling model considers the impact of cooling with mass flow $\dot{m}_{1,\text{cool}}$ and temperature $T_{1,\text{cool}}$ [102]. A part of the cooling air is introduced in the nozzle guide vane (NGV) with the share q_{NGV}, and perfectly mixed with the main mass flow $\dot{m}_{1,\text{main}}$ according to Eq. (3.24) and Eq. (3.25). It fully contributes to the work extraction in the rotor. The remainder of the cooling air is introduced after the rotor and does not produce useful work. If the single-stage cooling model is applied to a multi-stage turbine, the rotor inlet temperature does not match the actual temperature. Relations for cooling air amount calculation need to account for that.

$$h_2 = \frac{h_1 - \frac{P_{\text{req}}}{\dot{m}_1}}{\eta_{\text{is}}} \tag{3.22}$$

$$\mathit{\Pi} = \exp\left(\Psi(T_2) - \Psi(T_1)\right) \tag{3.23}$$

$$\dot{m}_1 = \dot{m}_{1,\text{main}} + q_{\text{NGV}} \cdot \dot{m}_{1,\text{cool}} \tag{3.24}$$

$$h_1 = \frac{\dot{m}_{1,\text{main}} \cdot h_{1,\text{main}} + q_{\text{NGV}} \cdot \dot{m}_{1,\text{cool}} \cdot h_{1,\text{cool}}}{\dot{m}_1} \tag{3.25}$$

The gross thrust F_{G} created in the nozzle is obtained through isentropic expansion to ambient conditions, indicated with subscript "0". The nozzle exit velocity v_2 is obtained through Eq. (3.27). If it is supersonic, the velocity is limited[2] to the speed of sound a_2, and the

[2]Theoretically, the flow could be over-expanded to supersonic velocities with a convergent-divergent nozzle. The increase in thrust is, however, marginal for low supersonic speeds $M < 2$ as present in turbofan engines [83].

Mach number to $M_2 = 1$. In that case, the static nozzle exit pressure $p_{2,\mathrm{s}}$ is recalculated accordingly. The pressure thrust obtained in that case is additionally dependent on the nozzle exit area A_2. The nozzle discharge c_D describes the effectively used cross-sectional area of the nozzle, and the thrust coefficient c_{FG} the actual thrust received from the ideal thrust as a fraction is lost due to a non-uniform exit velocity profile.

$$\Psi_{2,\mathrm{s,id}} = \Psi_1 - \ln\left(\frac{p_1}{p_{0,\mathrm{s}}}\right) \tag{3.26}$$

$$v_{2,\mathrm{id}} = \sqrt{2 \cdot (h_1 - h_{2,\mathrm{s}})} \tag{3.27}$$

$$v_2 = \begin{cases} v_{2,\mathrm{id}} & M_2 < 1 \\ a_2 & M_2 = 1 \end{cases} \tag{3.28}$$

$$F_\mathrm{G} = \underbrace{c_{FG} \cdot \dot{m}_2 \cdot v_2}_{\text{momentum thrust}} + \underbrace{A_2 \cdot (p_{2,\mathrm{s}} - p_{0,\mathrm{s}})}_{\text{pressure thrust}} \tag{3.29}$$

$$A_2 = \frac{\dot{m}_2}{\rho_2 v_2 c_\mathrm{D}} \tag{3.30}$$

Additional components in the engine simulation environment of the CCE architecture are the piston engine, described in Section 3.3, and heat exchangers, described in Section 3.4.

Engine integrated metrics are calculated subsequently. From this point, the engine station nomenclature as depicted in Figure 3.2 (top) is used. The numbering is in accordance with GasTurb [92]. A state-of-the-art (SoA) two-spool GTF architecture, as used in the Pratt & Whitney PW1100G engine, is used throughout the thesis as a baseline platform. Many projected future engines are geared turbofans [11, 13, 18]. Here, a high-speed low-pressure turbine (LPT) drives a high-speed IPC, and through a gearbox a slowly turning fan. This decouples the fan tip speed v_tip from the turbomachinery on the low-pressure spool. This allows for lower stage counts in the LPT, higher fan efficiency and lower fan noise emissions. The HPC is driven by the HPT.

The net thrust F_N is calculated according to Eq. (3.31) in dependence of the flight speed v_0. Eq. (3.32) shows the calculation of TSFC. Overall engine efficiency η_o can be split into propulsive efficiency η_p, transmission efficiency η_tr, and core efficiency η_core according to Eqs. (3.33) to (3.35). The core work potential $\mathrm{WP}_\mathrm{core}$ is defined as the work potential in the LPT after the required power for inner fan and IPC have been subtracted. The product of core and transmission efficiency is thermal efficiency η_th.

$$F_{\mathrm{N}} = F_{\mathrm{G,core}} + F_{\mathrm{G,bypass}} - \dot{m}_2 \cdot v_0 \tag{3.31}$$

$$\mathrm{TSFC} = \frac{\dot{m}_{\mathrm{fuel}}}{F_{\mathrm{N}}} \tag{3.32}$$

$$\eta_{\mathrm{core}} = \frac{P_{\mathrm{core}}}{P_{\mathrm{fuel}}} = \frac{\dot{m}_{\mathrm{core}} \cdot (\mathrm{WP}_{\mathrm{core}} - \frac{1}{2} v_0^2)}{\dot{m}_{\mathrm{fuel}} \cdot \mathrm{FHV}} \tag{3.33}$$

$$\eta_{\mathrm{tr}} = \frac{P_{\mathrm{kinetic}}}{P_{\mathrm{core}}} = \frac{\frac{1}{2}\left(\dot{m}_9 v_9^2 + \dot{m}_{19} v_{19}^2 - \dot{m}_2 v_0^2\right)}{\dot{m}_{\mathrm{core}} \cdot (\mathrm{WP}_{\mathrm{core}} - \frac{1}{2} v_0^2)} \tag{3.34}$$

$$\eta_{\mathrm{p}} = \frac{P_{\mathrm{propulsive}}}{P_{\mathrm{kinetic}}} = \frac{F_{\mathrm{N}} \cdot v_0}{\frac{1}{2}\left(\dot{m}_9 v_9^2 + \dot{m}_{19} v_{19}^2 - \dot{m}_2 v_0^2\right)} \tag{3.35}$$

$$\eta_{\mathrm{o}} = \eta_{\mathrm{core}} \cdot \eta_{\mathrm{tr}} \cdot \eta_{\mathrm{p}} = \frac{v_0}{\mathrm{TSFC} \cdot \mathrm{FHV}} \tag{3.36}$$

A typical engine setup specifies several parameters, which are outputs of the engine simulation, such as engine thrust $F_{\mathrm{N,st}}$. These need to be adjusted by iteration. A typical iteration scheme is shown in Table 3.2. Thrust and fan tip diameter $d_{2,\mathrm{tip}}$ are adjusted via intake mass flow rate and outer fan pressure ratio $\Pi_{2,\mathrm{o}}$. Losses inside the stream tube are accounted for by correcting the net thrust calculated. All thrusts quoted in this thesis denote stream tube thrust. Outer nacelle losses are accounted for in the scope of the aircraft.

Table 3.2: Standard design iteration scheme for a GTF.

Input variable	**Target**
Standard corrected fan mass flow $\dot{m}_{2,\mathrm{corr,std}}$	Fan diameter $d_{2,\mathrm{tip}}$
Outer fan pressure ratio $\Pi_{2,\mathrm{o}}$	Stream tube thrust $F_{\mathrm{N,st}}$
Inner fan pressure ratio $\Pi_{2,\mathrm{i}}$	Fan work split $\Delta h_{o/i}$
IPC pressure ratio Π_{IPC}	Overall pressure ratio OPR
Bypass ratio BPR	Ideal nozzle velocity ratio $(v_{19}/v_9)_{\mathrm{id}}$
IPC tip speed $v_{\mathrm{IPC,tip}}$	IPC speed n_{IPC} = LP spool speed n_{LP}

Other engine performance parameters are defined according to best practice rules within this thesis. The ratio of exhaust jet velocities of bypass to core v_{19}/v_9 was optimised for efficiency. The optimum ratio is approximated with Eq. (3.37), based on bypass duct and turbine exit duct pressure ratios Π_{13-16} and Π_{5-6}, as well as their respective isentropic efficiencies $\eta_{\mathrm{is,fan,o}}$ and $\eta_{\mathrm{is,LPT}}$ [83]. The fan tip speed is estimated in dependence of its pressure ratio $\Pi_{\mathrm{fan,o}}$ [99]. The specific work of the inner fan Δh_{i} reduces with BPR [99]. For the CCE design point, additionally the fan load coefficient ψ is kept constant to the GTF to ensure aerodynamic similarity. It is defined according to Eq. (3.38) with the outer fan specific work Δh_{o} and mean speed of the outer fan $v_{\mathrm{m,o}}$.

$$\frac{v_{19}}{v_9} = \frac{\Pi_{13-16}}{\Pi_{5-6}} \cdot \eta_{\mathrm{is,fan}} \cdot \eta_{\mathrm{is,LPT}} \tag{3.37}$$

$$\psi = \frac{2\Delta h_{\mathrm{o}}}{v_{\mathrm{m,o}}^2} \tag{3.38}$$

To simulate off-design behaviour of the turbomachinery, component maps are used. In off-design, pressure ratio Π and component efficiency are calculated in dependence of standard corrected mass flow $\dot{m}_{\mathrm{corr,std}}$ and spool speed $n_{\mathrm{corr,std}}$. Turbo compressor maps additionally specify the surge line (SL), which may not be exceeded. The surge margin SM in this thesis is defined according to Eq. (3.39). It relates to the surge pressure ratio Π_{SL} at given corrected mass flow rate. During the design point calculation, component maps are scaled to the specified design point pressure ratio, mass flow rate and efficiency. This approach assumes that turbo components of different stage count, loading, and technological standard feature similar off-design behaviour. Therefore, it is important to choose a component map that is close to the desired application in terms of pressure ratio and stage count to avoid significant deviations. The commercial software GasTurb® offers a comprehensive collection of component maps in a standardised format [103]. Sizing effects are considered through the RNI as defined in Eq. (3.13).

$$\mathrm{SM} = \left.\frac{\Pi_{\mathrm{SL}} - \Pi}{\Pi - 1}\right|_{\dot{m}_{\mathrm{corr.}}=ct.} \tag{3.39}$$

Figure 3.3 (p. 28) shows a typical component map with design and off-design points. The auxiliary parameter β is used to parameterise the map. It lies between 0.0 and 1.0, where $\beta = 0.0$ is in proximity of the choke line, and $\beta = 1.0$ in proximity of the surge line. The corrected spool speed $n_{\mathrm{corr,std}}$ and the β value need to be found by iteration to satisfy power equilibrium on the spools and respective inlet mass flow rate. A standard iteration scheme in off-design is shown in Table 3.3 (p. 28). The combustor exit temperature T_4 is the only freely selectable parameter, typically used to achieve a required thrust $F_{\mathrm{N,st}}$.

The simulation environment has been validated against GasTurb® for a GTF model for design and off-design conditions. The difference in all important overall engine performance metrics was less than 0.2 %. The main difference is the interpolation scheme of the thermodynamic data. GasTurb uses only linear interpolation as opposed to spline interpolation in APSS, which leads to minor differences particularly at low temperatures, as present in the bypass stream. Another minor difference is the calculation of FAR after combustion, where GasTurb employs additional empirical calibration factors.

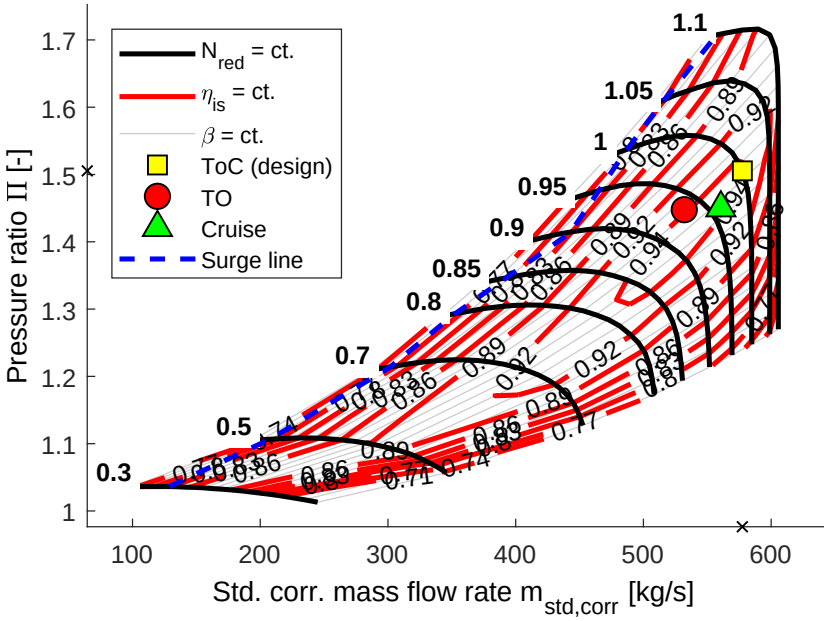

Figure 3.3: Component map of a low pressure ratio outer fan with efficiency iso-contours and typical design and off-design operating points.

Table 3.3: Standard off-design iteration scheme for a GTF.

Input variable	**Target**
$\beta_{\text{fan,o}}$	Bypass nozzle mass flow rate $\dot{m}_{\text{bypass}}$
$\beta_{\text{fan,i}}$	Core nozzle mass flow rate $\dot{m}_{\text{core}}$
β_{IPC}	Mass flow rate in IPC component map $\dot{m}_{21}$
β_{HPC}	Mass flow rate in HPC component map $\dot{m}_{25}$
β_{HPT}	Mass flow rate in HPT component map $\dot{m}_{41}$
β_{LPT}	Mass flow rate in LPT component map $\dot{m}_{45}$
HP spool speed n_{HP}	HP spool power equilibrium
LP spool speed n_{LP}	LP spool power equilibrium
Std. corrected fan mass flow $\dot{m}_{2,\text{corr,std}}$	Combined fan component map mass flows $\dot{m}_2$
Combustor exit temperature T_4	Stream tube thrust $F_{\text{N,st}}$

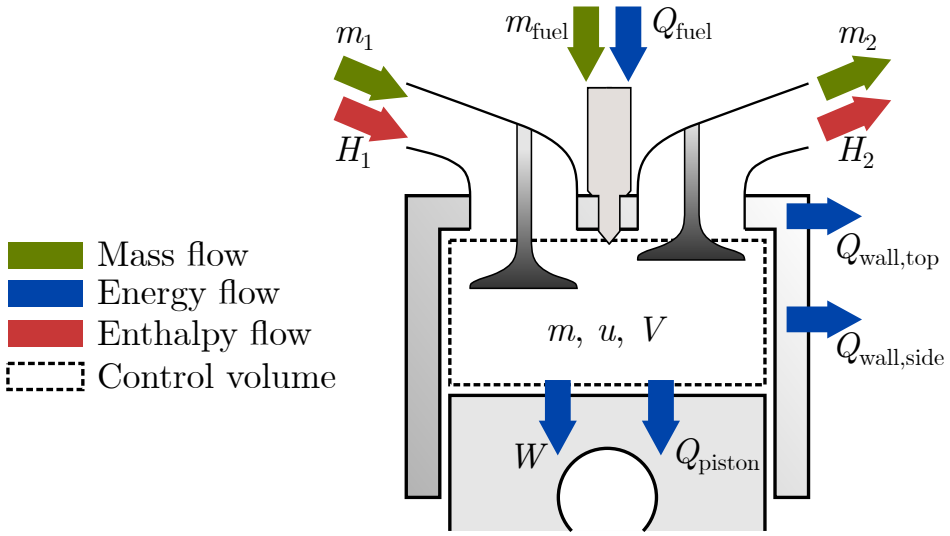

Figure 3.4: Single-zone cylinder control volume with relevant mass, energy and enthalpy flows.

3.3 Piston System Simulation

A common simple model for simulation of a piston engine cycle is the representation with a *Seiliger* cycle. It consists of polytropic compression, isochoric combustion, isobaric combustion and polytropic expansion. This model is too simplistic to achieve the desired accuracy in this thesis. It was shown to have major deviations from the more-detailed *0-dimensional model* in terms of efficiency, shaft power and peak temperatures [17]. The main reasons are that the Seiliger cycle does not resolve the scavenging process and the superposition of heat addition and piston expansion. Moreover, wall heat losses are neglected.

Therefore, a 0-dimensional approach, also known as *Single-zone cylinder model*, is pursued in this thesis. It resolves time but not the cylinder volume [104]. The model is a thermodynamic view of the cylinder volume as a single control volume with all relevant mass, energy and enthalpy flows as illustrated in Figure 3.4. The state of the cylinder volume is expressed by its temperature T, the working fluid mass m, and the current Volume V in dependency of the crankshaft angle ϕ.

$$p = \frac{mRT}{V} \tag{3.40}$$

$$V(\phi) = \frac{\pi}{4} \cdot d^2 s \cdot \left(\frac{1}{\text{CR} - 1} + \frac{1}{2} \left(1 - \cos\phi + \frac{\lambda_s}{4} (1 - \cos(2\phi)) \right) \right) \tag{3.41}$$

$$t = \frac{\phi}{360°} \frac{2s}{v_{\text{mean}}} \tag{3.42}$$

The cylinder pressure p results directly from cylinder volume V and the equation of state (3.40). The volume V depends on the piston bore d, stroke s, connecting rod ratio $\lambda_s = s/(2 \cdot l_{\text{con rod}})$, and geometric compression ratio CR. The latter is defined as the ratio of

maximum to minimum cylinder volume. The relation between simulation time t and the crankshaft angle ϕ is given by Eq. (3.42) with the mean piston velocity v_{mean}.

The mass flow balance is shown in Eq. (3.43) with the differential mass flow rate $\mathrm{d}m_1$ through the intake and $\mathrm{d}m_2$ through the exhaust. The mass flow rate calculated with Eq. (3.44) depends on the effective valve area $A_{\text{valve,eff}}$, the fluid conditions of the mass flow source, and the flow function FF according to Eq. (3.45) [105]. The pressure ratio Π across the valve is limited to the critical pressure ratio, where $M = 1$ is reached. Depending on the pressure conditions, reverse flow through inlet or outlet valve may occur. In any case, the fluid properties of the source need to be supplied to the equations. If reverse flow through the inlet occurs, the exhaust gas is assumed to be re-ingested completely before fresh air enters.

$$\frac{\mathrm{d}m}{\mathrm{d}\phi} = \frac{\mathrm{d}m_1}{\mathrm{d}\phi} + \frac{\mathrm{d}m_2}{\mathrm{d}\phi} + \frac{\mathrm{d}m_{\text{fuel}}}{\mathrm{d}\phi} \tag{3.43}$$

$$\frac{\mathrm{d}m_{\text{valve}}}{\mathrm{d}\phi} = A_{\text{valve,eff}} \cdot \sqrt{\frac{2}{RT}} \cdot p \cdot \mathrm{FF} \tag{3.44}$$

$$\mathrm{FF} = \sqrt{\frac{\gamma}{\gamma - 1} \cdot \left(\Pi^{\frac{2}{\gamma}} - \Pi^{\frac{\gamma+1}{\gamma}} \right)} \tag{3.45}$$

$$\Pi = \min\left(\frac{p_2}{p_1}; \left(\frac{2}{\gamma + 1} \right)^{\frac{\gamma}{\gamma-1}} \right) \tag{3.46}$$

The effective valve area is phase resolved to represent valve opening characteristics according to Eq. (3.47). The valve lift l_{valve} is provided with a synthetic opening function displayed in Eq. (3.50) and Figure 3.5 (p. 31). The opening function assumes that full valve lift is obtained after 25 % of the total opening time between exhaust valve opening (EVO) and exhaust valve closing (EVC). The attainable opening characteristics depend on the actuation mechanism, which will be discussed in Section 4.3.

$$A_{\text{valve,eff}} = n_{\text{valve}} \cdot c_{\text{D}} \cdot \pi d_{\text{valve}}^2 \cdot l_{\text{valve}}(\phi) \tag{3.47}$$

$$d_{\text{valve}} = 0.75 \cdot (\sqrt{2} - 1) \cdot d \tag{3.48}$$

$$l_{\text{valve}}(\phi) = l_{\text{valve,max}} \cdot \begin{cases} \frac{1}{2}\left(1 - \cos\left(\frac{\pi \cdot f(\phi)}{0.25}\right)\right) & f(\phi) < 0.25 \\ 1 & 0.25 < f(\phi) < 0.75 \\ \frac{1}{2}\left(1 - \cos\left(\frac{\pi \cdot (1 - f(\phi))}{0.25}\right)\right) & 0.75 < f(\phi) \end{cases} \tag{3.49}$$

$$\text{with} \qquad f(\phi) = \frac{\phi - \mathrm{EVO}}{\mathrm{EVC} - \mathrm{EVO}} \tag{3.50}$$

During scavenging, perfect mixing with the contents of the cylinder is assumed. This assumption is conservative, if scavenging is effective, i.e. most of the gas from the last cycle is exhausted and little mixing with fresh air takes place. For example, uni-flow scavenged two-stroke engines achieve a scavenging efficiency η_s, which is equivalent to a perfect dis-

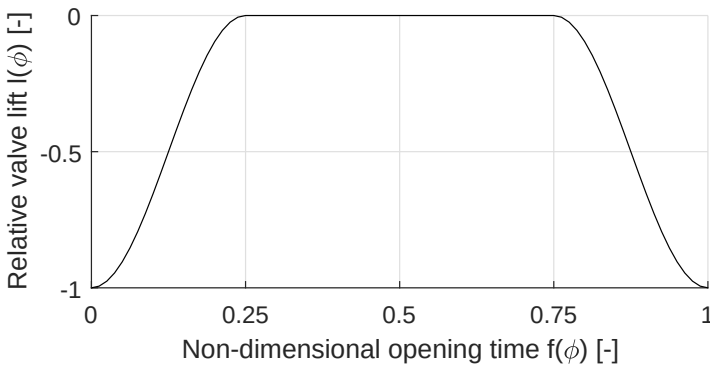

Figure 3.5: Synthetic valve lift characteristic over non-dimensional opening time.

placement of 60 % to 70 % as illustrated in Figure 3.6 (p. 32) [106]. Scavenging efficiency denotes the ratio of fresh air to total air in the cylinder according to Eq. (3.51), and delivery ratio λ the ratio of inducted air to cylinder mass. For scavenging with two valves located at the piston head corresponding to loop scavenging, the perfect mixing model is approximately accurate [106, 107]. If scavenging effectiveness was improved, lower cycle temperatures could be achieved. This would enable better utilisation of the piston volume and lower heat losses. Thus, uni-flow scavenging leads to lighter and more efficient engines [23]. Another important metric is the air efficiency η_{air} according to Eq. (3.52). It denotes the ratio of processed mass per cycle and swept volume. A high η_{air} indicates a high mass flow rate that can be processed in relation to the swept mass. It is usually close to one in a four-stroke engine. In a two-stroke engine, it strongly depends on the pressure difference between inlet and outlet, and can exceed one, if high amounts of air are passed directly from inlet to exhaust during scavenging.

$$\eta_{\text{s}} = \frac{m_{\text{cylinder,fresh}}}{m_{\text{cylinder}}} \tag{3.51}$$

$$\eta_{\text{air}} = \frac{m_{\text{cycle}}}{m_{\text{swept}}} = \frac{m_{\text{cycle}}}{V_d \cdot \rho} \tag{3.52}$$

The rate of heat release is prescribed by the empirical Wiebe[3] function in Eq. (3.53) with the two Wiebe parameters w_a and w_m [108, 109]. In the simulation, addition of fuel m_{fuel} and heat release Q_{fuel} are assumed to concur. The function provides a synthetic rate of heat release, which includes the superimposed effects of the rate of fuel injection, fuel evaporation and combustion. Novel developments like arbitrary injection profiles or multiple injections through electro-magnetic actuation cannot be mapped with the Wiebe function. They may be represented through double-Wiebe functions or polynomial surrogate functions [110]. The combustion time t_{c} from start of combustion (SOC) to end of combustion (EOC) is expressed with the non-dimensional time of heat release y according to Eq. (3.54). In the original formulation, the parameter $w_a = 6.908$ was chosen to represent a combustion efficiency η_{c} of

[3]Depending on the transcription sometimes spelled "Vibe".

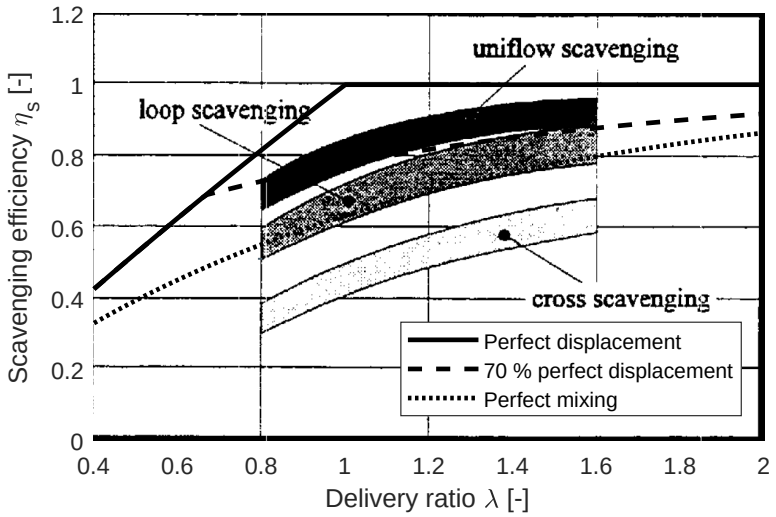

Figure 3.6: Comparison between scavenging efficiency η_s over delivery ratio of different scavenging models against uni-flow, loop and cross scavenging [106].

99.9 %. Eq. (3.53) has been modified to always yield complete combustion, while combustion efficiency η_c is supplied as an additional parameter in Eq. (3.55). The impact of the Wiebe parameters on the rate of heat release is illustrated in Figure 3.7 (p. 33).

$$\frac{\mathrm{d}Q_{\mathrm{fuel}}}{\mathrm{d}\phi} = \frac{\mathrm{d}t}{\mathrm{d}\phi} \cdot \frac{Q_{\mathrm{fuel,tot}}}{1 - \mathrm{e}^{-w_a}} \cdot w_a \cdot (w_m + 1) \cdot \frac{y^{w_m}}{t_c} \cdot \exp\left(-w_a \cdot y^{w_m+1}\right) \tag{3.53}$$

$$y = \frac{t - t_{\mathrm{SOC}}}{t_c} \tag{3.54}$$

$$\frac{\mathrm{d}m_{\mathrm{fuel}}}{\mathrm{d}\phi} = \frac{\mathrm{d}Q_{\mathrm{fuel}}}{\mathrm{d}\phi} \cdot \frac{1}{\mathrm{FHV} \cdot \eta_c} \tag{3.55}$$

The energy balance of all energy and enthalpy flows shown in Figure 3.4 is summarised in Eq. (3.56). The change in total inner energy U is used to determine the change in specific inner energy u over crank angle ϕ. The released work W is determined according to Eq. (3.57). Calculation of heat loss Q is described in Subsection 3.3.1.

$$\frac{\mathrm{d}U}{\mathrm{d}\phi} = m\frac{\mathrm{d}u}{\mathrm{d}\phi} + u\frac{\mathrm{d}m}{\mathrm{d}\phi} = c_{p,1}\frac{\mathrm{d}m_1}{\mathrm{d}\phi} + c_{p,2}\frac{\mathrm{d}m_2}{\mathrm{d}\phi} + \frac{\mathrm{d}W}{\mathrm{d}\phi} + \frac{\mathrm{d}Q}{\mathrm{d}\phi} + \frac{\mathrm{d}Q_{\mathrm{fuel}}}{\mathrm{d}\phi} \tag{3.56}$$

$$\frac{\mathrm{d}W}{\mathrm{d}\phi} = -p\frac{\mathrm{d}V}{\mathrm{d}\phi} \tag{3.57}$$

The ideal gas model neglects the finite displacement of molecules as well as the attractive forces between the molecules [111]. Thus, the pressure obtained with the ideal gas law is lower than the real pressure, except for temperatures below 250 K and low pressures. The effect is alleviated at higher temperatures due to the reduced density for a given pressure. This effect can be expressed with the compressibility factor Z. It denotes the ratio of the real

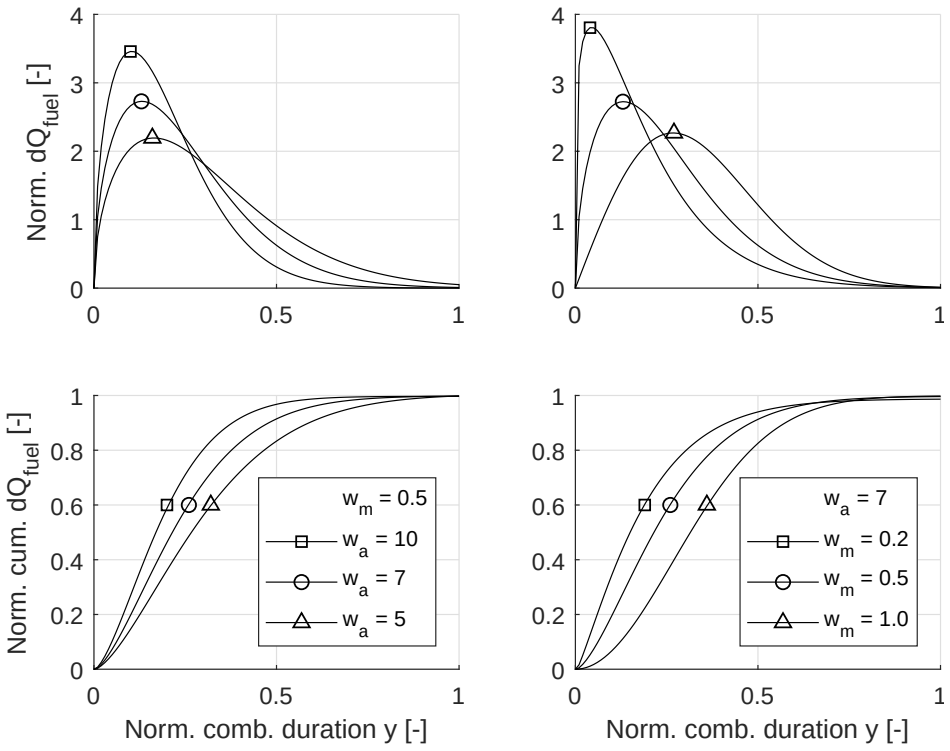

Figure 3.7: Normalised rates of heat release $\mathrm{d}Q_{\mathrm{fuel}}$ (top) and their cumulative rates (bottom) for variations of the Wiebe parameters w_a (left) and w_m (right).

gas pressure p_{real} to the pressure obtained via the ideal gas law p_{ideal} according to Eq. (3.58). Tabulated data for Z in dependency of temperature, pressure and FAR is used here [111, 112]. It does not cover the full range of temperatures and pressures required. Therefore, this data was blended with other data for clean air at low temperatures down to 200 K [113] as displayed in Figure 3.8 (p. 34).

$$p_{\mathrm{real}} = Z \cdot p_{\mathrm{ideal}} = Z \cdot \frac{mRT}{V} \tag{3.58}$$

The compressibility correction is particularly important at high pressure conditions with more than 100 bar. Therefore, it was only used to investigate the piston engine simulation program for impact on peak pressure and shaft power. For example, at a peak pressure of 250 bar and temperature of 2 500 K, $Z = 1.037$ leads to a deviation in peak pressure of 9.3 bar, or 3.7 %[4]. Considering real gas properties leads to higher peak pressures and, thus, higher shaft power.

To evaluate the impact of real gas on the engine simulation, a cycle representative of CCE take-off (TO) operating conditions was used. Using real gas, peak pressure p_{peak} increases by 3.7 %, while shaft power increases by 1.6 %. Peak temperature and mass flow rate are mostly unaffected. To retain the specified peak pressure and shaft power, compression ratio

[4] In contrast, for a gas turbine combustor exhaust operating at 60 bar and 2 000 K, an error of only 0.5 bar, or 0.7 %, would result.

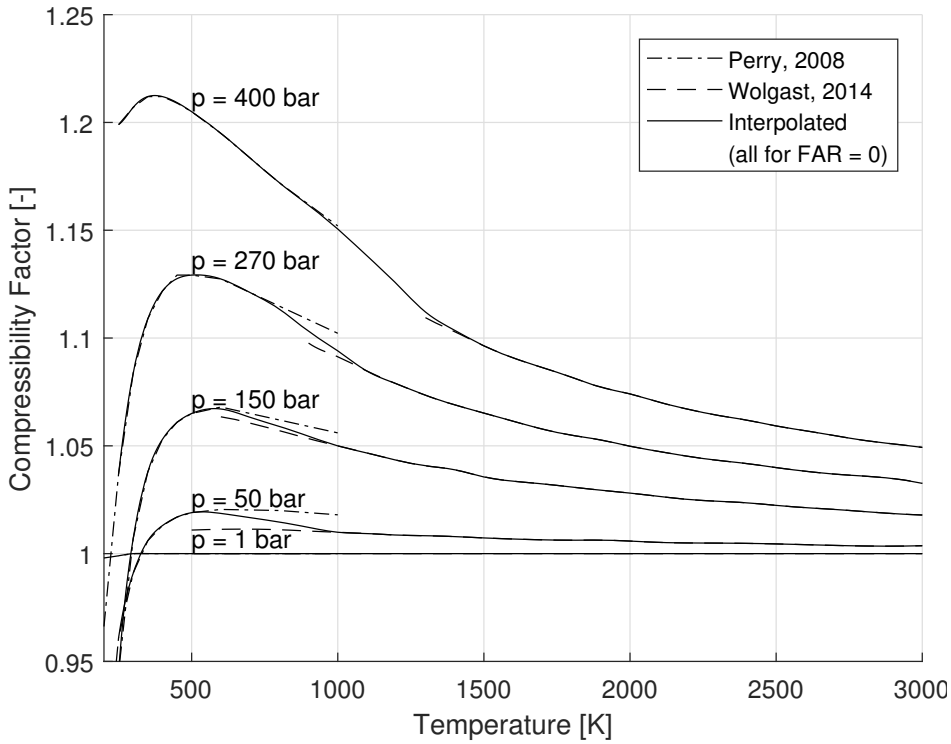

Figure 3.8: Compressibility factor Z for various pressures and temperatures for FAR = 0 as provided in literature and interpolation used here.

CR and injected fuel were adapted. The impact on the cycle is shown in Figure 3.9 (p. 35). Geometric compression ratio was reduced from 6.39 to 6.15 in order to stay below 250 bar. Net fuel flow reduces by 0.2 % to achieve the same shaft power. Hence, a small net improvement is obtained through real gas properties. This impact will be considered later in the engine efficiency calculation via a fuel flow correction factor.

3.3.1 Heat Losses

Heat losses are caused by a temperature gradient between fluid in the cylinder and the cylinder wall, and by radiation of the hot combustion gases to the wall. Accurate representation of all physical effects requires knowledge of the time- and space-resolved flow field, and the state of soot particles, which have an impact on the amount of radiation. Since most of these parameters are unknown in a 0-dimensional simulation model, a semi-empirical model for the heat transfer coefficient α according to Woschni is used [104, 114, 115]. The numbers in Eq. (3.59) need to be supplied in SI units, except for the pressure p, which needs to be supplied in units of bar. Further relevant parameters are the swirl velocity v_u, the displacement volume V_d, the reference fluid properties after EVC T_ref, p_ref and V_ref, and motoring pressure p_0. The latter is obtained, when no fuel is injected. It is estimated by assuming isentropic compression and expansion after EVC.

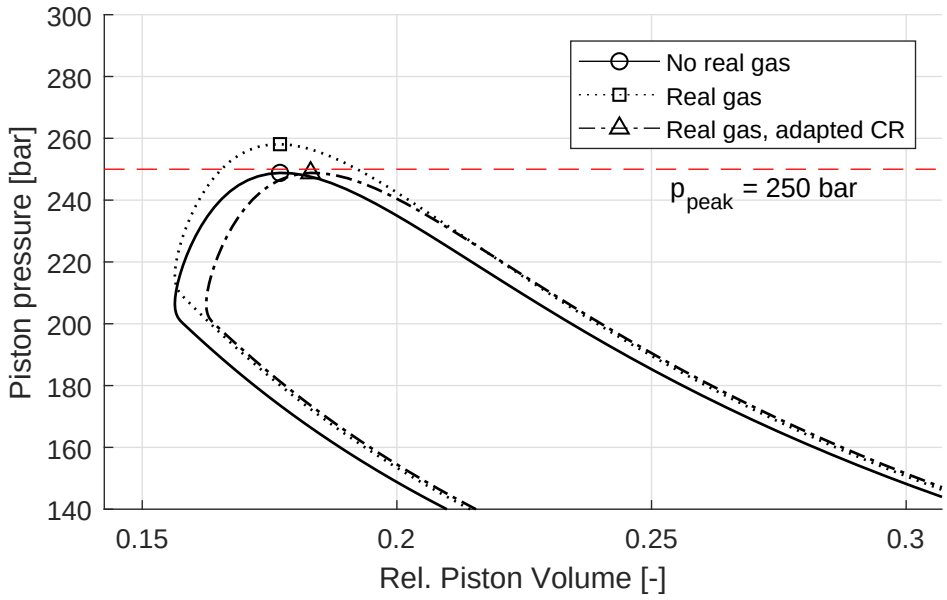

Figure 3.9: Impact of real gas correction for typical CCE piston engine TO conditions.

$$\alpha = 130 \frac{\mathrm{W}}{\mathrm{m}^2\,\mathrm{K}} \cdot d^{-0.2} \cdot p^{0.8} \cdot T^{-0.53} \cdot C^{0.8} \tag{3.59}$$

$$C = k_1 \cdot (2.280 \cdot v_{\mathrm{mean}} + 0.308 \cdot v_u) + C_2 V_\mathrm{d} \frac{T_\mathrm{ref}}{p_\mathrm{ref} V_\mathrm{ref}} \cdot (p - p_0) \tag{3.60}$$

with
$$k_1 = \begin{cases} 1.0 & \text{Intake valve closed} \\ 7.0 & \text{Intake valve open} \end{cases} \tag{3.61}$$

$$C_2 = \max\left(3.24 \times 10^{-3}; 2.3 \times 10^{-5} \cdot (T_\mathrm{wall,i} - 600\,\mathrm{K}) + 5 \times 10^{-3}\right) \tag{3.62}$$

$$\frac{\mathrm{d}Q}{\mathrm{d}\phi} = \alpha \cdot A_{\mathrm{wall},i} \cdot (T - T_{\mathrm{wall},i}) \cdot \frac{\mathrm{d}t}{\mathrm{d}\phi} \tag{3.63}$$

The factor k_1 in Eq. (3.60) corrects heat transfer during induction of fresh air, where considerable turbulence is created, according to Eq. (3.61) [110]. The second correction term C_2 according to Eq. (3.62) comes into action, when wall temperatures are higher than 520 K. The temperature boundary layer is then thinner, and combustion takes place closer to the wall [116].

The wall is divided into cylinder head, cylinder and piston. Each wall's temperature $T_{\mathrm{wall},i}$ is prescribed in the model. The cylinder needs to be cooled according to the obtained heat flow. The respective wall areas $A_{\mathrm{wall},i}$ are simplified to circles for cylinder head and piston surface, and a cylinder shell for the cylinder wall, as illustrated in Figure 3.10 (p. 36). In contrast to the real piston geometry, the heat flow into the piston is underestimated, because the real surface is larger. On the other hand, heat flow into the cylinder is overestimated, because the cylinder wall is almost entirely covered by the piston at top dead centre (TDC). Furthermore, constant wall temperatures are implied. The real cylinder temperature decreases continuously

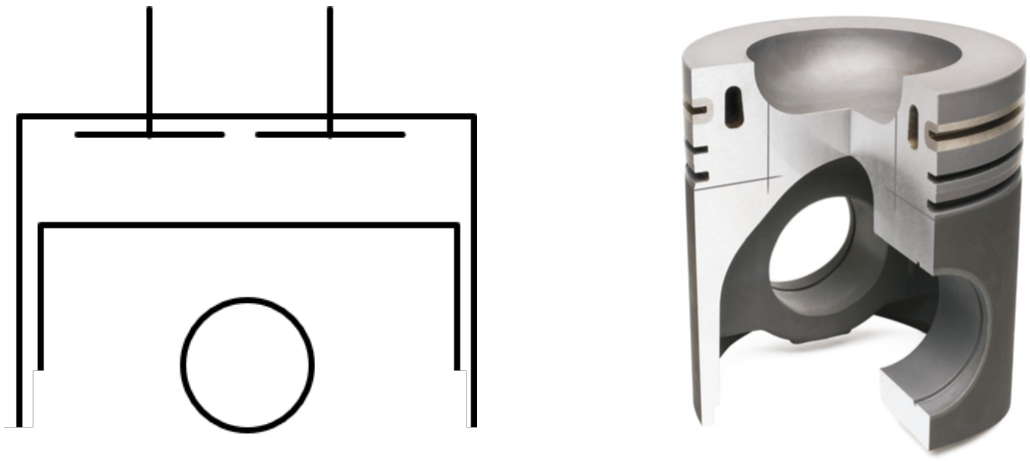

(a) (b)

Figure 3.10: (a) Simplified piston geometry used here in contrast to (b) a real high-performance piston [118].

from top to bottom [117]. To take these effects into account, the cylinder wall area at TDC is attributed to cylinder head and piston to equal shares. The actual cylinder wall temperature needs to be considered for piston lubrication. The lubricant is typically injected at the top piston ring.

3.3.2 Numerical Integration

The numerical integration of the derivatives shown before in the crank angle domain results in the calculation of a full engine cycle. The integration is initiated at the crankshaft angle, when all valves are closed, because the fluid state can be best estimated at this point. It is assumed to be equal to the intake conditions. Many derivatives are zero at this point, since no mass exchange or heat release takes place. The simulation needs to run several times until start and end conditions match. At this point the simulation has converged. This process typically requires 10 to 20 iterations. Then, time-averaged performance metrics such as power, heat flow, fuel flow, and air mass flow can be calculated. Only these will be used in the engine simulation.

The integration is performed with an ordinary differential equation (ODE) solver. In this case, the Adams-Bashforth-Moulton Predict-Evaluate-Correct-Evaluate (PECE) solver is used, which is implemented in MATLAB as the `ode113` solver [119]. The step size is adaptive to resolve sudden changes in derivatives finely, but advance quickly when the derivatives are relatively steady. Also, the solver uses a number of previous results for more accurate prediction to reduce the number of simulation steps. This is particularly useful for such a computationally expensive problem. To further reduce computational time, corrections of fluid conditions and particularly FAR are employed after each simulation cycle.

3.3.3 Implementation into Engine Simulation Environment

The integral results are used within the engine simulation environment APSS described in Section 3.2. Since the computational time of a single piston engine simulation run is about 30 s, and the piston engine is run hundreds of times during a single engine calculation until all iteration targets have been obtained, a surrogate model of the piston simulation was used. Artificial neural networks allow mapping a multi-dimensional input space to a multi-dimensional output space with arbitrary relations between the parameters. A work flow as described in [120] was used to create artificial neural networks from pre-calculated engine simulations with the input variables specified in Table 3.4. A total of 9 000 simulations were run for each of the two engines, which were distributed across the input space with Latin hypercube sampling [121].

Table 3.4: Input parameters for the four-stroke piston engine surrogate artificial neural network with ranges and output parameters.

Input	**Unit**	**Range**
Intake temperature T_1	K	300 – 1 200
Intake pressure p_1	kPa	200 – 7 000
Piston bore d	m	0.08 – 0.30
Piston pressure ratio Π	–	0.70 – 3.00
Geometric compression ratio CR	–	4 – 18
Mean piston velocity v_{mean}	m/s	5 – 25
Valve lift l_{valve}	m	0.010 – 0.040
Fuel-air-ratio FAR_2 at EVO	–	0.010 – 0.080
Cylinder wall temperature	K	400 – 1 000
Output	**Unit**	**Mean rel. error [%]**
Exhaust temperature T_2	K	0.04
Shaft power P	W	0.37
Heat loss $\dot{Q}$	W	0.60
Mass flow rate $\dot{m}_1$	kg/s	0.24
Exhaust fuel air ratio FAR	–	0.01
Peak pressure p_{peak}	Pa	0.04

Several neural network layer set-ups were evaluated for creation of the neural networks. Up to three layers were used with varying total number of neurons and varying distribution of neurons across the layers. 85 % of the simulations were used for neural network training. Further 10 % were used for validation to verify that the network actually improves and does not over-fit the training points. The remaining 5 % of simulations were used for independent testing of the neural network quality[5].

The results are shown in the bottom half of Table 3.4. The best network quality, i.e. the lowest error was achieved with three neural network layers with 75, 50 and 25 neurons in

[5]This is recommended practice in addition to the validation points, since the latter have an impact on the network training process.

the first, second and third layer, respectively. The mean errors are generally below 1 %. The largest errors can be observed with engine power P and heat loss $\dot{Q}$. Exhaust temperature, peak pressure and FAR can be predicted particularly well. Neural networks for a two-stroke engine were similarly created and results are reported in Table A.1 (p. 144). The input parameter ranges were narrowed down as experience from the four-stroke engine for required ranges was available. The resulting mean errors are lower than 0.1 %.

A major drawback of the chosen implementation with a surrogate model is the fixed set-up. Only the parameters that were selected during the model creation process can be changed after the surrogate model was created. This is a compromise between reduced model resolution and effort for creating a model. In case of the piston engine, some parameters that could be used for off-design variability are kept fixed within the neural networks. Namely, this concerns the heat release characteristics, which are expressed with four variables: start and end of combustion, as well as two Wiebe parameters w_a and w_m. The four valve timings for intake and exhaust opening and closing are fixed, which may however be flexible when using adaptable cam shafts. In total, the parametric space of the neural networks would have needed to be increased from currently 9 to 17 parameters. In consequence, the required number of simulations would have been much higher with a lower expected neural network quality.

As a solution, the geometric compression ratio CR was used as a surrogate to the above-mentioned parameters in off-design. Lowering CR leads to lower shaft power and lower peak pressure p_{peak}, which is preferable under TO conditions to reduce peak pressure. An actual mechanical implementation for changing CR has not been considered to be viable for aero engines[6]. The same effect is achieved by retarding heat release, or by closing valves later and, thus, lowering the effective CR. Both measures are in use in production engines, with electronically controlled injectors and additional kinematics on the cam shaft for valve actuation.

To verify that CR can indeed be used as a surrogate, typical operating points were simulated with both conditions: first with modified CR and then with design CR but adapted valve and combustion timings. As boundary conditions, the same mass flow rate $\dot{m}_1$, peak pressure p_{peak} and engine power P should be achieved. An optimiser was used that could freely vary the timing parameters for minimum fuel flow.

First, TO conditions were simulated. In the surrogate model, CR was reduced from a design value of 9.6 to 6.4. The reduction leads to lower peak pressures and allows to stay below the limit of 250 bar during multi-point engine design. When changing CR back to the design point value, peak pressure increases to 360 bar as shown in Figure 3.11 (p. 39). Adapted timings reduce peak pressure below the 250 bar limit with two measures: first, the heat release is delayed beyond TDC. Thus, the peak pressure is not increased through combustion beyond the pressure, which is achieved via pure compression during the compression stroke. Second,

[6]Note that former engine concepts investigated the feasibility of variable compression ratios. Two notable solutions are an additional kinematics on the crankshaft, which is very complex, or the displacement of the casing like the Saab tilting monohead, which is easier to achieve [122]. Other solutions are hydraulic pistons, eccentricities on bearings, and transformable dead volumes in cylinder or cylinder head.

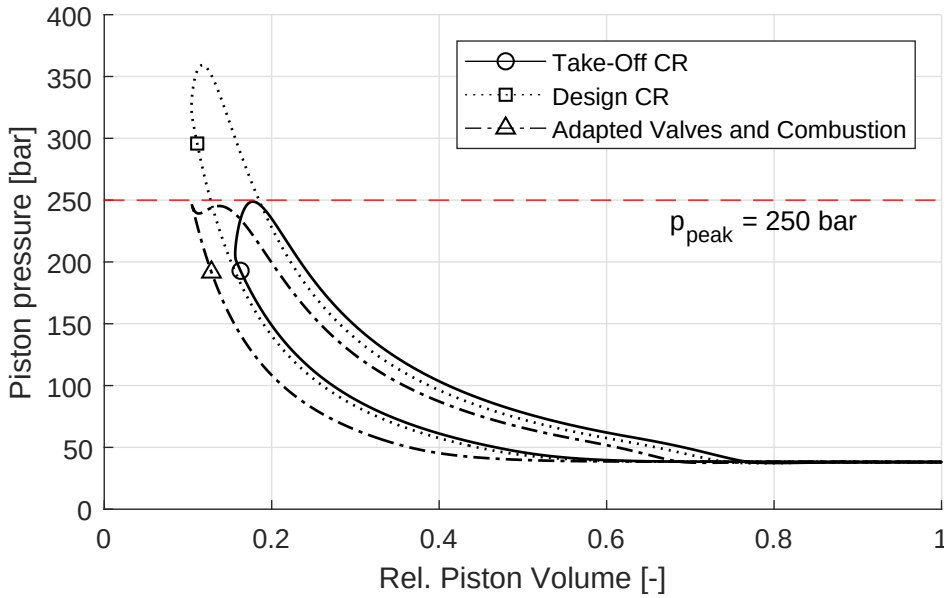

Figure 3.11: Cylinder pressure p over relative volume V diagram contrasting cycles with surrogate solution and adapted valve timing and combustion parameters for TO conditions.

intake and exhaust closing are retarded to reduce the effective CR of the engine. The area enclosed by the cycle is evidently similar to the cycle with the lower CR but shifted to the left, i.e. to lower effective volumes.

The other performance characteristics are met as summarised in Table 3.5 (p. 40). The results show that the adapted timings can save 0.7 % fuel in the piston engine. These savings were not considered in the later simulations, since the valve timings possibly cannot be adapted as flexibly as required to achieve the saving. A fuel flow neutral adaptation with the suggested measures appears feasible.

Then, cruise was investigated. Here, CR changes in the opposite direction to 18.0 in the surrogate model. When using design CR, peak pressure reduces from 166 bar to 109 bar and shaft power accordingly. Hence, opposing adaptation of valve timings and combustion parameters is required as shown in Figure 3.12 (p. 40) and Table 3.6 (p. 41). Valves need to close earlier, and combustion completes earlier to achieve almost the same peak pressure. The results show that fuel flow with the adaptations is 0.4 % higher. This effect is incorporated into the engine simulations. A surrogate change of CR beyond 18.0 cannot be represented by changes in valve and combustion characteristics and, consequently, would require higher penalties on piston engine fuel flow.

3.3.4 Validation

The piston simulation program was validated against publicly available crank-shaft resolved performance data from a two-stroke piston engine simulation program [123, 124]. The main

Table 3.5: Adaptation of valve timings and combustion parameters for TO conditions to meet piston engine specified performance.

Parameter	**Unit**	**Surrogate**	**Adapted**
Wiebe parameter w_a	–	6.91	6.80
Wiebe parameter w_m	–	1.40	1.80
Start of combustion	°	-5	1
End of combustion	°	45	52
Inlet valve opening	°	120	89
Inlet valve closing	°	265	299
Exhaust valve opening	°	95	94
Exhaust valve closing	°	285	281
Trapped FAR	–	0.0496	0.0550
Output			
Mass flow rate	kg/s	1.914	1.914
Shaft power P	kW	537.0	536.3
Peak pressure p_{peak}	bar	248.8	247.8
Fuel flow	g/s	46.1	45.7

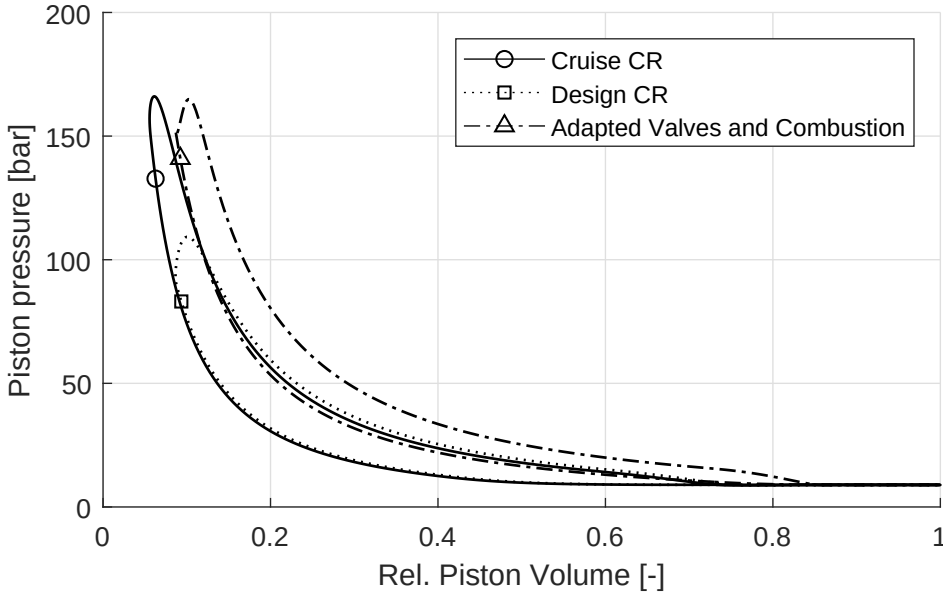

Figure 3.12: Cylinder pressure p over relative volume V diagram contrasting cycles with surrogate solution and adapted valve timing and combustion parameters for cruise conditions.

Table 3.6: Adaptation of valve timings and combustion parameters for cruise conditions to meet piston engine specified performance.

Parameter	**Unit**	**Surrogate**	**Adapted**
Wiebe parameter w_a	–	6.91	7.07
Wiebe parameter w_m	–	1.40	1.93
Start of combustion	°	−5	0
End of combustion	°	45	28
Inlet valve opening	°	120	125
Inlet valve closing	°	265	227
Exhaust valve opening	°	95	111
Exhaust valve closing	°	285	246
Trapped fuel-air-ratio	–	0.0680	0.0537
Output			
Mass flow rate	kg/s	0.387	0.328
Shaft power P	kW	186.8	186.8
Peak pressure p_{peak}	bar	166.1	164.9
Fuel flow	g/s	11.99	12.04

engine set-up specifications and time-averaged results are displayed in Table 3.7. The main performance indicators mass flow rates $\dot{m}_1$ and $\dot{m}_2$ as well as indicated power P are met with an error of less than 0.1 %. Other important metrics display a maximum error of up to 0.7 %.

Table 3.7: Input parameters for the piston engine validation and comparison between outputs in reference and simulation.

Input parameter	**Unit**	**Value**		
Intake temperature T_1	K	492		
Intake pressure p_1	kPa	1 034		
Piston bore d	m	0.079		
Piston pressure drop $p_1 - p_2$	kPa	86.2		
Geometric compression ratio CR	–	9.2		
Mean piston velocity v_{mean}	m/s	15.2		
Cylinder wall temperature	K	811		
Output parameter	**Unit**	**Reference [123]**	**Simulation**	**Error [%]**
Air mass flow rate $\dot{m}_1$	g/s	148.42	148.45	0.0
Fuel mass flow rate $\dot{m}_{\text{fuel}}$	g/s	5.080	5.081	0.0
Exhaust temperature T_2	K	1 143.1	1 151.0	0.7
Indicated power P	kW	80.57	80.65	0.1
Heat loss $\dot{Q}_{\text{loss}}$	W	17.48	17.59	0.7
Peak pressure p_{peak}	MPa	19.14	19.23	0.4
Peak temperature T_{peak}	K	2 536.4	2 524.9	−0.5

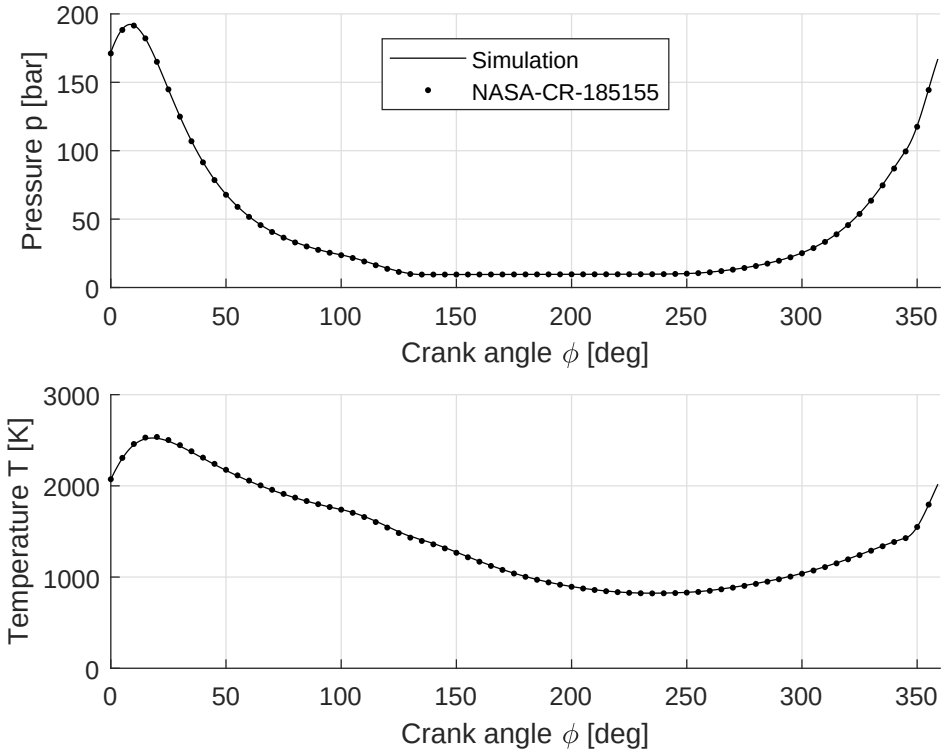

Figure 3.13: Crank-angle resolved temperature T and pressure p of published data [123] against the piston engine simulation program.

The simulation results for temperature T and pressure p over crank angle ϕ are plotted in Figure 3.13 showing a very good agreement. The root mean square error between published and simulated data in crankshaft resolved temperature T is 0.4 %, and in pressure p 1.0 %. Therefore, a good agreement across the entire cycle including scavenging phase could be shown.

3.3.5 Mechanical Losses

Piston engine losses are composed of three main components: mechanical losses, scavenging work, and accessory work. Due to the oscillating nature of the piston engine and the lateral forces between piston and cylinder head induced by the connecting rod, a piston engine has higher frictional losses than a turbo machine. Required scavenging work is considered in the scavenging process as described earlier. Hence, it does not need to be estimated empirically. Accessory work is estimated for fuel, coolant and oil pump.

Mechanical friction can be decomposed into the share of all moving parts [125]. It can be approximated with empirical formulas. These are obtained by decomposing the engine gradually and measuring the respective engine friction on a motored test rig. Some uncertainty is incurred, since the motored measurements are carried out on a cold engine, where viscosity is higher, clearances between components are larger, and the firing pressure is missing. Friction

is typically expressed as friction mean effective pressure (FMEP), which is the normalised friction power P_f according to Eq. (3.64).

$$\mathrm{FMEP} = \frac{2 \cdot P_\mathrm{f}}{V_d \cdot n} \tag{3.64}$$

In this thesis, semi-empirical relations from literature are used [125–128], which cover the dominant physical dependencies of mechanical friction. Friction related to the crankshaft consists of bearing friction $\mathrm{FMEP}_\mathrm{bear,main}$ in Eq. (3.65) and seal friction $\mathrm{FMEP}_\mathrm{seal}$ in Eq. (3.66). Bearing friction depends on the number of bearings n_b, the rotational speed n in units of rpm, the bearing diameter d_b, the bearing length l_b, the number of cylinders per crankshaft n_c. The crankshaft FMEP is then obtained with the proportionality constants c_b and c_s. The bearing dimensions d_b and l_b can be estimated according to Eq. (3.67) [127].

$$\mathrm{FMEP}_\mathrm{bear,crank} = c_\mathrm{b} \cdot \frac{n_\mathrm{b} \cdot n^{0.6} \cdot d_\mathrm{b}^3 \cdot l_\mathrm{b}}{n_\mathrm{c} \cdot d^2 \cdot s} \tag{3.65}$$

$$\mathrm{FMEP}_\mathrm{seal} = c_\mathrm{s} \cdot \frac{d_\mathrm{b}}{n_\mathrm{c} \cdot d^2 \cdot s} \tag{3.66}$$

$$\text{with} \quad c_\mathrm{b} = 0.202 \, \frac{\mathrm{kPa\,min}^{0.6}}{\mathrm{mm}} \qquad c_\mathrm{s} = 9.36 \times 10^4 \, \mathrm{kPa\,mm}^2$$
$$d_\mathrm{b} = 0.62 \cdot b \qquad l_\mathrm{b} = 0.40 \cdot b \tag{3.67}$$

Piston friction consists of skirt friction, ring friction and gas friction. The latter is caused by the gas pressure during fired operation. It depends on piston intake pressure p_1 and ambient pressure p_0. The connecting rod bearing dimensions $d_\mathrm{b,cr}$ and $l_\mathrm{b,cr}$ can be estimated according to Eq. (3.72) [127].

$$\mathrm{FMEP}_\mathrm{skirt} = c_\mathrm{ps} \cdot \frac{v_\mathrm{mean}}{b} \tag{3.68}$$

$$\mathrm{FMEP}_\mathrm{rings} = c_\mathrm{pr} \cdot \left(1 + \frac{1\,000}{n}\right) \frac{1}{b^2} \tag{3.69}$$

$$\mathrm{FMEP}_\mathrm{gas} = c_\mathrm{g} \cdot \frac{p_1}{p_0} \cdot \left(0.088 \cdot \mathrm{CR} + 0.182 \cdot \mathrm{CR}^{1.33 - 2 \cdot K \cdot v_\mathrm{mean}}\right) \tag{3.70}$$

$$\mathrm{FMEP}_\mathrm{bear,conrod} = c_\mathrm{bc} \cdot \frac{n_b \cdot n \cdot d_\mathrm{b,cr}^3 \cdot l_\mathrm{b,cr}}{n_c \cdot d^2 \cdot s} \tag{3.71}$$

$$\text{with} \quad c_\mathrm{ps} = 0.294 \, \mathrm{kPa\,s} \qquad c_\mathrm{pr} = 4.06 \times 10^4 \, \mathrm{kPa\,mm}^2$$
$$c_\mathrm{g} = 6.89 \, \mathrm{kPa\,s} \qquad K = 0.0238 \, \frac{\mathrm{s}}{\mathrm{min}} \qquad c_\mathrm{bc} = 3.03 \times 10^{-4} \, \frac{\mathrm{kPa\,min}}{\mathrm{mm}}$$
$$d_\mathrm{b,cr} = 0.57 \cdot b \qquad l_\mathrm{b,cr} = 0.39 \cdot b \tag{3.72}$$

Valvetrain friction consists of camshaft, seal, and valve friction including hydrodynamic and mixed oscillating friction. The relations for valve friction are for flat follower valves and single

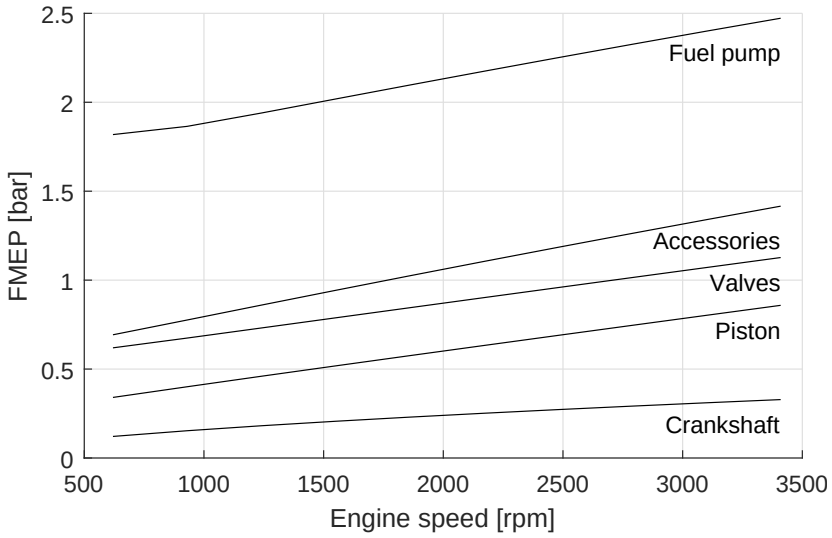

Figure 3.14: Stacked contributions to FMEP by various components over engine speed for typical TO conditions.

overhead cams. The relations use the number of camshaft bearings n_{cs}, the total number of valves n_v, and the valve lift l_{valve}. The dynamic viscosity μ is assumed to be 10 mPa s like SAE 10W-30 oil at 90 °C [125].

$$\text{FMEP}_{\text{camshaft}} = c_{\text{c}} \cdot \frac{n^{0.6} \cdot n_{cs}}{n_c b^2 s} \tag{3.73}$$

$$\text{FMEP}_{\text{seal,camshaft}} = 1.2\,\text{kPa} \tag{3.74}$$

$$\text{FMEP}_{\text{valve}} = c_{\text{ff}} \cdot \left(2 + \frac{10}{5 + \mu N}\right) \cdot \frac{n_v}{n_c s} \tag{3.75}$$

$$\text{FMEP}_{\text{valve,osc,hydro}} = c_{\text{oh}} \cdot \frac{l_{\text{valve}}^{1.5} n^{0.5} n_v}{b \cdot s \cdot n_c} \tag{3.76}$$

$$\text{FMEP}_{\text{valve,osc,mixed}} = c_{\text{om}} \cdot \left(2 + \frac{10}{5 + \mu N}\right) \cdot \frac{l_{\text{valve}} \cdot n_v}{n_c s} \tag{3.77}$$

$$\text{with} \qquad c_{\text{c}} = 6\,720\,\text{kPa}\,\text{mm}^3\,\text{min}^{0.6} \qquad c_{\text{ff}} = 200\,\frac{\text{kPa}}{\text{mm}}$$
$$c_{\text{oh}} = 0.50\,\text{kPa}\,(\text{mm}\,\text{min})^{0.5} \qquad c_{\text{om}} = 10.7\,\text{kPa}$$

The accessory work includes the fuel feed pump, the common rail pump, the lubrication pump and the cooling pump. The power required for the fuel pumps was estimated with Eq. (3.78) based on volume flow $\dot{V}$ and pressure increment Δp [129]. The common rail pressure here is 2 500 bar. The work of oil and coolant pump was estimated with Equations (3.79) and (3.80). The resulting loss composition for typical CCE TO conditions and different rotational speeds is illustrated in Figure 3.14. As can be seen, the fuel pump constitutes a major share of the losses. The injection pressure should, therefore, be chosen as low as possible, while maintaining good combustion efficiency and low smoke numbers.

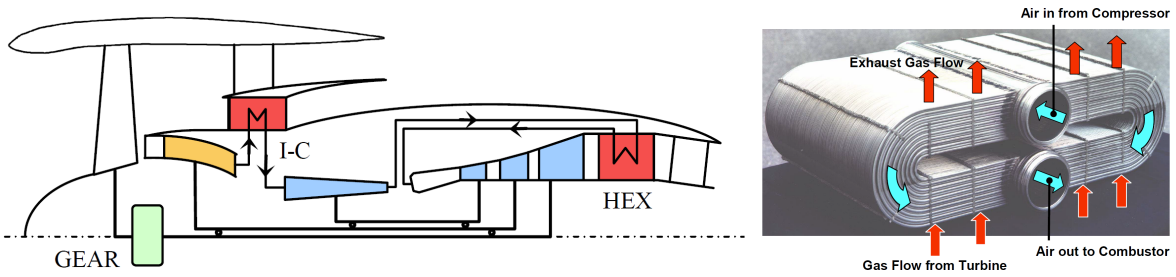

(a) (b)

Figure 3.15: (a) Schematic of an intercooled recuperated engine, and (b) MTU profile tube heat exchanger [130].

$$P_{\text{access}} = \dot{V} \cdot \Delta p = \frac{\dot{m}}{\rho} \cdot \Delta p \tag{3.78}$$

$$\text{FMEP}_{\text{oil}} = 1.28\,\text{kPa} + 0.0079\,\text{kPa min} \cdot N - 8.4 \times 10^{-7}\,\text{kPa min}^2 \cdot N^2 \tag{3.79}$$

$$\text{FMEP}_{\text{coolant}} = 0.13\,\text{kPa} + 0.002\,\text{kPa min} \cdot N + 3 \times 10^{-7}\,\text{kPa min}^2 \cdot N^2 \tag{3.80}$$

3.4 Heat Exchanger Modelling

Heat exchangers can be used inside a CCE architecture for intercooling, for dissipation of piston engine heat losses, and for recuperation. Heat exchangers add mass, bulk and pressure losses to the engine, which need to be compensated by improving engine efficiency or by reducing overall engine mass. In this thesis, specifications of heat exchangers as used in the EU-funded Horizon 2020 project Ultra Low emission Technology Innovations for Mid- century Aircraft Turbine Engines (ULTIMATE) are applied [81]. The assumed pressure losses are summarised in Table 3.8. For the ducts, a higher loss for recuperators is assumed, because the ducting length and number of bends are notably higher as illustrated in Figure 3.15(a).

Table 3.8: Pressure losses in heat exchanger.

Location	Pressure loss [%]
Hot side	6.0
Cold side	5.7
Intercooler duct	1.0
Recuperator duct	2.0

An important design parameter of heat exchanges is the heat exchanger effectiveness ϵ, which describes the ratio of transferred heat Q to maximum transferable heat Q_{max}. ϵ is defined according to Eq. (3.81). In this thesis, the heat capacity rates on hot side and cold side, C_{hot} and C_{cold}, are assumed to be equal to achieve minimum heat exchanger losses [131]. In that case, the equation for heat exchanger effectiveness simplifies to a ratio of temperature

differences according to Eq. (3.82). Other ratios may be beneficial to optimise on overall engine level or when available space is constrained.

$$\epsilon = \frac{Q}{Q_{\max}} \tag{3.81}$$

$$= \frac{T_{1,\text{hot}} - T_{2,\text{hot}}}{T_{1,\text{hot}} - T_{1,\text{cold}}} \qquad \text{, if } C_{\text{hot}} = C_{\text{cold}} \tag{3.82}$$

$$C = c_p \cdot \dot{m} \tag{3.83}$$

Two strategies for increasing ϵ are possible: Either the heat exchanger size is increased, while the pressure losses are kept constant, or pressure losses are increased – for example by increasing flow velocity or by using turbulators – to keep heat exchanger size constant. In this thesis, the first approach is pursued, since pressure losses are typically more dominant than heat exchanger mass with respect to fuel burn. Heat exchanger size is assumed to scale with number of transfer units NTU according to Eq. (3.84), with the heat transfer coefficient k and the heat exchange area A. The relation in Eq. (3.85) is derived from a cross-flow lancet heat exchanger for engine application [99] as illustrated in Figure 3.15(b). With a fully resolved heat exchanger model, other optima may be found.

$$\text{NTU} = \frac{k \cdot A}{C} \tag{3.84}$$

$$= \frac{0.9 \cdot \epsilon}{0.882 - \epsilon} \tag{3.85}$$

Heat exchanger mass was assumed to be proportional to NTU, in accordance with [99]. The equations for matrix and ducting mass are summarised in Equations (3.86) to (3.89) for intercooler (IC) and recuperators (REC) [81].

$$m_{\text{mat,IC}} = 3.2\,\text{s} \cdot \dot{m}_{\text{IC}} \cdot \frac{\epsilon}{0.882 - \epsilon} \tag{3.86}$$

$$m_{\text{mat,REC}} = 9.0\,\text{s} \cdot \dot{m}_{\text{IC}} \cdot \frac{\epsilon}{0.882 - \epsilon} \tag{3.87}$$

$$m_{\text{duct,IC}} = 0.2 \cdot m_{\text{mat,REC}}(\epsilon = 0.75) \tag{3.88}$$

$$m_{\text{duct,REC}} = 0.8 \cdot m_{\text{mat,REC}}(\epsilon = 0.75) \tag{3.89}$$

For off-design, the heat exchanger effectiveness is assumed to increase linearly with reduction in mass flow according to Eq. (3.90) [92], because the lower mass flow still has the same surface area for heat exchange. The pressure loss was assumed to scale with the square of the corrected mass flow on both sides.

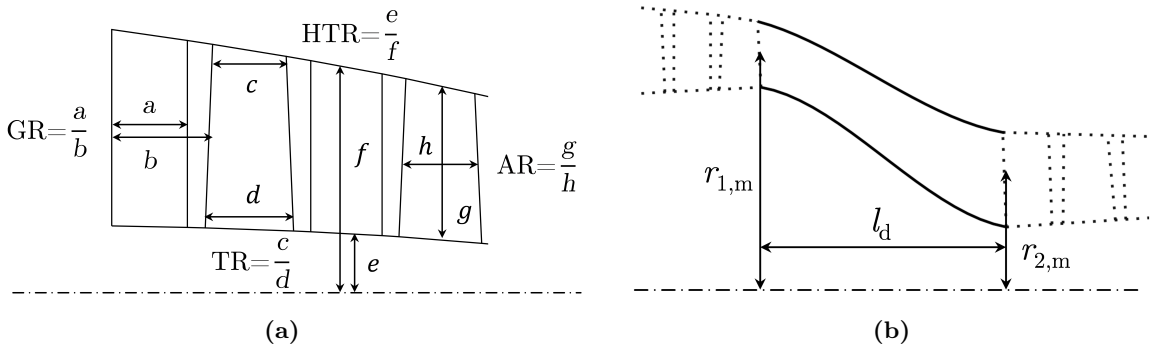

Figure 3.16: Important geometric ratios on (a) turbo components, and (b) ducts.

Table 3.9: Summary of geometric properties of turbo components.

Component	AR_1	AR_2	GR_1	GR_1	TR_1	TR_2	HTR_1	HTR_2	M_1	M_2
Fan	2.6	–	0.25	–	0.88	–	0.30	–	0.68	0.48
IPC	3.0	1.9	0.30	0.30	0.75	0.85	0.65	0.73	0.33	0.25
HPC	3.1	1.5	0.30	0.30	0.50	0.90	0.49	0.90	0.27	0.12
HPT	2.0	1.8	0.40	0.40	0.90	0.75	0.79	0.76	0.07	0.32
LPT	2.5	2.5	0.35	0.35	0.90	0.80	0.74	0.60	0.15	0.45

$$\epsilon = 1 - \frac{\dot{m}}{\dot{m}_{\text{des}}} \cdot (1 - \epsilon_{\text{des}}) \tag{3.90}$$

$$\Delta p = 1 - \frac{\dot{m}^2_{\text{corr,std}}}{\dot{m}^2_{\text{corr,std,des}}} \cdot (1 - \Delta p_{\text{des}}) \tag{3.91}$$

3.5 Flow Path Generation

The generation of the flow path layout is a prerequisite for estimating engine size and to determine, whether all components foreseen can be placed into the core cowling. The sizes are additionally used in this thesis for component mass estimations.

Turbo component cross-sectional areas are obtained via Eq. (3.10) with prescribed typical axial Mach numbers M [95]. Turbo component sizes were generated on a stage resolved level with typical hub-to-tip ratios HTR, gap ratios GR, aspect ratios AR, and taper ratios TR as illustrated in Figure 3.16(a). The values were derived from a PW1100G general arrangement drawing [132] in conjunction with an approximate performance simulation of the engine. The results are summarised in Table 3.9. Axial flow Mach numbers M were determined with the flow path cross-sections and mass flow rates from the engine simulation. Radial compressor geometry is based on empirical relations [133].

Duct geometry was derived from general arrangement drawings of contemporary aero engines. Its axial length l_d was correlated with the relative mean radius reduction as illustrated in

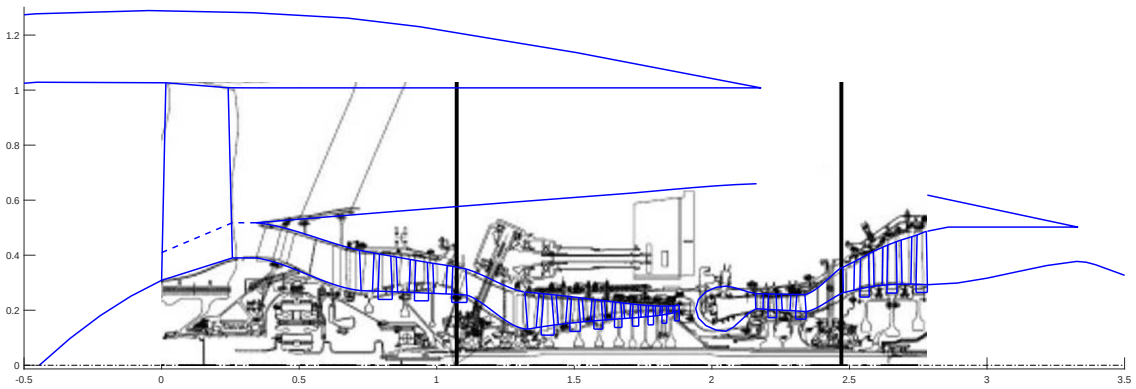

Figure 3.17: Flow path visualisation (blue solid lines) over a PW1100G general arrangement drawing [132].

Figure 3.16(b). The regressions are separated for compressor intake duct in Eq. (3.92) and ducts between turbo components in Eq. (3.93). The bypass nozzle is assumed to have an opening angle of 12°, and the core nozzle of 20°.

$$\frac{l_{\mathrm{d,compressor\ intake}}}{r_{1,\mathrm{m}}} = 3.3 - 3.0 \cdot \frac{r_{2,\mathrm{m}}}{r_{1,\mathrm{m}}} \tag{3.92}$$

$$\frac{l_{\mathrm{d,inter\ turbo}}}{r_{1,\mathrm{m}}} = 1.79 - 1.64 \cdot \min\left(\frac{r_{2,\mathrm{m}}}{r_{1,\mathrm{m}}}; \frac{r_{1,\mathrm{m}}}{r_{2,\mathrm{m}}}\right) \tag{3.93}$$

$$\tag{3.94}$$

The general arrangement is then obtained by sequential positioning of all components. Their boundary coordinates are propagated to the adjacent component. An overlay of the result over the PW1100G engine general arrangement in Figure 3.17 shows the validity of the approach.

Piston engine dimensions were obtained in a bottom-up manner as well [129]. Piston, cylinder head, cylinder liner and casing sizes were approximated based on high-performance motors, mainly from [134]. The relevant set-up and dimensions are illustrated in Figure 3.18 (p. 49) based on piston bore d. Cylinder liner thickness is proportional to piston power, with a reference nominal power of 520 kW.

3.6 Mass Estimation

For engine mass estimation, many semi-empirical approaches are available [135–137]. The disadvantage of such approaches is that they are based on established engine architectures. The CCE architecture is significantly different from a turbofan architecture. Therefore, a component-based bottom-up approach was pursued. This ensures that conceptual decisions are represented physically correct in the engine mass.

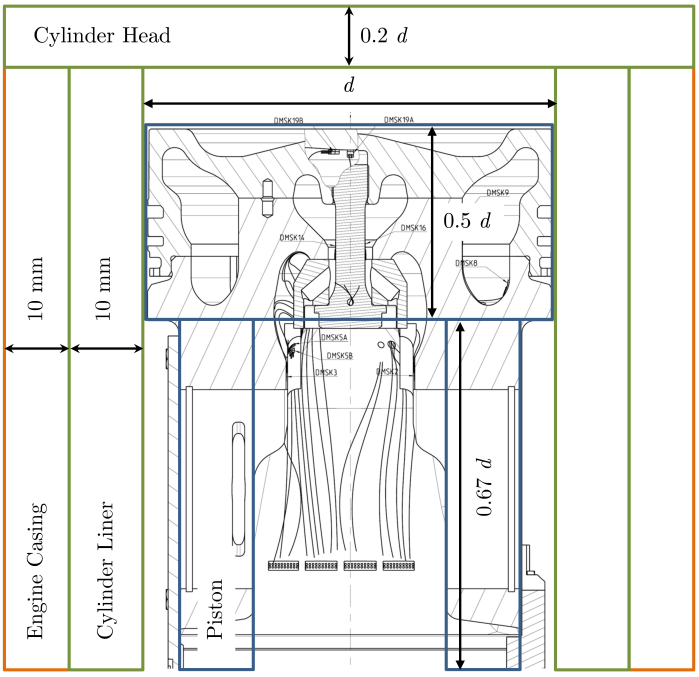

Figure 3.18: Cross-section of a high-performance piston [134] with derived basic geometric relations for other piston components.

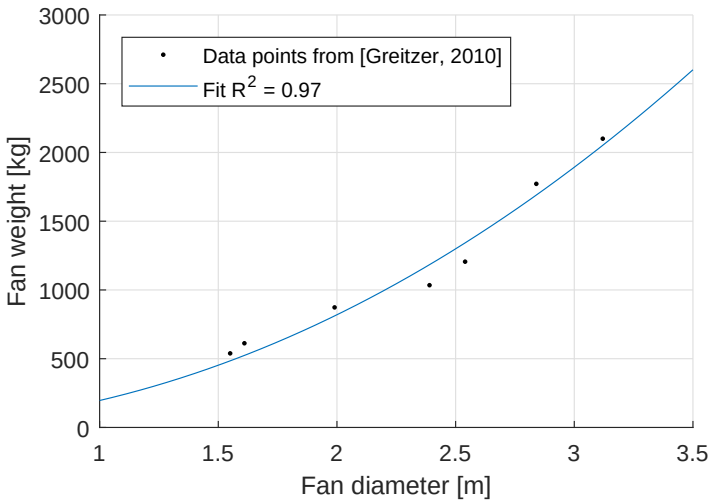

Figure 3.19: Fan mass estimates [138] and regression (solid line).

Fan mass is estimated based on fan diameter. A regression on existing mass estimations from [138] is shown in Eq. (3.95) and Figure 3.19. The data points feature both titanium and composite material fans.

Fan drive gear system (FDGS) mass is evaluated as a function of gear ratio and torque [139, 140]. Eq. (3.96) uses the power on the low-pressure spool (LPS) during TO conditions, the rotational speeds n_1 of LPS and n_2 of the fan. A refined mass estimation can be achieved with a component build-up method [141], but was not used here.

$$m_{\text{fan}} = 196\,\text{kg} \cdot d_{\text{fan}}^{2.06} \tag{3.95}$$

$$m_{\text{GB}} = -16.98\,\text{kg} + 0.01715\,\text{kg} \cdot \left(\frac{P_{\text{GB}}}{n_2}\right)^{0.75} \cdot \left(\frac{n_1}{n_2}\right)^{0.15} \tag{3.96}$$

The masses of the turbo components, i.e. compressors and turbines, are estimated via the volume of their flow paths. Their volume is assumed to be proportional to their mass. The volume is obtained via triangulation of the flow path coordinates, which were calculated as described in Section 3.5. The volume is then multiplied with the density of the material of the respective stage. For compressors, titanium alloy is assumed with a density of $4\,450\,\text{kg/m}^3$ and a cut-off temperature of 650 K at TO conditions [142]. Beyond that temperature, nickel alloy with a density of $7\,900\,\text{kg/m}^3$ is used. Nickel alloy is used in the turbines, too. In the LPT, titanium aluminide (TiAl) with a density of $3\,900\,\text{kg/m}^3$ is used below 1 000 K.

The obtained turbo component mass needs to be adapted for stage solidity, disks, and casings. The final form of the turbo component mass estimation is shown in Eq. (3.97) with the calibration constant c. High pressure components exhibit a higher volume-specific mass than low pressure components due to higher stage aspect ratios, higher disk masses, and sturdier casings. Turbines have a higher volume-specific mass than compressors due to higher stage solidity and heavier disks. In consequence, the calibration constants shown in Eq. (3.98) were determined. Additionally, the area-averaged mean circumferential speed v_m was taken into consideration [143]. The exponent e is 0.5 for compressors and 0.6 for turbines. Shaft masses are included in the turbines.

$$m = c \cdot \rho \cdot V \cdot \left(\frac{v_m}{350\,\text{m/s}}\right)^e \tag{3.97}$$

$$c_{\text{IPC}} = 0.35 \qquad c_{\text{HPC}} = 1.0 \qquad c_{\text{HPT}} = 1.4 \qquad c_{\text{LPT}} = 0.8 \tag{3.98}$$

Combustion chamber mass is proportional to mean combustor diameter d_{m} according to Eq. (3.99) [143]. Accessories – such as engine anti-icing, fire extinguishing, aircraft/engine interface, and ventilation – and the accessory gearbox with starter, generator and hydraulic pumps are scaled linearly to ToC sizing thrust $F_{\text{N,ToC}}$ as suggested by [143]. Residual engine masses for systems (electrical, oil, air, etc.) and dressings (sensors, fuel heat exchanger, fairings, mountings, etc.) are assumed to contribute a fixed share of 15 % of the engine mass as suggested by [143], and based on empirical data of modern turbofan engines [144].

$$m_{\text{combustor}} = 196\,\frac{\text{kg}}{\text{m}^2} \cdot d_{\text{m}}^2 \tag{3.99}$$

$$\text{with} \quad d_{\text{m}} = \frac{1}{2}\left(d_{\text{m,HPC,2}} + d_{\text{m,HPT,1}}\right) \tag{3.100}$$

$$m_{\text{accessories}} = 5\,\frac{\text{kg}}{\text{kN}} \cdot F_{\text{N,ToC}} \tag{3.101}$$

$$m_{\text{residual}} = 0.15 \cdot m_{\text{engine}} \tag{3.102}$$

Nacelle mass is modelled according to semi-empirical relations based on wetted area with nacelle length l_{Nacelle} and diameter d_{Nacelle} shown in Eq. (3.103) [145]. The dimensions were correlated from general arrangement drawings of contemporary aero engines. A correction factor of 0.70 was applied to adapt for high BPR engines. While reference [145] suggests doubling wetted area, only the single wetted area was considered as thrust reverser mass was modelled separately. The latter scales linearly with TO thrust $F_{\text{N,TO}}$ based on data from [144]. Masses of core cowling, bypass nozzle and core nozzle are estimated in accordance with Eq. (3.103) with the respective dimensions but without the correction factor 0.70.

$$m_{\text{Nacelle}} = 0.70 \cdot 24.88\,\frac{\text{kg}}{\text{m}^2} \cdot l_{\text{Nacelle}} \cdot \pi d_{\text{Nacelle}} \tag{3.103}$$

$$\text{with} \quad d_{\text{Nacelle}} = 1.056\,d_{\text{fan}} + 0.41\,\text{m} \tag{3.104}$$

$$\text{and} \quad l_{\text{Nacelle}} = 1.7 \cdot d_{\text{fan}} \tag{3.105}$$

$$m_{\text{thrust rev}} = 3.37\,\frac{\text{kg}}{\text{kN}} \cdot F_{\text{N,TO}} \tag{3.106}$$

The complete structure of the engine and power plant system (PPS) mass estimation is summarised in Table 3.10 (p. 52) based on the suggested breakdown in [144]. The method was validated with a simulation model of the PW1100G engine. The result was compared to the type-certificate data sheet (TCDS) engine mass [146]. Pylon mass is included in the aircraft control balance.

The mass estimation of the piston system is crucial for the accurate evaluation of the CCE concept, since the added mass constitutes one of its main drawbacks. One option is to use a top-down approach based on empirical data collected from series, experimental and concept piston engines. Valuable approximations for piston system mass can be derived from the data and the dominating parameters can be identified [23, 129]. As a major drawback of this approach, the masses are specified for entire engine systems, including accessories for water, fuel and oil, gearing, output shaft with flange, and potentially a turbocharger. Therefore, top-down mass estimations tend to overestimate the base piston system mass. Moreover, the estimation for piston systems with very different operating conditions requires extrapolation from available data, which incurs further uncertainty. Sensitivities for individual mass items would not be physically appropriate.

Table 3.10: Structure of engine masses and validation values.

Component	**Method**	**PW1100G model [kg]**	**TCDS [kg]**
Fan, incl. fan casing and intermediate casing	Regression on data [138] dependent on fan diameter	851	
FDGS, incl. lubrication system	Relation [140] dependent on torque and gear ratio	309	
Turbo components	Based on volume and speed		
- IPC		140	
- HPC		266	
- HPT		178	
- LPT		492	
Combustor	Regression on data [144]	77	
Systems & Dressings	15 % of engine mass	431	
Accessories	Prop. to ToC thrust	132	
Engine	Sum of above	2 875	2 858 (-0.6 %)
Nacelle, incl. intake, external fairings, acoustic linings	Prop. to wetted area [145]	498	
Thrust reverser	Prop. to TO thrust	496	
Core cowl	Prop. to wetted area [145]	64	
Bypass nozzle	Prop. to wetted area [145]	86	
Core nozzle	Prop. to wetted area [145]	19	
PPS	Engine mass + sum of above	4 038	

Therefore, a component-based bottom-up mass modelling was pursued. The mass-driving components were modelled, in particular cylinder liner, cylinder head, casing, piston, connecting rod, crankshaft and valvetrain. The piston is divided into piston head with a solidity of 80 % and the skirt with a solidity of 30 % as indicated in Figure 3.18. Piston bore and stroke are equal. The connecting rod between piston and crankshaft is 1.7 times as long as the stroke, based on best practice [147]. Connecting rod cross-sectional area is sized to receive the peak load with a safety factor of 3.0. The crankshaft has a baseline diameter of 0.19 m, and is scaled with torque $T^{1/3}$. Mass of the above-mentioned parts is obtained via their volume and an assumed material. Most piston parts (cylinder liner and head, connecting rod, crankshaft, camshaft) are steel-based alloys with a density of 7 730 kg/m^3. The pistons are assumed to be made of TiAl, which has appealing properties for reciprocating parts with a low density of 3 900 kg/m^3, high-temperature capability and good oxidation resistance [148, 149]. The use of TiAl for valves, connecting rods and piston pins has been successfully tested, but it was not used for pistons before. It is used in the aeronautical industry for light-weight high-temperature parts, in particular LPTs. The motor block is assumed to be made from

magnesium alloy due to its low density of 1 800 kg/m^3. Magnesium alloys for casings are proven technology in the automotive industry and in aviation [150].

The valves are actuated with camshafts with an assumed shaft diameter of 50 mm. Masses of bearings, injectors, and common rail fuel pump are estimated by scaling masses of known components with diameter or power. Masses of other minor items such as crankshaft casing and back plate, valves, ducts and piston rings are not specifically modelled and considered to be included in the overall piston engine mass. The results from the bottom-up estimation were developed and verified in a master's thesis [129]. They showed very good agreement with estimations from a top-down approach based on empirical data, which by itself had a mean error of 10 % with an empirical database.

3.7 Aircraft Level Assessment

Novel engine concepts have three major impacts at the aircraft level. First, an improvement in engine efficiency reduces required fuel aboard the aircraft for a given mission. As a result, MTOW reduces, and wing area and aircraft structural mass can be reduced at constant wing loading. Second, additional PPS mass requires more thrust as well as a sturdier pylon and wing structure [17] with similar cascading effects mentioned above. Third, a larger fan diameter increases nacelle drag and possibly landing gear weight to maintain a given ground clearance. The last impact is not relevant in this thesis, because fan diameter is kept constant. The fan diameter was optimised for the application, and no major deviation due to the CCE is expected. Thus, simulation complexity was reduced.

To take full account of these cascading effects, a fully resizable short-to-medium range aircraft (180 passengers, design range 2 850 nmi) is used. The aircraft was sized in the commercial aircraft design platform Pacelab APD [151]. The aircraft represents a technological standard of an entry into service year 2035. The aircraft subsystem architecture is all-electric (AE), i.e. all aircraft subsystems are driven electrically, and no bleed off-takes are taken from the engine. The customer bleed, particularly cabin air and anti-icing, are provided externally with auxiliary compressors and electric heating. This requires a higher, mission averaged power off-take of 184 kW per engine.

The resulting impact at the aircraft level was evaluated for mission fuel burn, operating empty weight (OEW) and MTOW for several combinations of engine TSFC improvement and change in PPS mass. The results are provided in the simulation environment as gridded data and spline interpolation is used to get the aircraft impact. At each mission point, the required thrust in all simulated mission points can be obtained. Trade factors (sometimes referred to as exchange factors) can be used to map changes in TSFC and PPS mass m_{PPS} on changes in mission fuel burn (FB). The change in m_{PPS} is nearly linear in fuel burn as shown in past studies [152]. Thus, a linearised trade factor can be used as shown in Eq. (3.107). For TSFC, a parabolic relation can be used as shown in Eq. (3.108). Cascading effects abate with increasing improvements, since the mass share of fuel in the aircraft reduces progressively. The linearised equations show the trade between PPS weight and TSFC. An improvement in

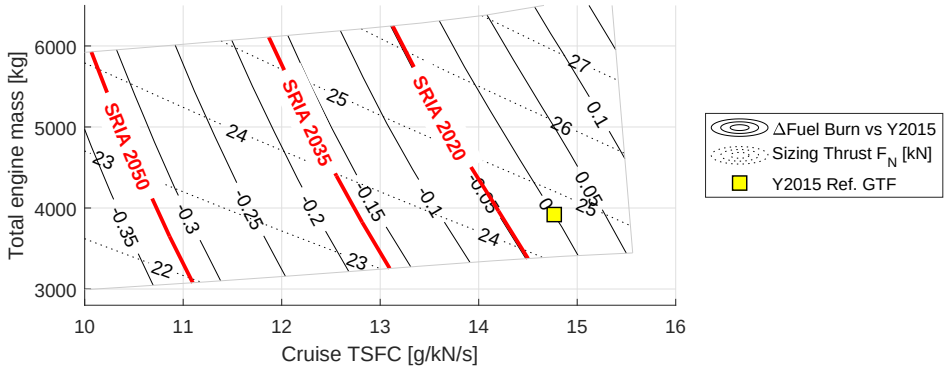

Figure 3.20: Iso-contours of change in fuel burn depending on TSFC and total engine mass m_{PPS} on a year 2035 short-to-mid range aircraft. Red lines indicate engine-related emission reduction targets.

TSFC by 1 % allows a 290 kg higher PPS mass for equal fuel burn. A linearisation of relative change in sizing thrust is displayed in Eq. (3.110).

$$\Delta \mathrm{FB}_{m,\mathrm{PPS}} = \frac{1\,\%}{201\,\mathrm{kg}} \cdot \Delta m_{\mathrm{PPS}} = \frac{0.498\,\%}{100\,\mathrm{kg}} \cdot \Delta m_{\mathrm{PPS}} \tag{3.107}$$

$$\Delta \mathrm{FB}_{\mathrm{TSFC}} = 1.443 \cdot \Delta \mathrm{TSFC} + 0.930 \cdot \Delta \mathrm{TSFC}^2 \tag{3.108}$$

$$\Delta \mathrm{FB} = (1 + \Delta \mathrm{FB}_{m,\mathrm{PPS}}) \cdot (1 + \Delta \mathrm{FB}_{\mathrm{TSFC}}) - 1 \tag{3.109}$$

$$\Delta F_{\mathrm{N,ToC}} = 0.425 \cdot \Delta \mathrm{TSFC} + \frac{0.490\,\%}{100\,\mathrm{kg}} \cdot \Delta m_{\mathrm{PPS}} \tag{3.110}$$

The resulting iso-contour plots on the tabulated data are illustrated in Figure 3.20[7]. The engine-related SRIA 2020 goals are achieved with a moderate TSFC improvement by 3.6 % against the present technological standard, if engine mass remains constant. The SRIA 2035 targets require a weight-neutral TSFC improvement by 13.3 %. Achieving SRIA 2050 targets requires a very significant, weight-neutral leap by 27.0 %.

3.8 Instationary Operation

3.8.1 Impact of Pulsating Flow on Turbo Components

The instationary operation of piston engines imposes pulsating flow conditions on the adjacent turbo components. The IPC is subject to pulsating outlet conditions, and the HPT to pulsating inlet conditions. The secondary combustor operation may be impaired by pulsating flow conditions, affecting fuel atomisation. This could potentially lead to thermo-acoustic vibrations through resonant response of the heat release rate.

[7]The power plant mass is reduced compared to the PW1100G model mass presented in Section 3.6 as the advanced aircraft platform requires less sizing thrust

Investigations of the impact of pulsating flow on turbine efficiency revealed a dependency on pulsation frequency f_{pulse} and amplitude $\Delta p/p$ [153]. Higher amplitudes lead to an almost linear increase in losses. For a pulsation frequency of 2 500 Hz in a two-stage turbine, isentropic efficiency drops by 0.33 % for an amplitude of 2.5 % of the total pressure, and up to 1.05 % for an amplitude of 7.5 %. The pulsation frequency in the CCE is of the order of 500 Hz. Higher frequency increases losses in an almost linear relation as the pressure gradient increases for a given amplitude. The losses mainly occur in the first stage of the turbine. After the first stage, oscillation amplitude is reduced to a third. For simplification, it is assumed that the entire loss is created in the first stage. The concluding relation used within this thesis is shown in Eq. (3.111).

For the IPC, pulsating exit conditions impair efficiency and blade vibrations [154]. Again, both amplitude and frequency were found to play an important role in the magnitude of efficiency losses. The relation with respect to amplitude is approximated as a quadratic function as shown in Eq. (3.112) with $R^2 = 0.998$. An amplitude of 20 % of the total pressure p results in a 6 % efficiency loss in the last stage, when the pulsation frequency is much larger than the blade passing frequency. When blade passing frequency in the compressor is similar to the pulsation frequency f losses are minimal with a loss of 4 % per 20 % amplitude.

$$\Delta\eta_{\text{is,HPT}} = 13.4\,\% \cdot \frac{\Delta p}{p} \cdot \frac{2}{n_{\text{stages}}} \cdot \frac{f_{\text{pulse}}}{2\,500\,\text{Hz}} \tag{3.111}$$

$$\Delta\eta_{\text{is,IPC}} = 150\,\% \cdot \left(\frac{\Delta p}{p}\right)^2 \cdot \frac{1}{n_{\text{stages}}} \tag{3.112}$$

Buffering volumes before and after the piston engine are foreseen to reduce the oscillations seen by the turbo components, and thus efficiency losses. The buffering volumes are sized to keep the loss in the full component below 0.05 % and, thus, negligible. Reducing the pulsations helps to prevent high cycle fatigue in the blade roots due to vibrations [154]. Additional volumes that contribute to buffering – such as ducting, the combustor and its annulus – may further reduce the oscillations seen by the turbo components, but they are neglected for sizing.

The volume is approximated with simple estimations. The pistons on one shaft are assumed to be equally phase shifted. The resulting pulsation frequency f_{pulse} is calculated with Eq. (3.113). It is assumed that the mass change peak-to-peak in the buffering volume $2 \cdot \Delta m$ is equal to the mass inducted during one cycle according to Eq. (3.114). This is a conservative assumption, since valve opening times overlap, which leads to lower mass oscillations. Buffering volume V_{buff} is then derived according to the ideal gas law with Eq. (3.115), where the permissible pressure oscillation Δp was determined with Eq. (3.111) or Eq. (3.112).

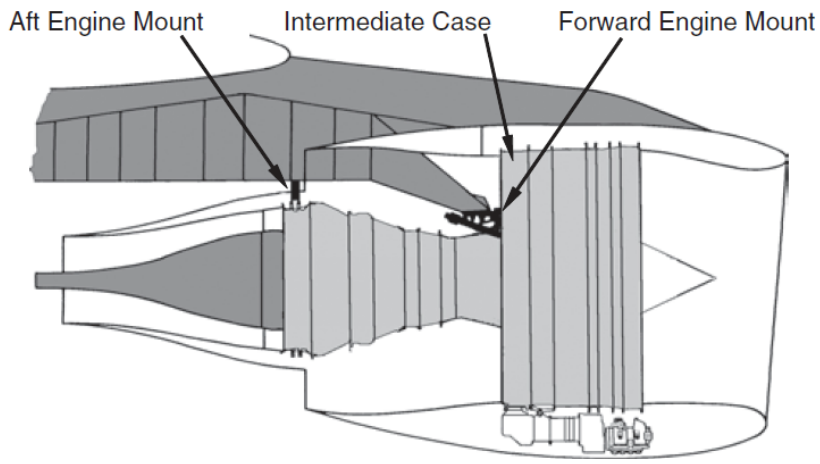

Figure 3.21: Schematic illustration of the two engine mountings [155].

$$f_{\text{pulse}} = \frac{n_{\text{cyl}} \cdot f}{2} \tag{3.113}$$

$$\Delta m = \frac{\dot{m}}{2 \cdot n_{\text{cyl}} \cdot f} \tag{3.114}$$

$$V_{\text{buff}} = \frac{\Delta m R T}{2 \Delta p} \tag{3.115}$$

3.8.2 Mechanical Oscillation

Mechanical oscillations in piston engines are a result of their oscillatory mode of operation. Here, only a first consideration of the dynamic loads imposed by pistons and connecting rods is presented, in order to judge the extent of forces and moments within the piston engine assembly.

The engine mounting is illustrated in Figure 3.21. The front mount takes the axial loads – mainly the thrust – of the engine. The rear mount carries transversal forces and torque. Other moments are carried by both mounts [155]. In some engines the thrust loads are transferred directly to the rear mount via thrust links, when space is confined. The forward engine mount is then attached to the fan casing. The piston engine should be mounted close to the forward mount to reduce the impact on the remaining engine. Otherwise, detrimental effects on tip clearances and surge margins may occur.

In the concept used in this thesis, which will be presented later in greater detail, two V-type piston engines are used, which are arranged around the engine axes. The piston engines are synchronised through gearing, which allows balancing forces between both engines. It is assumed that the piston engines are mounted to a separate, rigid frame, so all forces and moments can be first equalised between the two engines. This frame is then connected to the engine mounting, which receives the remaining forces. One engine is installed on the top of the core engine with hanging pistons. The other engine is mounted on the bottom with its

pistons facing upwards. This mirrored arrangement allows always having two pistons moving in exactly opposing direction. Thus, all net forces are balanced. This does not balance all moments created by pistons, however. On the crankshaft, for each rod bearing journal a counterweight can be applied to reduce the net force of the moving piston. Additionally, two balance weights on front and rear of the shaft can be applied to counteract moments created by shaft, con rod and pistons. Their masses and eccentricities are two degrees of freedom for balancing. The remaining third moment can be fully extinguished with further means such as balance shafts or moment balancing gears [147]. Generally, more pistons make balancing easier. On a V10-engine for example, all forces and moments of first order can be equalised and the second order moment is small [156]. Therefore, mechanical oscillations are not further evaluated. The potentially required added mass and space may, however, imply detrimental impact on fuel burn of unknown magnitude. Also, it may be required to balance each piston engine separately, if the frame cannot be built rigidly enough with reasonable effort.

3.9 Emissions

Aircraft emissions regulations are a major driver for technological developments. CO_2 and NO_x emissions will be quantified as they are important for fuel saving evaluation and for certification. Apart from these, noise and other emissions, and how they may change in contrast to a turbofan are discussed in this chapter qualitatively.

3.9.1 CO_2 Emissions

Assuming usage of kerosene as fuel, CO_2 emissions are directly proportional to fuel burn as shown in Reaction (3.4). The assessment of fuel burn is described in Section 3.7. Emissions of CO_2 are regulated due to their radiative forcing impact on climate warming. Aviation CO_2 accounted for a total of 2 % of the total anthropogenic emissions in 1992, about 2.5 % in 2005 [157], and is projected to increase to at least 3 % by 2050 [158]. It is predicted to increase by a factor of 2.4 to 3.6 compared to the year 2005 [157]. The SRIA specifies targets of -36 %, -51 % and -68 % for the years 2020, 2035 and 2050 respectively against year 2000 certification standard per passenger and kilometre on aircraft level (not including air traffic management, infrastructure and operational improvements). For the propulsion system only, targets of -20 %, -30 % and -43 %[8] are targeted. Global aviation CO_2 emissions are subject to the Air Transport Action Group (ATAG) goals [159]. These foresee a carbon-neutral growth from 2020 onwards, and a 50 % reduction by 2050 compared with year 2005 global emissions from aviation. These targets should be achieved by improvements in technology and air traffic management, but also market-based measures such as carbon off-setting and biofuels. The ATAG goals are not further discussed in this thesis, as market trends are out of the scope.

[8] Assuming equal split between airframe and propulsion system.

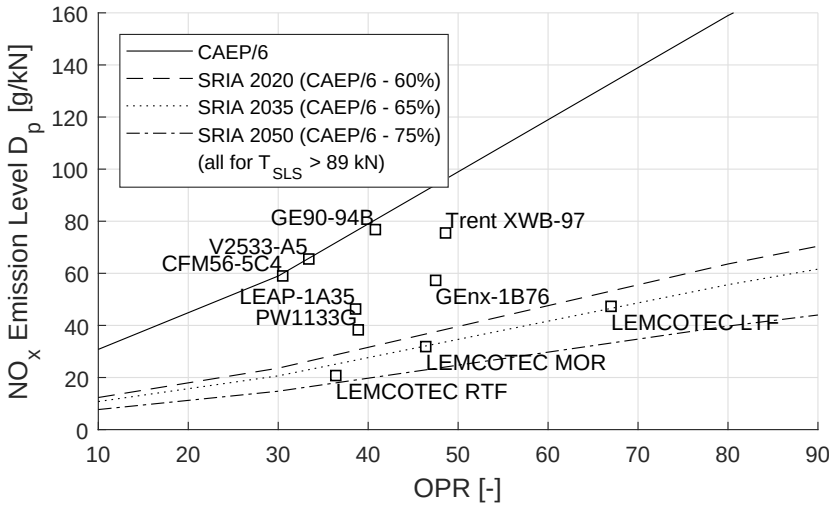

Figure 3.22: Limits of NO_x emissions in the LTO cycle with future SRIA reduction targets, and some current in-service and projected aircraft engines.

3.9.2 NO_x Emissions

Nitrogen oxide (NO) and nitrogen dioxide (NO_2) are environmentally harmful trace gases [158]. They impair local air quality around airports. They lead to respiratory disorders. Moreover, NO_x promotes ground-level ozone, which is a pulmonary irritant [160]. Aviation can contribute as much as 5 % of the NO_x in proximity of large airports [161]. Hence, they are subject to emission reduction agendas. Altitude NO_x has an impact on radiative forcing indirectly via other species as described in Section 3.9.4.

The SRIA [1] specifies targets of -60 %, -65 % and -75 % for the years 2020, 2035 and 2050 respectively in the landing and take-off (LTO) cycle against the year 2008 certification standard per kg of fuel burnt (CAEP/6, [162]). The targets are shown in Figure 3.22 with relevant reference engines. They are dependent on engine thrust and OPR, where higher thrust-specific NO_x emissions in the LTO cycle are permitted if OPR is increased. This promotes higher efficiency engines by allowing for a trade-off between CO_2 and NO_x emissions.

This target is supported by shortfall of emissions during taxiing through emission-free taxiing by the year 2050, which may be achieved by infrastructure measures such as electric towing vehicles or with electric taxiing with the fan as proposed by [152]. Moreover, high altitude NO_x has an impact on ozone chemistry, leading to increased ozone production. Targets of -80 %, -84 % and -90 % for the years 2020, 2035 and 2050 respectively during cruise per passenger kilometre against a year 2000 technological standard have been specified[9]. Global in-flight NO_x emissions on international flights are expected to increase by a factor between 2.2 and 3.0 from 2010 to 2040 [161]. A similar relative increase in LTO cycle emissions is predicted.

[9]This translates into -75 %, -77 % and -78 % per kilogram fuel burnt, respectively, assuming the targeted improvements in combined engine and airframe efficiency will be met. In consequence, cruise emission index NO_x (EINOx) is allowed to stay almost constant from 2020 onwards.

For the estimation of NO_x emissions in conventional gas turbine engines, well established semi-empirical relations are available. The CCE concept requires additional effort: In the piston engine, the gas turbine relations cannot be used, because the process is highly instationary. While peak temperatures and pressures are higher than in a gas turbine combustor, residence times at these conditions are much shorter. In the secondary combustor, these relations need to be corrected for the reduced oxygen content due to the preceding piston engine. Suitable NO_x emissions models for both are presented in the following.

Piston Engine

Several chemical pathways exist to form NO from the contents of the combustion gases. The most commonly considered and predominant pathway is the *Zeldovich* mechanism, which results in the creation of *Thermal NO*. It consists of Reactions (3.116)-(3.118). In conventional diesel engines, it generates approximately 95 % of NO_x [163].

$$N_2 + O \overset{k_1}{\rightleftarrows} NO + N \tag{3.116}$$

$$N + O_2 \overset{k_2}{\rightleftarrows} NO + O \tag{3.117}$$

$$N + OH \overset{k_3}{\rightleftarrows} NO + H \tag{3.118}$$

Under fuel rich conditions with relevant amounts of CH in the flame, the prompt NO mechanism is important. The two dominant pathways are the Fenimore pathway in Reaction (3.119) and the Moskaleva in Reaction (3.120) [164, 165]. Under high pressure conditions, the N_2O mechanism becomes important as shown in Reaction (3.121) and (3.122). Since the first reaction requires a third arbitrary agent M, the reaction rates grow faster than those of other pathways at high density. A fourth, more recently discovered pathway is the NNH mechanism shown in Reaction (3.123) [166]. It requires three agents for the initial reaction but is not very well understood, yet. A fifth source is fuel NO, which is created, when the fuel contains nitrogen. In kerosene, nitrogen concentrations are negligible [164].

$$N_2 + CH \rightarrow HCN + N \rightarrow \ldots \rightarrow NO \tag{3.119}$$

$$N_2 + CH \rightarrow NCN + H \rightarrow \ldots \rightarrow NO \tag{3.120}$$

$$N_2 + H + M \rightarrow N_2O + M \tag{3.121}$$

$$N_2O + O \rightarrow 2NO \tag{3.122}$$

$$N_2 + H + M \rightarrow NNH + M \rightarrow \ldots \rightarrow NO \tag{3.123}$$

In this thesis, only the *Zeldovich* pathway is considered. The prompt NO pathway is not relevant, since fuel rich conditions are avoided for fuel efficiency. Because most publications for simulation only consider this pathway, a calibration to these simulation results is most

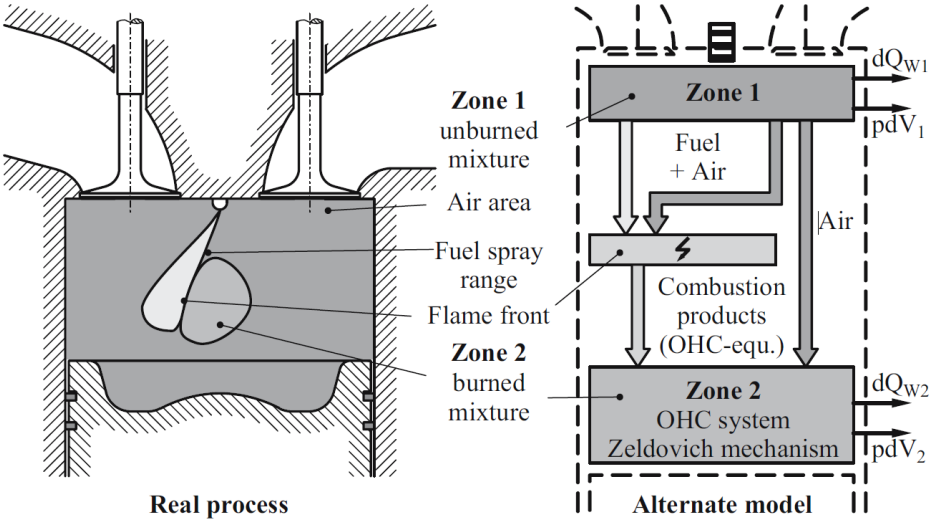

Figure 3.23: Schematic illustration of the relations of the zones of the 2-zone model [105].

accurate. Further pathways are implicitly included in this way. This approach introduces a systematic error, when other NO_x creation pathways grow more than the Zeldovich mechanism in the CCE operating conditions in comparison to the reference conditions used for model calibration. This could be the case for the N_2O and NNH pathways, since they become relevant under high pressure conditions.

NO_x generation is highly dependent on fluid state. Therefore, it is time- and space-dependent in the piston engine. Time-resolved mean cylinder temperature and pressure are available from the 0D simulation model presented in Section 3.3. NO_x is produced in the combustion zones in the cylinder, where the temperatures are highest. The NO_x generation is assumed to be fully decoupled from combustion [167], i.e. the chemical reactions of the NO_x generation process occur after the combustion reactions are complete. This assumption is justified as the combustion reactions are fast enough and, hence, the combustion reaction zone and time is small in relation to the NO_x generating process. It allows to execute the performance simulation first, and run the NO_x simulation subsequently.

The simplest model with a spatial resolution is the *2-zone model* [105, 168, 169]. Here, the fluid is divided into a fresh air zone and a zone that contains the fluid after combustion took place. A third, non-resolved zone is the flame front, which is assumed to be negligibly small. The relation of the zones is displayed in Figure 3.23.

NO_x is assumed to be produced only in the combustion zone, Zone 2. Its generation is simulated with reaction kinetics, i.e. with the chemical non-equilibrium generation rates [170]. The reaction rate for NO according to Reactions (3.116)-(3.118) is shown in Equation (3.124). The reaction rate is dependent on the reactant concentrations, and the reaction rates for the forward reaction k_f and the reverse reaction k_r. The reaction rates can be obtained from respective databases. In this thesis, the rates have been obtained from CHEMKIN 3.0 [171], and are displayed in Equations (3.125)-(3.127) for the Zeldovich mechanism.

$$\begin{aligned}\frac{\mathrm{d}[\mathrm{NO}]}{\mathrm{d}t} &= k_{1,\mathrm{f}}[\mathrm{N_2}][\mathrm{O}] - k_{1,\mathrm{r}}[\mathrm{NO}][\mathrm{N}] \\ &\quad + k_{2,\mathrm{f}}[\mathrm{N}][\mathrm{O_2}] - k_{2,\mathrm{r}}[\mathrm{NO}][\mathrm{O}] \\ &\quad + k_{3,\mathrm{f}}[\mathrm{N}][\mathrm{OH}] - k_{3,\mathrm{r}}[\mathrm{NO}][\mathrm{H}] \end{aligned} \tag{3.124}$$

$$k_{1,\mathrm{r}} = 2.70 \times 10^7 \, \frac{\mathrm{m}^3}{\mathrm{mol\,s}} \cdot \exp\left(-\frac{355\,\mathrm{cal/mol}}{R_m T}\right) \tag{3.125}$$

$$k_{2,\mathrm{f}} = 9.00 \times 10^3 \, \frac{\mathrm{m}^3}{\mathrm{mol\,s}} \cdot T \cdot \exp\left(-\frac{6\,500\,\mathrm{cal/mol}}{R_m T}\right) \tag{3.126}$$

$$k_{3,\mathrm{f}} = 3.36 \times 10^7 \, \frac{\mathrm{m}^3}{\mathrm{mol\,s}} \cdot \exp\left(-\frac{385\,\mathrm{cal/mol}}{R_m T}\right) \tag{3.127}$$

They typically follow the form of the Arrhenius equation $A \cdot \exp\left(-E_0/(R_m T)\right)$, where A is a constant, E_0 is the reaction's activation energy, $R_m = 1.987\,\mathrm{cal/mol/K}$ is the universal gas constant and T the reaction temperature [170]. Hence, reaction rates increase exponentially with temperature and quadratically with pressure, since concentration increases with density. This shows why $\mathrm{NO_x}$ is generated particularly at high temperatures and pressures. The corresponding reaction coefficients $k_{1,\mathrm{f}}$, $k_{2,\mathrm{r}}$ and $k_{3,\mathrm{r}}$ are not specified in CHEMKIN 3.0 [171], but can be obtained via the equilibrium constant K_c with

$$K_c = \frac{k_\mathrm{f}}{k_\mathrm{r}} \tag{3.128}$$

K_c expresses the ratio of concentrations of reactants and products [171], at which forward and reverse reactions are in equilibrium:

$$K_c = K \cdot \left(\frac{p_\mathrm{std}}{R_m T}\right)^{\Delta\nu} \tag{3.129}$$

$$\text{with} \quad K = \exp\left(\sum_i^{n_\mathrm{species}} G_{\mathrm{std,i}}\right) \tag{3.130}$$

$$\text{and} \quad G_{\mathrm{std},i} = \nu_i \cdot (S_{\mathrm{std},i} - H_{\mathrm{std},i}) \tag{3.131}$$

$$\text{and} \quad \Delta\nu = \sum_i^{n_\mathrm{species}} \nu_i \tag{3.132}$$

Here, the standard molar entropy $S_{\mathrm{std},i}$ and the standard molar enthalpy $H_{\mathrm{std},i}$ can be obtained with the NASA nine-term polynomials for the respective temperature T for arbitrary species as described in Section 3.1. These are used to calculate the standard molar Gibbs energy $G_{\mathrm{std},i}$. The mole number ν indicates the number of the species in the reaction, with reactants being negative and products being positive. The change in mole number $\Delta\nu$ is the sum of all mole numbers. $\Delta\nu$ is positive for reactions with a growing number of molecules. A reaction with $\Delta\nu = 0$ is independent from pressure. As can be seen, K_c can be calculated without the knowledge of the reaction coefficients k. The correct calculation of the equilib-

rium constant has been verified with published data of both forward and reverse reaction coefficients. An example is shown in Figure A.1 (p. 145) in Appendix A.3.

For calculation of the NO_x generation rates, the concentrations of species N, O and OH must be known in zone 2. To this end, the *OHC-System* can be employed according to Eq. (3.133)-(3.137) [105]. These reactions are fast enough in comparison to the Zeldovich mechanism, so that they can always be assumed to be in equilibrium in zone 2. This is referred to as *quasi-steady state approximation* [164].

$$H_2 \rightleftarrows 2H \tag{3.133}$$

$$O_2 \rightleftarrows 2O \tag{3.134}$$

$$H_2O \rightleftarrows \frac{1}{2}H_2 + OH \tag{3.135}$$

$$H_2O \rightleftarrows \frac{1}{2}O_2 + H_2 \tag{3.136}$$

$$CO_2 \rightleftarrows CO + \frac{1}{2}O_2 \tag{3.137}$$

Additionally, the three atomic balances for C, O and H must be satisfied, giving a total of eight conditions. This allows to solve for the concentrations of the eight species CO_2, H_2O, CO, OH, H_2, H, O_2, and O. The implementation of the model has been validated against other publications [115, 172][10]. The validation quality of the implemented model is illustrated in Figure A.2 (p. 145) in Appendix A.3.

The simulation starts when valves close. It integrates the NO_x generation in time according to Eq. (3.124). No distinction between the two zones is made until combustion starts. This provides the initial conditions. At that point, zone 2 is initiated. The air ratio λ_0 is defined according to Eq. (3.138), and held constant in zone 2. Thus, the mass in zone 2 m_2 can be calculated with Eq. (3.139). Therefore, m_2 is prescribed by the rate of heat release according to the Wiebe function as given in Eq. (3.53). The difference between the fuel mass m_f and the initial fuel mass $m_{f,0}$ constitutes the injected fuel. The residual fuel from the previous cycle remains evenly distributed over both zones with fuel-air ratio FAR_1.

$$\lambda_0 = \frac{FAR_{stoich}}{FAR_2} \tag{3.138}$$

$$m_2 = (1 + \frac{1}{FAR_2 - FAR_1}) \cdot (m_f - m_{f,0}) \tag{3.139}$$

The initial temperature difference between both zones A^* is an empirical value specific to an engine. Due to lack of comparable engines for calibration of A^*, the value is defined relative to the increase in temperature due to combustion with air ratio λ_0 at SOC as in Eq. (3.140). The

[10] As a caveat, the concentrations of atomic nitrogen N displayed in [115] are two orders of magnitude too low.

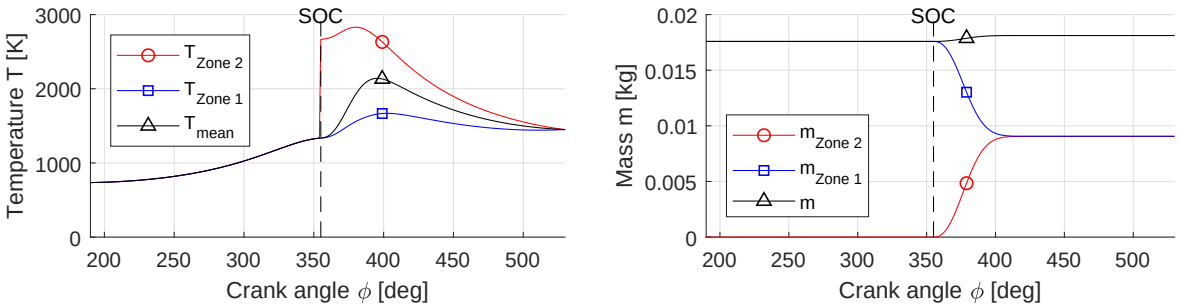

Figure 3.24: Qualitative scope of (a) temperature and (b) mass in both zones of the 2-zone-model in contrast to mean values.

flame temperature T_{fl} is estimated by assuming a stoichiometric gas composition. The phase-resolved temperature difference between both zones is then adapted empirically according to Eq. (3.141). In this equation, the pressure of the motored engine p_0 is calculated by assuming isentropic compression and expansion according to the prescribed cylinder volume $V(\phi)$. The temperature difference is assumed to level out until EVO. With the temperature difference prescribed, the actual temperatures T_1 and T_2 are calculated with the conditions of equal pressure p in both zones and the volume of both zones V_1 and V_2 being equal to the cylinder volume according to the ideal gas equation.

$$A^* = c_A \cdot (T_{\mathrm{fl}} - T_{\mathrm{SOC}}) \tag{3.140}$$

$$T_2(\phi) - T_1(\phi) = B(\phi) \cdot A^* \quad \text{with} \tag{3.141}$$

$$B(\phi) = 1 - \frac{\int_{\phi_{\mathrm{SOC}}}^{\phi} (p(\phi) - p_0(\phi))\, m_2(\phi)\, \mathrm{d}\phi}{\int_{\phi_{\mathrm{SOC}}}^{\phi_{\mathrm{EVO}}} (p(\phi) - p_0(\phi))\, m_2(\phi)\, \mathrm{d}\phi}$$

The resulting conditions in both zones are displayed in Figure 3.24 for typical TO conditions, i.e. with highest cylinder temperatures. Until SOC, the entire control volume is only one zone. Thus, the temperature in the fresh air zone 1 is equal to the mean temperature, because the combustion zone contains no mass. The mean temperature approaches T_2 during combustion, while the temperature difference between both zones reduces and eventually becomes zero, when the exhaust valves open. The mass m_2 is zero at start of combustion and increases until end of combustion. Some air always remains in zone 1 depending on FAR. Coincidentally, the mass in zone 1 and zone 2 is almost equal in the plot displayed in Figure 3.24(b).

As can be seen, the mean temperature barely reaches 2 200 K. The creation of NO reaches notable orders of magnitude only above this temperature. The simulated NO creation for the example is depicted in Figure 3.25 (p. 64). The temperature T_2 starts a at much higher value, resulting in high NO creation rates. This underlines the importance of resolving the combustion zone. After the peak temperature is reached, the equilibrium NO concentration

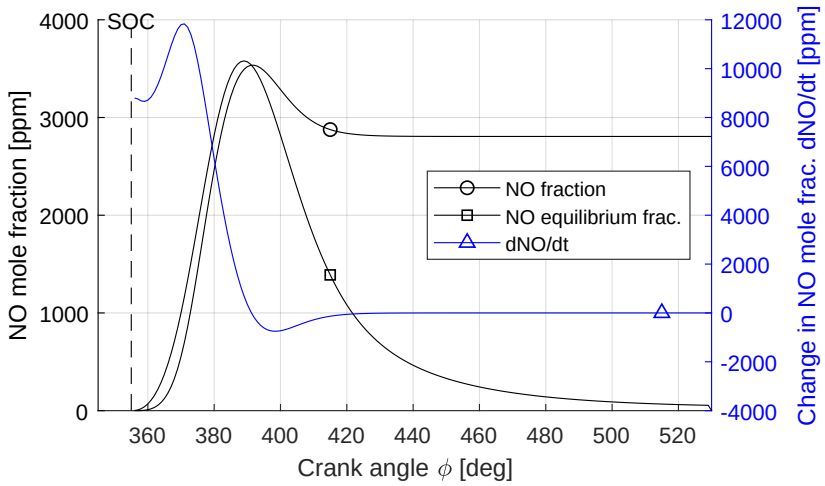

Figure 3.25: Creation of NO over crank angle in contrast to equilibrium NO concentration.

gets below the actual NO concentration and reverse reaction occurs for a short period. At this point, however, the reaction coefficients are much smaller than during creation. Thus, only a small fraction of the created NO is reduced. After T_2 falls below approximately 2 200 K, equilibrium concentration further declines, but the reaction is virtually frozen.

After the verification of sub-models of the NO_x generation simulation, in particular the reaction kinetics and the OHC-System, the integrated model has been verified by comparing simulation results to published data. Since performance data are required for simulating NO_x emissions in the two-zone model, only sources that provide enough detail about engine performance were considered. A major challenge was the accurate reproduction of the engine performance simulation, because the simulation model requires a total of 20 parameters, such as boundary conditions, geometry, valve timings and rate of heat release. Where available, the time-resolved rate of heat release was replicated by adapting the Wiebe parameters with a least squares solver. As can be seen in Table 3.11 (p. 65), for none of the engines all required data for reproduction of the engine performance were available. Some of the published data were contradictory. Missing and inconsistent data were supplemented with best practice values or – where available – were matched to integral performance metrics, such as power, mass flow, fuel flow and peak pressure.

Then, the two engine calibration parameters for the NO_x simulation model c_A and λ_0 were calibrated to the design point of the piston engine, to yield similar NO_x emissions as published. Part-load NO_x emissions were then simulated with a fixed setup. A mean error across the entire range of operating conditions of 11.9 % against experimental data and 7.4 % against simulated data was determined. Individual results for all five engines are shown in Figure 3.26 (p. 65). The trends in part load are well replicated in general. The methodology tends to slightly over-predict NO_x emissions at full load and slightly under-predict in lower part load. The characteristic shown in sub-figure (a) deviates considerably from the simulation. The main cause here might be the change in rate of heat release going into part load. The chosen calibration parameters c_A and λ_0 with mean simulation errors are shown in Table 3.11 (p. 65).

Table 3.11: Diesel engines and references used for the validation of the NO_x simulation model, completeness of simulation data, and simulation error.

Engine & References	Stroke	Boundary Conditions	Valve Timings	Performance	Heat Release	λ_0	c_A	Error Exp.	Error Sim.
Mercedes-Benz OM355 [173–176]	4	–	x	x	x	1.01	0.90	24.1 %	–
Natur. asp. diesel engine [177–179]	4	–	x	d	d	1.03	0.90	8.0 %	6.9 %
Large-scale generator [180]	2	x	x	x	–	1.05	0.90	5.4 %	5.7 %
MAN B&W L70MC [181, 182]	2	x	–	x	–	1.15	0.90	11.3 %	–
MAN B&W 4T50ME [183–186]	2	i	–	x	x	1.15	0.90	10.9 %	9.5 %
Mean								11.9 %	7.4 %

x – full availability of data; d – only design point; i – incomplete

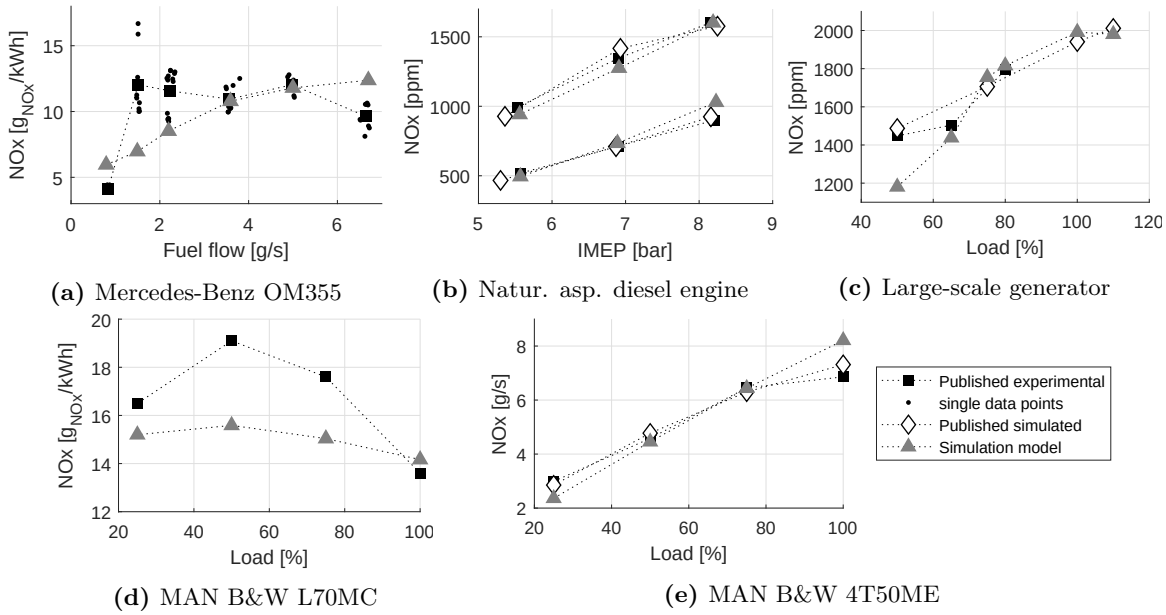

(a) Mercedes-Benz OM355 **(b)** Natur. asp. diesel engine **(c)** Large-scale generator

(d) MAN B&W L70MC **(e)** MAN B&W 4T50ME

Figure 3.26: Simulated NO_x emissions in contrast to published data from piston engines.

The parameter $c_A = 0.90$ can be kept constant across all engines. For two-stroke engines, λ_0 is in the range between 1.05 and 1.15. For four-stroke engines, a smaller range between 1.01 and 1.03 was found. The main reason for the difference between the two engine types may be the residual gas in the two-stroke engine, modifying the combustion chemistry. The ranges identified during the verification will be used for simulation in this thesis. A mean error of 10 % will be added on top as uncertainty in accordance with the mean simulation error shown in Table 3.11.

Higher fidelity NO_x simulation methods resolve the combustion space into more than two zones in *multi-zone models* [187], or use computational fluid dynamics (CFD). More chemical reaction pathways may be considered at the expense of computational effort. This is typically done to investigate the impact of alternative NO_x generation pathways. The split of NO and NO_2 is not resolved here, because NO_2 is generated equivalently from NO according to Reactions (3.142)-(3.144) [188]. Therefore, the creation of NO_2 does not alter the NO_x concentration.

$$NO + O_3 \rightarrow NO_2 + O_2 \tag{3.142}$$

$$2NO + O_2 \rightarrow 2NO_2 \tag{3.143}$$

$$NO + O \leftrightarrows NO_2 + h\nu \tag{3.144}$$

Gas Turbine Combustion Chamber

For conventional gas turbine engines semi-empirical relations are used for estimation of NO_x emissions. These require at least the inlet conditions T_3 and p_3. As displayed in Eq. (3.145) and used in the gas turbine simulation environment GasTurb [92], the NO_x severity parameter s_{NOx} grows exponentially with the combustor inlet temperature T_3 and less than linearly with pressure p_3. According to [189], EINOx scales linearly with s_{NOx} with a proportionality factor c_s. A factor $c_s = 12.4$ was calculated for near-future projected lean direct injection (LDI) combustion chambers [18].

$$s_{NOx} = \left(\frac{p_3}{2\,965\,\mathrm{kPa}}\right)^{0.4} \cdot \exp\left(\frac{T_3 - 826\,\mathrm{K}}{194\,\mathrm{K}} + \frac{6.29 - 100 \cdot \mathrm{WAR}}{53.2}\right) \tag{3.145}$$

$$\mathrm{EINOx} = c_s \cdot s_{NOx} \tag{3.146}$$

$$\mathrm{EINOx} = (8.4 + 0.0209 \cdot e^{0.0082 T_3}) \cdot e^{19(\mathrm{WAR} - 0.006344)} \cdot \left(\frac{\Delta T_{\mathrm{combustor}}}{300\,\mathrm{K}}\right)^0 \tag{3.147}$$

Although the relation was calibrated to modern combustor technological levels, the sensitivities were first derived for rich-burn quick-quench lean-burn (RQL) combustors and might not represent accurate trends. In general, relations are only accurate within the range of inlet temperatures and pressures, for which data was available. The combustor exit temperatures and inlet pressures are relatively low in the CCE concept similar to past combustors, but

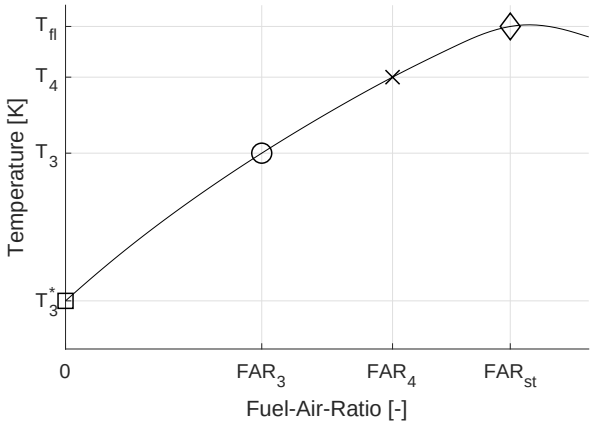

Figure 3.27: Plot of combustion temperature over fuel-air-ratio for assessment of equivalent combustor inlet temperature T_3^*.

the inlet temperature is very high and the oxygen content lower than in fresh air. Flame temperature T_{fl}, combustor exit temperature T_4, and water-air-ratio may be considered in addition [190]. A more recent semi-empirical relation displayed in Eq. (3.147) takes account of the temperature increase in the combustion chamber on top [191]. The last exponent was specified as zero in the publication but may be used to calibrate results to advanced technological levels. In this thesis, the first presented relation will be used as the author has good confidence in it and experience with using it.

The inlet air into the combustion chamber needs to account for the conditions coming from the piston engine. Since available oxygen is lower, the resulting flame temperature T_{fl} is lower, too. To incorporate this effect, an equivalent combustor inlet temperature T_3^* is calculated, which yields the same flame temperature with fresh air. The principle is illustrated in Figure 3.27. For given combustor inlet conditions T_3 and FAR_3, the equivalent inlet temperature for clean air is calculated.

NO_x is present at combustor inlet from the piston engine. Depending on fluid conditions, equilibrium NO_x may be lower than actual NO_x, which would result in a reverse reaction. The extent of reverse reaction is difficult to estimate as residence times in the combustor are unknown. If temperatures are too low, the reaction rates will be very small. Hence, there may be only a narrow temperature range, which will result in significant reverse reaction. In the GT-24 and GT-26 gas turbines with sequential combustion by Alstom, very low NO_x emissions in the secondary combustor were presented [192]. Under highly consumed oxygen conditions with NO_x in the inlet of the secondary combustor, a consumption of NO_x is possible through reverse reaction [193].

3.9.3 Noise Emissions

Noise is harmful to residents close to airports. It is targeted to be reduced by 11 dB by 2035, and 15 dB by 2050 against the year 2000 technological standard for the entire aircraft. In

the CCE concept, a new noise source is introduced with the piston engine. The literature on piston engine noise is, however, inconclusive.

The two dominant frequencies introduced are the piston revolution speed with about 50 Hz and the aerodynamic pulsation before and after the piston engine with about 250 Hz, which is of the order of the LPT revolution speed. The human perceived noise, the so-called *A-weighted noise*, is 30 dB and 9 dB lower at these frequencies, respectively, than at best perception at 1 000 Hz [194]. Atmospheric attenuation for these frequencies is negligible. The piston engine source noise is attenuated through the turbo components. Experimental measurements with heat exchangers placed in the exhaust flow path, which can be expected to impose a similar effect as turbomachinery, showed an attenuation by 4 dB on turbine noise due to a muffling effect [195]. Studies with early piston engines with propellers claimed that piston engine combustion noise is masked by propeller noise, and is effectively attenuated with mufflers. Almost no combustion noise radiates from the piston engine, since the cylinder is closed during combustion. Piston and cylinder are stiff enough to confine the noise inside the piston engine [196].

Notable examples for comparison between turbo and piston engines are the Piper PA-46 M350 and M500 as discussed in Section 2.2. Both are very similar aircraft with almost equal MTOW. The M350 has a Lycoming TIO-540 turbo-charged piston engine, while the M500 has a Pratt & Whitney PT6A-42A turboprop engine. Since airframe noise can be expected to be very similar, certification noise differences can be accounted to the engine. With 83.1 dB, the M350 is considerably louder than the M500 with 72.0 dB TO certification noise [197]. The first was, however certified with an 80 in. three-bladed propeller, the second with a larger, four-bladed 82.5 in. propeller. So, the off-set may at least be partially caused by the propeller. Today's aero piston engines are noisier due to air cooling and poor exhaust muffling [198].

Quantitative estimates of piston engine source noise are difficult to obtain. The change of other main engine noise sources can be evaluated according to empirical relations [199]. Impact on noise generation of turbo components arises through change in fan rotational speed, and due to changes in jet mass flows and velocities. The sizing thrust likely increases for an aircraft with CCE because of higher engine mass. Bypass jet noise would then increase due to higher excess velocity. Fan noise would increase because the required fan speed is higher for a given load coefficient. Core jet noise would reduce due to lower core mass flow rate.

3.9.4 Other Emissions and Interference between Emission Targets

Other aviation-related emissions and their impact are mentioned in the following. The emissions are not quantified here, but potential changes due to the CCE architecture will be outlined.

- **Soot** is created during combustion in fuel rich conditions. When oxygen is missing for complete combination with the hydrocarbons locally, solid carbon particles form. These will create visible smoke from the engine exhaust, which must be omitted on the ground for reasons of environmental perception. The radiative forcing by soot directly is

small [158]. In high altitudes, soot serves as condensation nucleus for water vapour and, hence, fosters cloud formation. Thus, soot emissions in cruise have a significant impact on radiative forcing [200]. In the CCE concept, increased soot production may occur in the piston engine due to non-uniform combustion. Quantification of soot production requires precise knowledge of the spray break-up and combustion process, which is not available in the required detail at this point. Oxidation of soot may occur within the piston engine at high temperatures or in the secondary combustor. A maximum permissible FAR = 0.055 at exhaust valve opening is used in this thesis to avoid notable soot production.

- **Water vapour** has a radiative forcing impact, just like contrails and cirrus clouds that result from these emissions [158]. Clouds in lower altitudes tend to cool the earth by reflecting more irradiated sunlight than rejecting heat to the earth, while the opposite is true for high altitude clouds in the troposphere and lower stratosphere [158, 201]. Therefore, water vapour released in aircraft cruising altitudes has a climate warming effect. Water vapour is created during combustion of fuel according to Reaction (3.4). Hence, water vapour will be reduced proportionately to the reduction in fuel burn. The impact on contrails is more difficult to project, since it is amongst others dependent on exhaust conditions, flight altitude, and soot.

- **Ozone** has a radiative forcing effect, too. It is created through NO_x chemistry, i.e. reduced NO_x emissions will reduce ozone creation. Increased ozone concentration in the upper troposphere reduces ultraviolet radiation on the earth's surface. On the northern hemisphere, ultraviolet irradiation is projected to be reduced by 1.3 % in 2050 due to aviation emissions.

- **Methane** has a strong radiative forcing effect in high altitudes. Aircraft engines fuelled by kerosene do not emit methane, but the NO_x emitted by them decreases methane concentration. The mitigating effect on radiative forcing has a similar magnitude as the effect by ozone production [158]. Recent research indicates that the impact additional ozone on radiative forcing is about 1.6 times as high as that of methane reduction [157, 202]. The reduction of methane has a much longer lasting impact of the order of 20 to 50 years.

- **Carbon monoxide** acts as a respiratory poison and has, therefore, negative effects on local air quality around airports [203]. CO is created in piston engines mainly in fuel rich conditions. Since the concept laid out in this thesis operates only in fuel lean conditions, no significant increase in CO emissions is expected. Due to highly non-uniform conditions during combustion, this assumption needs to be verified.

- **Unburned hydrocarbons (UHC)** impair local air quality. UHC emissions in the CCE are assumed to be generally on a low level, since UHC from the piston engine can still be oxidised in the secondary combustor. Since the secondary combustor runs very fuel lean, it might be prone to incomplete combustion as well.

The radiative forcing impact of water vapour, contrails and cirrus clouds is greater than the impact of CO_2 by a factor of one to three. Since both are reduced likewise by reducing fuel burn, no additional optimisation target is required.

Emission reduction targets interfere with each other. A typical example is the trade-off between CO_2 and NO_x emissions. Gas turbine engines typically improve cycle efficiency, when OPR is increased. However, NO_x emissions increase with OPR as well. This is reflected in the ICAO NO_x certifications limits, which permit higher NO_x emissions in engines with higher OPR [162]. Modern LDI combustors may not feature such characteristics [204]. Another typical trade-off is between noise and fuel burn [205]. For example, a larger fan may result in reduced fan speed with lower noise, but higher mass and nacelle drag, and thus fuel burn. In open rotor design, the GE36 nominally achieved CAEP/4 noise compliance by sacrificing 5 % cruise efficiency over the GE UDF demonstrator [41].

Chapter 4

Conceptual Design of Composite Cycle Engine

In this chapter, an evaluation platform is presented, which is a GTF extrapolated to a possible year 2035 technological standard. At this time, a CCE engine could enter service. Conceptual design options for the CCE and the piston engine specifically are presented in Sections 4.2 and 4.3. Annexed technologies, which can enhance the potential of the CCE are presented in Section 4.4. A set of technologies that promises the best potential for application in a CCE based on the evaluation platform is selected and investigated in Chapter 5.

4.1 Evaluation Platform

The primary figure of merit for evaluating and selecting CCE architectures in this thesis is mission fuel burn, or CO_2 as discussed in Sections 3.7 and 3.9.1. Fuel burn is an important metric for airlines when selecting engines, as it directly relates to fuel cost. It includes the effects of improved efficiency and heavier engines. A further future driver for fuel burn optimisation is planned environmental certification limit on CO_2 emissions [206]. Not all environmental effects are covered by fuel burn, however, as pointed out in Section 3.9.4.

With current legislation, only a minor financial incentive is provided for reduction of other emissions. Optimising for NO_x emissions will be important, if environmental charges at airports are significant. As a current example, however, Heathrow airport charges 20.15 $ [207][1] per kg of NO_x. For a turnaround with an A320neo with PW1127G-JM engines, this results in charges of 130.73 $ [208]. In total, only approximately 3 % of the landing charges are for NO_x emissions [209]. Therefore, no significant monetary incentive is applied today for reducing LTO NO_x emissions beyond the certification limit. Noise emissions are mainly driven by airframe, fan noise and jet noise. Core noise is a minor contributor and thus optimisation target, as long as noise regulations are met.

An engine with a year 2015 technological standard on a short-to-medium range aircraft is the base platform [17]. The evaluation platform was then obtained by implementing expected

[1] Calculated with the closing exchange rate of 1.306 $/£ on 07/10/2017.

technological improvements until the year 2035 time frame. The airframe represents a year 2035 technological standard for both the reference engine and the investigated CCEs, to eliminate changes in fuel burn due to airframe improvements. Thus, specified changes in fuel burn represent isolated engine level improvements. Multiple operating points are used for engine design: The aerodynamic engine sizing point is ToC, because the maximum flow capacity of the turbo components is reached here for low specific thrust engines [95]. At TO conditions, the turbine cooling air mass flow and mass-relevant parameters are calculated. In the CCE piston engine, peak pressure p_{peak} reaches its limit. Lastly, cruise (CR) conditions are simulated for TSFC calculation, which feeds into mission fuel burn[2]. Sea level static (SLS) conditions are simulated for NO_x emissions in the LTO cycle. Here, no power off-take is used in accordance with regulations [162].

The turbine cooling system is laid out to provide enough cooling for each turbine stage to sustain a prescribed material temperature T_{M}. The ratio of turbine cooling air mass flow $\dot{m}_{\mathrm{cool}}$ to hot gas mass flow $\dot{m}_{\mathrm{gas}}$ is estimated according to Eq. (4.1) with the cooling technology parameter c_{cool}. The cooling effectiveness η_{cool} is defined according to Eq. (4.3). A maximum permissible material temperature of 1 350 K for stators and 1 250 K for rotors has been assumed [210] for the SoA engine. The effect of cooling is resolved down to cascade level [102]. Sealing air of 3 % of $\dot{m}_{25}$ per stage in the turbine is always ensured and included in the turbine cooling air amount, but it is not part of the cooling mass flow in Eq. (4.1). Below a cut-off temperature of 1 250 K, neither cooling nor sealing air is used. The sealing air amount is linearly reduced down from 1 300 K for convergence reasons. In the LPT, no cooling is foreseen as the entry temperature is low enough. In reality, small amounts of cooling and sealing air are still required, which is neglected here.

$$\frac{\dot{m}_{\mathrm{cool}}}{\dot{m}_{\mathrm{gas}}} = c_{\mathrm{cool}} \frac{\eta_{\mathrm{cool}}}{1-\eta_{\mathrm{cool}}} \tag{4.1}$$

$$\text{with} \quad c_{\mathrm{cool}} = 0.052 \tag{4.2}$$

$$\eta_{\mathrm{cool}} = \frac{T_{\mathrm{gas}} - T_{\mathrm{M}}}{T_{\mathrm{gas}} - T_{\mathrm{cool}}} \tag{4.3}$$

A cooling technology parameter of $c_{\mathrm{cool}} = 0.052$ provides total turbine cooling air of approximately 25 % of the core mass flow $\dot{m}_{25}$ for the year 2015 engine [99, p. 255 ff.]. The distribution of cooling air on the cascades is illustrated in Figure 4.1 (p. 73). About 16 % of the core mass flow $\dot{m}_{25}$ are used in the first stage and 9 % in the second stage. For the year 2035 engine technological level, an increase in permissible material temperature of 50 K is assumed [211]. This could be achieved through improved materials or thermal barrier coatings (TBCs).

[2]Mission fuel burn is an integral value taking account of fuel flows in along the entire mission including TO and climb. Since, however, about 90 % of the mission fuel is burnt during cruise in a short-to-medium range mission (excluding taxiing and descent), this thesis assumes that cruise is representative for mission fuel burn estimation.

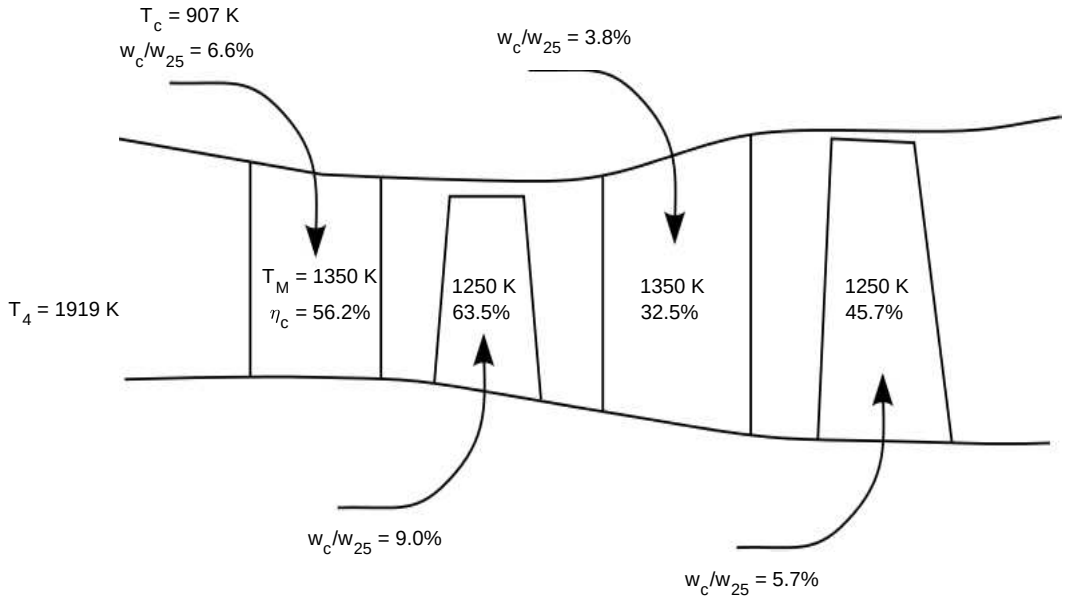

Figure 4.1: Turbine cooling air distribution on cascades for given material temperatures for the year 2015 engine.

Size effects on HPC efficiency were analysed. Tip losses in the compressor stages become significant below a reduced corrected mass flow rate $\dot{m}_{\mathrm{red,corr}}$ of 4.5 kg/s due to tip clearances and surface finishes [212]. Although the last HPC stages have a reduced corrected mass flow rate of 1.4 kg/s, the logarithmic mean mass flow rate of the HPC is 6.3 kg/s, i.e. higher than the threshold. Therefore, the impact on component efficiency has been considered negligible. In the CCE, corrected mass flow rates are generally higher than in a GTF due to lower OPR.

For the year 2035 evaluation platform, an evolutionary improvement of the year 2015 baseline GTF has been assumed using technologies being researched at a low TRL level [213, 214] and by extrapolating mid-term projections by engine manufacturers [2, 10, 14, 215, 216]. The improvements are assumed to be achieved on the component level without break-through technologies. The chosen technological assumptions are summarised in Table 4.1 (p. 74). Mainly, turbo component efficiencies are improved by 1 % through measures like improved aerodynamic design, and active clearance control (ACC) [217] or other active control. HPT efficiency receives a larger improvement to account for reduced turbine cooling air losses, while the LPT receives a smaller increment, since it is already at a high level. Combustor pressure loss includes annular and dump diffuser losses, and reduces due to use of LDI technology. Auxiliary technologies such as variable pitch fans or variable area nozzles may be required to achieve satisfactory off-design behaviour. They are not further reflected in the fan component map or weight modelling. Design OPR is increased to 50 as the optimum shifts due to higher component efficiencies [17]. Component mass savings through technologies, such as blisks, are assumed to cancel with added mass required for measures for efficiency improvement, such as lower aspect ratio blades or ACC. Thus, the weight calibration factors presented in Eq. (3.98) were kept constant.

Table 4.1: Assumptions for reference GTF ToC design point with a year 2035 technological standard.

Performance Parameter	**Unit**	**Value**	**Δ vs. 2015**
Polytropic outer fan efficiency	%	92.5	+1.0
Polytropic inner fan efficiency	%	90.0	+1.0
Polytropic IPC efficiency	%	91.0	+1.0
Polytropic HPC efficiency	%	91.0	+1.0
Isentropic HPT efficiency	%	92.0	+1.5
Isentropic LPT efficiency	%	94.0	+0.5
Intake pressure loss	%	0.3	–
Compressor intake, inter compressor, and turbine exhaust duct pressure loss	%	1.0	–
Combustor pressure loss	%	4.0	−1.0
Combustion efficiency	%	99.99	+0.09
Cooling technology factor c_{cool}	–	0.0468	−10 %
Shaft and planetary gearbox losses (each)	%	1.0	–
Bypass duct pressure loss	%	1.0	–
Core thrust coefficient c_{FG}	–	0.980	–
Bypass thrust coefficient c_{FG}	–	0.993	–
Nozzle discharge coefficients c_{D}	–	0.995	–
Component Limits		**Value**	
IPC tip speed	m/s	410	–
HPC tip speed	m/s	450	–
Max. IPC stage pressure ratio Π_{st}	–	1.45	–
Max. HPC stage pressure ratio Π_{st}	–	1.40	–
Max. mean HPT load coefficient $\psi_{\text{st,m}}$	–	3.8	–
Max. mean LPT load coefficient $\psi_{\text{st,m}}$	–	2.5	–

The evaluation logic is displayed in Figure 4.2 (p. 75)(a), showing the individual contributions going from the year 2000 to the year 2035 reference architecture. The year 2015 GTF engine offers a 16 % fuel burn improvement on the year 2000 aircraft platform [4, 5]. It uses a conventional customer bleed for anti-ice and cabin of 5 g/s per passenger, totalling 0.45 kg/s per engine. The mission averaged power off-take is 67 kW.

Then, the aircraft platform is switched over to the year 2035 technological level. Fuel burn increases by 1.1 % at the aircraft level through the change to an AE subsystem architecture with higher power off-takes of a mission-averaged 184 kW. All sub-systems are driven electrically including environmental control system for cabin air, and anti-icing. Hence, no customer bleed is taken from the engine. The detriment is here accounted to the engine.

Moving the technological level then to the expected year 2035 standard, TSFC reduces by 6.5 %, and PPS mass from 3 951 kg to 3 530 kg. In total, fuel burn reduces by 10.3 %. Thus, fuel burn improvement due to the engine is 23.8 % against the year 2000. This is insufficient to meet SRIA 2035 targets as shown in Figure 4.3 (p. 75).

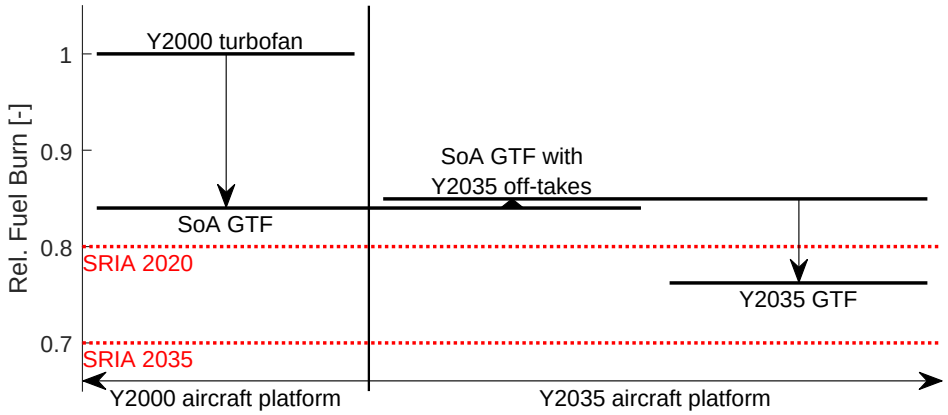

Figure 4.2: Evaluation logic for assessing the year 2035 GTF.

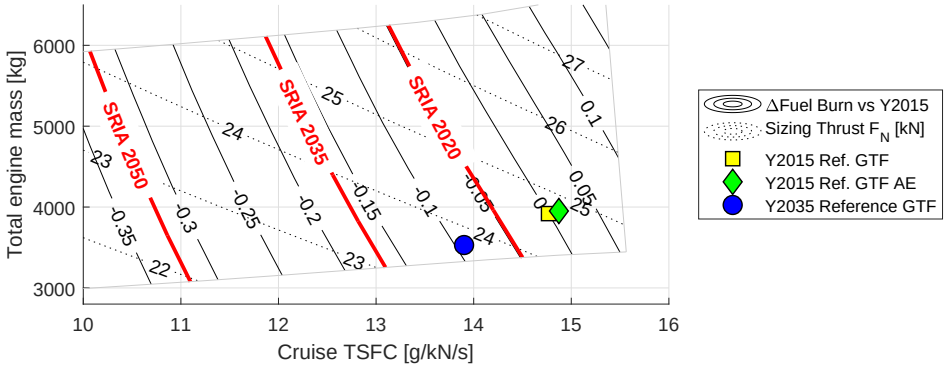

Figure 4.3: Changes in fuel burn and sizing thrust F_N for a year 2015 and year 2035 GTFs.

The resulting aircraft thrust requirements and engine efficiencies are displayed with other performance metrics in Table 4.2 (p. 76). The ToC Mach number is higher than cruise to provide thrust margin in design. The actual mission is flown with a lower Mach number. The fan diameter is 1.98 m and will be kept fixed for all following studies. The diameter was optimised for the year 2035 GTF platform. Small deviations from the optimum may originate from different bypass ratios and, hence, transmission efficiencies, as well as reduced required sizing thrust. Bypass ratio increases from 12.1 (ToC) to 14.4, due to improved technology, reduced thrust requirement, and reduced turbine cooling air demand of 21.3 %. The engine is visualised in Figure 4.4 (p. 76). The decrease in core mass flow leads to smaller turbo components. As a result, the engine is 0.17 m shorter.

NO_x emissions were simulated according to Section 3.9.2 in the LTO cycle and for cruise conditions, to evaluate in-flight emissions. The results are summarised in Table 4.3 (p. 77). The 7 % idle point could not be simulated, because it was beyond the limits of the component maps and did not converge. Idle emissions of SoA engines (LEAP-1A35A, GEnx-1B76, PW1133G-JM, and Trent XWB-84) were averaged [208], resulting in 13.7 % of the LTO emissions. Simulated total LTO emissions were corrected accordingly. The SRIA 2035 NO_x emission target can be met clearly. The level is almost sufficient to meet SRIA 2050 targets (20.6 g/kN). The cruise emissions are 36 % below year 2000, which was simulated to be

Table 4.2: Specifications for main operating points for reference GTF design with a year 2035 technological standard on a year 2035 airframe.

Operating Point	**Unit**	**ToC**	**CR**	**TO**
Altitude	m	10 668	11 278	0
Mach number	–	0.78	0.76	0.20
ΔT_{ISA}	K	10	10	10
Streamtube Thrust	kN	23.75	18.49	102.9
TSFC	g/kN/s	13.96	13.90	8.63
T_3	K	835	799	917
T_4	K	1 767	1 681	1 928
OPR	–	50.0	45.4	42.8
BPR	–	14.4	15.0	14.7

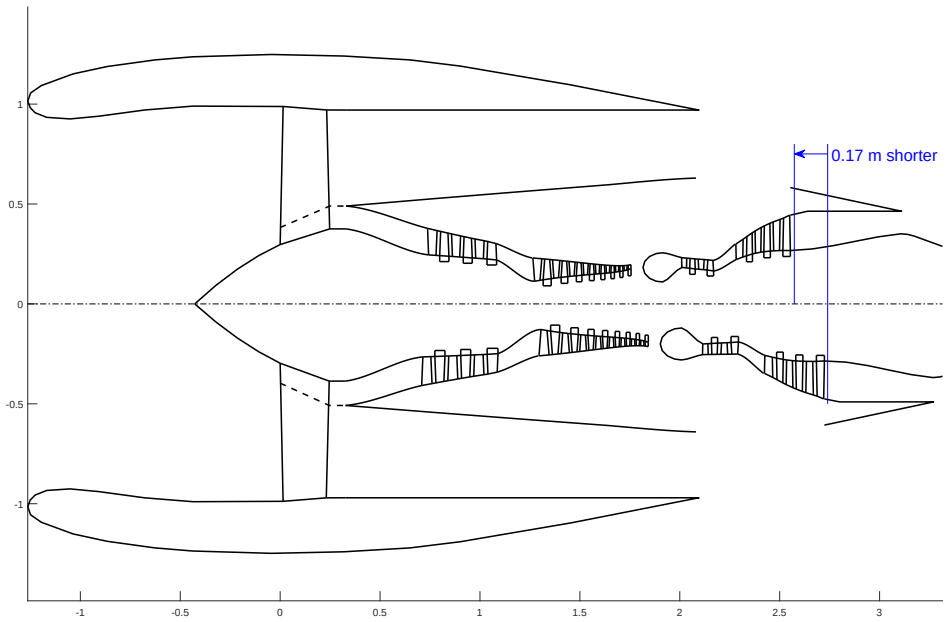

Figure 4.4: Comparison between engine general arrangement drawings for (bottom) a present and (top) a year 2035 technological standard.

3.67 g/s. This clearly misses the SRIA target of reduction by 84 %. This result may be taken cautiously, since the semi-empirical relations were derived for SLS conditions and may be inaccurate in cruise.

Table 4.3: NO_x emission estimates for LTO cycle and cruise.

Operating Point	**Unit**	**SLS**				**Cruise**
		100 %	85 %	30 %	7 %	
EINOx	g/kg_{fuel}	21.2	16.2	3.7	–	9.1
Fuel flow	kg/s	0.816	0.666	0.216	–	0.260
Time	s	42	132	240	–	–
Emission D_p	g	726.3	1 422.6	194.5	372.0*	2.36 g/s
Total D_p	g		2 715.4			–
$D_p/F_{N,SLS}$	g/kN		21.5			–
CAEP/6−65 %	g/kN		28.8			–

*estimated 13.7 % of total D_p

4.2 Overall Engine Design

In this section, design options for features of the CCE architecture are discussed. All technological assumptions of the reference GTF platform are retained for the CCE. Design characteristics of the piston engine are discussed in the next Section 4.3.

Market segment: The choice of the optimum market segment for CCEs is not obvious. Engines for short-range aircraft have a higher potential efficiency improvement over turbofans, because of smaller core sizes. This leads to significant tip-losses in HPC and HPT, limiting optimum OPR. In CCEs, tip losses are less pronounced in the turbo compressors due to much lower turbo pressure ratio. Clearances in pistons are much lower than in turbomachinery. Therefore, the peak pressure ratio in the CCEs is not restricted by core size as in turbofan engines. This leads to a higher improvement potential through CCEs. A slow aircraft equipped with propellers would give even higher improvements as less thrust is required and, hence, the weight penalty by pistons is lower. On the other side, the cascading benefits on fuel burn due to improved efficiency are higher on a long-range aircraft. The ratio of fuel to total aircraft weight is particularly high here. Moreover, additional engine weight has a lower penalty due to high aerodynamic efficiency of the aircraft. These effects favour application to long-range aircraft, even though the efficiency potential is smaller, because turbofan engines have higher OPR and overall efficiency.

In this thesis, an engine for short-to-medium range aircraft will be investigated. The large market volume of this segment justifies higher development costs for such a new technology, as in the past the power gearbox for the GTF. The amount of publicly available data for this segment facilitates a more accurate and reliable assessment. General trends are nonetheless applicable to all market segments. This is particularly true, since the piston engine can be

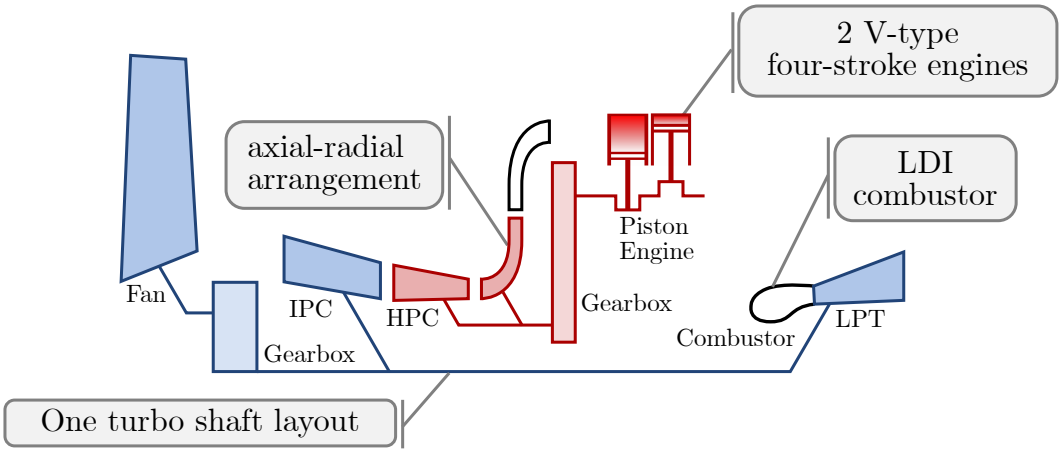

Figure 4.5: Schematic of the investigated CCE engine architecture.

sized in power simply by changing the number of pistons, making it applicable across engine families.

Engine architecture: The basic engine architecture is illustrated in Figure 4.5. The turbo components are arranged on a single shaft, including fan, IPC and LPT. No HPT is used. In previous investigations, the IPC was on a separate shaft driven by the HPT [16], but the load on the HPT was low. Thus, the power extraction can be combined into a single turbine for lower part count, complexity and overall engine length. Fan and IPC speed are decoupled via the gearbox in any case. Analysis of off-design behaviour confirmed that the operational requirements can be met with just one turboshaft as will be shown later. Transient analysis has not been carried out to prove that rapid acceleration is feasible within operability margins.

The piston banks are arranged around the core as two V-type engines. With the cylinder head accessories, i.e. valves, valvetrain and ducting, it was not possible to fit three V-type engines into the cross-section of the core. The top engine is hanging. A dry sump lubricating system is foreseen to prevent ingestion of large amounts of oil into the piston engine. Earlier inverted piston engines with hanging cylinders and wet sump, such as the Daimler-Benz DB 605, experienced this problem. In a dry sump lubrication, oil is actively removed from the crank casing [129, 147].

Intake and exhaust valves of the piston engine are far away from the engine centreline and close to the core cowling. Hence, the core air needs to be guided outwards. The space enclosed by the two V-engines in the chosen configuration is insufficient to contain a compressor. As a space-saving solution, an axial-radial compressor connected to the piston engine was selected. The radial compressor guides air outwards to the intake valves. The axial length of the turbo component is reduced, limiting overall engine length. Other options not considered here could be to move the piston engine outward radially to create enough space for an axial compressor, at the price of extending the core cowl and potentially increasing bypass duct pressure losses.

Coupling between piston engine and HPC: The piston engine has a large speed mismatch to the turbo components. While the piston engine rotates with 3 200 rpm in design point (limited by the maximum permissible mean piston velocity v_{mean}) the HPC rotates with

14 000 rpm at typical compressor tip speeds. Hence, a gearing is required between turbo components and piston engine. To achieve the required transmission ratio of approximately 4.5, a couple of engineering solutions can be conceived. A bevel gear can achieve large transmission ratios on a small space. This solution was disregarded here as it has higher transmission losses than a spur gear, is difficult to manufacture with helical gearing, and has high axial reactive loads [218].

A single spur gear stage is not feasible, since the transmission ratio would require a large gear to be on the piston engine. The resulting gears on the piston engine would block wide parts of the bypass cross-section. Other possible gearing options are illustrated in Figure 4.6 (p. 80). Options (a) to (c) involve planetary (epicyclic) gearboxes, which offer an even and balanced load distribution across the gears as is used on the PW-1000G engine. Option (d) uses a two-stage transmission to cope with the geometric constraints created by the core cowling. Geometry and individual transmission ratios were estimated to identify the best solution.

In option (a), the sun gear of the planetary gearbox drives the HPC. The piston engine drives the ring gear directly through a spur gear on the outer side. This set-up results in an additional transmission ratio of 0.43 from spur gear to ring gear due to geometrical constraints by the core cowling. This leads to a very high transmission ratio on the planetary gearbox of 10.4. Geometrically, this can be only realised with two gears on the planet carrier, which contradicts the target of even load distribution across the planet gears. Option (b), therefore, drives the ring gear indirectly with a transmission ratio of 1.0 from piston engine to ring gear. Although this enables a planetary gearbox with a transmission ratio of 4.5 with four to five gears on the planet carrier, the piston engine spur gear now violates the core cowling. In option (c), the piston engine drives the planet carrier instead, again with a transmission ratio of 1.0. As an advantage, the transmission ratio can be realised more easily with five to six gears on the planet carrier, but the violation of the core cowling persists. If the piston engine gear size was reduced to a permissible level, the gear ratio on the planetary gear would again be very high.

As planetary gearboxes were not viable, a two-stage spur gear shown as option (d) was selected. It transmits the piston engine power in a compact arrangement without violating the core cowling. The distribution of the transmission ratio can be freely chosen to optimise for size or losses, while obeying geometrical constraints. Here, the overall size of the gears was minimised as objective. As constraints, the core cowling radius of 0.60 m should not be violated, and the gears should not become too small. The lower limit is given by the torque transmitted and the space required for the low-pressure spool, going through the gear connected to the radial compressor. The parametric space and the selected configuration are displayed in Figure 4.7 (p. 80)(a). The respective gear labelling is displayed in Figure 4.7 (p. 80)(b). As can be seen, the transmission ratio should be performed completely on stage 2, to minimise the size of gears on stage 1. The size of gear 21 is limited by the minimum required diameter of gear 22 to transmit the applied torque. For gear 12, a minimum radius of 100 mm was specified to provide space for the low-pressure spool. The study suggests that higher transmission ratios on stage 2 with transmission ratios below 1 would result in even smaller gears on stage 1, but higher losses can be expected.

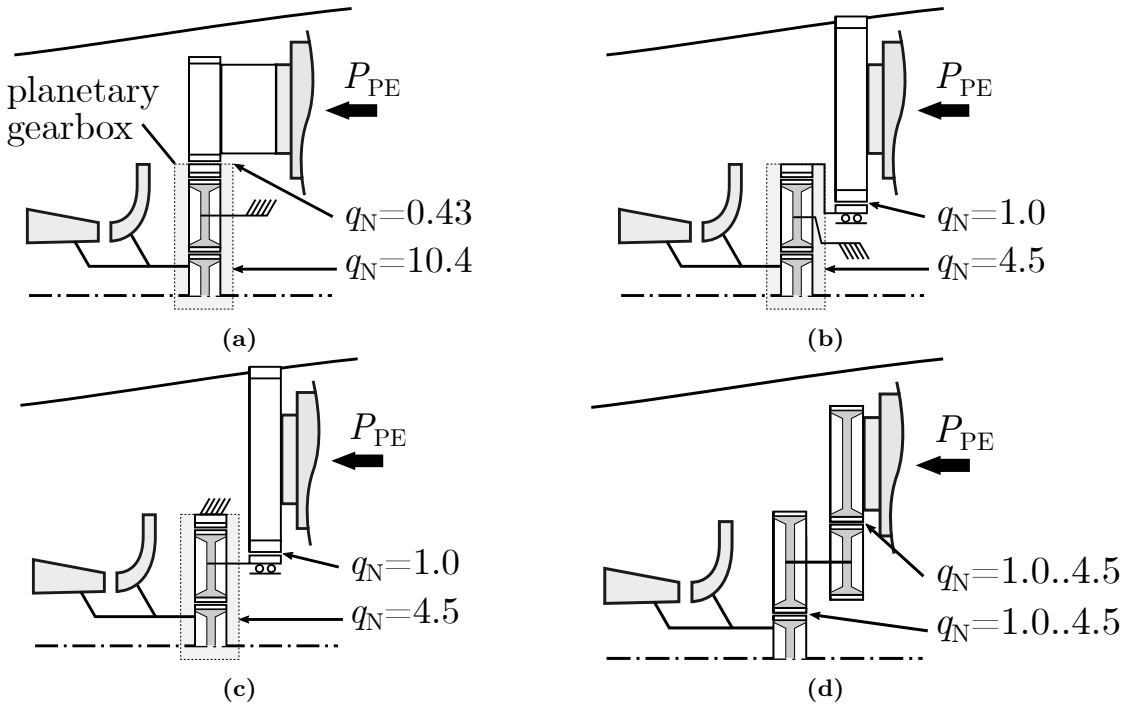

Figure 4.6: Schematics of gearing options with (a-c) planetary gearbox, and (d) a two-stage spur gear transmission.

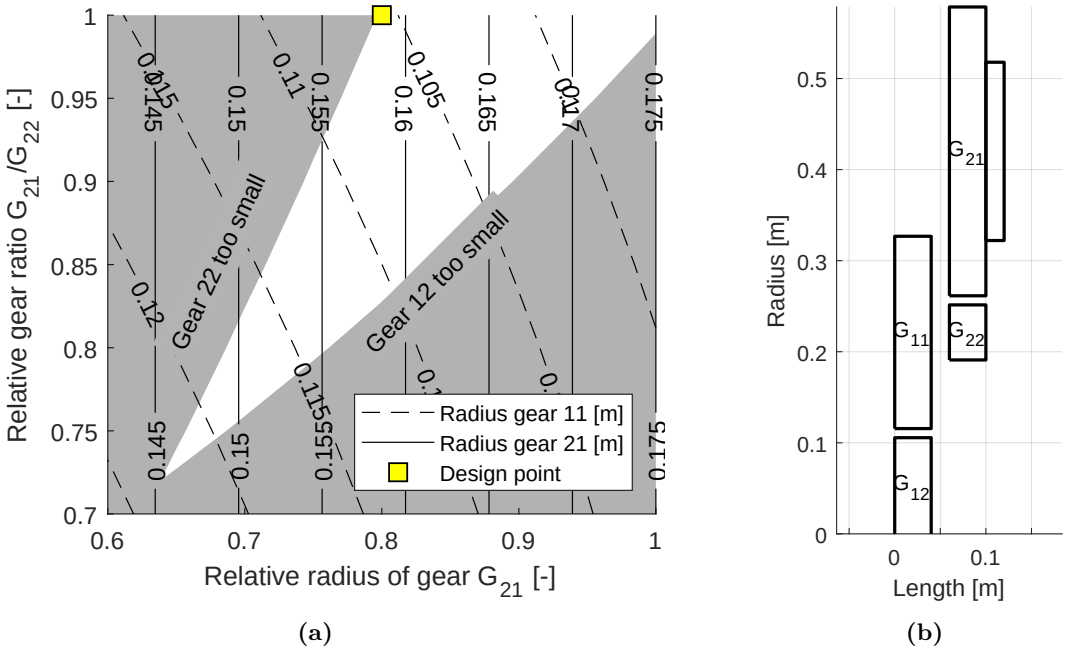

Figure 4.7: (a) Parametric study of gearbox geometric properties, and (b) gearing nomenclature.

A coupling of piston engine directly to the fan would be desirable since the rotational speed of both is similar. The mechanical connection of both is, however, complicated by the IPC and the planetary gearbox between both. A complex gearing and transmission system with implied losses and weight would be required. Moreover, additional losses and distortions in the compressor intake duct would result from potentially bulky fairings around the transmission. Start-up and off-design behaviour might be another issue.

Combustor: The inlet temperature of the secondary combustor is very high. Thus, autoignition of the fuel may be possible without complicated nozzle design, as demonstrated in the stationary gas turbines GT-24 and GT-26 by Alstom [219, 220]. These achieve autoignition in the second combustor at inlet temperatures of 1 270 K with very low NO_x emissions [192]. This concept of *flameless* combustion is suggested for the CCE. With this concept, the flame temperature is highly reduced and NO_x formation almost entirely suppressed [221]. Flameless combustion is feasible above inlet temperatures of 1 100 K, even with highly reduced oxygen content or exhaust gas recirculation [221].

4.3 Piston Engine Design

The technical feasibility of a CCE concept is tightly coupled to its conceptual design. Items of these will be discussed in the following, and the choice used within this thesis will be motivated. The characteristics of alternative design options are reviewed and compared to the design chosen. Mechanical limits of piston engines restrict the operational performance that can be achieved, when optimising the cycle. A reasonable choice for those limits is, therefore, important in assessing the potentials of the CCE architecture. No similar piston engine application is available today, which can be used to derive these limits. Recent studies dealt with the application of piston engines for large transport category aircraft [129, 222].

Empirical data of built engines can support the choice of specified performance characteristics of piston engines. A database with 300 piston engines was established. Publicly available data sources [22, 46, 147, 223–232], technical publications, type certificate data sheets and product data sheets were used. The sources range over applications in aviation (170 engines), automotive (70), marine (20), utility vehicles, race cars and auxiliary units. They cover displacement volumes from 0.1 L to 30 m^3, powers from 1 kW to 90 MW, and engine masses from 3 kg to 2 000 t. In the following charts, the ranges of the envisaged CCE piston engines, which will be presented in Chapter 5, are indicated for reference. The numbers from the database have limited significance as in most of these applications the design goals were different from an aeronautical engine. Engine cost was more important and weight less important.

Peak pressure: The peak pressure in the piston engine defines the peak mechanical loads on piston and cylinder material. Values range from 200 bar to 250 bar in high demand applications [233], and up to 365 bar in experimental engines [134, 233]. Therefore, a mid-term limit of 250 bar and a long-term limit of 300 bar appear feasible.

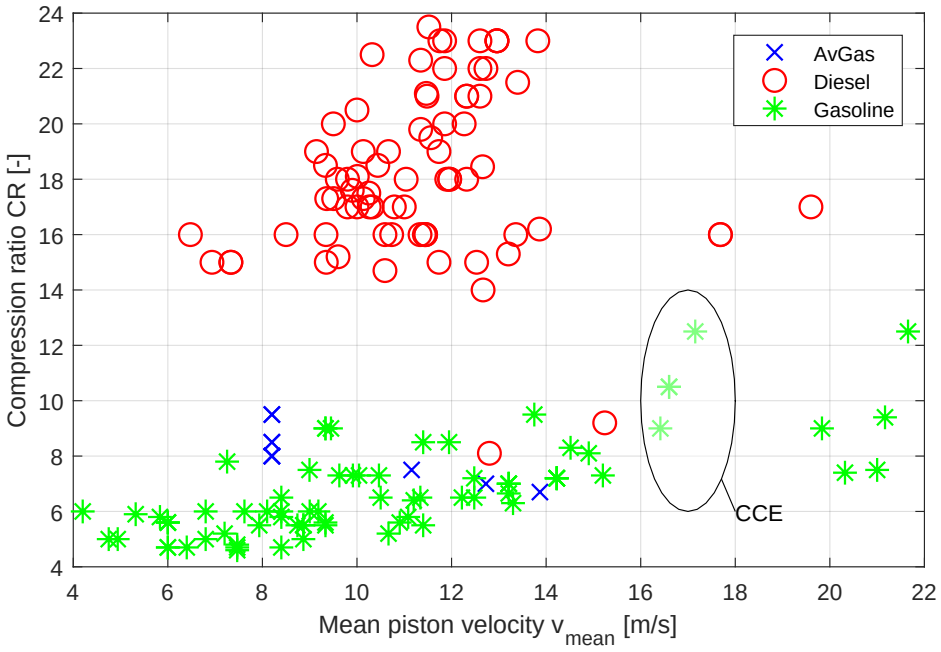

Figure 4.8: Geometric compression ratio CR over mean piston velocity v_{mean} categorised by engine fuel.

Mean piston velocity: It represents mechanical stress on piston and liner through acceleration and lateral forces. Empirical values are shown in Figure 4.8 against compression ratio CR categorised by fuel type. The v_{mean} of most diesel engines is limited to 14 m/s. In this thesis, a maximum v_{mean} of 18 m/s is assumed to be feasible. The only diesel engines in the database achieving such high velocities were the Junkers Jumo opposing piston engines [223], and the projected HALE piston engines from the ERAST programme [46]. Therefore, the piston velocity can be considered an ambitious technological target.

Geometric compression ratio: It dictates the obtained pressure at TDC. The CR of engines running on gasoline is limited to about 10. Above this value, knock initiates with uncontrolled, premature detonations. Diesel engines attain much higher CR up to 24, since fuel is only added to the air when combustion initiates. Higher values of CR would lead to excessive peak pressures. In this thesis, CR is selected so that a peak pressure of 250 bar is never exceeded. The resulting CR of 6 to 12 is low compared to other diesel engines due to the high charging.

Operational mode: Two-stroke and four-stroke operation is possible. The advantage of two-stroke operation is that every stroke performs work, suggesting higher power-to-weight ratios. Four stroke operation, on the other hand, offers almost perfect scavenging, reducing mean fluid temperature in the piston and providing predictable fluid conditions. Their valve timings enable better utilisation of the displacement volume, while in a two-stroke engine valves can be open up to 50 % of the stroke, which reduces effective compression ratio and utilisation of the displacement volume. As a result, the displacement-specific power can be almost equal in both operating modes [66]. Considering the reduced mean fluid temperature

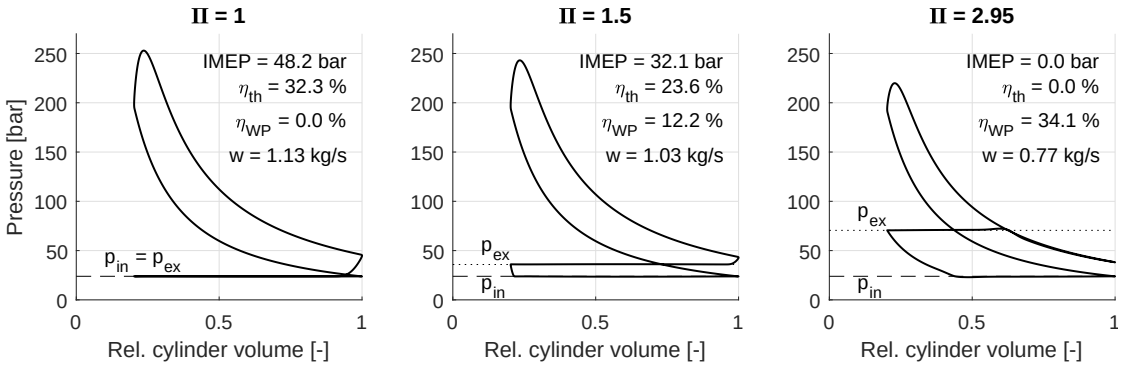

Figure 4.9: Pressure over volume diagram for a four-stroke engine with no pressure rise (left), a pressure ratio of 1.5 (middle), and operating as a gas generator (right).

as well as the resulting reduced heat losses and material strain, a four-stroke piston engine is chosen as a baseline for the CCE.

A special characteristic of the four-stroke engine is the chronological separation of inlet and outlet valve opening. This allows for independent inlet and outlet pressure levels and, hence, a pressure rise across the piston engine. Previous studies showed that a pressure rise across the piston engine with a pressure ratio of 1.5 to 1.6 can improve overall engine efficiency [59]. A comparison between constant pressure and a pressure ratio of 1.5 across the piston engine is shown in Figure 4.9. A further benefit of this mode of operation is the reduction of net shaft power, reducing the weight of power transmission devices such as shafts, bearings and gears. Instead, more work potential is generated by the engine. As can be seen, the sum of thermal efficiency and work potential is indeed greater than the thermal efficiency of the engine creating only shaft power. Secondary air circumventing the piston engine, such as turbine cooling air, needs to be pressurised elsewhere. In this thesis, a small, auxiliary radial compressor is foreseen. A piston compressor may also be a viable option for small secondary airflows. Possibly, not all the turbine cooling air needs to be pressurised, if the available pressure level is sufficiently high for later turbine stages.

The exhaust pressure level could be increased to the point where no net shaft power is provided at all as illustrated on the right graph of Figure 4.9. In that case, the piston engine operates as a gas generator and provides work potential only. This operating mode leads to equal areas in the p-V-diagram during work and scavenging strokes. Thus, no consumer of the piston engine power, i.e. turbo or piston compressor, is required, reducing engine complexity. As a drawback, the required piston displacement volume is higher since mass flow is more than 30 % lower, and hence no reduction in engine weight can be expected. This concept is not further investigated in this thesis.

In a previous study of CCE concepts comparing operating modes, two-stroke engines yielded inferior results compared to four-stroke engines [66]. For this thesis, valve timings and scavenging pressure difference of the two-stroke engine have been optimised for the application case. Thus, scavenging efficiency significantly improves from 50 % [66] to 80 % to 90 %. As a result, the piston engine can be utilised to a higher degree while reducing bore, and hence piston engine mass. In the previous study, arbitrary cylinder wall temperatures were permit-

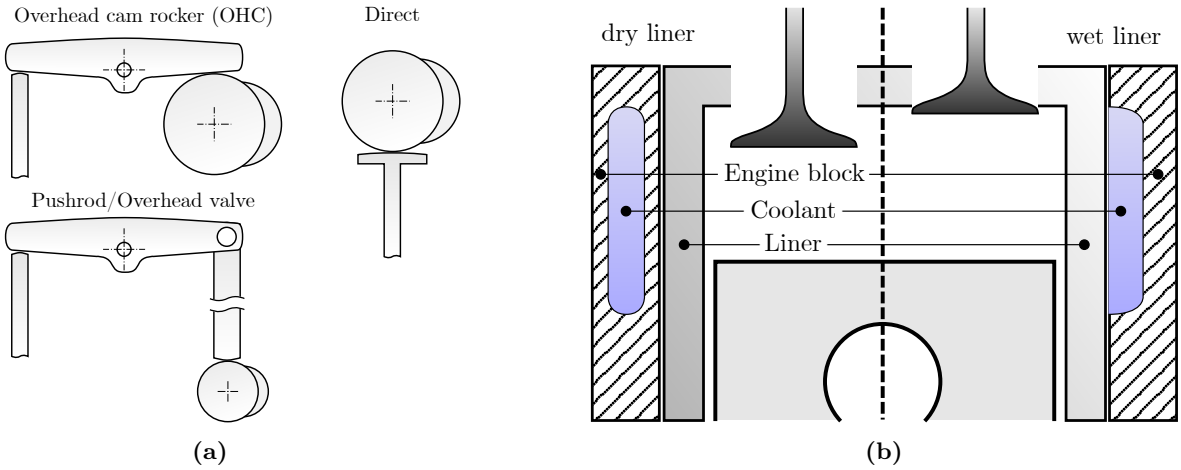

Figure 4.10: (a) Options for valve drive trains, and (b) comparison of wet and dry cylinder liner cooling.

ted, while it is now restricted to 500 K. This warrants a review of the original findings, and two-stroke operation will be benchmarked against four-stroke operation in Chapter 5.

Stroke: The engine stroke has an impact on engine size, weight, and mechanical loads. A shorter stroke leads to smaller engines but higher accelerations of the piston and reactive forces on the drive train for a given mean piston velocity v_{mean}. For this reason, large marine piston engines have stroke-to-bore ratios up to 5.0, while high-speed piston engines such as in racing cars have ratios as low as 0.4 [234]. In this thesis, a stroke equal to the bore, also referred to as *square stroke*, is chosen as used in most automotive engines. It serves as a good compromise between size and weight on the one hand, and mechanical loads on the other hand.

Valves: The valves are actuated by overhead camshaft driven as shown in the top left of Figure 4.10(a). More weight- and space-saving options would be hydraulically driven valves as used in large diesel and race car engines, or electro-mechanically, electro-hydraulically, or electro-pneumatically driven valves as in the *FreeValve* concept by Koenigsegg [235]. Further advantages of these types are fully variable opening timings and characteristics, which can be tailored to off-design conditions. The timings can be optimised for performance, fuel burn, or other emissions. Such actuators open and close valves faster, improving scavenging and engine efficiency. These effects are not included in the simulation. Pushrod actuation, also called overhead valves, as seen in historic piston engines can save space in the cylinder head. They are not used here due to poor dynamic behaviour and higher weight.

The cylinder head is assumed to house two intake and two exhaust valves with equal diameter[3]. The valve diameter d_{valve} is assumed to be 75 % of the maximum feasible diameter in accordance with real engine designs [125].

[3]Some piston engines features larger intake than exhaust valves. During the exhaust stroke the air is pushed out, which leads to higher pressure ratios and, thus, higher mass flows for a given valve area. Moreover, the speed of sound is higher in the exhaust flow. In this manner, scavenging losses can be minimised. This measure is neglected in this thesis.

The temperature capabilities of valves and outlet duct limit the permissible piston engine exhaust temperature. In a 1980s NASA study, a temperature of 1 230 K was specified for rated power at sea level, standard day, and 1 370 K under hot and high conditions [23]. Since nickel-based valves are limited to about 1 300 K, advanced valve technology such as ceramic valves may be required to achieve the specified limit for TO and climb [236, 237]. A limit temperature of 1 350 K appears feasible for TO conditions.

Fuel injection: Fuel injection options are pre-mixing with induced ignition and direct injection with auto-ignition. The first is used in the Otto-cycle. Through pre-mixing, higher utilisation of oxygen in the combustion air can be achieved and a rapid rate of heat release with a high ratio of isochoric combustion. Pre-mixing is limited to the auto-ignition temperature of the fuel-air mixture. If it is reached before TDC, combustion starts too early with adverse effects on engine efficiency and mechanical integrity. This phenomenon is known as *knock* [125]. This limits the permissible CR in Otto engines to approximately 12 [104]. The auto-ignition temperature for kerosene is about 500 K [88]. The envisaged cycles for the CCE have higher charging temperatures of the order of 700 K to 800 K under TO conditions. Therefore, only direct injection is viable with main disadvantages of lower oxygen utilisation and inhomogeneous combustion leading to soot and NO_x emissions.

The minimum permissible air number λ to stay below the soot limit is in the range of 1.2 to 1.4 [107, 238], i.e. FAR below 0.055. High charging pressures increase the tendency towards soot production [107]. Good fuel atomisation is, therefore, mandatory for avoiding soot. A common rail injection system was chosen with 2 500 bar [147], which is at the top end of the range.

Lubrication: All surfaces with relative movement to each other require lubrication to avoid metal-to-metal contact. This particularly concerns contact between piston and liner. The stability limits of the lubricating fluid restrict the permissible cylinder liner temperature at TDC position of the top piston ring. Oil decomposes, if the liner is too hot. Lubricating oil is used up to about 500 K [126]. Therefore, cylinder liner temperature was limited to 500 K. The piston and cylinder head can bear higher temperatures, because the surfaces exposed to the combustion gases do not need to be lubricated. Steel pistons can achieve peak temperatures up to 740 K. Temperatures of 600 K were assumed here in accordance with other applications [118]. Higher temperatures were avoided to prevent a mismatch between thermal expansion of piston and liner, with resulting thermal stresses or leakage, and adverse effects on injector lifetime.

A ceramic coating can be used to protect the metal surfaces from high temperatures, similar to TBCs on turbine blades. Expected benefits are lower heat transfer during scavenging, resulting in higher volumetric efficiency, and thus higher torque [239]. Heat losses at higher temperatures during combustion might be reduced. Contradictory results from other studies claim, however, that higher wall temperatures lead to a smaller thermal boundary layer at the wall resulting in combustion closer to the wall with the consequence of higher heat transfer [116] during combustion. This results in the opposite of what is aspired. Therefore, no ceramic coating of piston and cylinder surfaces is foreseen.

Cooling: The piston engine is actively cooled to maintain the required material temperatures. All components are assumed to be oil cooled as water is temperature limited due to boiling[4]. The piston is cooled to about 50 % via oil cooling, about 30 % are transmitted to the cylinder liner via the piston rings, and the remaining 20 % to the connecting rod and the surrounding on the bottom of the piston [118]. About 2 g/s of oil per kW of power is required. The cylinder is cooled with a wet liner as depicted in Figure 4.10(b). The coolant is in direct contact with the liner and absorbs heat directly, but is more difficult to seal.

Free-piston concepts: The baseline piston engine for this thesis has a conventional crankshaft binding. Unconventional piston implementations feature appealing properties for aero engine applications [240]. One such solution is the *free-piston engine*. Its piston has no axial kinematic restrictions, and is controlled only by fluid forces. A solution particularly suitable as an aeronautical engine was proposed in a patent by Klingels [241] as illustrated in Figure 4.11 (p. 87). Here, the power produced by the engine is directly transferred to a piston compressor.

Omitting the crankshaft reduces weight and size of the engine and enables free placement within the core cowling. Lateral forces between piston and cylinder are eliminated. Therefore, the lubrication only needs to bear the piston weight and mechanical losses reduce [242]. This could allow lubricating the piston with pressurised air instead of oil [243]. In turn, this eliminates wall temperature restrictions. If the walls are hotter, the piston engine can be cooled with core air instead of bypass air, retaining the piston engine heat losses within the core engine and raising thermal efficiency. If no oil is used for lubrication, uni-flow scavenging can be used, because no oil is ingested during scavenging. Scavenging efficiency improves and, thus, other cycle parameters during operation. Since mechanical loads on the piston are lower in this setup, higher mean piston velocities are feasible. NO_x generation could reduce through lower residence times in the piston and quick piston acceleration after fuel injection [242]. The compression ratio is variable in such an engine, which enables higher part-load efficiency.

The operational principle works best with a two-stroke operating characteristic. A four-stroke characteristic could be realised with additional effort. For example, four separate cylinders could be connected via a coupling rod. The rod would need to be in the centre of the combustion chamber in case of a single coupling rod. This infers combustion chamber geometry and challenging coupling rod operating conditions. An alternative usage of the free-piston excess power is the generation of electrical power, e.g. for hybrid electric propulsion [244]. In Section 5.2.3, a two-stroke free-piston engine will be used to illustrate a further leap in improvement potential of the CCE.

Free-piston engines generally suffer from difficult engine control and high cycle to cycle variations [242]. Small variations in stroke amplify to large variations in compression pressure, which can be as high as 15 % [242]. Engine control can be improved with an opposed piston design, which also mitigates vibrations, but a piston synchronisation link is required. Viable operating frequencies of a free-piston engine are limited, which can lead to unsatisfactory operating characteristics in part load. The simulation of free-piston engines is more difficult

[4] A water pressure of about 5 bar shifts the boiling point to 420 K. Depressurisation of the cooling circuit would then result in breakdown of engine cooling.

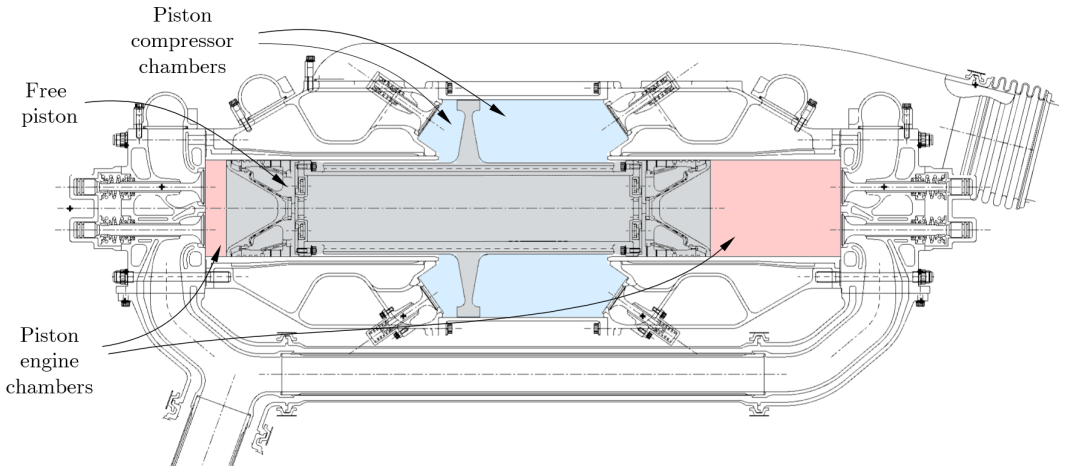

Figure 4.11: Free double piston arrangement with the engine on the centre line and piston compressors around the piston using the engine power [241].

as the piston kinematics are not prescribed but a result of the relationship between power source and sink.

4.4 Synergistic Technologies

The combination of the CCE concept with other radical engine component technologies is viable, if further significant improvements in engine efficiency or reductions in engine mass can be expected. Since engine complexity already increases considerably through the piston engine, marginal improvements are unlikely to justify additional components. Core engine size can become critical, if further bulky components are added. Options for synergistic components are discussed in the following.

Heat exchangers are featured in many novel concepts with the target of improving engine efficiency by utilising waste heat. For example, the intercooled recuperated aero engine (IRA) concept promises a TSFC improvement of 8 % against a GTF of same technological level [130]. In the CCE, heat exchangers could serve two purposes: As intercoolers, they could reduce thermal load in the piston engine and save weight by increasing fluid density. As recuperators, they could recover waste heat from the exhaust to increase thermal efficiency, or core specific work to reduce core size.

Multiple combinations with the CCE can be envisaged for such configurations as displayed in Figure 4.12 (p. 88). These were assessed with simplified thermodynamic evaluations [81]. Parametric studies varying T_4 and OPR were performed to evaluate TSFC, engine mass and fuel burn on a long-range aircraft. They demonstrated the fundamental improvement potential of the CCE cycle.

In the baseline three-shaft CCE architecture used for these studies, the LPT drives the fan, and HPT drives the IPC. The high-pressure core of the engine is composed of a piston compressor (PC) driven by a piston engine (PE). Optimum operating conditions are OPR =

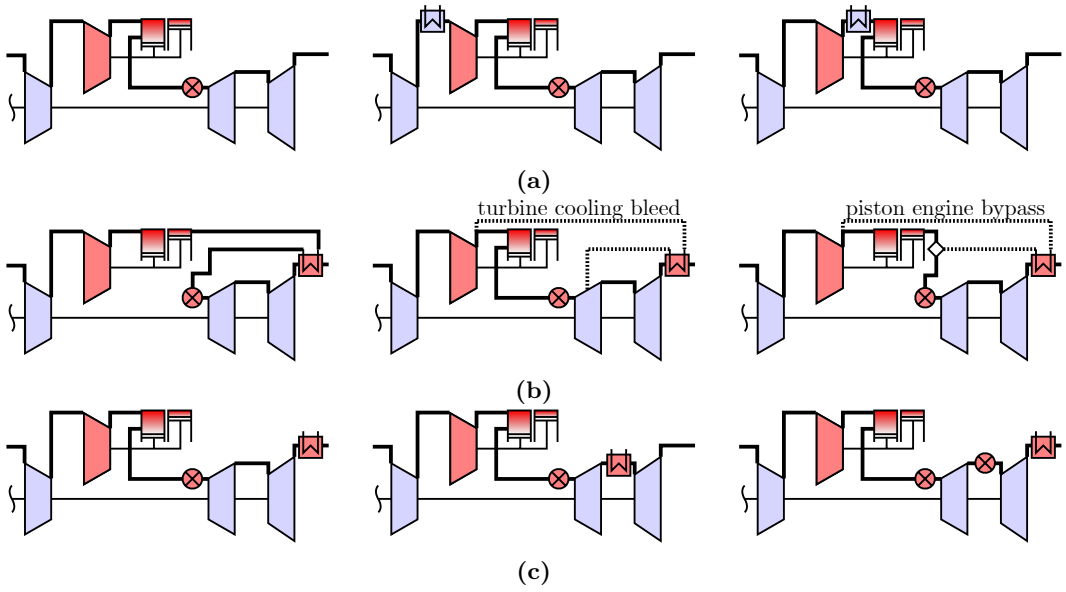

Figure 4.12: (a) Options for including intercoolers into the CCE baseline (top left). Options for recuperators (b) with different working fluids, and in (c) different locations.

33 and $T_4 = 1\,400\,\mathrm{K}$. This leads to 16 % fuel burn improvement over a reference GTF, although engine mass increases by 20 %.

For intercooling, two options were evaluated, as shown in Figure 4.12(a). First, the intercooler (IC) could be placed between IPC and PC. This reduces required compression work and significantly reduces thermal load in the PE. Second, the IC could be placed directly in front of the piston engine, to further reduce its thermal load. However, no benefit in reducing compression work would be obtained, and heat would be rejected at high pressure, which is detrimental to thermal efficiency.

The studies showed that the first option for an intercooled CCE has a fuel burn improvement potential of 1 % to 2 % against the baseline. While TSFC remains almost constant, piston mass decreases notably. Piston size and cost reduce, but the intercooler is added. Optimum OPR is considerably higher than in the baseline, enabled through reduced temperatures after the compression process. Optimum T_4 is slightly higher. The optimum IC effectiveness ϵ was found between 50 % to 70 %. Higher ϵ leads to further mass savings, but TSFC progressively deteriorates. In conclusion, the intercooler introduces beneficial features to the CCE and offers further modest fuel burn improvements. Therefore, an intercooled CCE will be investigated in Chapter 5.

For recuperation, the IRA-equivalent configuration is shown in Figure 4.12(b) and (c), in the respective left configurations. There, the flow before the secondary combustor would be diverted to the engine exhaust to recover waste heat. The fundamental issue with this configuration is the inept temperature condition as illustrated in Figure 4.13 (p. 89). In the baseline cycle, the temperature before the combustor T_{35} is about 600 K higher than the engine exhaust T_5. Generally, CCE cycles tend to have low exhaust temperatures.

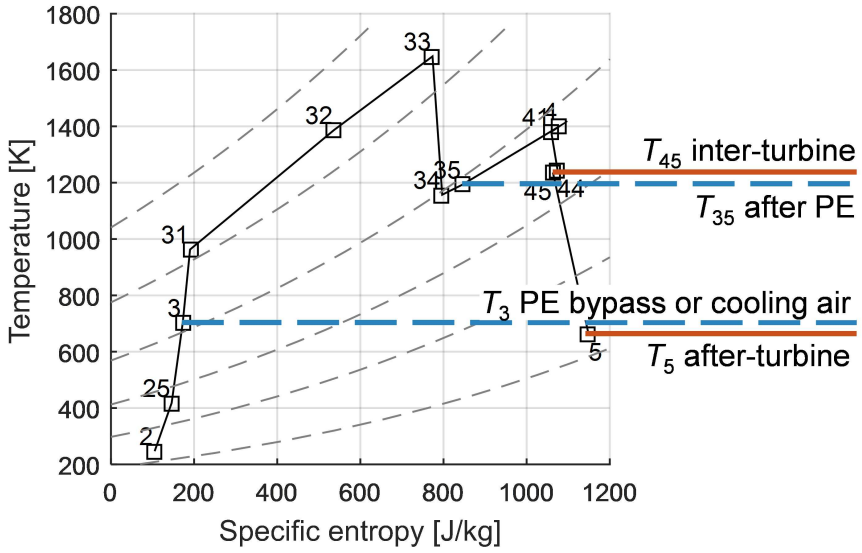

Figure 4.13: Temperature T over specific entropy s diagram of the baseline CCE cycle [81]. Station nomenclature according to Figure 3.2. Stations 31-34 piston engine internal, instationary states. Station 41 after addition of turbine stator cooling air, station 44 after turbine work extraction in equivalent single stage turbine model [102].

To create a viable temperature difference, the baseline cycle conditions could be modified, by both decreasing T_{35}, and increasing T_5. To get meaningful heat flows in the correct direction, a temperature difference of at least 200 K was assumed to be required. To achieve this, T_4 would need to be increased to over 2 000 K at an OPR of 20. This would reduce TSFC of the base cycle by 20 %. This efficiency gap cannot be closed by the savings through recuperation.

Therefore, other options were investigated, involving both other recuperating mass flows and recuperator locations. Figure 4.12(b) shows the option to use the turbine cooling bleed (middle) for recuperation. Although this considerably increases required turbine cooling air, it helps to reduce temperature gradients in the turbine blades. The other option uses a separate small bleed of the order of 10 % of the core mass flow (Figure 4.12(b), right). The advantage of both options is that they recuperate to only a small mass flow, reducing the weight and size of the heat exchanger matrix. The coolant temperature T_3 is lower, because it is extracted before the piston engine.

Another measure is to relocate the recuperator between HPT and LPT (Figure 4.12(c), middle), to utilise the higher temperature T_{45}. As a major drawback, LPT work potential reduces. A further option would be to introduce a third combustor between HPT and LPT to increase T_5. Here, heat is added at relatively low pressure, reducing thermal efficiency.

All options were combined amongst each other and numerically investigated, with a total of 18 recuperated configurations. These offered at best marginal improvements over the baseline CCE [81]. Despite existing optimisation potentials on heat exchanger level, major technical uncertainty exists about the heat exchangers. They would need to operate at highly elevated temperatures of 1 400 K, and weight and pressure loss would need to be reduced considerably, to obtain a relevant cycle improvement. Therefore, recuperation is not further regarded in

this thesis. If the piston compressor was exchanged with a turbo compressor in these studies, similar general deltas and results could be expected. An additional gearbox would be required, the compression efficiency would decrease, but engine weight would reduce.

These findings should be revisited, if novel technologies improved the viability of heat exchangers. Heat exchanger designs need to be compact with small pressure losses. An enabling technology for these requirements may be the use of secondary fluid heat exchangers, possibly operating with liquid metals. These could reduce pressure losses on the gas side [245].

Bottoming cycles are another approach to utilise waste heat potential. Typically, they use a closed Rankine cycle that operates on an organic fluid or CO_2. The bottoming cycle can only contribute power based on the heat available in the exhaust. The required two heat exchangers and the turbine consume considerable space and weight. As a result, fuel burn improvement potential is only 1 % to 2 % [246, 247] in a turbofan architecture. In the CCE concept, this share is more restricted due to lower exhaust temperature and core mass flow. Therefore, bottoming cycles were omitted as annexed technology. It could be combined into the concept synergistically, when the technology further matures.

Chapter 5

Results of Selected Composite Cycle Engines Concepts

This chapter demonstrates the capabilities of the methods presented in Chapter 3 on an engine with the conceptual design characteristics discussed in Chapter 4. Several potential implementations of the CCE are presented and benchmarked against a year 2035 GTF and against SRIA 2035 emission reduction targets. Sensitivity studies for crucial technology parameters indicate the robustness of the results. Finally, a technology roadmap shows the potential way forward.

The studies are performed for a short-to-medium range aircraft and an engine with a year 2035 technology standard as described in Section 3.7 and Section 4.1. The baseline CCE illustrates a possible engineering solution for the implementation of the cycle with technology that is as conventional as possible. Solutions in the following Section 5.2 with a two-stroke engine, an intercooler, and a free-piston illustrate further development and improvement potentials. The studies include multi-point design in ToC, TO, and CR conditions. Changes in TSFC and engine mass are used to evaluate fuel burn improvement. NO_x emissions are separately evaluated for the LTO cycle and cruise conditions.

5.1 Baseline Four-Stroke Engine Concept

The baseline CCE features a four-stroke piston engine driving an axial-radial compressor. A single turbine drives the fan and the IPC. The engine is first scrutinised for optimum operating conditions. Therefore, the available design parameters are varied and their impact on fuel burn and component operating limits is evaluated. Engine specifications complementary to the GTF are summarised in Table 5.1 (p. 92). HPC efficiency is assumed to be 2 % worse to account for inferior efficiency of axial-radial compressors compared to an axial compressor in this component size. The load coefficient of the radial compressor stage of 1.8 leads to a ToC pressure ratio between 2.5 and 3.0, depending on OPR. Axial stages are added to achieve higher pressure ratios. Piston system transmission efficiency was evaluated according to Section 3.3.5 for all operating points. Piston engine mechanical losses are assumed to reduce by

20 % compared to the model due to improved surface quality and lubrication technology. The 2-stage high pressure spool gearbox was assumed to lose further 0.5 % of transmitted power per stage. Pressure losses of 1 % in intake and exhaust duct respectively appear justified as flow speeds are low in the buffering volume and the distributing pipes. The power off-take is extracted from the high pressure spool as in the GTF.

Table 5.1: Assumptions for CCE design point performance.

Performance Parameter	**Unit**	**Value**
Polytropic axial-radial HPC efficiency	%	89.0
Auxiliary compressor efficiency	%	85.0
Piston system transmission losses rel. to model in Section 3.3.5	%	−20.0
HP spool gearbox transmission efficiency	%	99.0
Piston intake and exhaust duct pressure loss (each)	%	1.0
Component Limits		
HPC tip speed	m/s	500
HPC radial stage load coefficient $\psi_{\mathrm{st,tip}}$	–	1.8
Piston engine peak pressure p_{peak}	bar	250
Piston engine exhaust temperature T_{35}	K	1 350
Piston bore	m	0.17
Compressor surge margin SM	%	15.0

The limit of radial compressor tip speed at impeller outlet was set to 500 m/s. The maximum permissible piston engine exhaust temperature is limited to 1 350 K by the capabilities of outlet duct and valves. For compressor surge margin, a limit of 15 % was specified. The piston bore was limited to 0.17 m to fit the piston engine assembly into the core cowling. Larger bores would lead to major interference with the core cowling at both crankshaft casing and valvetrain.

Modelling of piston components and interaction with turbo components requires several corrections on efficiency. These are summarised in Table 5.2 (p. 93). These were applied to the engine simulation with fuel flow correction factors. Real gas effects lead to 0.2 % lower piston engine fuel flow as shown in Section 3.3. The use of compression ratio as a surrogate for adapted valve timings and combustion parameters requires an increase in piston engine fuel flow of 0.4 % in cruise as described in Section 3.3.2. The stages of HPC and LPT adjacent to the piston engine are subject to pulsation according to Section 3.8.1. The buffering volumes are respectively sized to ensure that efficiency losses are negligible.

The piston engine introduces many new design and off-design parameters, which need to satisfy many constraints. To handle the simulation complexity, a gradient-based optimiser[1] was used, which obeys the equality and non-equality constraints discussed before. Fuel burn is the minimisation objective. Since the solver is gradient based, it may not surmount obstacles such as changes in stage count, and could converge to a local optimum depending on the starting solution.

[1] The MATLAB built-in solver `fmincon` was used.

Table 5.2: Efficiency corrections for CCE simulation.

Parameter	Value
Real gas correction on piston engine fuel flow	−0.2 %
Surrogate model correction on piston engine fuel flow in cruise	+0.4 %
Pulsation correction on HPC efficiency	<0.05 %
Pulsation correction on LPT efficiency	<0.05 %

To ensure that a global optimum is found, global search algorithms were used. Genetic algorithms randomly permute the solution variables and combine the best solutions to find new optima[2]. Furthermore, global search algorithms, which are supplied with start solutions randomised around a previously found local optimum were used[3]. Subsequently, again a gradient-based optimiser finds the local optimum from the best newly generated solutions. Eventually, the global optimum is assumed to be the best local optimum found. This approach showed that the global solvers found the same optimum as the gradient-based solver before.

The resulting baseline CCE engine cycle properties found by the optimisation procedure are summarised in Table 5.3 (p. 94). The TO combustor outlet temperature $T_4 = 1397\,\mathrm{K}$ and OPR = 29 are much lower than in the reference GTF with $T_4 = 1928\,\mathrm{K}$ and OPR = 43. The peak pressure ratio (PPR) is, however, much higher with 241. Moving T_4 to lower values implies a higher share of fuel burned in the piston engine, which leads to better engine efficiency. The optimum OPR is constrained by permissible peak pressure and exhaust temperature of the piston engine. In ToC and CR, small fractions of the core flow (5 % and 2 % respectively) circumvent the piston engine. Piston engine pressure ratio is between 1.17 and 1.31 . The value is lower than the optimum found by previous authors in the range of 1.5 to 1.6 [59]. This may be a result of the much higher charging. Cruise TSFC is 12.3 % lower than that of the GTF. The turbine cooling air ratio reduces from 21.3 % to 3.9 % of the core mass flow $\dot{m}_{25}$, due to low T_3 and T_4.

The temperature over specific entropy diagram of the CCE cycle is shown in Figure 5.1 (p. 94) for ToC conditions. The lower OPR and T_4 are clearly visible. The piston cycle on top of the Joule-/Brayton-cycle reaches higher pressures and temperatures than the reference GTF cycle. The compression process in the piston starts at a higher temperature than T_3 due to mixing of residual gas and fresh air. Compression in the piston appears to have a polytropic efficiency higher than 100 % as specific entropy decreases. This is a result of heat rejection from the cylinder walls, leading to intercooled compression. It causes a decrease in entropy during expansion. Note that the isobaric lines are displayed for clean air without combustion products. Thus, peak pressure is indeed higher than indicated by the graph.

Piston engine-related parameters and important figures of merit are summarised in Table 5.4 (p. 95). The highly charged piston engine leads to a volume specific power in the range of charged automotive engines, and high net indicated mean effective pressure (IMEP) of 43 bar with scavenging work already subtracted. The compression ratio CR is lower than

[2]The MATLAB built-in solver `ga` (for *genetic algorithm*) was used.
[3]The MATLAB built-in solvers `GlobalSearch` and `MultiStart` were used.

Table 5.3: Baseline CCE cycle properties.

Operating Point	Unit	ToC	TO	CR
Streamtube Thrust	kN	25.36	109.88	19.97
T_3	K	709	767	667
T_{35}	K	1 221	1 350	1 100
T_4	K	1 226	1 397	1 152
TSFC	g/kN/s	12.51	7.59	12.19
OPR	–	32.9	29.1	30.1
PPR	–	406	241	389
BPR	–	18.1	18.8	18.7
Peak pressure	bar	144	250	123
IPC pressure ratio	–	3.0	3.4	3.0
HPC pressure ratio	–	7.2	6.2	7.1
Piston engine pressure ratio	–	1.309	1.175	1.215
Trapped FAR	–	0.030	0.030	0.025
Piston engine circumv. fraction	%	5.4	0.0	1.7
Piston engine power	MW	4.59	9.91	3.50
Piston engine heat loss	MW	1.89	4.13	1.39
Piston engine transmission eff.	%	92.3	94.9	91.5

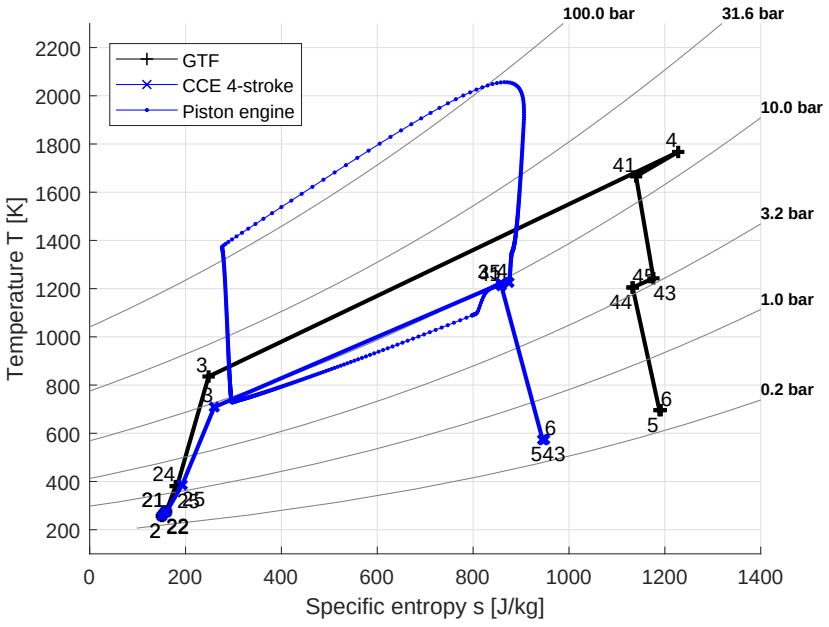

Figure 5.1: Temperature T over specific entropy s diagram of CCE against GTF at ToC conditions. Station nomenclature according to Figure 3.2. Station 41 after addition of turbine stator cooling air, station 43 after turbine work extraction, and station 44 after addition of rotor cooling air in equivalent single stage turbine model [102].

in automotive Otto engines, to stay below the peak pressure limit. The piston engine has a volume specific mass of 22.4 kg/L. The value is close to the value extrapolated for piston engines with contemporary manufacturing technology of 20 kg/L specified by [59], while a traditional design of historic large aero piston engines would yield specific masses up to 37 kg/L. The piston area load is twice as high as in automotive engines, which indicates a challenge for piston design.

Table 5.4: Piston engine limit properties. Operating point TO if not specified otherwise.

Parameter	**Unit**	**Value**
Piston bore	m	0.169
Number of pistons	–	24
Displacement volume	L	91.2
Piston area load	W/mm^2	18.4
Net IMEP	bar	42.6
CR	–	7.3
Max. v_{mean} (ToC)	m/s	18.0
Max. engine speed (ToC)	rpm	3 192
Volume specific mass	kg/L	22.4
Volume specific power	kW/L	108.7

A power and heat balance for the core engine is prepared in Figure 5.2 (p. 96). On the low-pressure spool, the majority of power is consumed by the fan. Losses are a small fraction of the shaft power. On the high pressure spool, losses, off-takes and power for compression of secondary air flows constitute 7.5 % of the piston engine power. Auxiliary power for compression of piston engine circumventing air is not required under TO conditions as all air passes the piston engine. Mechanical losses and piston engine heat losses sum up to 4.4 MW. They are dissipated with 34.8 kg/s of bypass air. These are mixed downstream with the remaining bypass air before the bypass nozzle.

5.1.1 Flow Path and Mass

The flow path of the CCE is shown in contrast to the reference GTF in Figure 5.3 (p. 97)(a). The CCE is 1.38 m longer than the GTF, mainly due to the large piston engine. Reduced turbo component sizes, lower core mass flow rate and lower stage counts due to reduced turbo pressure ratio can only partially compensate for this. The dashed circles indicate buffering volumes. The second buffering volume collecting the piston engine exhaust flow is arranged around the engine centreline enclosed by the piston engines and cut by line A–A. Both buffering volumes fit well into the available headspace.

Figure 5.3 (p. 97)(b) displays the cross-sectional view through the piston engine with the arrangement inside the core cowling (two outer dotted lines). The core cowling has a small interference towards the rear of the piston engine. Only a small fraction of the circumference is affected. At the cylinder head, enough space is available for the valvetrain. Between cylinder walls and core cowling, some space is remaining, which could be used for piston

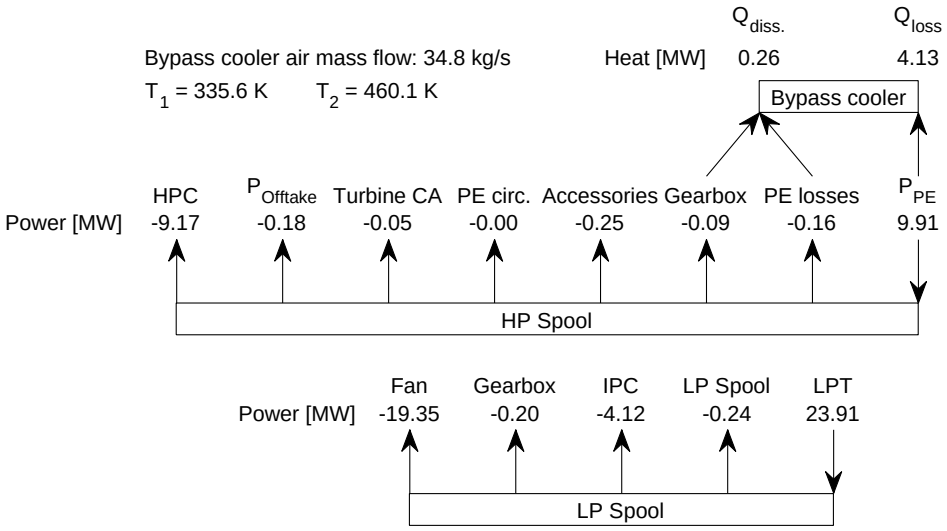

Figure 5.2: Power and heat balance for the core engine under TO conditions.

engine cooling. The piston banks have an opening angle of 110°. The two inner dashed lines indicate the contour of the exhaust buffering volume at maximum extent.

The component mass breakdown is summarised in Table 5.5. Total turbo component masses (excluding fan) decrease considerably by 195 kg, or 24 %, in total. This compensates only a small fraction of the piston system mass of 2 208 kg including piston engine gearbox. In total, engine mass doubles, and PPS mass increases by 2 432 kg (69 %).

Table 5.5: Mass breakdown of CCE against GTF.

Component	**GTF [kg]**	**CCE [kg]**	**Δ [%]**
Fan	782.3	786.1	0.5
FDGS	278.2	292.3	5.1
IPC	101.2	74.0	-26.9
HPC	177.0	174.3	-1.5
Combustor	56.4	41.9	-25.6
HPT	115.2	–	-100.0
LPT	363.7	328.1	-9.8
Piston engine gearbox	–	168.8	–
Piston engine	–	2 039.3	–
Systems & dressings	351.6	711.5	102.3
Accessories	118.7	126.8	6.8
Engine	2 344.3	4 743.2	102.3
Nacelle	464.5	464.5	0.0
Thrust reverser	416.1	444.3	6.8
Core cowl	153.2	151.5	-1.1
Bypass nozzle	119.7	136.6	14.1
Core nozzle	32.4	21.7	-33.1
PPS	3 530.2	5 961.8	68.9

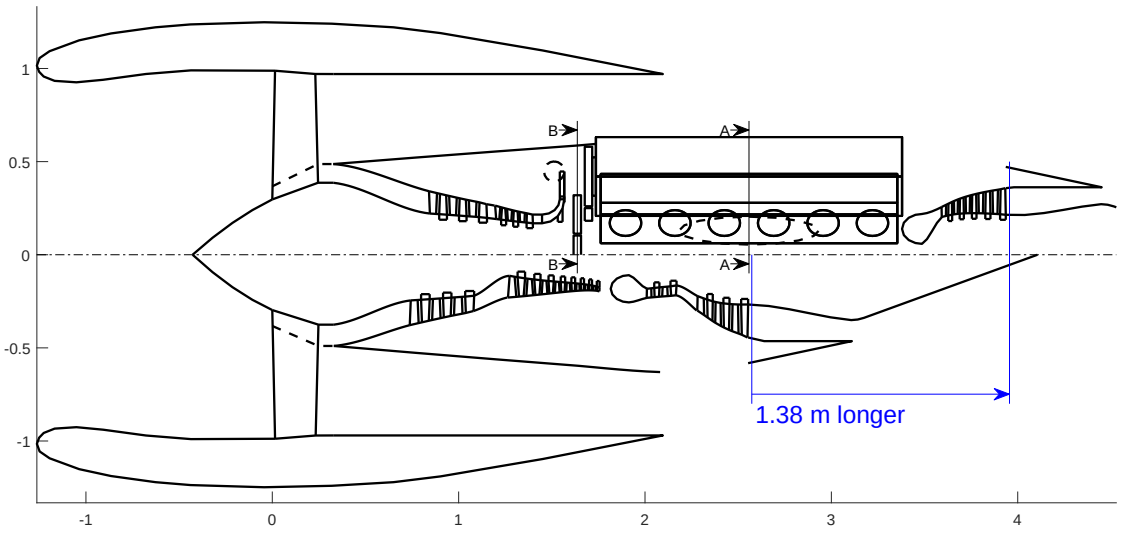

(a)

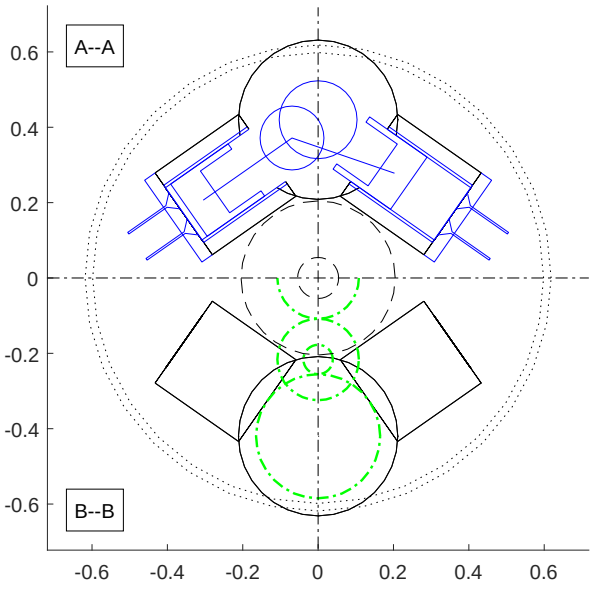

(b)

Figure 5.3: (a) General arrangement of the baseline CCE (top) drawn against the reference GTF (bottom). (b) Cross-sectional view through the piston engine (top) with piston engine gearbox (bottom).

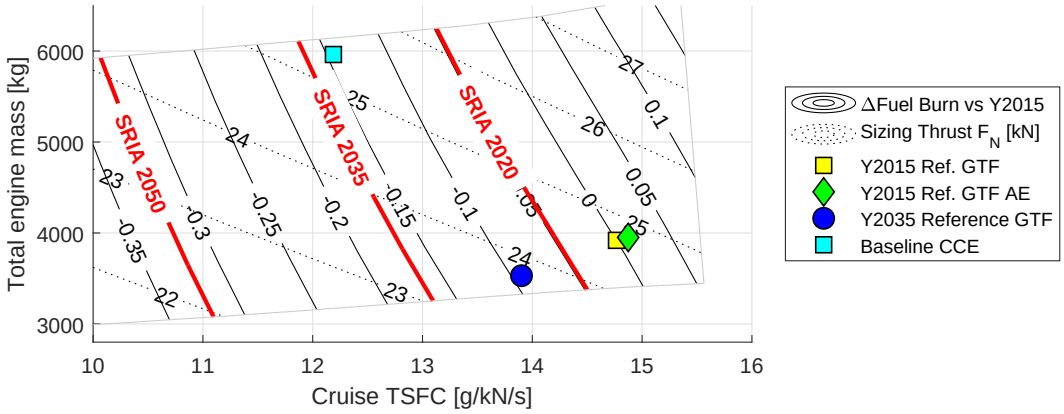

Figure 5.4: Changes in fuel burn and sizing thrust F_N for baseline CCE.

5.1.2 Fuel Burn

The locale of the baseline CCE is illustrated in Figure 5.4, and important aircraft level metrics are summarised in Table 5.6. The baseline CCE misses the year 2035 emission reductions target by 1.9 %. The fuel burn improvement due to improved engine efficiency is largely consumed by increased engine mass[4]. As a result, the improvement over the GTF of similar technology level is significant but condensed to 5.7 %.

This underlines the importance of achieving low piston engine mass. Nevertheless, aircraft structural weight (OEW without engines) increases only by 1.9 %, which implies minor changes in aircraft design and manufacturing cost. MTOW is 6.4 % higher, incurring higher landing fees. The sizing thrust in ToC is higher than the year 2015 level.

Table 5.6: Aircraft level metrics with baseline CCE.

Parameter	Unit	Value
ΔFB vs. Y2000	%	-28.1
ΔFB vs. Y2035	%	-5.7
ΔFB vs. Y2035 due to TSFC	%	-14.7
ΔFB vs. Y2035 due to mass	%	11.7
OEW w/o engines	t	32.3
MTOW	t	76.8

The optimum number of 24 pistons was found by altering their number by multiples of 4, to change the number by one on each piston bank. More pistons lead to decreased overall engine mass as piston engine mass scales favourably with a smaller bore. However, TSFC increases as piston heat loss rises with the surface-to-volume ratio of the pistons. The overall engine is 16 cm longer. Detailed results are shown in contrast to the other CCEs investigated in Section 5.2.4. Increasing the number of pistons to 28 increases fuel burn by 1.2 % due to

[4] Adding the deltas of changes due to TSFC and mass delivers a smaller improvement of 3.0 % as opposed to the specified 5.7 %. The difference has two reasons: First, the relative changes need to be multiplied rather than added. Second, the cascading effects of TSFC are greater at the true (higher) mass.

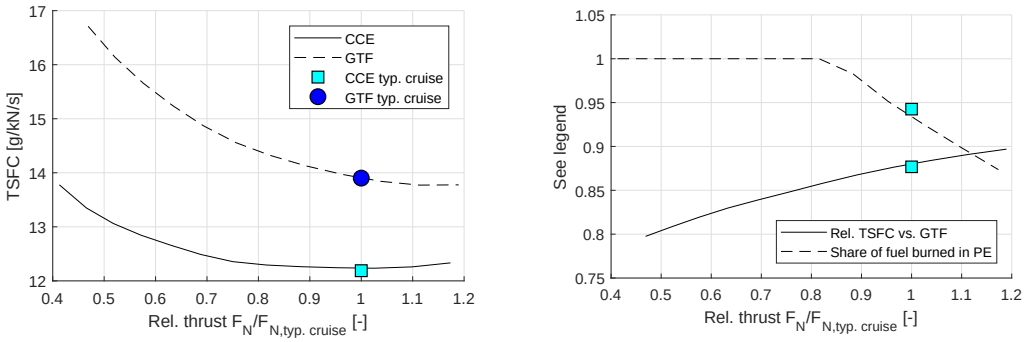

(a) **(b)**

Figure 5.5: CCE part power characteristics (a) TSFC, and (b) change in TSFC against GTF and fuel ratio burned in the piston engine.

1.1 % inferior TSFC. PPS mass reduces by 0.8 %, piston engine mass by 1.5 %. Reducing the number of pistons to 20 increases TSFC by 3.0 % as the piston engine bore is now limited and the fuel split is shifted towards the secondary combustor. Although engine mass decreases by 4.0 %, fuel burn increases by 2.8 %.

5.1.3 Part-Load Behaviour

This section shows how the CCE behaves in off-design under part-load conditions. Cruise conditions are chosen, because part-load behaviour is important considering performance on off-design aircraft missions, and in particular shorter missions or missions with less than maximum permissible payload. Short-to-medium aircraft are typically utilised on much shorter mission ranges than the design range of about 3 000 nmi. More than 79 % of the missions are less than 1 000 nmi [39].

The part power TSFC curve is displayed in Figure 5.5(a). The curve is visibly flatter than that of the GTF because of many degrees of freedom, which can be used in part load for efficiency optimisation. As displayed in Figure 5.5(b), the advantage against the GTF increases towards lower thrusts, up to 20 % at a relative mechanical spool speed $N_{\mathrm{L,mech,rel}}$ of 0.78 at 47 % of the typical cruise thrust. Thus, the fuel burn advantage on off-design short-range missions with lower fuel load and payload may be higher than on the design mission. Moreover, short-range missions are typically flown on lower altitude and at lower cruise speed, which would further favour the CCE. The economically optimal cruise speed and altitude will be lower than with a turbofan. The higher MTOW has a detrimental impact, though. The ratio of fuel burned shifts towards the more efficient piston engine in lower part load. The secondary combustor is deactivated below $N_{\mathrm{L,mech,rel}} = 0.90$ at 82 % of typical cruise thrust. The TSFC is almost constant down to this thrust, while it already increases steeply in the GTF at this point.

5.1.4 NO_x Emissions

NO_x emissions were simulated in the LTO cycle and for typical cruise conditions. The LTO cycle consists of four operating points that represent the typical emission footprint for a single rotation of an aircraft. These have a rated thrust of 100 % for 42 s to represent TO, 85 % for 132 s to represent climb, 30 % for 4 min to represent approach, and 7 % for 26 min to represent taxiing and ground idle. All points are simulated at SLS conditions without power off-takes or customer bleeds at ISA conditions in accordance with certification requirements.

The NO_x emission results are summarised in Table 5.7. In total, emissions are 3.2 times as high as those of the GTF in the LTO cycle. The main reason is the significantly higher EINOx in the piston engine, which is 3.6 times as high as in the GTF under 100 % conditions. More than 99 % of NO_x is created in the piston engine. Notably, the emission index of the piston engine only declines in the approach rating. The cruise emissions are 8 times as high. EINOx is on a similarly high level as the 100 % SLS point despite lower peak pressures and temperatures due to a higher CR. As a result, high pressures and combustion temperatures appear earlier at TDC, leading to a shift in NO_x production towards start of combustion.

Table 5.7: CCE NO_x emission estimates in LTO cycle and cruise.

Operating Point	**Unit**	**SLS**			**Cruise**
		100 %	85 %	30 %	
PE EINOx	g/kg_{fuel}	75.7 ±14	71.2 ±13	44.9 ±8[d]	80.5 ±12
PE fuel flow	kg/s	0.648	0.451	0.120[d]	0.232
Combustor EINOx	g/kg_{fuel}	0.8	0.8	0.3[d]	0.3
Combustor fuel flow	kg/s	0.138	0.194	0.099[d]	0.014
Total D_p	g	8 826[a] ±18%			18.7 g/s ±15%
ΔD_p vs. GTF	%	+225			+691
$D_p/F_{N,SLS}$	g/kN	65 ±12			–
CAEP/6−65 %	g/kN	20[b] / 150[c]			–

[a] incl. estimated 13.7 % of total D_p for 7 % thrust point.
[b] based on OPR = 27.9
[c] based on peak pressure ratio $p_{peak}/p_2 = 247.5$
[d] extrapolated from 60 % thrust

The degrees of freedom available for operating the CCE can be used to minimise NO_x emissions in the LTO cycle. The cycle can be tailored for high local air quality on the ground, and for high efficiency in-flight. With this optimisation, NO_x emissions can be reduced compared to typical operating conditions used for TO by 10 % under TO conditions, and by increasingly more for low power conditions. These measures are included in the table. Optimising for minimum NO_x essentially minimises piston engine fuel flow to shift it to the secondary combustor. The reduction potential is limited by off-design component limits and turbine cooling capabilities. This strategy is not desirable in cruise as a shift of fuel flow to the secondary combustor would impair efficiency.

Depending on the choice of the certification reference pressure ratio, the limit is significantly exceeded by a factor of 3.2 when using OPR, or easily met with a margin of 57 % when using PPR, being defined as the ratio of peak pressure p_{peak} and p_2. A reference pressure ratio of 100 would be required to stay within the year 2035 limit. This highlights the importance of defining an appropriate reference pressure ratio for engine certification. It should account for the improved efficiency of CCE and permit higher emission levels than GTF engines but still pose a challenge for engine designers.

Measures for NO_x reduction in piston engines can be used to reduce the emission levels. The use of ammonia (NH_3) for selective catalytic reduction (SCR) appears only feasible for the LTO cycle, since 5 % to 10 % NH_3 of the fuel flow rate are required for effective reduction. For an entire mission, it would require substantial additional tanks in the aircraft. Catalytic surfaces in the engine exhaust may be necessary.

Another option is to inject water into the piston engine [248]. Multiple options are available to achieve this: First, a fuel-water emulsion dispenses with the need for multiple tanks. With this measure, NO_x can be reduced by up to 50 %. However, problems with corrosion and rated power may occur. Second, water may be injected into the cylinder via a separate injector. The amount of water injection can be tailored to the operating point. Third, water can be fumigated before the piston engine. As with SCR, the problem with this technique lies in the large amounts of water of the order of 10 % to 20 % of the fuel flow rate. As positive side effects, rated power increases and thermal load decreases.

The secondary combustor is a further option to reduce NO_x. The secondary combustor would need to be operated in an appropriate temperature window to achieve this. Reduction of piston engine NO_x could be achieved through exhaust gas recirculation (EGR). A higher fraction of residual gas in the piston engine reduces flame temperature and, thus, NO_x creation rates. This could be achieved through internal EGR. By tailoring valve timings, the amount of residual gas could be increased. In two-stroke engines, this can also be achieved by reducing the scavenging pressure ratio. EGR decreases engine power, however.

5.1.5 Technology Sensitivity Study

Many assumptions made in this thesis are uncertain to a degree. Some limits could be exceeded with high-end development, manufacturing and material technology, while others may not be reached considering the operating environment and the required component lifetimes. Therefore, a sensitivity study shows the impact of the most critical technology assumptions made. This reveals the most important technology parameters, which require attention during development, or can otherwise pose a show-stopper, if they cannot be achieved. The changes performed were chosen to represent a bandwidth, which appears to be reasonably within the true technology level that can be expected at entry into service time frame.

Individual sensitivities are displayed in Table 5.8 (p. 102). The table shows the reference value used in all studies and the high-end value. The changes in TSFC, power plant system mass m_{PPS} and fuel burn FB are respectively evaluated. For example, if the piston peak pressure p_{peak} could reach 300 bar instead of 250 bar under TO conditions, fuel burn can improve by

1.7 %, because TSFC improves considerably. Engine mass increases by 1.1 %, because some piston component masses scale with peak pressure.

Table 5.8: CCE sensitivities of technology assumptions on TSFC, power plant system mass m_{PPS} and fuel burn FB in order of highest fuel burn improvement potential.

Parameter	**Unit**	Ref.	High	ΔTSFC [%]	Δm_{PPS} [%]	ΔFB [%]
Piston peak pressure p_{peak}	bar	250	300	-1.6	1.1	-1.7
Mean piston velocity v_{mean}	m/s	18	20	-1.0	-1.4	-1.6
Piston exhaust temp. T_{35}	K	1 350	1 400	-0.7	-0.2	-0.9
PE mechanical losses	%	-	-2	-0.7	-0.3	-0.9
Liner temperature	K	500	600	-0.6	1.5	-0.5

Increasing v_{mean} improves both TSFC and power plant system mass, because the available displacement volume of the piston engine can be utilised to a higher degree. Therefore, increasing v_{mean} is very desirable, and yields the same order of fuel burn improvement as increasing peak pressure. Increasing piston exhaust temperature T_{35} and reducing piston engine mechanical losses by 2 % (abs.) both yield almost one percent improvement, mainly through improvement of TSFC. Increasing liner temperature – despite reducing piston engine heat losses – is the least effective measure, because the mean temperature of the fluid in the piston increases and, therefore, the volumetric efficiency of the piston goes down. The resulting increase in required displacement volume and power plant mass consumes a large part of the efficiency improvement.

Superimposing the effects of all high-end parameter, the fuel burn improvement of the CCE could be doubled from 5.7 % to 10.9 %. Vice versa, the fuel burn improvement in the baseline CCE could be entirely consumed, if all nominal values were instead surpassed in the opposite direction. This underlines the importance of conceptual design and reasonable component limits beyond just the improvements by the cycle.

5.2 Alternative Piston Engine Concepts

In this section, alternative CCE concepts are investigated, which alleviate major drawbacks of the baseline but may incur higher complexity or use components, which are currently at a low TRL. The potential of these concepts is shown here to highlight the further development potential of CCEs.

5.2.1 Two-Stroke Piston Engine

The two-stroke engine requires a pressure drop from intake to exhaust in contrast to the four-stroke engine. The pressure drop Δp is specified as a ratio of the absolute intake pressure p_1, and is freely varied by the optimiser. While higher Δp improves scavenging and lowers mean piston temperature, it also infers higher losses. The trapped fuel-air-ratio FAR in a two-stroke engine is typically higher than in a four-stroke engine due to inferior scavenging. While a

four-stroke engine cycle starts with almost fresh air, a two-stroke engine has considerable amounts of residual gas from the previous cycle. To release the same amount of heat, the final trapped FAR is higher. It is bounded by the soot limit set to FAR = 0.055.

The optimum number of pistons reduces from 24 in the four-stroke engine to 16 as the mass flow rate per displacement volume increases. The fuel burn optimal results are summarised in Table 5.9. The two-stroke engine is less efficient, because of imperfect scavenging. Although cycle temperature is higher, exhaust temperature can be handled, because fresh air directly passes through the cylinder during the scavenging process. OPR increases from 29 to 39. The scavenging pressure drop across the piston engine is about 3 %.

Table 5.9: Two-stroke CCE cycle properties.

Operating Point	**Unit**	**ToC**	**TO**	**CR**
Streamtube Thrust	kN	24.21	104.89	18.99
T_3	K	818	877	783
T_{35}	K	1 129	1 350	1 116
T_4	K	1 212	1 406	1 135
TSFC	g/kN/s	12.78	7.84	12.64
OPR	–	43.7	38.7	40.1
PPR	–	703	241	551
BPR	–	12.8	13.2	13.1
Peak pressure	bar	250	250	175
IPC pressure ratio	–	12.9	15.5	12.1
HPC pressure ratio	–	2.9	2.2	2.9
Piston engine pressure ratio	–	0.968	0.972	0.968
Trapped FAR	–	0.055	0.055	0.055
Piston engine circumv. fraction	%	0.0	0.0	0.0
Piston engine power	MW	4.34	7.79	3.55
Piston engine heat loss	MW	1.28	2.27	1.05
Piston engine transmission eff.	%	92.6	94.4	91.8

The two-stroke CCE burns about 90 % of the total fuel in the piston engine. The cycles are compared in Figure 5.6 (p. 104). The higher OPR is apparent and mean piston cycle temperature is 370 K higher. Incomplete scavenging shifts the piston cycle to higher temperatures. Despite higher temperature, the heat losses of the piston engine reduce by 45 % in TO due to lower pistons surface area. Since the two-stroke engines process higher mass flow rates, the core flow increases, and core specific work reduces. T_4 is similar to the 4-stroke CCE. The peak pressure in cruise is higher with 175 bar compared to 123 bar.

A comparison between the general arrangement of two-stroke and four-stroke CCE is shown in Figure 5.7 (p. 104). The engine is 0.76 m shorter. In addition to the reduced number of pistons, bore reduces from 0.17 m to 0.12 m. The engine has a 3.7 % higher TSFC, but is 23.2 % lighter. Driven by the marked mass reduction, fuel burn reduces by 1.1 %. Mass

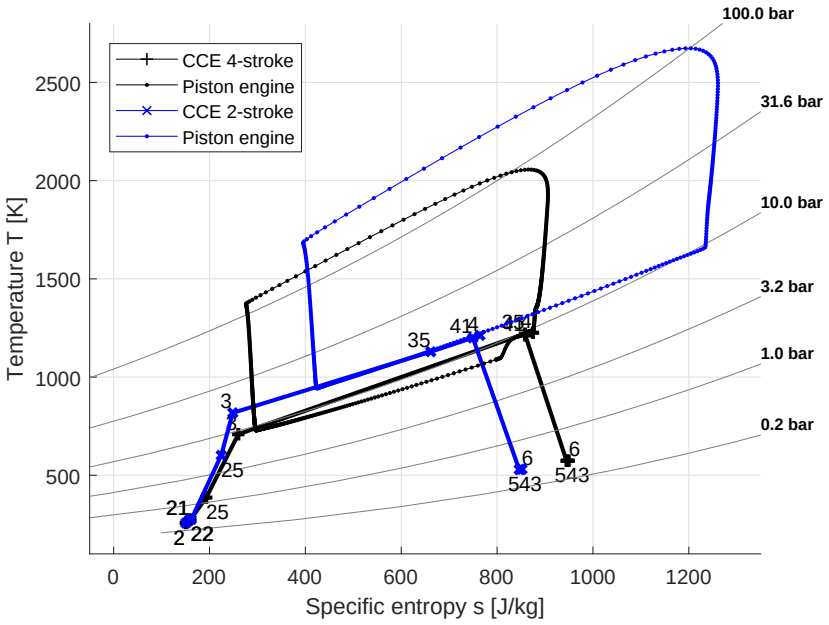

Figure 5.6: Comparison between four-stroke and two-stroke CCE in a temperature T over specific entropy s diagram at ToC conditions.

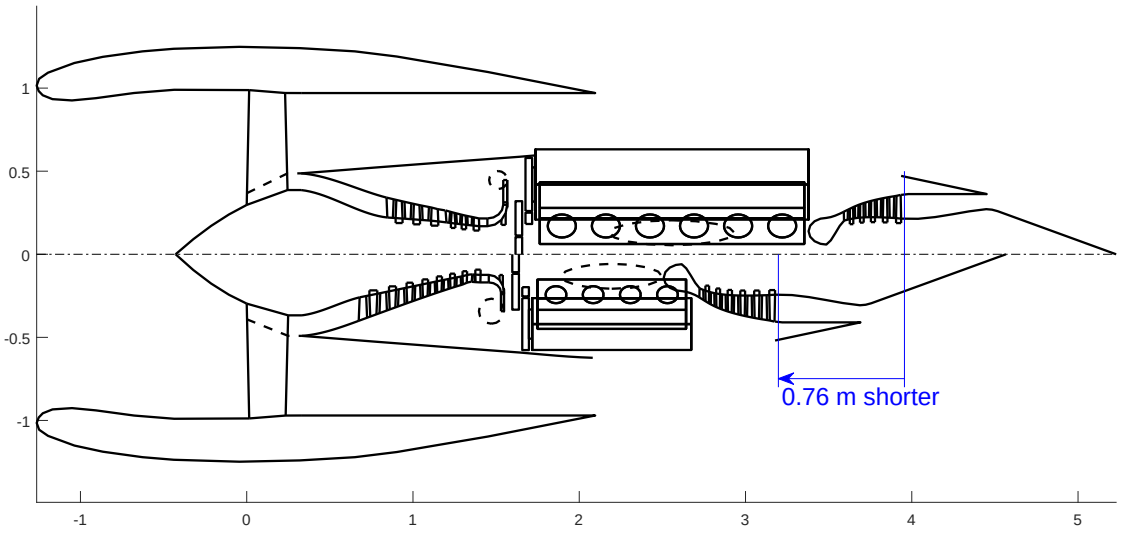

Figure 5.7: General arrangement of the baseline four-stroke CCE (top) drawn against two-stroke CCE (bottom).

breakdown is presented in Appendix A.4 in Table A.2 (p. 147). Results for variation in cylinder numbers are presented later in Section 5.2.4. A lower number of pistons offers slightly better TSFC, but higher engine mass. The net fuel burn would be 0.1 % worse.

NO_x emissions of the two-stroke piston engine are shown in Table 5.10 (p. 105). The thrust-specific LTO emissions are 50 % higher than in the four-stroke engine. Two changes can be identified: First, EINOx is twice as high due to higher cycle temperatures induced by inferior scavenging in two-stroke engines. Second, the two-stroke CCE burns less fuel in SLS in the

piston engine compared to the four-stroke engine. As a result, the certification limit for the year 2035 can only be met when using a reference pressure ratio over 160. In cruise, EINOx and total emissions are twice as high as in the four-stroke engine and 16 times as high as in the GTF. Measures for active NO_x reduction such as water injection would probably be needed to be implemented.

Table 5.10: CCE two-stroke NO_x emission estimates in LTO cycle and cruise.

Operating Point	**Unit**	**SLS**			**Cruise**
		100 %	85 %	30 %	
PE EINOx	g/kg_{fuel}	141.9 ±44	139.3 ±41	35.1 ±5[d]	159.6 ±45
PE fuel flow	kg/s	0.534	0.369	0.114[d]	0.237
Combustor EINOx	g/kg_{fuel}	5.6	4.4	0.0[d]	1.4
Combustor fuel flow	kg/s	0.244	0.282	0.042[d]	0.006
Total D_p	g	12 907[a] ±29%			37.8 g/s ±28%
ΔD_p vs. GTF	%	+375			+1 502
$D_p/F_{N,SLS}$	g/kN	100 ±29			–
CAEP/6−65 %	g/kN	26[b] / 150[c]			–

[a] incl. estimated 13.7 % of total D_p for 7 % thrust point.
[b] based on OPR = 37.0
[c] based on peak pressure ratio $p_{peak}/p_2 = 247.5$
[d] extrapolated from 45 % thrust

The two-stroke CCE configuration with 16 cylinders is used as a reference for comparison with the following two concepts. In addition to the reduced fuel burn and highly reduced engine mass, the two-stroke engine is conceptually simpler, since no auxiliary compressor for pressurisation of turbine cooling air and the flow circumventing the piston engine is required. The resulting sizing thrust of 24.2 kN is still higher than the reference GTF (23.7 kN), but aircraft structural mass, i.e. OEW without engines, is only 0.5 % higher.

5.2.2 Intercooled Composite Cycle Engine

An intercooler is used to reduce required power for compression in the HPC and thermal load in the piston engine. Main intercooler specifications were shown in Table 3.8 in Section 3.4. Intercooler mass including ducting mass estimation was presented in this section in Eq. (3.86) and Eq. (3.88). The intercooler effectiveness ϵ_{IC} constitutes an additional optimisation parameter. As start value, 60 % effectiveness was chosen in accordance with previous results [81, 249] that found the optimum to be in the range of 50 % to 70 %. Higher intercooler effectiveness tends to bring only minor improvements, which are then consumed by intercooler mass. The optimum design ϵ_{IC} is 61 % in the CCE, which is in the range identified in previous studies.

The fuel burn optimal engine has 12 cylinders. Results of it are summarised in Table 5.11 (p. 106). The intercooler reduces the power required for compression on the HPC. As a result, the split of compression shifts from low-pressure to high-pressure spool, and piston engine

size does not reduce. Thus, PPS mass is almost equal to the uncooled two-stroke CCE. Mass breakdown is presented in Appendix A.4 in Table A.3 (p. 148). The secondary combustor exit temperature T_4 is as low as in the four-stroke and two-stroke engines presented before. The turbine cooling air ratio is 3.7 %, which mainly consists of sealing flow (3.0 %) for the first stage. The following stages are uncooled.

The temperature over entropy diagram is shown in Figure 5.9 (p. 107). The piston engine inlet temperature T_3 is up to 250 K lower, leading to a lower cycle temperature inside the cylinder. Thus, heat losses of the piston engine reduce by 10 % to 20 %.

Table 5.11: Main cycle characteristics of a CCE with intercooler.

Operating Point	**Unit**	**ToC**	**TO**	**CR**
Streamtube Thrust	kN	24.24	105.02	19.01
T_3	K	647	633	595
T_{35}	K	1 032	1 208	975
T_4	K	1 228	1 406	1 148
TSFC	g/kN/s	12.88	8.00	12.69
OPR	–	37.7	33.4	34.5
PPR	–	693	241	511
BPR	–	18.0	18.4	18.5
Peak pressure	bar	246	250	162
IPC pressure ratio	–	4.8	5.8	4.7
HPC pressure ratio	–	7.5	5.4	6.9
Piston engine pressure ratio	–	0.976	0.981	0.976
Trapped FAR	–	0.055	0.055	0.050
Piston engine circumv. fraction	%	0.0	0.0	0.0
Piston engine power	MW	4.15	7.70	3.11
Piston engine heat loss	MW	1.12	1.86	0.82
Piston engine transmission eff.	%	92.6	94.8	91.7
Intercooler effectiveness ϵ	–	0.61	0.71	0.63

The general arrangement is shown in Figure 5.8 (p. 107). Intercooler size was approximated with a specific matrix density of 1 600 kg/m^3 [99] for a lancet type heat exchanger, and an assumed 50 % void space. Engine length increases by 0.68 m, leading to a length between uncooled two-stroke and four-stroke engine. Compacter heat exchanger configurations could reduce intercooler length and potentially also mass [250–252]. TSFC and fuel burn are 0.4 % worse than in the two-stroke engine. The results from these studies confirm earlier findings [81, 249] that intercooled CCEs do not improve cycle efficiency.

NO_x emissions in the intercooled CCE are almost as low as in the four-stroke CCE, and 28 % lower than in the uncooled two-stroke engine. The results are summarised in Table 5.12 (p. 108). The mean predicted emissions in the LTO cycle are 3.3 times as high as in the GTF. The LTO emissions are within the limit when applying a reference pressure ratio of 110 for emission regulation. During cruise, emission levels are ten times as high as in the GTF but 35 % lower than in the uncooled two-stroke CCE.

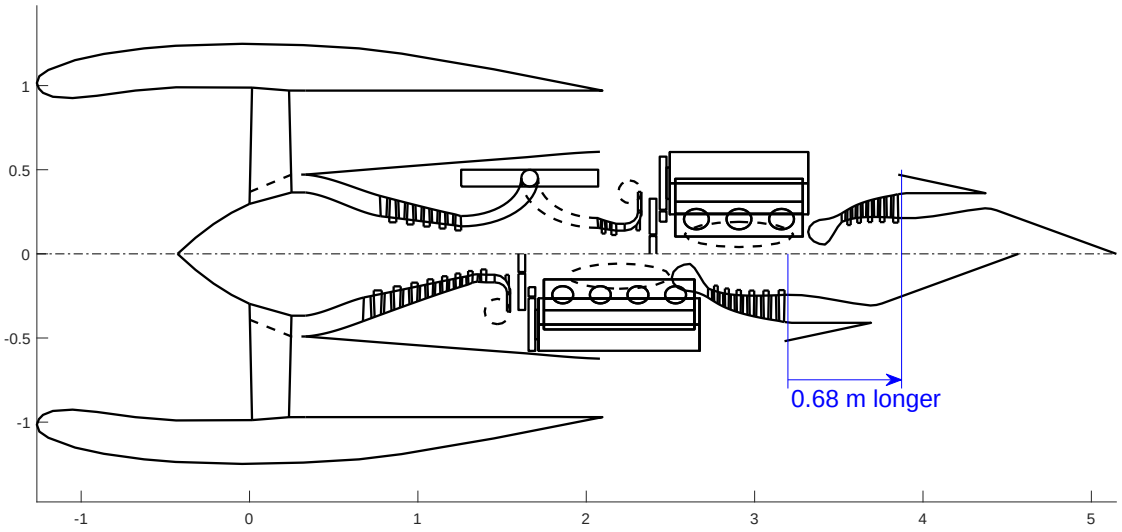

Figure 5.8: General arrangement of the intercooled two-stroke CCE (top) drawn against a two-stroke CCE (bottom).

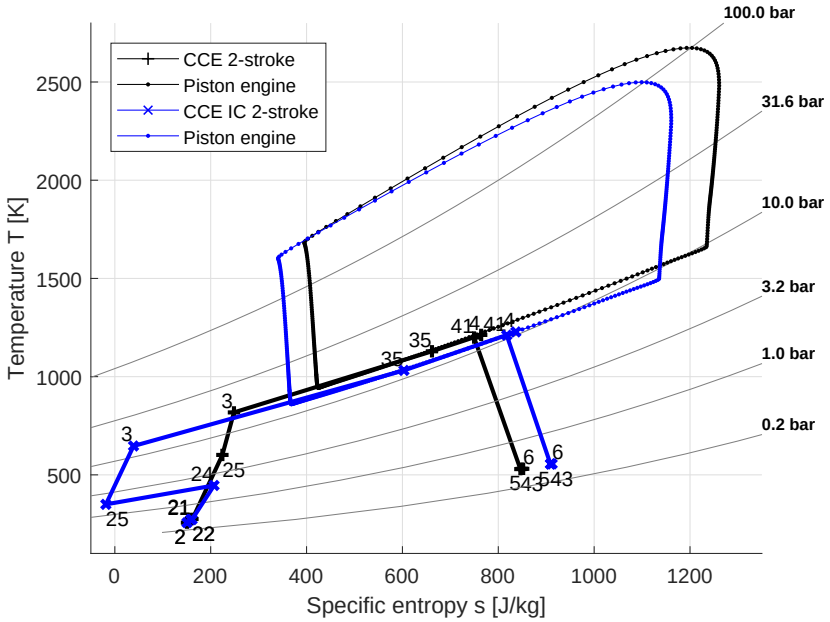

Figure 5.9: Temperature T over specific entropy s diagram of CCE with and without intercooler at ToC conditions.

Table 5.12: Intercooled CCE NO_x emission estimates in LTO cycle and cruise.

Operating Point	Unit	SLS			Cruise
		100 %	85 %	30 %	
PE EINOx	g/kg_{fuel}	111.8 ±26	89.9 ±17	72.5 ±14[d]	127.0 ±29
PE fuel flow	kg/s	0.492	0.332	0.098[d]	0.194
Combustor EINOx	g/kg_{fuel}	0.9	0.8	0.3[d]	0.4
Combustor fuel flow	kg/s	0.299	0.312	0.090[d]	0.049
Total D_p	g	9 289[a] ±20%			24.7 g/s ±23%
ΔD_p vs. GTF	%	+242			+945
$D_p/F_{N,SLS}$	g/kN	72 ±14			–
CAEP/6−65 %	g/kN	22[b] / 150[c]			–

[a] incl. estimated 13.7 % of total D_p for 7 % thrust point.
[b] based on OPR = 31.9
[c] based on peak pressure ratio $p_{peak}/p_2 = 247.5$
[d] extrapolated from 45 % thrust

5.2.3 Free-Piston Engine

A free piston (FP) engine concept as described in Section 4.3 was simulated. The concept was originally proposed by Klingels as a free double piston [241], and transfers the power by the piston engine directly to a piston compressor. Pressurised air lubrication and higher wall temperatures are assumed, since lateral forces are small. Heat losses are partially dissipated to the core flow. A heat exchange effectiveness ϵ from cooling fins to the core flow of 50 % is assumed. Mechanical losses of 0.5 % are assumed as lateral forces are small, and no crankshaft is used. The power off-take is, therefore, taken from the low-pressure spool. It increases by 60 kW to cater for fuel pump, lubrication and valve actuation. This is the approximate time-averaged value across the mission. The assumptions are summarised in Table 5.13.

Table 5.13: Parameter assumptions for FP engine.

Parameter	Unit	Baseline	FP
Mean piston velocity	m/s	18.0	24.0
Cylinder wall temperature	K	500	up to 1 000
PE transmission efficiency	%	93.0	99.5
Power off-take	kW	184	244
Heat sink	–	bypass	core and bypass
Piston operating mode	–	2- and 4-stroke	only 2-stroke
Piston compressor CR	–	n/a	24.0

The compression side of the piston system is represented with neural networks like the piston engines with equal modelling detail level as described in Section 3.3. Note that changing CR in off-design is possible in free-piston engines, since stroke is not prescribed by a crankshaft. This is an additional degree of freedom for off-design optimisation. The compressor CR

should be chosen as high as possible, to minimise dead volume losses. A mechanically feasible compression ratio of 24 was chosen. In past application, CR up to 50 were reported, which declined in part load [253]. The piston compressor uses passively actuated valves, driven only by the pressure difference. Hence, no camshaft is required for these.

The fuel burn optimal number of pistons is 12, i.e. six free-piston units with two engine cylinders each. Performance characteristics of the free-piston engine are shown in Table 5.14. The combustor exit temperature T_4 is further reduced by about 90 K compared to the two-stroke engine. As a result, TSFC is 6 % better. OPR is lower with 28 instead of 39. Lower engine inlet temperature T_3 and higher purging pressures ratios reduce heat loss by 20 % to 30 % from the intercooled two-stroke CCE. Due to the low TO T_4, an uncooled turbine is feasible.

Table 5.14: Main cycle characteristics of a CCE with free piston.

Operating Point	**Unit**	**ToC**	**TO**	**CR**
Streamtube Thrust	kN	23.15	100.33	18.20
T_3	K	738	819	706
T_{35}	K	1 052	1 316	1 011
T_4	K	1 213	1 320	1 139
TSFC	g/kN/s	12.18	7.21	11.90
OPR	–	32.4	27.7	29.7
PPR	–	440	241	393
BPR	–	15.0	15.5	15.5
Peak pressure	bar	157	250	125
IPC pressure ratio	–	7.6	7.0	6.9
Piston compressor pressure ratio	–	3.8	3.8	3.8
Piston engine pressure ratio	–	0.956	0.964	0.952
Trapped FAR	–	0.041	0.055	0.038
Piston engine circumv. fraction	%	5.9	8.4	4.9
Piston engine power	MW	3.50	9.17	2.82
Piston engine heat loss	MW	0.63	1.58	0.43
Piston engine transmission eff.	%	99.5	99.5	99.5

The general arrangement of the CCE with free pistons is shown in Figure 5.10 (p. 110). The entire high-pressure assembly is notably smaller. The six free-piston devices still occupy a large fraction of the core space. The core engine is 0.67 m shorter than the two-stroke CCE, and even slightly shorter than the GTF due to elimination of the high pressure spool. PPS mass is 14 % lower than the two-stroke CCE. The free pistons including the compressor assembly alone are 23 % lighter than the two-stroke piston engine. Mass breakdown is presented in Appendix A.4 in Table A.4 (p. 148). Fuel burn reduces by 9.6 %. The resulting aircraft is lighter than with a GTF (MTOW −2.6 %).

The power and heat balance of the CCE in TO and cruise is shown in Figure 5.11 (p. 110). Under TO conditions, the amount of heat to be dissipated is 3.7 times as high as in cruise. In cruise, about 20 % of the heat is cooled with piston engine circumventing air from the core

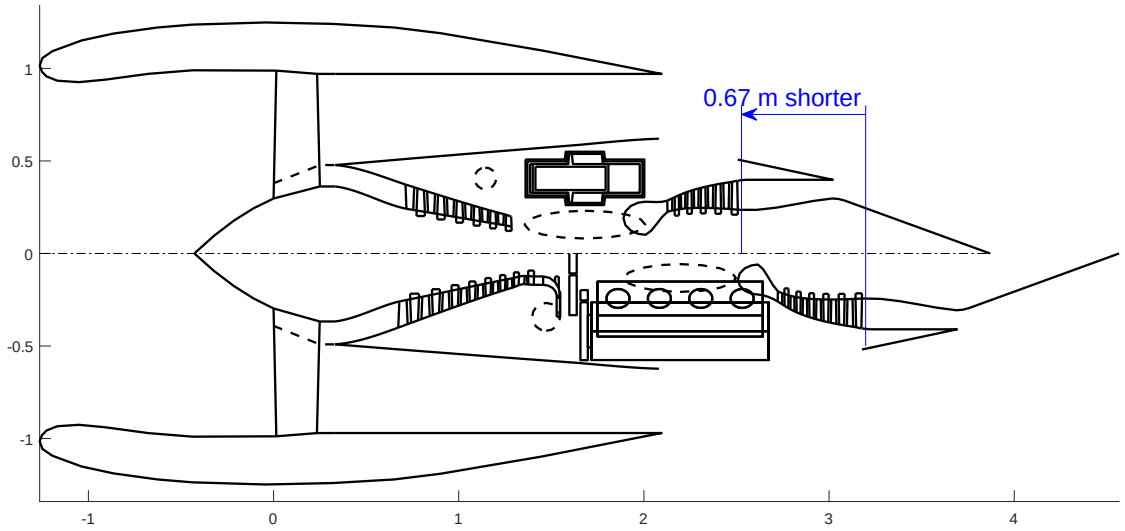

Figure 5.10: General arrangement of the free-piston CCE (top) drawn against two-stroke CCE (bottom).

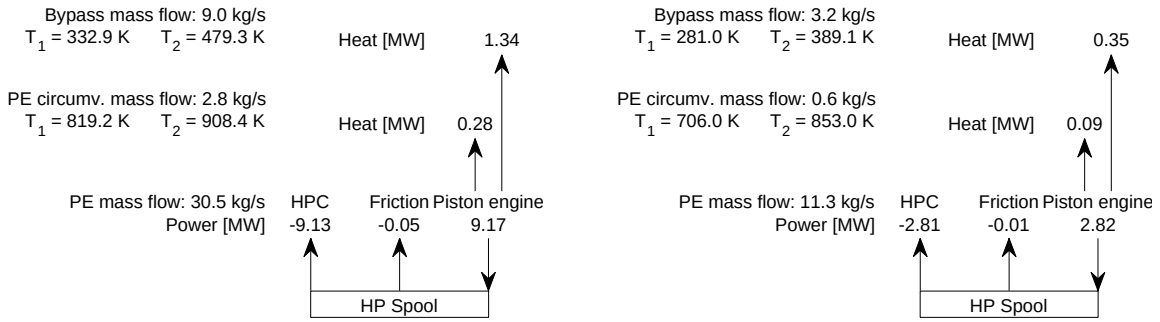

(a) TO **(b)** Cruise

Figure 5.11: Power and heat balance of the high pressure spool of the free-piston engine.

mass flow. Thus, almost 100 kW of heat is kept in the core engine cycle, reducing required fuel flow in the secondary combustor. This amounts to 1 % of the heat from combustion of fuel.

NO_x emissions of the free-piston CCE are 9 % lower than those of the two-stroke CCE, but 40 % higher than the four-stroke. The results are summarised in Table 5.15 (p. 111). Certification limits would be met when using a reference pressure ratio of 140. Emissions in cruise are 35 % lower than in the uncooled two-stroke CCE.

Besides the challenges with free-piston control mentioned in Section 4.3, some additional challenges become obvious. It needs to be proven that gas lubrication can be sustained under all operating conditions and manoeuvring loads. A dual piston cooling system – by the bypass cooler and the core air flow circumventing the piston engine – needs to be implemented. Thus, a free-piston CCE may be considered as a further development step with a later entry into service (EIS) year 2050.

Table 5.15: Free-piston CCE NO_x emission estimates in LTO cycle and cruise.

Operating Point	**Unit**	**SLS**			**Cruise**
		100 %	85 %	30 %	
PE EINOx	g/kg_{fuel}	142.7 ±40	132.6 ±36	73.2 ±18[d]	139.7 ±32
PE fuel flow	kg/s	0.395	0.318	0.093[d]	0.175
Combustor EINOx	g/kg_{fuel}	2.0	1.8	0.6[d]	1.3
Combustor fuel flow	kg/s	0.401	0.320	0.090[d]	0.044
Total D_p	g		11 235[a] ±27%		24.5 g/s ±23%
ΔD_p vs. GTF	%		+314		+936
$D_p/F_{N,SLS}$	g/kN		91 ±24		–
CAEP/6−65 %	g/kN		17[b] / 150[c]		–

[a] incl. estimated 13.7 % of total D_p for 7 % thrust point.
[b] based on OPR = 23.2
[c] based on peak pressure ratio $p_{peak}/p_2 = 247.5$
[d] extrapolated from 60 % thrust

5.2.4 Summary

The fuel burn reduction potential of all investigated CCE concepts is summarised in Figure 5.12 (p. 112). The four-stroke CCE has the smallest improvement potential of all concepts. It almost achieves SRIA 2035 targets. The significant engine efficiency improvement is spoiled by high engine mass. A two-stroke piston engine notably reduces piston engine mass, but TSFC is higher due to inferior scavenging. The remaining benefit is a 1.1 % fuel burn improvement over the four-stroke engine. The remaining gap of 1.1 % to SRIA 2035 targets could be closed with further improvements in propulsive efficiency. Intercooling leads to lower cycle temperatures, but engine mass is virtually equal, while TSFC increases. Net fuel burn increases by 0.4 %. Using a free-piston engine provides another step improvement in engine mass and TSFC, improving fuel burn substantially by 9.6 % over the two-stroke engine. Thus, the SRIA 2035 targets could be met, but the gap towards SRIA 2050 targets is still large.

Full station reports of all investigated engines can be found in Appendix A.4 in Tables A.5 to A.8. The quality of the simulation results with the surrogate model neural network was controlled by comparing the results with the original simulation model. The results are summarised in Tables A.9 to A.12. The deviation for the four-stroke piston engine neural network are mostly below 0.25 %. Only the power at altitude is over-predicted by about 1 %. The deviations for the two-stroke neural network are generally below 0.06 % and often below 0.02 %. The quality is highly improved compared to the four-stroke engine as the networks were generated for a smaller parametric space. This shows that neural networks can successfully be used as surrogate models for piston engine simulation to cut computational time.

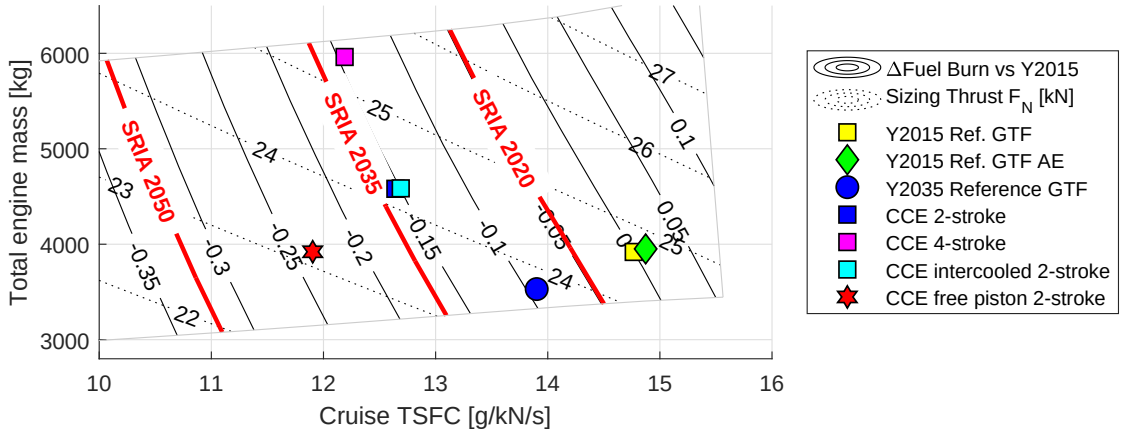

Figure 5.12: Changes in fuel burn and sizing thrust F_N for the CCE concepts and GTF engines.

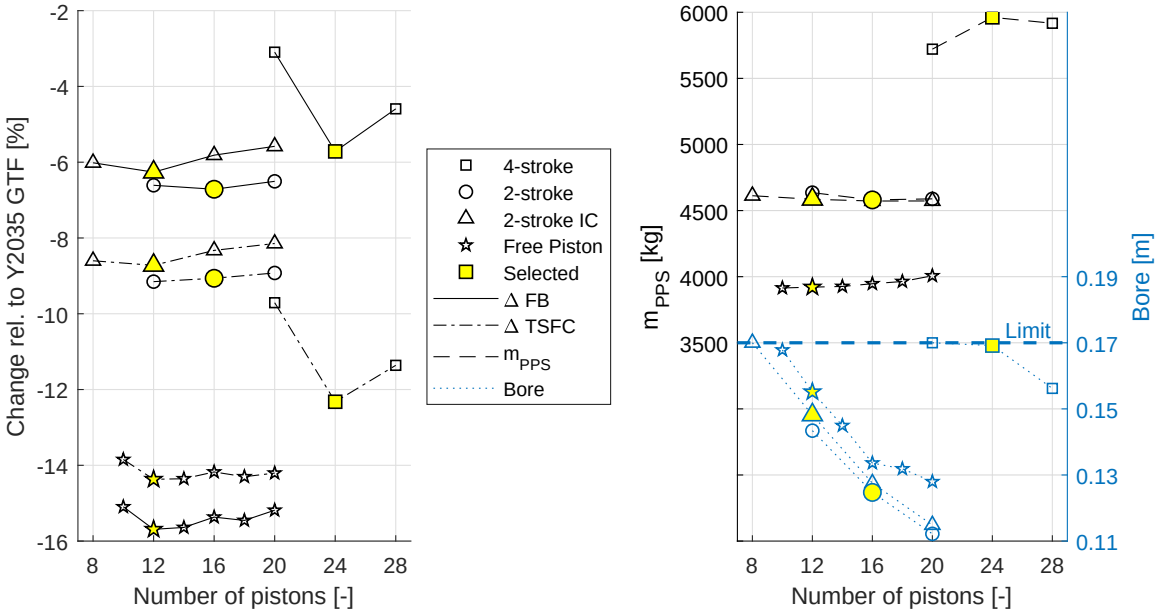

Figure 5.13: Changes in fuel burn FB, TSFC (left), PPS mass m_{PPS} and bore (right) of the investigated CCE concepts when varying number of cylinders.

The comparison of all concepts with a variation of the number of pistons is displayed in Figure 5.13. Changes in TSFC and fuel burn are displayed in the left graph. The four-stroke engine's improvement in TSFC has a very large penalty due to engine mass compared to the other concepts. The fuel burn improvement of the free-piston CCE is higher than the TSFC improvement due to cascading effects on aircraft level. On the right chart, engine mass and bore are displayed. The two-stroke and the intercooled version have a very similar weight. In the lines of the four-stroke CCE and the free-piston CCE, a kink appears where the bore hits the limit of 0.17 m. Smaller kinks in the lines can originate from discrete steps in stage counts or stage material choice.

The estimated NO_x emissions for the four concepts are illustrated in Figure 5.14 (p. 113) against SRIA targets. Uncertainty due to the emission modelling methods as well as the

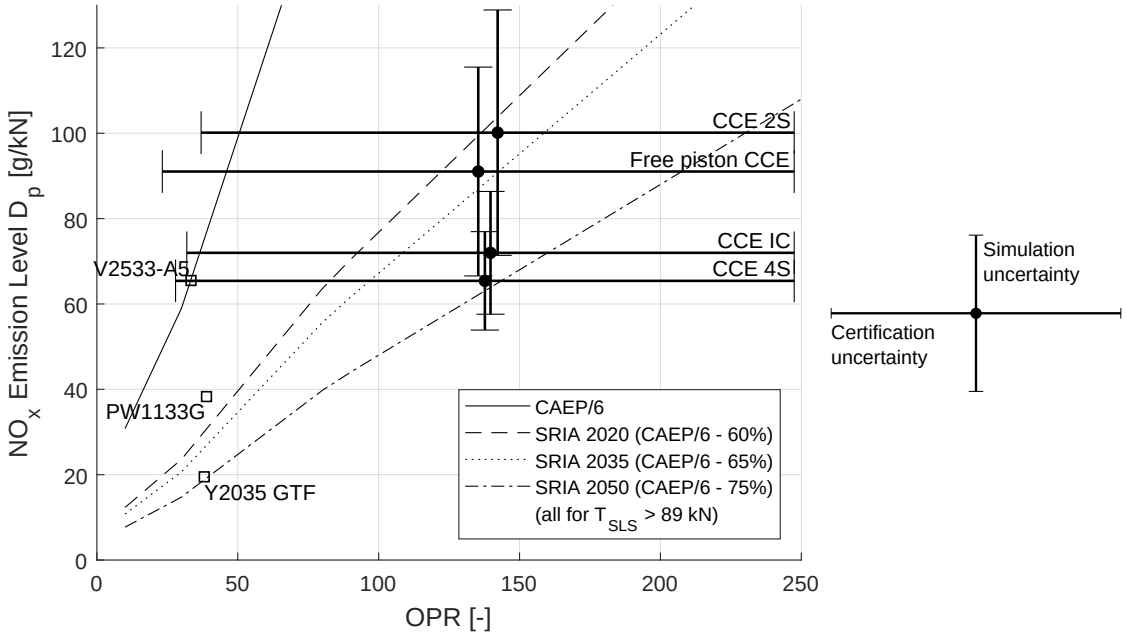

Figure 5.14: CCE NO_x emission levels in LTO cycle with respect to emission reduction targets.

applicable certification pressure ratio is displayed. Using steady turbo pressure ratio corresponds to the left end of the area, while using peak pressure ratio corresponds to the right end. The turbo pressure ratio is lower than the OPR of the GTF.

The four-stroke CCE achieves the lowest emissions D_p. It is, however, about three times as high as the year 2035 GTF, and about 50 % higher than that of the SoA GTF. A reference pressure ratio of about 100 would need to be applied to comply with SRIA 2035 targets. The intercooled and the free-piston CCE follow with higher emission levels. To comply with SRIA 2035 certification targets, reference pressure ratios of 110 and 140 would need to be applied. The uncooled two-stroke engine has the highest emissions and would require a reference pressure ratio of 160. Considering that the current certification permits higher NO_x emissions in more efficient engines, the use of turbo pressure ratio as reference appears inappropriate. Using the mean pressure in the piston for reference pressure ratio calculation would provide challenging yet realistic NO_x emission targets.

High charging is required in the CCE concept to achieve small enough piston engines. This leads to high mean effective pressures p_{mean} in the range of 25 bar to 40 bar as shown in Figure 5.15 (p. 114). Within the database of built piston engines introduced in Section 4.3, only race cars achieve p_{mean} above 30 bar. Top fuel engines used in drag racing go beyond 100 bar. Marine diesel engines have a charging boost of about 5 bar and achieve p_{mean} of about 25 bar in four-stroke engines and 20 bar in two-stroke engines.

The required p_{mean} is achieved with much higher charging than usual in piston engine applications, which typically top out at a pressure ratio of approximately 5.0 achieved in a single stage radial compressor. The challenge lies in sustaining the mean effective pressure at high reliability and lifetimes. The power per displacement volume P/V_{d} exhibits a similar

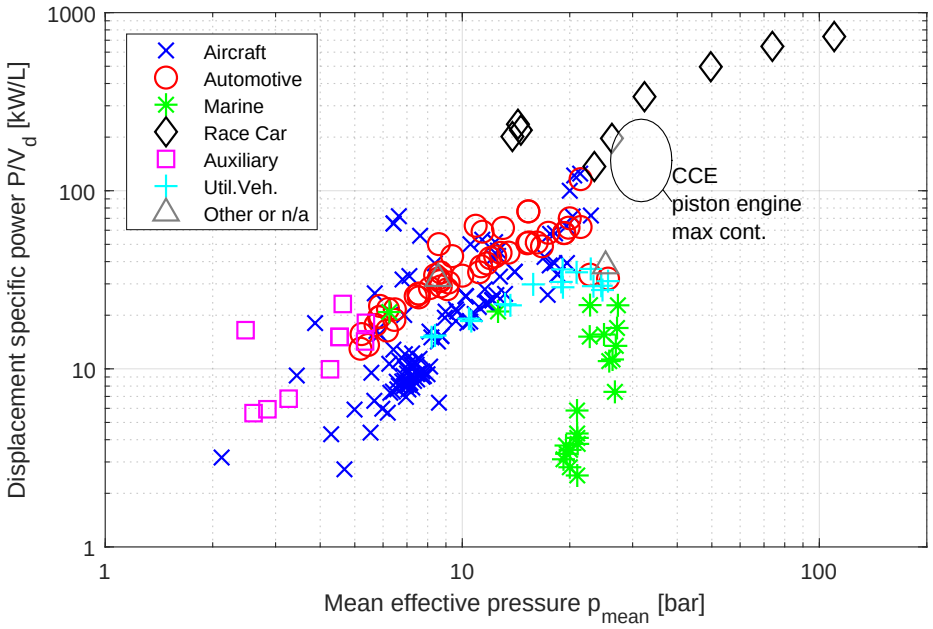

Figure 5.15: Displacement volume specific power over mean effective pressure p_{mean} categorised by engine application.

result due to charging. Marine piston engines fall short of other engines due to very low rotational speeds n despite high p_{mean}. The aeronautical piston engines coming closest to the specified target are the rotary engine SuperTec KKM 504d [254] and the modern diesel engine DieselJet CR 2.0 16V [255] both having a p_{mean} of about 20 bar. This shows that modern aeronautical piston engine designs clearly outperform historical piston engines, which had a p_{mean} of about 10 bar.

A similar trend can be read from Figure A.3 (p. 146) (see Appendix A.4) that shows power per volume flow over power per piston area. The power per volume flow expresses the utilisation of the available displacement volume V_{d} and rotational speed n. The CCE piston engine achieves values of the order of turbo-charged race cars. The resulting power per piston area is 1.5 to 3 times as high as values achieved today in marine long-stroke diesel engines at 1 kW/cm^2. This limit has been highlighted by another study about CCEs [256]. If the specified target cannot be achieved, more pistons with higher displacement volume and engine mass are required with adverse effects on fuel burn. To date, only race car engines in the database achieve such values. Consequently, piston durability at such high loads is a critical technological target.

The piston engine mass m is a pivotal factor in the benchmarking of the CCE. To compare the results with piston masses from the database meaningfully[5], they are displayed relative to maximum continuous power P and displacement volume V_{d}, respectively, in Figure 5.16 (p. 115). Aeronautical piston engines achieve a volume-specific mass about a full order of magnitude lower than automotive or marine engines. This shows the potential of light-

[5]Note that the numbers are subject to uncertainty as some components are not always included in the mass balance, such as gearings or coolers for manifold air, coolant and lubricant.

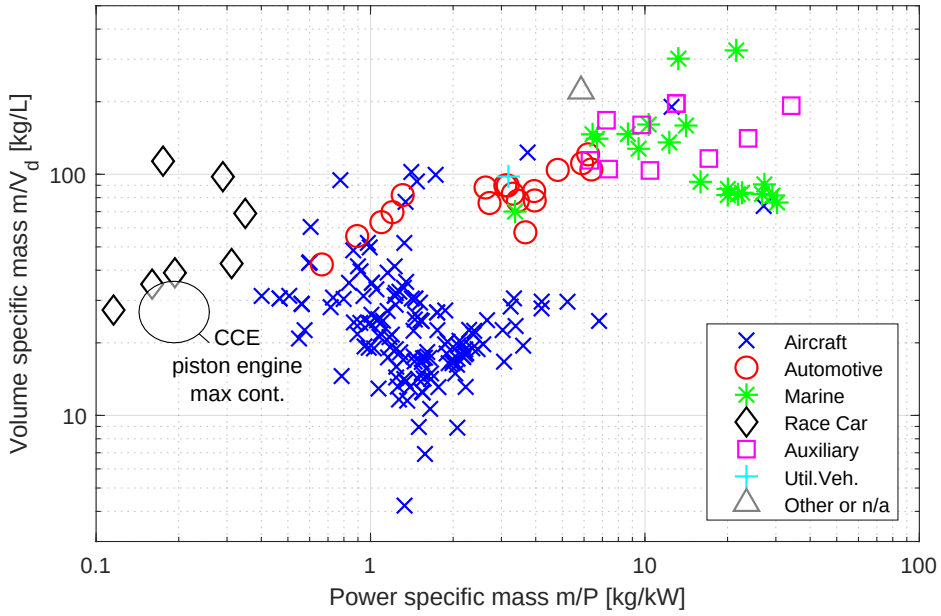

Figure 5.16: Displacement volume specific engine mass over power specific engine mass categorised by engine application.

weight piston engine designs. Even race car engines have higher volume-specific masses. However, race car engines achieve the lowest power-specific mass, followed by automotive and aeronautical engines, which have similar values.

The piston engine in the CCE has a power-specific mass of the order of race car engines of 0.15 kg/kW to 0.25 kg/kW with respect to estimated continuous power[6]. Quoted CCE piston engine mass here is systematically lower as it refers to the pure piston engine, while the masses in the database refer to full engine masses, including turbochargers, gears, and auxiliaries such as fuel and coolant pumps. The aeronautical engine with the closest power-specific mass is the turbo-compound Rolls-Royce Crecy with 0.40 kg/kW [23]. The high charging pressure in the CCE concept must not lead to an over-proportionate increase in mass. The volume-specific mass of 20 kg/L to 30 kg/L is not very ambitious when comparing to the bulk of aeronautical engines, but it needs to be maintained at much higher p_{mean}.

To conclude, some performance parameters of the CCE piston engine are beyond typical values that can be found in series piston engines. This is a result of a lack of comparable piston engine designs rather than proof that the applied loads are too high. In some respects, such as volume-specific mass, they are modest. The simultaneous achievement of high power density, relatively light-weight design, and a high lifetime appears to be most critical.

[6]Continuous power was estimated to be 83 % of the TO power derived on database values. The ratio of brake to indicated mean effective pressure was set to 0.95, to account for the piston engine mechanical efficiency.

5.3 Technology Road Mapping

Technological maturity is typically expressed with technology readiness level (TRL) [257]. The typical time to maturity for engine technology being at TRL 2 today is in the range of 10 to 20 years [214]. The CCE can be expected at the top end of the range as the involved complexity is high. The systems used in the CCE concept are of high TRL today and widely used in the aeronautical, automotive, marine, locomotive and energy industries. The main challenges lie in the simultaneous realisation of assumed component limits and the system integration of turbo and piston components.

For the CCE components, the piston system is the most challenging part of the power plant. The assumed technical parameters are in the range of today's feasibility when looking at mean piston velocity, peak pressure, wall temperatures and compression ratio. These need to be realised on a light-weight design at high loads. It needs to sustain the conditions for the typical operating cycles until overhaul of the order of 10 000 h to be competitive with turbofan engines. With regards to liner life of at least 10 000 h, the mean piston speed appears feasible with current technology level and a liner temperature of 500 K [23]. Higher piston speeds reduce liner life exponentially. The flameless combustor operates under pulsation with vitiated air, and higher inlet temperatures. Main challenges here are combustion stability and combustor cooling. For the adjacent turbo components, i.e. IPC exit and HPT inlet, the oscillating boundary conditions may impair surge margin or efficiency. The presented simple approximations suggest that no significant penalty may be expected. Higher fidelity investigations with circumferential resolution of the boundary conditions need to verify this. The piston cooling system's heat sink needs to handle megawatts compared to hundreds of kilowatts today for planetary gearbox cooling.

A TRL maturation road map is presented in Figure 5.17 (p. 117). The current TRL of the CCE is 2, with the concept and the application being formulated. Further development steps should include:

- TRL 2: Estimate manufacturing and maintenance cost to evaluate commercial viability.
- TRL 3: Elaborate critical piston engine characteristics. Prove operation of turbomachinery with pulsating boundary conditions with satisfactory efficiency and mechanical durability on lab scale. Detail piston engine design with components and subsystems with high-fidelity analytical methods with emphasis on structures, thermals, dynamic behaviour, and light-weight design. Test a scaled, charged single cylinder piston engine on lab scale to verify performance predictions and viability of component limits.
- TRL 4: Operate a scaled core engine with a small number of pistons coupled to a scaled HPC to validate integrated operational behaviour. Operate power turbine downstream of core engine to validate high-level requirements. Run fully designed engine with subsystems on lab scale. Validate complete piston cooling system with piston as heat source and bypass as heat sink. Show endurance capabilities. Validate combustor stability and cooling.

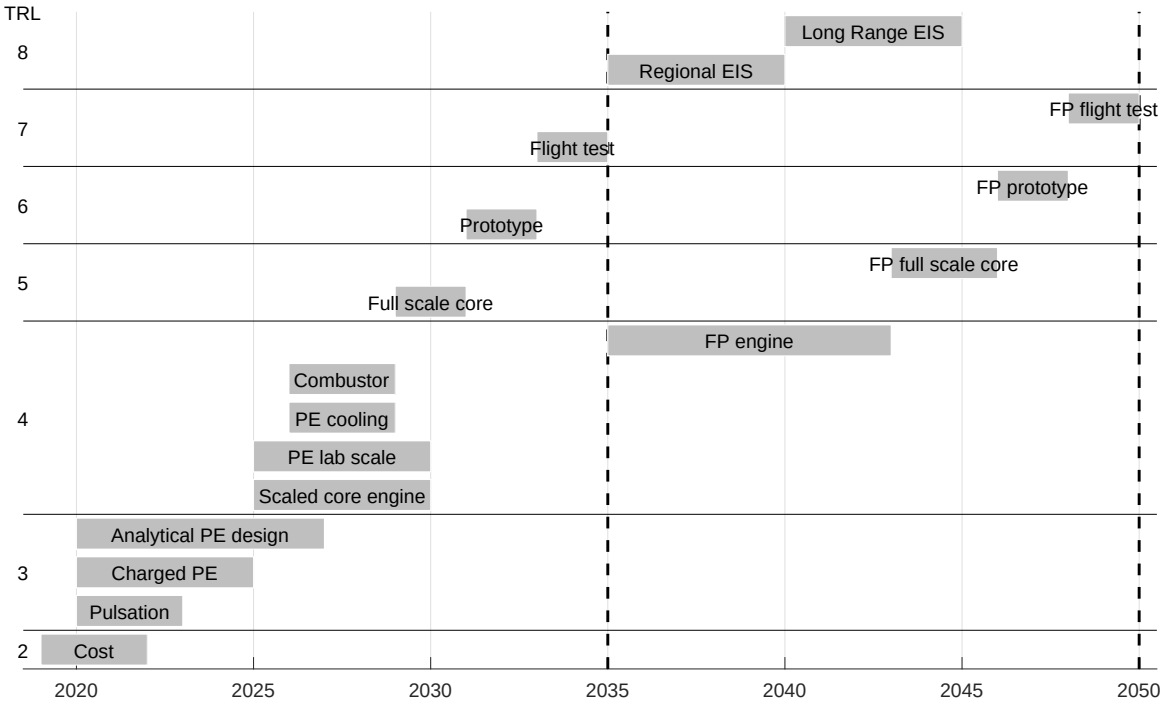

Figure 5.17: CCE TRL maturation road map.

- TRL 5: Validate a full-scale core with relevant operating conditions. Demonstrate predicted performance in a lab environment. Show operability with interaction of piston engine, buffering volume, combustion chamber and turbomachinery with respect to pulsation, vibration and transient behaviour. Demonstrate appropriate sizing of mounts for dynamic loads.
- TRL 6: Build and test full engine prototype for ground testing and autonomous operation of the full assembly. Demonstrate endurance and achievement of performance targets.
- TRL 7: In-flight testing of a prototype for flight envelope validation of engine.

From a technology maturation perspective, a regional or short-range application would permit to implement the piston engine on a less demanding and less costly platform. Since small turbofan engines operate on comparably low pressure ratios and turbo component efficiencies, the improvement potential through piston engines is still given. Entry into service on a regional platform in 2035 could later be followed by a long-range application. From a market segment perspective, the characteristics of the CCE favour a long-range application as the CCE has higher fuel burn improvement potential here. The cascading effects for efficiency are higher, while the penalties for engine mass are lower. Moreover, fuel cost forms a higher share of the cash operating cost on long-range applications.

FP development would need to start 10 to 15 years later to achieve an EIS year 2050. Additional research on low TRL is required to gain a better understanding of specific technical issues. Engine development and validation is certainly the greatest challenge in this concept.

Free-piston control and operation must be ensured in every point of the operating envelope. Air lubrication is a critical technology that is mandatory to fully utilise the benefits of a free-piston engine. The dual piston cooling system with air cooling to the core and liquid cooling to the bypass needs to be developed. Full engine prototyping and flight testing should be less complicated with the experience from the previous CCEs.

To conclude, the technical complexity of the integrated system suggests a higher than average but not excessive time to maturity. Therefore, an EIS may be realised around the year 2035, provided a high market incentive (mainly a high share of fuel in the cash operating costs) and support by policymakers. Engine manufacturers need to gather the know-how for design, operability, manufacture and certification.

Chapter 6

Conclusion and Outlook

Conclusion

This thesis presented methods for comprehensive analysis of a promising aero-engine that is based on the Joule-/Brayton-cycle and uses a closed volume topping cycle to improve thermal efficiency: the *Composite Cycle Engine*. The presented concept comprises a conventional turbofan architecture that has a piston engine operating in its high-pressure core. Piston engine performance modelling and integration into a comprehensive aero-engine simulation environment were shown. The Composite Cycle Engine architecture induces major changes to the core engine, which cannot be benchmarked by thermal efficiency only. Therefore, detailed methods for engine mass, size and NO_x emissions were presented. These were applied in the most important engine operating points at top of climb for sizing, take-off for maximum mechanical limits, and cruise for efficiency. The methods enable a comprehensive, multidisciplinary assessment of the proposed engine architecture with respect to its viability to meet the challenging future efficiency targets.

The herein conducted studies showed that the Composite Cycle Engine concept does not inherently achieve double-digit fuel burn improvement over a turbofan of similar technology level. Although thermal efficiency is higher, the added mass of the piston engine needs to be compensated for. Therefore, conceptual design options for engine architecture and piston design characteristics were presented, discussed and evaluated. The final engine architecture was selected based on the most promising technical viability. It features a piston engine driving an axial-radial compressor on the high-pressure spool, and a single turbine driving intermediate pressure compressor and fan on the low-pressure spool. A secondary combustor before the turbine augments core engine power. The piston engine is arranged in two V-motors around the engine rotational axis. It is connected to the high pressure compressor via a two-stage spur gear.

The chosen engine design was then evaluated on a short-to-medium range aircraft platform for overall efficiency, size, mass, fuel burn and NO_x emissions against a projected year 2035 geared turbofan engine. A four-stroke 24-cylinder piston engine was shown to improve specific fuel consumption by 12.3 %. While engine mass increases by 68.9 %, fuel burn still improves

by 5.7 %. The overall pressure ratio is 29 and combustor exit temperature is 1397 K at take-off conditions. Most fuel is burned in the piston engine, leading to high thermal efficiency. The efficiency improvement against a turbofan increases in part load to 20 %. Hence, the economically optimum cruise speed and altitude will be lower than with a turbofan. A technology sensitivity study revealed that the expected bandwidth of critical technology assumptions is of the order of the predicted fuel burn improvement. NO_x emissions are 3 times as high as in the turbofan and 50 % higher than the level of 2015. Mitigation of pressure oscillations to a negligible level is possible with buffering volumes.

Compared to the four-stroke engines, using two-stroke engines with 16 cylinders leads to a reduction of efficiency by 3.7 %, but a mass saving by 23.2 %, resulting in another 1.1 % fuel burn improvement. Overall pressure ratio is higher in this engine, and combustor exit temperature is on a similar level. The temperatures within the piston are higher resulting in 50 % higher NO_x emissions. As mitigation, an intercooler between the turbo compressors could reduce emissions almost to the level of the four-stroke engine. However, this comes at the cost of higher specific fuel consumption and 0.8 % higher fuel burn. Both engines miss the year 2035 carbon dioxide (CO_2) reduction targets, but could close the gap with minor improvements in propulsive efficiency, e.g. by us
ng a larger fan. As a technologically advanced but more challenging option, a free-piston gas generator was shown to decrease both specific fuel consumption and engine mass beyond the level of the two-stroke engine. Fuel burn improves by 9.6 %, allowing to exceed the year 2035 efficiency targets. NO_x emissions are 9 % lower than in the two-stroke engine.

Outlook

The innovation of a new technology relies on three factors according to design innovation [258]:

Technical feasibility — Business viability — Human desirability

All three must be present to facilitate innovation. This thesis mainly answered questions about the first part – if a Composite Cycle Engine can be built with today's knowledge and design methods. Business viability is partially addressed by assessing fuel burn and mass, which indicate the impact on operating and manufacturing cost. The impact on the airlines business model was not discussed in this thesis. It would be less prone to fuel price fluctuations but might require a more resilient network to cater for more frequent maintenance. Airframers would need to design for higher engine and lower fuel mass. Engine manufacturers would need to handle a high development risk. The third point, human desirability, addresses not only a potentially lower ticket price but also perceived passenger comfort and trust in the engine. The perceived environmental impact could be vital. Lower emissions in CO_2 may be appealing, but emissions in NO_x or noise should receive appropriate attention.

Independent from its architecture, the piston engine offers considerable room for exploration and potential improvement. One option was shown with the free-piston design. Many others were not scrutinised, such as opposing piston engines, radial engines, or swash plates. Parameters chosen fixed within this thesis could be altered and optimised, such as valve timings

and kinematics, heat release characteristics, and piston kinematics. For example, variable compression ratio may improve efficiency in cruise, while reducing peak pressures during take-off. Another architectural option is the use of piston compressors on the high-pressure spool coupled to the piston engine. Although piston mass and size increase tremendously, lower gearing losses and higher compression efficiency could eventually result in lower fuel burn.

The presented set of methods allows implementation and investigation of such configurations. A major improvement potential lies in the improved utilisation of the piston engine heat losses. A concept that would utilise these within the core engine cycle, could replenish a major share of the order of 5 % to 10 % of the fuel heat and improve engine efficiency by the same amount. One way to achieve this was shown with the free-piston engine. Another way could be the use of a secondary heat pump cycle. This cycle could elevate the temperature level of the piston engine cooling fluid to a level that would enable heat dissipation to the core fluid.

The chosen piston engine specifications are ambitious but have the potential to be exceeded in a high-end aeronautical application. To identify if margins are available, the following disciplines need to be detailed and investigated: structural design of crankshaft, piston, and cylinder, masses, materials, life estimation with realistic load collectives, lubrication, valve actuation, and piston cooling. The entirety of these disciplines determines whether single component limits specified in this thesis are viable. Particularly the high piston area specific power appears critical.

On engine integrated level, dynamic loads, vibrations, noise, and engine accessories need to be detailed further. Turbo components need to be shown to operate under mechanical and aerodynamic oscillations without impairments to efficiency, surge margin, and component life. The foreseen buffering volumes need to mitigate temporal and spatial oscillations for the engine. Elaboration of the secondary air system needs to prove that all components can be cooled appropriately, specifically the secondary combustor with high entry temperatures. This combustor needs to be shown to operate under lean conditions with vitiated air.

Bibliography

[1] *Strategic Research & Innovation Agenda – Volume 1*. Tech. rep. Advisory Council for Aviation Research and Innovation in Europe (ACARE), Sept. 2012.

[2] Christopher Hughes, Dale Van Zante and James Heidmann. "Aircraft Engine Technology for Green Aviation to Reduce Fuel Burn". In: *3rd AIAA Atmospheric Space Environments Conference*. Honolulu, Hawaii: American Institute of Aeronautics and Astronautics, June 2011. DOI: 10.2514/6.2011-3531.

[3] *International Standards and Recommended Practices - Annex 16 - Environmental Protection - Volume III - CO2 Certification Requirement*. Draft International Standard. International Civil Aviation Organization (ICAO), 2014.

[4] *Pratt & Whitney – PurePower – Family of Engines*. Brochure. East Hartford, Connecticut: Pratt & Whitney, 2015. URL: http://newsroom.pw.utc.com/download/PurePowerFamily-S16154.pdf.

[5] *LEAP – The Power of the Future*. Brochure. Cincinnati, Ohio: CFM International, 2017. URL: https://www.cfmaeroengines.com/wp-content/uploads/2017/09/Brochure_LEAPfiches_2017.pdf.

[6] Silke Hansen. "Saving fuel is in - Sustainability in aviation: an overview". In: *AEROREPORT*. Ed. by Eckhard Zanger. 02I16. Munich, Germany: MTU Aero Engines, 2016, pp. 22–23.

[7] J. Sieber. *Triebwerkstechnologien für den zukünftigen Luftverkehr*. Presentation. Washington, D.C.: MTU Aero Engines, June 2010.

[8] R. Martens. *Das Technologieprogramm CLAIRE der MTU Aero Engines*. Presentation. MTU Aero Engines, July 2007.

[9] A. Epstein. *Engines for Green Aviation's Future*. Presentation. Salzburg, Austria: Pratt & Whitney, Oct. 2010.

[10] F. Haselbach, A. Newby and R. Parker. "Concepts & Technologies for the Next Generation of Large Civil Aircraft Engines". In: *29th Congress of the International Council of the Aeronautical Sciences*. St. Petersburg, Russia, Sept. 2014.

[11] Rob Mitchell and Mike Whitehead. "The Rolls-Royce UltraFan Engine® – Delivering the Next Generation of Aerospace Propulsion System". In: *23rd International Symposium of Air Breathing Engines*. ISABE-2017-22511. Manchester, UK, Sept. 2017.

[12] David Joyce. *GE Investor Meeting at the Paris Air Show*. Presentation. Paris, France: GE Aviation, June 2017.

[13] Jörg Sieber and Edgar Merkl. "Low Pressure System Technologies for Ultra High Bypass Ratio Engines". In: *23rd International Symposium of Air Breathing Engines*. ISABE-2017-21392. Manchester, UK, Sept. 2017.

[14] Jörg Sieber. "European Technology Programs for Eco-Efficient Ducted Turbofans". In: *22nd International Symposium of Air Breathing Engines*. ISABE-2015-20029. Phoenix, Arizona, Sept. 2015.

[15] J. E. Johnson. "Advanced Aero-Engine Concepts and Controls". In: *AGARD Conference Proceedings 572*. Advisory Group for Aerospace Research and Development. Hull, Canada: North Atlantic Treaty Organization, June 1996.

[16] Sascha Kaiser et al. "Composite Cycle Engine Concept with Hectopressure Ratio". In: *Journal of Propulsion and Power* 32.6 (2016), pp. 1413–1421. DOI: 10.2514/1.B35976.

[17] Sascha Kaiser et al. "Unified Thermodynamic Evaluation of Radical Aero Engine Cycles". In: *Proceedings of the ASME Turbo Expo 2016*. GT2016-56313. Seoul, South Korea, June 2016. DOI: 10.1115/GT2016-56313.

[18] Ralf von der Bank et al. "Advances in Ultra-High Pressure Ratio Core-Engines". In: *65. Deutscher Luft- und Raumfahrtkongress*. DLRK2016-420006. Sept. 2016.

[19] Oliver Schmitz. "Methodical Assessment of Electric Propulsion Systems for Transport Category Aircraft". Dissertation. Munich, Germany: TU Munich, 2016.

[20] Konstantinos G. Kyprianidis and Andrew M. Rolt. "On the Optimization of a Geared Fan Intercooled Core Engine Design". In: *Journal of Engineering for Gas Turbines and Power* 137.4 (2015). DOI: 10.1115/1.4028544.

[21] *A Flying Machine that Flies a Little*. News Paper Article Friday Evening, July 26, 1901. Minneapolis, Minnesota: The Minneapolis Journal, July 1901.

[22] C. F. Taylor. "Aircraft Propulsion – A Review of the Evolution of Aircraft Piston Engines". In: *Smithsonian Annals of Flight*. Vol. 1. 4. Washington: Smithsonian Institution – National Air and Space Museum, 1971.

[23] J. Castor, J. Martin and C. Bradley. *Compound Cycle Engine for Helicopter Application*. Tech. rep. NASA CR-180824. Phoenix, Arizona: Garrett Turbine Engine Company, Sept. 1987.

[24] H. Sammons and E. Chatterton. *Napier Nomad Aircraft Diesel Engine*. SAE Technical Paper 550239. SAE International, 1955. DOI: 10.4271/550239.

[25] Victor Kotelnikov. *Russian Piston Aero Engines*. The Crowood Press, 2005. ISBN: 9781861267023.

[26] Paul H. Wilkinson. *Aircraft Engines of the World 1966/67*. Washington, D.C.: Paul H. Wilkinson, 1967.

[27] M. Daly. *Jane's Aero Engines 2013/2014*. Coulsdon, England, U.K: Jane's Information Group, 2013.

[28] *M350 – Specifications – Pricing*. Brochure. Vero Beach, Florida: Piper Aircraft, Inc., 2018.

[29] *Introducing the 2018 M500*. Brochure. Vero Beach, Florida: Piper Aircraft, Inc., 2018.

[30] *Getting to Grips with ETOPS*. Tech. rep. Blagnac Cedex, France: Airbus S.A.S., Oct. 1998.

[31] C. Ekstrand and M. Pandey. "New ETOPS Regulations". In: *Boeing Aero*. Ed. by S. Szehner. 22. Seattle, Washington: The Boeing Company, Apr. 2003, pp. 3–11.

[32] *CAP 513 – Extended Range Twin Operations (ETOPS)*. Tech. rep. Cheltenham, UK: Civil Aviation Authority – Safety Regulation Group, Oct. 2002.

[33] H. Soekkha. *Aviation Safety: Human Factors, System Engineering, Flight Operations, Economics, Strategies & Management*. Rotterdam, The Netherlands: CRC Press, 1997. ISBN: 9067642584.

[34] *Accidents Involving Engine Failure/Malfunction US General Aviation*. Special Study NTSB-AAS-72-10. Washington, D.C.: National Transportation Safety Board, Nov. 1972.

[35] *Supplementary Techniques – Handling Engine Malfunctions*. Flight Operations Briefing Notes. Blagnac Cedex, France: Airbus S.A.S., Dec. 2006.

[36] Franklin D. Harris, Eugene F. Kasper and Laura E. Iseler. *U.S. Civil Rotorcraft Accidents, 1963 Through 1997*. Tech. rep. NASA TM-2000-209597. Moffett Field, California: NASA Ames Research Center, Dec. 2000.

[37] Bill Gunston, ed. *The Illustrated Encyclopedia of Propeller Airliners*. 1st. London, UK: Phoebus Publishing, 1980.

[38] R. Singh, G. Amayugo and F. Noppel. "Innovation in Aeronautics". In: ed. by T. Young and M. Hirst. 1st. Oxford, UK: Woodhead Publishing, 2012. Chap. Jet Engine Design Drivers: Past, Present and Future, pp. 56–82. ISBN: 978-0-85709-609-8.

[39] M. Schmidt. "Ground-Operational Assessment of Novel Aircraft Cabin Configurations". Dissertation. Munich, Germany: TU Munich, 2018.

[40] *BP Statistical Review of World Energy*. Tech. rep. 67. Sunbury on Thames, Middlesex: BP plc, June 2018.

[41] S. Arif Khalid et al. *FAA CLEEN Program - Open Rotor Engine Aeroacoustic Technology Final Report*. Research rep. DOT/FAA/AEE/2014-03. Evendale, OH: General Electric, May 2013.

[42] *Whatever happened to propfans?* news article. Flight International, June 2007. URL: https://www.flightglobal.com/news/articles/whatever-happened-to-propfans-214520/.

[43] Jean-François Brouckaert et al. "Clean Sky research and demonstration programmes for next-generation aircraft engines". In: *The Aeronautical Journal* 122.1254 (July 2018), pp. 1163–1175. DOI: 10.1017/aer.2018.37.

[44] *Skyline – Show Time: Demonstrators in the Sky*. Brochure 15. Brussels, Belgium: Clean Sky Joined Undertaking, Mar. 2015.

[45] *MAN B&W S90ME-C9.2-TII*. Project Guide. Copenhagen, Denmark: MAN Diesel & Turbo, Mar. 2012.

[46] J. Bettner, C. Blandford and B. Rezy. *Propulsion System Assessment for Very High Altitude UAV Under ERAST*. Tech. rep. NASA CR-195469. Indianapolis, Indiana: Allison Engine Company, May 1995.

[47] Habib Aghaali and Hans-Erik Ångström. "A Review of Turbocompounding as a Waste Heat Recovery System for Internal Combustion Engines". In: *Renewable and Sustainable Energy Reviews* 49 (Sept. 2015), pp. 813–824. DOI: 10.1016/j.rser.2015.04.144.

[48] *Facts about the Wright Turbo Compound*. Tech. rep. Wood-Ridge, New Jersey: Curtiss-Wright Corporation, Wright Aeronautical Division, Oct. 1956.

[49] M. A. Smith. "Napier Nomad – An Engine of Outstanding Efficiency". In: *Flight and Aircraft Engineer*. Vol. 65. 2362. London, UK: Flight International, Apr. 1954, pp. 543–551.

[50] Larry Dwyer. *Wright R-3350*. Oct. 2013. URL: http://www.aviation-history.com/engines/r3350.htm.

[51] Napier & Son Limited. "Napier Nomad – The World's Finest Composite Aircraft Engine". In: *Flight and Aircraft Engineer*. Vol. 60. 2227. London, UK, Sept. 1951, p. 9.

[52] R. E. Wilkinson and R. B. Benway. "Liquid Cooled Turbocharged Propulsion System for HALE Application". In: *Volume 2: Aircraft Engine; Marine; Microturbines and Small Turbomachinery*. ASME, June 1991. DOI: 10.1115/91-gt-399.

[53] Luca Piancastelli et al. "High Altitude Operations with Piston Engines Power Plant Design Optimization, Turbo-Charging, Turbo Matching, Efficiency and Serial Arrangement Optimization". In: *ARPN Journal of Engineering and Applied Sciences* 11.7 (Apr. 2016), pp. 4333–4345. ISSN: 1819-6608.

[54] Andrzej Jeziorski. "High and Dry – The German Government's Unexpected Withdrawal of Funding Could Kill a Unique High-Altitude Aircraft". In: *Flight International*. Vol. 149. 4508. Sutton, UK: Reed Business Publishing, Jan. 1996, pp. 66–67.

[55] D. Bents et al. *Propulsion Selection for 85kft Remotely Piloted Atmospheric Science Aircraft*. Tech. rep. NASA TM-107302. Cleveland, Ohio: Lewis Research Center, July 1996.

[56] M. Brands, J. Werner and J. Hohne. *Vehicle Testing of Cummins Turbocompound Diesel Engine*. Tech. rep. NASA CR-159840. Columbus, Indiana: Cummins Engine Company, June 1980.

[57] J. Hoehne and J. Werner. *The Cummins Advanced Turbocompound Diesel Engine Evaluation*. Tech. rep. NASA CR-168042. Columbus, Indiana: Cummins Engine Company, Dec. 1982.

[58] P. Eilts. “Investigation of Engine Processes with Extreme Pressures and Turbocompounding”. In: *SAE Technical Paper Series*. 2016-01-0567. SAE International, Apr. 2016. DOI: 10.4271/2016-01-0567.

[59] P. Eilts and J. Friedrichs. “Investigation of a Diesel Engine for Aircraft Application”. In: *53rd AIAA/SAE/ASEE Joint Propulsion Conference*. Atlanta, GA: American Institute of Aeronautics and Astronautics, July 2017. DOI: 10.2514/6.2017-4792.

[60] Felix Klein and Stephan Staudacher. “Plausibility Study of Hecto Pressure Ratio Concepts in Large Civil Aero Engines”. In: *ASME Turbo Expo 2017: Turbomachinery Technical Conference and Exposition – Volume 1: Aircraft Engine; Fans and Blowers; Marine; Honors and Awards*. ASME, June 2017. DOI: 10.1115/gt2017-64214.

[61] John Whurr. *Aircraft Compound Cycle Propulsion Engine*. U.S. pat. US patent 5,692,372. London, England, Dec. 1997.

[62] P. Meng, W. Hady and R. Barrows. *An Overview of the NASA Rotary Engine Research Program*. Tech. rep. NASA TM-83699. Cleveland, Ohio: Nasa Lewis Research Center, Aug. 1984.

[63] C. Vilmann. *Deformation Analysis of Rotary Combustion Engine Housings*. Tech. rep. NASA-CR-188187. Houghton, Michigan: Michigan Technological University, 1991.

[64] Ritsuharu Shimizu et al. “Mazda 4-Rotor Rotary Engine for the Le Mans 24-Hour Endurance Race”. In: *SAE Technical Paper Series*. 920309. SAE International, Feb. 1992. DOI: 10.4271/920309.

[65] H. P. Berg et al. “Turbowankel-Triebwerks-Familien - Neuartige Antriebskonzepte fuer die Allgemeine Luftfahrt der Zukunft”. In: *Deutscher Luft- und Raumfahrtkongress 2015*. Rostock, Germany, Sept. 2015.

[66] M. Nickl and S. Kaiser. “Evaluation of Piston Engine Modes and Configurations in Composite Cycle Engine Architectures”. In: *6th CEAS Conference*. 867. Bucharest, Romania, Oct. 2017.

[67] M. Picard, T. Tian and T. Nishino. “Predicting Gas Leakage in the Rotary Engine – Part I: Apex and Corner Seals”. In: *Journal of Engineering for Gas Turbines and Power* 138 (June 2016), pp. 062503-1–8. DOI: 10.1115/1.4031873.

[68] M. Picard, T. Tian and T. Nishino. “Predicting Gas Leakage in the Rotary Engine – Part II: Side Seals and Summary”. In: *Journal of Engineering for Gas Turbines and Power* 138 (June 2016), pp. 062503-1–8. DOI: 10.1115/1.4031874.

[69] John Whurr. “Otto Cycle Core Turbofan Concepts”. MA thesis. Cranfield University, Mar. 1995.

[70] Markus Nickl et al. “Performance Modeling of a Composite Cycle Engine with Rotary Engine”. In: *Deutscher Luft- und Raumfahrtkongress 2016*. Braunschweig, Germany, Sept. 2016.

[71] Daniele Littera et al. “Development of the XMv3 High Efficiency Cycloidal Engine”. In: *JSAE/SAE 2015 Small Engine Technologies Conference & Exhibition*. 2015.

[72] G. D. Roy et al. “Pulse Detonation Propulsion: Challenges, Current Status and Future Perspective”. In: *Progress in Energy and Combustion Science* 30.6 (Jan. 2004), pp. 545–672. DOI: 10.1016/j.pecs.2004.05.001.

[73] Dale Van Zante, Edmane Envia and Mark G. Turner. *The Attenuation of a Detonation Wave by an Aircraft Engine Axial Turbine Stage*. Tech. rep. NASA TM-2007-214972. Cleveland, Ohio: Nasa Glenn Research Center, Sept. 2007.

[74] C. Xisto et al. “The Efficiency of a Pulsed Detonation Combustor-Axial Turbine Integration”. In: *Aerospace Science and Technology* (2018).

[75] C. Xisto et al. “Analytical Model for the Performance Estimation of Pre-Cooled Pulse Detonation Turbofan Engines”. In: *ASME Turbo Expo 2017*. GT2017-63776. Charlotte, NC: ASME, June 2017. DOI: 10.1115/GT2017-63776.

[76] Scott M. Jones and Gerard E. Welch. *Performance Benefits for Wave Rotor-Topped Gas Turbine Engines*. Tech. rep. NASA TM X-2406. Cleveland, Ohio: University of Toledo, Dec. 1996.

[77] Gerard E. Welch et al. *Wave-Rotor-Enhanced Gas Turbine Engine Demonstrator*. Tech. rep. NASA TM-1999-209459. Cleveland, Ohio: Nasa Glenn Research Center, Oct. 1999.

[78] P. Akbari, R. Nalim and N. Mueller. “A Review of Wave Rotor Technology and Applications”. In: *Journal of Engineering for Gas Turbines and Power* 128.4 (Jan. 2006), pp. 717–735. DOI: 10.1115/1.2204628.

[79] Patrick C. Vratny. “Conceptual Design Methods of Electric Power Architectures for Hybrid Energy Aircraft”. Dissertation. Munich, Germany: TU Munich, 2019.

[80] Clement Pornet. “Conceptual Design Methods for Sizing and Performance of Hybrid-Electric Transport Aircraft”. Dissertation. Munich, Germany: TU Munich, Apr. 2018.

[81] Sascha Kaiser et al. “Investigations of the Synergy of Composite Cycle and Intercooled Recuperation”. In: *The Aeronautical Journal* 122.1252 (June 2018), pp. 869–888. DOI: 10.1017/aer.2018.46.

[82] B. Ketterer et al. *Lithium-Ion Batteries State of the Art and Application Potential in Hybrid-, Plug-In Hybrid- and Electric Vehicles*. Tech. rep. FZKA 7503. Karlsruhe, Germany: Institut für Materialforschung I, Oct. 2009.

[83] Nicholas Cumpsty. *Jet Propulsion - A Simple Guide to the Aerodynamic and Thermodynamic Design and Performance of Jet Engines*. 1st. Cambridge, UK: Cambridge University Press, Cambridge, UK, 2003.

[84] Gordon. *Computer Program for Calculation of Complex Chemical Equilibrium Compositions and Applications - P1 - Analysis*. Tech. rep. RP-1311. NASA, 1994.

[85] Bonnie J. McBride and Sanford Gordon. *Computer Program for Calculation of Complex Chemical Equilibrium Compositions and Applications - II. User Manual and Program Description*. Tech. rep. RP-1311. Cleveland, Ohio: NASA, 1996.

[86] Alexander Burcat and Branko Ruscic. *Third Millennium Ideal Gas and condensed Phase Thermochemical Database for Combustion with Updates from Active Thermochemical Tables*. Tech. rep. ANL-05/20. Argonne, Illinois: Technion – Israel Institute of Technology, Sept. 2005.

[87] Carmen M. Gracia-Salcedo, Theodore A. Brabbs and Bonnie J. McBride. *Experimental Verification of the Thermodynamic Properties for a Jet-A Fuel*. Tech. rep. NASA TR-101475. Cincinnati, Ohio: NASA Lewis Research Center, 1988.

[88] *Handbook of Aviation Fuel Properties*. Tech. rep. Coordinating Research Council, Inc., 1983.

[89] Desmond E. Winterbone. *Advanced Thermodynamics for Engineers*. 1st. Arnold London, 1997.

[90] S. Kaiser. *Introduction to Aircraft Propulsion System Simulation (APSS)*. Internal Report IB-16001. Munich, Germany: Bauhaus Luftfahrt e.V., Aug. 2016.

[91] *MATLAB R2017b*. Comp. software. Natick, Massachusetts: The MathWorks, Inc., 2017.

[92] Joachim Kurzke. *GasTurb 12 – Design and Off-Design Performance of Gas Turbines*. GasTurb GmbH. 2013.

[93] Joachim Kurzke. *GasTurb Details 6 – An Utility for GasTurb*. GasTurb GmbH. Aachen, Germany, 2015.

[94] P. Pilidis. "Digital Simulation of Gas Turbine Performance". PhD thesis. Glasgow, UK: University of Glasgow, Nov. 1983.

[95] Reinhold Schaber. "Numerische Auslegung und Simulation von Gasturbinen". Dissertation. Munich, Germany: TU Munich, 2000.

[96] T. Grönstedt. "Development of Methods for Analysis and Optimization of Complex Jet Engine Systems". PhD thesis. Göteborg, Sweden: Chalmers University of Technology, 2000.

[97] V. A. Pachidis. "Gas Turbine Advanced Performance Simulation". PhD thesis. Cranfield, UK: Cranfield University, Jan. 2006.

[98] K. G. Kyprianidis. "Multi-Disciplinary Conceptual Design of Future Jet Engine Systems". PhD thesis. Cranfield, UK: Cranfield University, Apr. 2010.

[99] H. Grieb. *Projektierung von Turboflugtriebwerken*. 1st. Basel, Switzerland: Springer Basel AG, 2004. DOI: 10.1007/978-3-0348-7938-5.

[100] Philip P. Walsh and Paul Fletcher, eds. *Gas Turbine Performance*. 2nd. Oxford, UK: Blackwell Science Ltd, Mar. 2004. DOI: 10.1002/9780470774533.

[101] *Manual of the ICAO Standard Atmosphere – extended to 80 kilometres*. Tech. rep. Doc 7488. International Civil Aviation Organization (ICAO), 1993.

[102] J. Kurzke. "Performance Modelling Methodology – Efficiency Definitions for Cooled Single and Multistage Turbines". In: *ASME Turbo Expo 2002*. 2002-GT-30497. Amsterdam, Netherlands, June 2002. DOI: 10.1115/GT2002-30497.

[103] Joachim Kurzke. *Compressor and Turbine Maps for Gas Turbine Performance Computer Programs – Issue 3*. GasTurb GmbH. 2013.

[104] Günter P. Merker and Rüdiger Teichmann, eds. *Grundlagen Verbrennungsmotoren – Funktionsweise, Simulation, Messtechnik*. 7th. Springer Vieweg, Wiesbaden, 2014. ISBN: 978-3-658-03195-4. DOI: 10.1007/978-3-658-03195-4.

[105] Günter P. Merker et al. *Simulating Combustion*. 2nd. Springer-Verlag Berlin Heidelberg, 2006. DOI: 10.1007/3-540-30626-9.

[106] G. Merker and M. Gerstle. *Evaluation on Two Stroke Engines Scavenging Models*. SAE Technical Paper 970358. SAE International, 1997. DOI: 10.4271/970358.

[107] Alfred Urlaub. *Verbrennungsmotoren*. 2nd. Springer-Verlag Berlin Heidelberg, 1995. DOI: 10.1007/978-3-642-79114-7.

[108] I. I. Wiebe. *Brennverlauf und Kreisprozess von Verbrennungsmotoren*. VEB Verlag Technik Berlin, 1970.

[109] J. I. Ghojel. "Review of the development and applications of the Wiebe function: A tribute to the contribution of Ivan Wiebe to engine research". In: *International Journal of Engine Research* 11.4 (2010), pp. 297–312. DOI: 10.1243/14680874JER06510.

[110] Michael Gerstle. "Simulation des instationaeren Betriebsverhaltens hochaufgeladener Vier- und Zweitakt-Dieselmotoren". Dissertation. Universität Hannover, 1999.

[111] Eike Jens Wolgast. "Ein Beitrag zur Prozessrechnung an Verbrennungsmotoren unter Berueckichtigung der realen Gaseigenschaften". Dissertation. Helmut-Schmidt-Universität / Universität der Bundeswehr Hamburg, 2014.

[112] F. Zacharias. "Analytische Darstellung der thermodynamischen Eigenschaften von Verbrennungsgasen". Dissertation. TU Berlin, 1966.

[113] Don W. Green and Robert H. Perry, eds. *Perry's Chemical Engineers' Handbook*. 8th. McGraw-Hill New York, 2008.

[114] G. Woschni. "Die Berechnung der Wandverluste und der thermischen Belastung der Bauteile von Dieselmotoren". In: *MTZ – Motortechnische Zeitschrift*. Vol. 31. 12. Stuttgart, Germany: Vieweg Verlag, 1970.

[115] Rudolf Pischinger, Manfred Klell and Theodor Sams. *Thermodynamik der Verbrennungskraftmaschine*. 3rd. Springer-Verlag Wien, 2009. DOI: 10.1007/978-3-211-99277-7.

[116] G. Woschni and W. Spindler. "Heat Transfer With Insulated Combustion Chamber Walls and Its Influence on the Performance of Diesel Engines". In: *Journal of Engineering for Gas Turbines and Power* 110.3 (1988). DOI: 10.1115/1.3240146.

[117] Gerhard Woschni, Benedikt Klaus and Klaus Zeilinger. "Untersuchung des Wärmetransportes zwischen Kolben, Kolbenringen und Zylinderbüchse". In: *MTZ – Motortechnische Zeitschrift*. Vol. 59. 9. Springer Fachmedien Wiesbaden, 1998, pp. 556–563. DOI: 10.1007/bf03251379.

[118] Mahle GmbH, ed. *Pistons and Engine Testing*. 1st. Wiesbaden, Germany: Vieweg+Teubner Verlag, 2012. DOI: 10.1007/978-3-8348-8662-0.

[119] Lawrence F. Shampine and Mark W. Reichelt. "The MATLAB ODE Suite". In: *SIAM Journal on Scientific Computing* 18.1 (1997), pp. 1–18. DOI: 10.1137/S1064827594276424.

[120] Arne Seitz. "Advanced Methods for Propulsion System Integration in Aircraft Conceptual Design". Dissertation. München: TU Munich, 2012.

[121] M. D. McKay, R. J. Beckman and W. J. Conover. "A Comparison of Three Methods for Selecting Values of Input Variables in the Analysis of Output from a Computer Code". In: *Technometrics* 21.2 (May 1979), pp. 239–245. DOI: 10.2307/1268522.

[122] B. Manescu, I. Dragomir and N. Stanescu. *A Background of Variable Compression Ratio Engines*. Scientific Bulletin. Apr. 2016.

[123] Jon H. VanGerpen. *A Two-Stroke Diesel Engine Simulation Program*. Tech. rep. NASA CR-185155. Ames, Iowa: Iowa State University, Feb. 1990.

[124] Jon H. VanGerpen. *Simulation of a Combined-Cycle Engine*. Tech. rep. NASA CR-188232. Ames, Iowa: Iowa State University, June 1991.

[125] Colin R. Ferguson and Allan T. Kirkpatrick. *Internal Combustion Engines – Applied Thermosciences*. 3rd. Chichester, UK: John Wiley & Sons, 2016.

[126] John B. Heywood. *Internal Combustion Engine Fundamentals*. 1st. New York: McGraw-Hill, Inc., 1988.

[127] K. Patton, R. Nitschke and J. Heywood. *Evaluation on Two Stroke Engines Scavenging Models*. SAE Technical Paper 890836. SAE International, 1989. DOI: 10.4271/890836.

[128] Daniel Sandoval. "An Improved Friction Model for Spark Ignition Engines". Bachelor's Thesis. Massachusetts Institute of Technology, May 2002.

[129] Paul Keller. "Piston Engine Conceptualization for Composite Cycle Engines". MA thesis. TU Munich, May 2017.

[130] S. Boggia and K. Rüd. "Intercooled Recuperated Gas Turbine Engine Concept". In: *41st AIAA/ASME/SAE/ASEE Joint Propulsion Conference & Exhibit*. AIAA 2005-4192. Tucson, Arizona: American Institute of Aeronautics and Astronautics, July 2005. DOI: 10.2514/6.2005-4192.

[131] J. E. Hesselgreaves, Richard Law and David Reay. *Compact Heat Exchangers*. 2nd. Oxford, UK: Butterworth-Heinemann, 2016.

[132] G. R. Kappler and S. Staudacher. "Gewichtsstudie zu Niederdrucksystemen moderner Turbofan-Triebwerke". In: *Deutscher Luft- und Raumfahrtkongress*. München, Sept. 2012.

[133] H. Grieb. *Verdichter für Turbo-Flugtriebwerke*. 1st. Basel, Switzerland: Springer Berlin Heidelberg, 2009. DOI: 10.1007/978-3-540-34374-5.

[134] S. G. Schneider. "Mechanische und thermische Beanspruchung in Großdieselmotoren bei extrem hohen Mitteldrücken". Dissertation. München: TU Munich, 2012.

[135] B. H. Oman. *Vehicle Design Evaluation Program*. Tech. rep. NASA CR-145070. Hampton, Virginia: NASA Langley Research Center, Jan. 1977.

[136] Pasquale M. Sforza. *Commercial Airplane Design Principles*. 1st. Oxford, UK: Butterworth-Heinemann, 2015.

[137] R. J. Pera et al. *Vehicle Design Evaluation ProgramA Method to Estimate Weight and Dimensions of Aircraft Gas Turbine Engines*. Tech. rep. NASA CR-135170. Seattle, Washington: Boeing Military Airplane Development, May 1977.

[138] E. M. Greitzer. *Volume 2: Appendices – Design Methodologies for Aerodynamics, Structures, Weight, and Thermodynamic Cycles*. Tech. rep. NASA/CR–2010-216794/VOL2. Cambridge, Massachusetts: The MIT, Aurora Flight Sciences, and Pratt&Whitney Team, Dec. 2010.

[139] C. N. Reynolds. *Advanced Prop-Fan Engine Technology (APET) Single- and Counter-Rotation Gearbox-Pitch Change Mechanism*. Tech. rep. CR-168114. East Hartford, Connecticut: NASA Lewis Research Center, July 1985.

[140] Eric S. Hendricks and Michael T. Tong. *Performance and Weight Estimates for an Advanced Open Rotor Core-Engines*. Tech. rep. TM-2012-217710. Cleveland, OH: NASA Glenn Research Center, Sept. 2012.

[141] A. Stroh, G. Wortmann and A. Seitz. "Conceptual Sizing Methods for Power Gearboxes in Future Gas Turbine Engines". In: *Deutscher Luft- und Raumfahrtkongress 2017*. 450100. Munich, Germany, Sept. 2017.

[142] K. Steffens and H. Wilhelm. *Werkstoffe, Oberflächentechnik und Fertigungsverfahren fuer die nächste Generation von Flugtriebwerken*. Tech. rep. NASA CR-189171. Toledo, Ohio: MTU Aero Engines, July 2001.

[143] D. A. Sagerser, S. Lieblein and R. P. Krebs. *Empirical Expressions for Estimating Length and Weight of Axial-Flow Components of VTOL Powerplants*. Tech. rep. Munich, Germany: NASA Lewis Research Center, 1971.

[144] *Luftfahrttechnisches Handbuch*. IABG mbH. Ottobrunn, Germany, 2015. URL: `www.lth-online.de`.

[145] A. J. B. Jackson. "Optimisation of Aero and Industrial Gas Turbine Design for the Environment". PhD thesis. Cranfield University, 2009.

[146] European Aviation Safety Agency (EASA). *Type-Certificate Data Sheet for PW1100G-JM Series Engines*. No. IM.E.093. Nov. 2015.

[147] R. van Basshuysen and F. Schäfer, eds. *Handbuch Verbrennungsmotor*. 7th. Springer Vieweg, Wiesbaden, 2015. ISBN: 978-3-658-04677-4. DOI: `10.1007/978-3-658-04678-1`.

[148] Hartmut Baur et al. "γ-TiAl for Aeroengine and Automotive Applications". In: *Intermetallics and Superalloys*. Wiley-VCH Verlag GmbH & Co. KGaA, Apr. 2006, pp. 384–390. DOI: `10.1002/3527607285.ch65`.

[149] Anil K. Sachdev et al. “Titanium for Automotive Applications: Challenges and Opportunities in Materials and Processing”. In: *JOM* 64.5 (Apr. 2012), pp. 553–565. DOI: 10.1007/s11837-012-0310-8.

[150] Mustafa Kemal Kulekci. “Magnesium and its Alloys Applications in Automotive Industry”. In: *The International Journal of Advanced Manufacturing Technology* 39.9-10 (Nov. 2007), pp. 851–865. DOI: 10.1007/s00170-007-1279-2.

[151] *Pacelab Engineering Workbench 5.1.1*. Comp. software. Berlin, Germany: Pacelab GmbH, 2012.

[152] Philipp Heinemann et al. “Advanced Tube and Wing Aircraft for Year 2050 Timeframe”. In: *55th AIAA Aerospace Sciences Meeting*. AIAA 2017-1390. Grapevine, Texas, Jan. 2017. DOI: 10.2514/6.2017-1390.

[153] F. Bakhtiari and H.-P. Schiffer. “Numerical Approach to the Modelling of Transient Interaction of Prospective Combustor Concepts and Conventional High Pressure Turbines”. In: *Deutscher Luft- und Raumfahrtkongress*. Berlin, Sept. 2017.

[154] V. Bicalho Civinelli de Almeida and D. Peitsch. “Aeroelastic Assessment of a Highly Loaded High Pressure Compressor Exposed to Pressure Gain Combustion Disturbances”. In: *Journal of the Global Power and Propulsion Society* 2 (Oct. 2018), F72OUU. DOI: 10.22261/jgpps.f72ouu.

[155] Andreas Linke-Diesinger. *Systeme von Turbofan-Triebwerken*. 1st. Hamburg, Germany: Springer Berlin Heidelberg, 2014. DOI: 10.1007/978-3-662-44570-9.

[156] Eduard Köhler and Rudolf Flierl. *Verbrennungsmotoren*. Vieweg+Teubner Verlag, 2011. DOI: 10.1007/978-3-8348-8309-4.

[157] David S. Lee et al. “Aviation and Global Climate Change in the 21st Century”. In: *Atmospheric Environment* 43.22-23 (July 2009), pp. 3520–3537. DOI: 10.1016/j.atmosenv.2009.04.024.

[158] Joyce E. Penner et al. *Aviation and the Global Atmosphere – Summary for Policy Makers*. Tech. rep. Intergovernmental Panel on Climate Change (IPCC), 1999.

[159] *The Right Flightpath to Reduce Aviation Emissions*. Brochure. Durban, South Africa: Air Transport Action Group (ATAG), Nov. 2011.

[160] Michael Kenney et al. *Aviation Emissions and Air Quality Handbook – Version 3 Update 1*. Tech. rep. Federal Aviation Administration – Office of Environment and Energy, Jan. 2015.

[161] *ICAO Environmental Report 2016 – Aviation and Climate Change*. Tech. rep. International Civil Aviation Organization (ICAO), 2016.

[162] *International Standards and Recommended Practices - Annex 16 - Environmental Protection - Volume II - Aircraft Engine Emissions*. International Standard. International Civil Aviation Organization (ICAO), 2008.

[163] A. N. Hayhurst and I. M. Vince. “Nitric oxide formation from N2 in flames: The importance of "prompt" NO”. In: *Progress in Energy and Combustion Science* 6.1 (1980), pp. 35–51. DOI: 10.1016/0360-1285(80)90014-3.

[164] J. Warnatz, Ulrich Maas and Robert W. Dibble. *Combustion*. Springer-Verlag Berlin Heidelberg, 2006. DOI: 10.1007/978-3-540-45363-5.

[165] Elke Goos et al. "Prompt NO Formation in Flames: The Influence of NCN Thermochemistry". In: *Proceedings of the Combustion Institute*. Vol. 34. 1. 2013, pp. 657–666. DOI: 10.1016/j.proci.2012.06.128.

[166] Joseph W. Bozzelli and Anthony M. Dean. "O + NNH: A possible new route for NOx formation in flames". In: *International Journal of Chemical Kinetics* 27.11 (Nov. 1995), pp. 1097–1109. DOI: 10.1002/kin.550271107.

[167] Matthew Blake Thames. "Experimentation and Modeling of Formation in a Small Turbo-Charged Diesel Engine". MA thesis. Auburn University, May 2013.

[168] Günter P. Merker, Bernd Hohlbaum and Martin Rauscher. "Two-Zone Model for Calculation of Nitrogen-Oxide Formation in Direct-Injection Diesel Engines". In: *International Off-Highway & Powerplant Congress & Exposition*. SAE International, Sept. 1993. DOI: 10.4271/932454.

[169] Günter Heider, Gerhard Woschni and Klaus Zeilinger. "2-Zonen Rechenmodell zur Vorausrechnung der NO-Emission von Dieselmotoren". In: *MTZ - Motortechnische Zeitschrift*. Vol. 59. 11. Vieweg Verlag, 1998, pp. 770–775. DOI: 10.1007/BF03226479.

[170] Tamas Turanyi and Alison S. Tomlin. *Analysis of Kinetic Reaction Mechanisms*. 1st. Springer-Verlag Berlin Heidelberg, 2014. DOI: 10.1007/978-3-662-44562-4.

[171] Robert J. Kee et al. *CHEMKIN-III - A FORTRAN Chemical Kinetics Package for the Analysis of Gas-Phase Chemical and Plasma Kinetics*. Tech. rep. UC-405. Livermore, CA: Sandia National Laboratories, May 1996.

[172] Daniel Sabathil. "Beitrag zur NOx - Simulation eines Beitrag zur NOx-Simulation eines Ottomotors im Instationärbetrieb". Dissertation. TU Darmstadt, 2010.

[173] J. Mohammadhassani et al. "Prediction of NOx Emissions from a Direct Injection Diesel Engine Using Artificial Neural Network". In: *Modelling and Simulation in Engineering* 2012 (2012), pp. 1–8. DOI: 10.1155/2012/830365.

[174] Amin Maghbouli et al. "A Multi-Dimensional CFD-Chemical Kinetics Approach in Detection and Reduction of Knocking Combustion in Diesel-Natural Gas Dual-Fuel Engines Using Local Heat Release Analysis". In: *SAE International Journal of Engines* 6.2 (Apr. 2013), pp. 777–787. DOI: 10.4271/2013-01-0865.

[175] Seyed Mohammad Mousavi et al. "A numerical investigation on combustion and emission characteristics of a dual fuel engine at part load condition". In: *Fuel* 166 (Feb. 2016), pp. 309–319. DOI: 10.1016/j.fuel.2015.10.052.

[176] S. Jafarmadar and M. Khanbabazadeh. "A Full-Cycle 3 Dimensional Numerical Simulation of a Direct Injection Diesel Engine". In: *International Journal of Automotive Engineering* 3.2 (2013).

[177] C. D. Rakopoulos, D. C. Rakopoulos and D. C. Kyritsis. "Development and validation of a comprehensive two-zone model for combustion and emissions formation in a DI diesel engine". In: *International Journal of Energy Research* 27.14 (2003), pp. 1221–1249. DOI: 10.1002/er.939.

[178] C. D. Rakopoulos et al. "Validation and sensitivity analysis of a two zone Diesel engine model for combustion and emissions prediction". In: *Energy Conversion and Management* 45.9-10 (June 2004), pp. 1471–1495. DOI: 10.1016/j.enconman.2003.09.012.

[179] C. D. Rakopoulos, K. A. Antonopoulos and D. C. Rakopoulos. "Development and application of multi-zone model for combustion and pollutants formation in direct injection diesel engine running with vegetable oil or its bio-diesel". In: *Energy Conversion and Management* 48.7 (July 2007), pp. 1881–1901. DOI: 10.1016/j.enconman.2007.01.026.

[180] Vasilios T. Lamaris et al. "Development and Validation of a Multi-Zone Combustion Model for Predicting Performance Characteristics and NOx Emissions in Large Scale Two-Stroke Diesel Engines". In: *Volume 3: Combustion Science and Engineering*. ASME, 2009. DOI: 10.1115/imece2009-11382.

[181] Laurie Goldsworthy. "Reduced Kinetics Schemes for Oxides of Nitrogen Emissions from a Slow-Speed Marine Diesel Engine". In: *Energy & Fuels* 17.2 (Mar. 2003), pp. 450–456. DOI: 10.1021/ef020172c.

[182] L. Goldsworthy. "Real time model for oxides of nitrogen emissions from a slow speed marine diesel". In: *Journal of Marine Engineering & Technology* 2.1 (2003), pp. 3–12. DOI: 10.1080/20464177.2003.11020166.

[183] A. Andreasen and S. Mayer. "Modelling of the Oxidation of Fuel Sulfur in Low Speed Two-Stroke Diesel Engines". In: *CIMAC Congress 2010*. 39. International Council on Combusiton Engines. Bergen, Norway, June 2010.

[184] A. Andreasen and K. Nyggard. *Water-in-Fuel Emulsion as Marine Engine Fuel for Reduced NOx and Particulate Emissions*. Tech. rep. Environmental Project No. 1380 2011. Danish Environmental Protection Agency, 2011.

[185] Fabio Scappin et al. "Validation of a zero-dimensional model for prediction of NOx and engine performance for electronically controlled marine two-stroke diesel engines". In: *Applied Thermal Engineering* 37 (May 2012), pp. 344–352. DOI: 10.1016/j.applthermaleng.2011.11.047.

[186] Spiridon I. Raptotasios et al. "Application of a multi-zone combustion model to investigate the NOx reduction potential of two-stroke marine diesel engines using EGR". In: *Applied Energy* 157 (Nov. 2015), pp. 814–823. DOI: 10.1016/j.apenergy.2014.12.041.

[187] Petra Andersson. "Models for Predicting the NOx Exhaust Pollutants in a Diesel Engine". MA thesis. Department of Physics Lund, 1989.

[188] Irvin Glassman, Richard A. Yetter and Nick G. Glumac. *Combustion*. 5th. Academic Press, 2014.

[189] National Research Council. *Aeronautical Technologies for the Twenty-First Century*. National Academy Press, 1992. DOI: 10.17226/2035.

[190] Stephen P. Lukachko and Ian A. Waitz. "Effects of Engine Aging on Aircraft NOx Emissions". In: *ASME 1997 International Gas Turbine and Aeroengine Congress and Exhibition*. Orlando, Florida, USA, 1997. DOI: 10.1115/97-GT-386.

[191] Konstantinos G. Kyprianidis and Devaiah Nalianda abd Erik Dahlquist. "A NOx Emissions Correlation for Modern RQL Combustors". In: *Energy Procedia* 75 (2015), pp. 2323–2330. DOI: 10.1016/j.egypro.2015.07.433.

[192] Daniel Guyot, Gabrielle Tea and Christoph Appel. "Low NOx Lean Premix Reheat Combustion in Alstom GT24 Gas Turbines". In: *Journal of Engineering for Gas Turbines and Power* 138.5 (2016). DOI: 10.1115/1.4031543.

[193] Felix Guethe, Marta de la Cruz García and Andre Burdet. "Flue Gas Recirculation in Gas Turbine: Investigation of Combustion Reactivity and NOX Emission". In: *ASME Turbo Expo 2009: Power for Land, Sea, and Air*. GT2009-59221. 2009, pp. 179–191. DOI: 10.1115/GT2009-59221.

[194] Gerhard Müller and Michael Möser, eds. *Handbook of Engineering Acoustics*. 1st. Munich, Germany: Springer Berlin Heidelberg, 2013. DOI: 10.1007/978-3-540-69460-1.

[195] C. Salpingidou et al. "Conceptual design study of a geared turbofan and an open rotor aero engine with intercooled recuperated core". In: *Proceedings of the Institution of Mechanical Engineers, Part G: Journal of Aerospace Engineering* (Apr. 2018), p. 095441001877088. DOI: 10.1177/0954410018770883.

[196] H. Hubbard. *Aeroacoustics of Flight Vehicles – Volume 1: Noise Sources*. Tech. rep. NASA RP-1258. Hampton, Virginia: NASA Langley Research Center, Aug. 1991.

[197] European Aviation Safety Agency (EASA). *Light propeller driven aeroplanes noise database – Issue 29*. Jan. 2018. URL: https://www.easa.europa.eu/easa-and-you/environment/easa-certification-noise-levels.

[198] J. Ivosevic, I. Mihalincic and T. Bucak. "Noise Analysis of a Twin Piston Engine Aircraft". In: *Congress on Sound and Vibration*. Ljubljana, Slovenia: European Acoustics Association, Sept. 2010.

[199] E. Bertsch. *Noise Prediction within Conceptual Aircraft Design*. Research rep. Forschungsbericht 2013-20. Braunschweig, Germany: Deutsches Zentrum für Luft- und Raumfahrt e.V., 2013.

[200] Ulrike Burkhardt, Lisa Bock and Andreas Bier. "Mitigating the Contrail Cirrus Climate Impact by Reducing Aircraft Soot Number Emissions". In: *npj Climate and Atmospheric Science* 1.1 (Oct. 2018). DOI: 10.1038/s41612-018-0046-4.

[201] O. Boucher et al. “Clouds and Aerosols”. In: *Climate Change 2013: The Physical Science Basis. Contribution of Working Group I to the Fifth Assessment Report of the Intergovernmental Panel on Climate Change*. Cambridge, United Kingdom and New York, NY, USA: Cambridge University Press, 2013. Chap. Clouds and Aerosols.

[202] D. S. Lee et al. “Transport impacts on atmosphere and climate: Aviation”. In: *Atmospheric Environment* 44.37 (Dec. 2010), pp. 4678–4734. DOI: 10.1016/j.atmosenv.2009.06.005.

[203] *Airport Air Quality Manual*. Tech. rep. Doc 9889. International Civil Aviation Organization (ICAO), 2011.

[204] Konstantinos G. Kyprianidis and Erik Dahlquist. “On the trade-off between aviation NOx and energy efficiency”. In: *Journal of Applied Energy* 185.2 (2017), pp. 1506–1516. DOI: 10.1016/j.apenergy.2015.12.055.

[205] A. Seitz, D. Schmitt and S. Donnerhack. “Emission comparison of turbofan and open rotor engines under special consideration of aircraft and mission design aspects”. In: *The Aeronautical Journal* 115.1168 (June 2011), pp. 351–360. DOI: 10.1017/s000192400000587x.

[206] *International Civil Aviation Organization’s CO2 Certification Requirement for New Aircraft*. Tech. rep. International Council on Clean Transportation (ICCT), Aug. 2013.

[207] *Conditions of Use including Airport Charges from 1 January 2017*. Brochure. Hounslow, Middlesex: Heathrow Airport Limited, Oct. 2016.

[208] ICAO Committee on Aviation Environmental Protection (CAEP). *ICAO Aircraft Engine Emissions Databank – version 23b*. Apr. 2017. URL: https://www.easa.europa.eu/easa-and-you/environment/icao-aircraft-engine-emissions-databank.

[209] Matt Gorman and Rick Norman. *Applying Environment & Sustainability to Airport Charges*. Presentation. Jan. 2015.

[210] Alexios Alexiou et al. “Performance Modelling of an Ultra-High Bypass Ratio Geared Turbofan”. In: *23rd International Symposium of Air Breathing Engines*. ISABE-2017-22512. Manchester, UK, Sept. 2017.

[211] Uwe Schulz et al. “Some Recent Trends in Research and Technology of Advanced Thermal Barrier Coatings”. In: *Aerospace Science and Technology* 7.1 (2003), pp. 73–80. DOI: 10.1016/S1270-9638(02)00003-2.

[212] A. J. Glassman. *Users Manual for Updated Computer Code for Axial-Flow Compressor Conceptual Design*. Tech. rep. NASA TM-107193. Cleveland, Ohio: Nasa Lewis Research Center, June 1992.

[213] *Technology Roadmap – Technical Annex*. Research rep. 3rd Edition. IATA, in collaboration with Georgia Institute of Technology, June 2009.

[214] *Technology Roadmap 2013 – 4th Edition*. Tech. rep. International Air Transport Association (IATA), June 2013.

[215] Ralf von der Bank et al. “LEMCOTEC – Improving the Core-Engine Thermal Efficiency”. In: *ASME Turbo Expo 2014*. GT2014-25040. Düsseldorf, Germany, June 2014. DOI: 10.1115/GT2014-25040.

[216] MTU Aero Engines AG. *High-tech made by MTU*. Brochure. Munich, Germany, May 2017.

[217] C. Mercer, W. Haller and M. Tong. “Adaptive Engine Technologies for Aviation CO2 Emissions Reduction”. In: *42nd AIAA/ASME/SAE/ASEE Joint Propulsion Conference & Exhibit*. AIAA 2005-4192. Sacramento, California: American Institute of Aeronautics and Astronautics, July 2006. DOI: 10.2514/6.2006-5105.

[218] Karl-Heinrich Grote and Jörg Feldhusen, eds. *Dubbel*. 24th. Springer Berlin Heidelberg, 2014. DOI: 10.1007/978-3-642-38891-0.

[219] Felix Güthe, Jaan Hellat and Peter Flohr. “The Reheat Concept: The Proven Pathway to Ultralow Emissions and High Efficiency and Flexibility”. In: *Journal of Engineering for Gas Turbines and Power* 131.2 (2009). DOI: 10.1115/1.2836613.

[220] A. Ciani et al. “Full-Scale Atmospheric Tests of Sequential Combustion”. In: *ASME Turbo Expo 2010: Power for Land, Sea, and Air*. GT2010-22891. Glasgow, UK, June 2010. DOI: 10.1115/GT2010-22891.

[221] J. A. Wünning and J. G. Wünning. “Flameless Oxidation to Reduce Thermal NO-Formation”. In: *Progress in Energy and Combustion Science* 23.1 (1997), pp. 81–94. DOI: 10.1016/S0360-1285(97)00006-3.

[222] Daniel Diez Alvarez. “Development of a Free-Piston Model for the Automated Preliminary Design of New Type Aero-Engines in the Development Environment Pacelab”. Bachelor’s Thesis. Universität Stuttgart, Nov. 2016.

[223] Stefan Ittner. *Dieselmotoren für die Luftfahrt – Innovation und Tradition im Junkers-Flugmotorenbau bis 1933*. 1st. Oberhaching, Germany: Aviatic Verlag, 1996.

[224] Hermann Hiereth and Peter Prenninger. *Aufladung der Verbrennungskraftmaschine*. 1st. Vienna, Austria: Springer Vienna, 2003. DOI: 10.1007/978-3-7091-0650-1.

[225] E. Bach and P. Pfeiffer. *Leistungssteigerung von Verbrennungsmotoren*. Lehrbrief V7. Dresden, Germany: Hochschule für Technik und Wirtschaft Dresden (FH), 2002.

[226] Paul H. Wilkinson. *Aircraft Engines of the World 1944*. New York: Paul H. Wilkinson, 1944.

[227] Klaus L. Schulte. *Gegenkolbenflugdiesel – Zurück in die Zukunft*. e-Journ Nr. Tt-08. K.L.S. Publishing, 2008.

[228] European Aviation Safety Agency (EASA). *Type-Certificate Data Sheet for L 2400 series engines*. TCDS EASA.E.084. Aug. 2006.

[229] “British Power Units - Principal Data of Current Aircraft Gas Turbines and Piston Enignes”. In: *Flight and Aircraft Engineer*. Ed. by C. M. Poulsen. Vol. 70. 2019. London, UK, Sept. 1947, pp. 250–251.

[230] K. von Gersdorff, H. Schubert and S. Ebert. *Die deutsche Luftfahrt - Flugmotoren und Strahltriebwerke*. 4th. Bonn, Germany: Bernard & Graefe, 2007.

[231] G. Hack. *Der schnelle Diesel – Alles über Diesel-Autos*. Stuttgart, Germany: Motorbuch Verlag, 1985. ISBN: 3613010488.

[232] A. Brouwers. *150 and 300 kW Lightweight Diesel Aircraft Engine Design Study*. Tech. rep. NASA CR-3260. Muskegon, Michigan: Teledyne Continental Motors, 1980.

[233] Sebastian B. Pflaum. "Entwicklung und Untersuchung eines Brennverfahrens fuer Niedrigstemissionen bei Dieselmotoren". Dissertation. TU Munich, 2011.

[234] M. Theissen et al. "10 Years of BMW F1 Engines". In: *31. Internationales Wiener Motorensymposium 2010*. Austrian Society of Automotive engineers. Wien, Apr. 2010.

[235] Robin Hamberg. "Optimization of FreeValve's Fully Variable Valve Control System for a Four-Cylinder Engine". MA thesis. Stockholm, Sweden: KTH Royal Institute of Technology, May 2017.

[236] N. K. Raghuwanshi, A. Pandey and R. K. Mandloi. "Failure Analysis of Internal Combustion Engien Valves: A Review". In: *International Journal of Innovative Research in Science, Engineering and Technology* 1.2 (Dec. 2012), pp. 173–181. ISSN: 2319-8753.

[237] Klaus Mollenhauer and Helmut Tschöke. *Handbook of Diesel Engines*. 1st ed. Berlin: Springer Berlin Heidelberg, 2010. DOI: 10.1007/978-3-540-89083-6.

[238] Klaus Schreiner. *Basiswissen Verbrennungsmotor*. 2nd. Springer Fachmedien Wiesbaden, 2015. DOI: 10.1007/978-3-658-06187-6.

[239] D. N. Assanis. "The Effect of Thin Ceramic Coatings on Petrol Engine Performance and Emissions". In: *International Journal of Vehicle Design* 13.4 (1992), pp. 378–387. DOI: 10.1504/IJVD.1992.061733.

[240] Stefan Zima. *Ungewöhnliche Motoren*. 1st. Munich, Germany: Vogel Communications Group, 2005.

[241] Hermann Klingels. *Wärmekraftmaschine mit Freikolbenverdichter*. DE patent 10 2012 206 123 A1. London, England, Oct. 2013.

[242] R. Mikalsen and A. P. Roskilly. "A Review of Free-Piston Engine History and Applications". In: *Applied Thermal Engineering* 27.14-15 (Oct. 2007), pp. 2339–2352. DOI: 10.1016/j.applthermaleng.2007.03.015.

[243] E. M. Khaimovich. *Hydraulic Control of Machine Tools*. Oxford, UK: Pergamon Press, 1965.

[244] Un-Jae Seo et al. "Design considerations of a linear generator for a range extender application". In: *Archives of Electrical Engineering* 64.4 (Dec. 2015), pp. 581–592. DOI: 10.1515/aee-2015-0043.

[245] C. Salpingidou et al. "Investigation and Assessment of the Performance of Various Recuperative Cycles based on the Intercooled Recuperation Concept". In: *ASME Turbo Expo 2018*. GT2018-76778. Oslo, Norway, June 2018.

[246] Khaled Zarati, Samer Maalouf and Askin Isikveren. “Investigations of Synergistic Combination of the Composite Cycle and Intercooled Recuperation”. In: *23rd International Symposium of Air Breathing Engines*. ISABE-2017-21345. Manchester, UK, Sept. 2017.

[247] F. Jacob et al. “Performance of a Supercritical CO2 Bottoming Cycle for Aero Applications”. In: *Applied Sciences* 7.3 (Mar. 2017), p. 255. DOI: 10.3390/app7030255.

[248] A. A. Iyer et al. “Experimental Study on the Effect of Water Injection in an Internal Combustion Engine”. In: *IOSR Journal of Mechanical and Civil Engineering* 17.10 (Mar. 2017), pp. 58–64. DOI: 10.9790/1684-17010055864.

[249] S. Kaiser et al. “A Composite Cycle Engine Concept for Year 2050”. In: *31st Congress of the International Council of the Aeronautical Sciences*. Belo Horizonte, Brazil, Sept. 2018.

[250] Xin Zhao et al. “Experimental Validation of the Aerodynamic Characteristics of an Aero-engine Intercooler”. In: *Journal of Engineering for Gas Turbines and Power* 139.5 (Nov. 2016), p. 051201. DOI: 10.1115/1.4034964.

[251] Zinon Vlahostergios et al. “Efforts to Improve Aero Engine Performance Through the Optimal Design of Heat Recuperation Systems Targeting Fuel Consumption and Pollutant Emissions Reduction”. In: *12th European Conference on Turbomachinery Fluid Dynamics and hermodynamics*. European Turbomachinery Society, 2017. DOI: 10.29008/etc2017-356.

[252] Pok-Wang Kwan et al. “Minimising Loss in a Heat Exchanger Installation for an Intercooled Turbofan Engine”. In: *Volume 1: Aircraft Engine; Ceramics; Coal, Biomass and Alternative Fuels; Wind Turbine Technology*. ASME, 2011. DOI: 10.1115/gt2011-45814.

[253] C. A. Amann. “Evaluating Alternative Internal Combustion Engines: 1950–1975”. In: *Journal of Engineering for Gas Turbines and Power* 121.3 (1999), p. 540. DOI: 10.1115/1.2818506.

[254] *Dieselmotor - KKM 500d*. Product data sheet. Cottbus, Germany: Wankel SuperTec GmbH, 2016.

[255] European Aviation Safety Agency (EASA). *Type-Certificate Data Sheet for DIESELJET TDA CR*. TCDS EASA.E.079. Mar. 2016.

[256] Dimitrios Chatzianagnostou and Stephan Staudacher. “Comparison of Piston Concept Design Solutions for Composite Cycle Engines – Part I: Similarity Considerations”. In: *Journal of Engineering for Gas Turbines and Power* 140.9 (June 2018), p. 091702. DOI: 10.1115/1.4039704.

[257] *Technology Readiness Assessment Guide*. Guide DOE G 413.3-4A. Washington, D.C.: U.S. Department of Energy, Sept. 2011.

[258] Tim Brown. *Change by Design*. Harper Collins Publ. USA, 2011. ISBN: 9780061766084.

[259] R. Plencner. *Plotting Component Maps in the Navy/NASA Engine Program (NNEP)– A Method and Its Usage*. Tech. rep. NASA TM-101433. Cleveland, Ohio: Lewis Research Center, Jan. 1989.

[260] R. Stabe, W. Whitneyu and T. Moffitt. *Performance of a High-Work Low Aspect Ratio Turbine Tested with a Realistic Inlet Radial Temperature Profile*. Tech. rep. NASA TM-83655. Cleveland, Ohio: Lewis Research Center, June 1984.

[261] G. K. Serovy. *Compressor and Turbine Prediction System Development – Lessons from Thirty Years of History*. Tech. rep. AGARD LS-83. AGARD, 1976.

Appendix A

Appendix

A.1 Turbo Component Setup

The following list summarises the used component maps with their references and their used design points for map scaling. The component maps in machine readable format are taken from the GasTurb Map Collection 3 [103].

Fan: Fan with pressure ratio 1.5 ; Rel. speed 1.0; $\beta = 0.5$ [87]
Fan core with pressure ratio 1.44; Rel. speed 1.0; $\beta = 0.5$ [87]

IPC: Compressor with pressure ratio 7.8 [259]; Rel. speed 1.0; $\beta = 0.5$

HPC: Compressor with pressure ratio 7.8 (same as IPC) [259]; Rel. speed 1.0; $\beta = 0.5$

Radial Compressor: Single stage radial compressor with pressure ratio 4.0; Rel. speed 1.0; $\beta = 0.5$

HPT: Single stage turbine with design pressure ratio 2.3 [260]; Rel. speed 1.0; $\beta = 0.5$

LPT: 2-stage turbine with design pressure ratio 2.4 [261]; Rel. speed 1.0; $\beta = 0.5$

A.2 Validation 2-Stroke Engine Neural Network

Table A.1: Input parameters for the two-stroke piston engine surrogate artificial neural network with ranges and output parameters.

Input	**Unit**	**Range**
Intake temperature T_1	K	500 – 900
Intake pressure p_1	kPa	400 – 4 500
Piston bore d	m	0.10 – 0.20
Piston pressure ratio Π	–	0.95 – 0.998
Geometric compression ratio CR	–	5 – 20
Mean piston velocity v_{mean}	m/s	10 – 25
Valve lift l_{valve}	m	0.030 – 0.030
Fuel-air-ratio FAR_2 at EVO	–	0.020 – 0.060
Cylinder wall temperature	K	450 – 1 050
Output	**Unit**	**Mean rel. error [%]**
Exhaust temperature T_2	K	0.01
Shaft power P	W	0.10
Heat loss $\dot{Q}_{\text{loss}}$	W	0.04
Mass flow rate $\dot{m}_1$	kg/s	0.03
Exhaust fuel air ratio FAR	–	0.01
Peak pressure p_{peak}	Pa	0.05

A.3 Supplementary figures

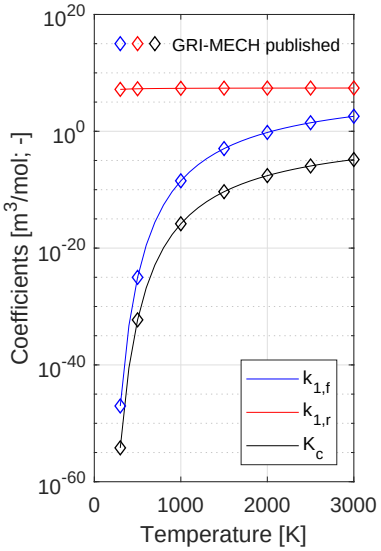

Figure A.1: Verifications of the calculation of the equilibrium constant K_c exemplary for Reaction (3.116).

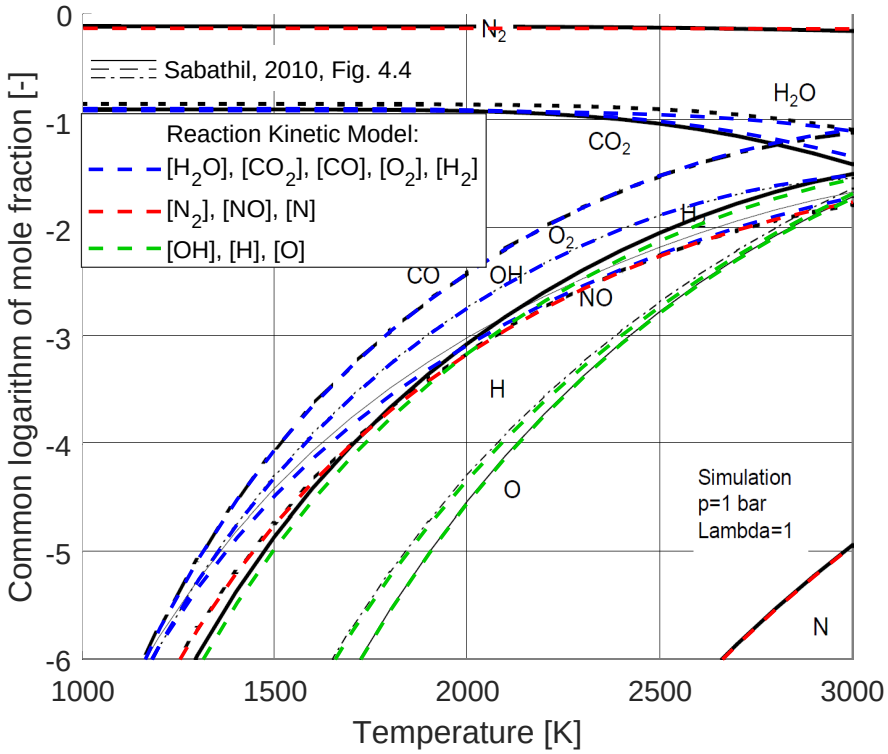

Figure A.2: Verifications of the equilibrium concentrations of the species of the OHC-System over temperature against published data [172].

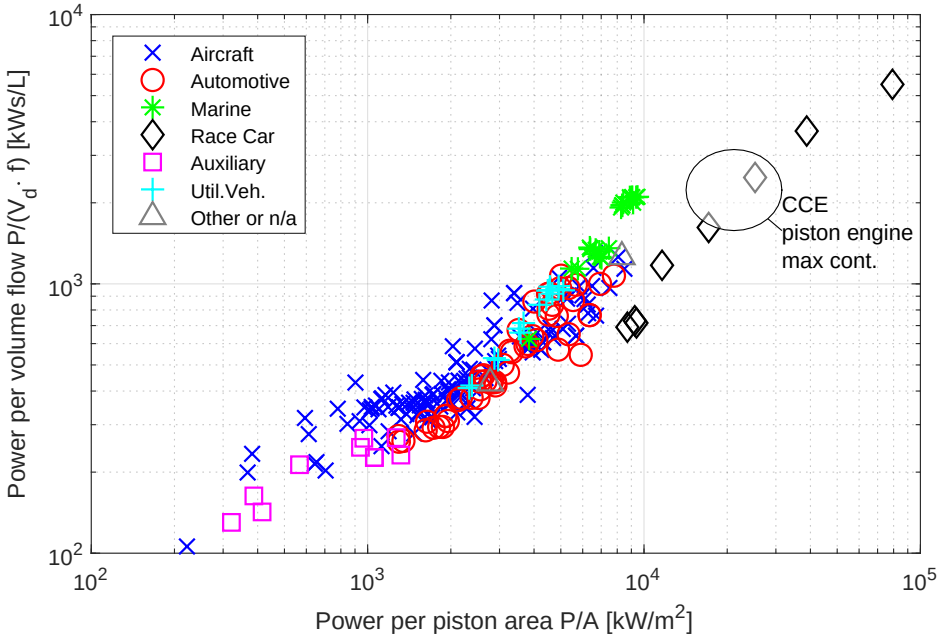

Figure A.3: Power per volume flow over power per area.

A.4 Supplementary Data

Table A.2: Structure of engine weights and validation values for 2-stroke CCE.

Component	**GTF [kg]**	**CCE [kg]**	**Δ [%]**
Fan	782.3	779.8	-0.3
fan drive gear system (FDGS)	278.2	277.6	-0.2
IPC	101.2	144.4	42.7
HPC	177.0	78.7	-55.5
Combustor	56.4	42.9	-23.8
HPT	115.2	–	-100.0
LPT	363.7	479.1	31.7
Piston engine gearbox	–	115.0	–
Piston engine	–	883.7	–
Systems & dressings	351.6	515.7	46.6
Accessories	118.7	121.0	1.9
Engine	2 344.3	3 437.9	46.6
Nacelle	464.5	464.5	0.0
Thrust reverser	416.1	424.2	1.9
Core cowl	153.2	152.3	-0.6
Bypass nozzle	119.7	75.5	-36.9
Core nozzle	32.4	26.4	-18.6
power plant system (PPS)	3 530.2	4 580.7	29.8

Table A.3: Structure of engine weights and validation values for intercooled 2-stroke CCE.

Component	**GTF [kg]**	**CCE [kg]**	**Δ [%]**
Fan	782.3	780.0	-0.3
FDGS	278.2	283.6	1.9
IPC	101.2	101.0	-0.2
HPC	177.0	62.1	-64.9
Combustor	56.4	36.9	-34.6
HPT	115.2	–	-100.0
LPT	363.7	303.1	-16.7
Piston engine gearbox	–	134.3	–
Piston engine	–	931.2	–
Systems & dressings	351.6	518.4	47.4
Accessories	118.7	121.2	2.1
Engine	2 344.3	3 455.9	47.4
Nacelle	464.5	464.5	0.0
Thrust reverser	416.1	424.7	2.1
Core cowl	153.2	147.3	-3.9
Bypass nozzle	119.7	71.6	-40.2
Core nozzle	32.4	21.6	-33.5
PPS	3 530.2	4 585.5	29.9

Table A.4: Structure of engine weights and validation values for free-piston CCE.

Component	**GTF [kg]**	**CCE [kg]**	**Δ [%]**
Fan	782.3	778.6	-0.5
FDGS	278.2	274.9	-1.2
IPC	101.2	123.5	22.1
HPC	177.0	–	-100.0
Combustor	56.4	67.6	20.0
HPT	115.2	–	-100.0
LPT	363.7	383.6	5.5
Free-Piston engine	–	678.0	–
Systems & dressings	351.6	427.4	21.5
Accessories	118.7	115.8	-2.5
Engine	2 344.3	2 849.5	21.5
Nacelle	464.5	464.5	0.0
Thrust reverser	416.1	405.7	-2.5
Core cowl	153.2	150.0	-2.1
Bypass nozzle	119.7	26.2	-78.1
Core nozzle	32.4	25.1	-22.4
PPS	3 530.2	3 921.0	11.1

Table A.5: Station report for four-stroke CCE.

	Top of climb				*Take-off*				*Cruise*			
Station	$\dot{m}$ kg/s	T K	p kPa	$\dot{m}_{\mathrm{R,std}}$ kg/s	$\dot{m}$ kg/s	T K	p kPa	$\dot{m}_{\mathrm{R,std}}$ kg/s	$\dot{m}$ kg/s	T K	p kPa	$\dot{m}_{\mathrm{R,std}}$ kg/s
2	226.41	256.72	35.54	609.34	562.48	300.53	103.88	560.33	197.05	252.90	31.67	590.63
13	214.56	290.56	53.50	408.07	534.03	335.63	150.38	388.34	187.04	283.05	45.93	408.96
16	214.56	300.38	52.66	421.54	534.03	343.79	148.35	398.42	187.04	291.51	45.22	421.55
21	11.85	274.00	43.58	26.86	28.45	317.90	124.73	24.28	10.01	268.69	38.36	25.52
25	11.85	386.40	128.50	10.82	28.45	460.95	426.43	8.55	10.01	377.58	114.11	10.17
3	11.85	708.82	912.02	2.06	28.45	766.56	2615.70	1.80	10.01	666.78	799.33	1.93
35	11.71	1221.09	1170.14	2.09	28.16	1349.97	3020.83	2.04	9.85	1100.26	953.68	2.05
4	11.71	1225.78	1123.33	2.18	28.20	1397.35	2904.97	2.17	9.87	1152.24	917.07	2.18
41	12.11	1211.92	1123.33	2.24	29.16	1379.58	2904.97	2.23	10.20	1138.65	917.07	2.24
43	12.11	573.54	41.11	42.12	29.16	697.42	129.23	35.57	10.20	536.54	34.14	41.33
5	12.17	574.43	41.11	42.35	29.29	697.90	129.23	35.74	10.25	537.32	34.14	41.55
6	12.17	574.43	40.70	42.78	29.29	697.90	128.31	36.00	10.25	537.32	33.81	41.95

Table A.6: Station report for two-stroke CCE.

	Top of climb				*Take-off*				*Cruise*			
Station	$\dot{m}$ kg/s	T K	p kPa	$\dot{m}_{\mathrm{R,std}}$ kg/s	$\dot{m}$ kg/s	T K	p kPa	$\dot{m}_{\mathrm{R,std}}$ kg/s	$\dot{m}$ kg/s	T K	p kPa	$\dot{m}_{\mathrm{R,std}}$ kg/s
2	226.41	256.72	35.54	609.34	556.94	300.53	103.88	554.81	196.77	252.90	31.67	589.78
13	209.97	288.88	52.49	405.86	517.65	333.79	147.50	382.72	182.86	281.52	45.11	405.95
16	209.97	296.46	51.73	417.18	517.65	338.98	145.72	390.40	182.86	288.80	44.46	417.19
21	16.44	275.27	44.04	36.96	39.28	319.00	126.12	33.21	13.91	269.83	38.80	35.14
25	16.44	601.48	562.02	4.28	39.28	710.67	1943.86	3.22	13.91	576.66	465.60	4.28
3	16.44	817.87	1634.66	1.72	39.28	876.92	4219.85	1.65	13.91	783.35	1339.76	1.73
35	16.03	1129.03	1551.29	2.07	38.42	1349.99	4022.92	2.09	13.56	1115.74	1269.98	2.13
4	16.07	1212.39	1489.24	2.24	38.48	1405.81	3858.56	2.23	13.57	1134.53	1216.33	2.24
41	16.66	1199.12	1489.24	2.31	39.91	1388.25	3858.56	2.30	14.08	1122.64	1216.33	2.31
43	16.66	529.32	42.20	54.23	39.91	657.29	131.30	46.51	14.08	493.18	34.95	53.39
5	16.75	530.81	42.20	54.59	40.11	658.41	131.30	46.79	14.15	494.69	34.95	53.75
6	16.75	530.81	41.78	55.14	40.11	658.41	130.34	47.14	14.15	494.69	34.61	54.27

Table A.7: Station report for intercooled two-stroke CCE.

	Top of climb				*Take-off*				*Cruise*			
Station	$\dot{m}$ kg/s	T K	p kPa	$\dot{m}_{\mathrm{R,std}}$ kg/s	$\dot{m}$ kg/s	T K	p kPa	$\dot{m}_{\mathrm{R,std}}$ kg/s	$\dot{m}$ kg/s	T K	p kPa	$\dot{m}_{\mathrm{R,std}}$ kg/s
2	226.41	256.72	35.54	609.34	555.95	300.53	103.88	553.83	197.06	252.90	31.67	590.66
13	214.48	288.43	52.22	416.40	527.32	333.68	147.19	390.63	186.96	281.04	44.86	417.08
16	214.48	300.48	51.33	432.35	527.32	345.73	145.06	403.47	186.96	291.95	44.10	432.36
21	11.93	272.96	42.87	27.45	28.63	316.73	123.17	24.69	10.10	267.70	37.82	26.07
25	11.93	349.81	189.38	7.03	28.63	392.48	677.22	5.00	10.10	337.50	166.04	6.67
3	11.93	646.86	1400.76	1.29	28.63	633.16	3608.30	1.19	10.10	595.16	1143.22	1.29
35	11.73	1031.71	1339.52	1.68	28.24	1208.09	3472.62	1.69	9.92	974.51	1093.96	1.69
4	11.80	1227.73	1285.93	1.92	28.42	1406.29	3332.40	1.91	9.97	1147.87	1049.70	1.92
41	12.19	1210.74	1285.93	1.97	29.36	1384.12	3332.40	1.96	10.30	1131.60	1049.70	1.97
43	12.19	555.45	41.26	41.57	29.36	680.06	129.70	35.23	10.30	516.23	34.23	40.79
5	12.24	555.83	41.26	41.76	29.48	679.87	129.70	35.37	10.34	516.55	34.23	40.98
6	12.24	555.83	40.85	42.18	29.48	679.87	128.77	35.63	10.34	516.55	33.90	41.38

Table A.8: Station report for free-piston CCE.

	Top of climb				*Take-off*				*Cruise*			
Station	$\dot{m}$ kg/s	T K	p kPa	$\dot{m}_{\mathrm{R,std}}$ kg/s	$\dot{m}$ kg/s	T K	p kPa	$\dot{m}_{\mathrm{R,std}}$ kg/s	$\dot{m}$ kg/s	T K	p kPa	$\dot{m}_{\mathrm{R,std}}$ kg/s
2	226.41	256.72	35.54	609.34	549.71	300.53	103.88	547.61	197.17	252.90	31.67	590.98
13	212.28	288.23	52.10	412.94	516.38	332.85	145.95	385.30	185.25	280.99	44.83	413.45
16	212.28	290.79	51.49	419.63	516.38	335.43	144.50	390.68	185.25	282.88	44.32	419.64
21	14.13	273.92	43.57	32.03	33.32	317.41	124.11	28.56	11.92	268.66	38.35	30.40
25	14.13	506.06	326.82	5.80	33.32	565.22	859.96	5.50	11.92	482.73	263.17	5.94
3	14.13	737.85	1244.02	1.84	33.32	818.94	3276.71	1.74	11.92	705.68	1001.23	1.89
35	14.35	1052.41	1149.77	2.42	34.06	1315.95	2874.86	2.57	12.09	1010.64	939.34	2.44
4	14.41	1212.88	1103.78	2.71	34.06	1319.66	2745.24	2.69	12.14	1139.15	900.92	2.71
41	14.41	1212.88	1103.78	2.71	34.06	1319.66	2745.24	2.69	12.14	1139.15	900.92	2.71
43	14.41	568.01	39.88	51.41	34.06	659.64	125.20	41.70	12.14	531.89	33.27	50.23
5	14.41	568.01	39.88	51.41	34.06	659.64	125.20	41.70	12.14	531.89	33.27	50.23
6	14.41	568.01	39.48	51.93	34.06	659.64	124.38	41.98	12.14	531.89	32.95	50.71

Table A.9: Comparison of results of piston engine surrogate artificial neural network with simulation model of four-stroke CCE.

Parameter	**Unit**	**Neural Network**	**Simulation**	**Delta [%]**
Top of climb				
Mass flow	kg/s	0.448	0.447	0.12
Exhaust temperature	K	1248.2	1248.1	0.01
Trapped FAR	-	0.030	0.030	-0.21
Power	kW	191.2	189.9	0.68
Heat loss	kW	-79.0	-78.9	0.03
Peak pressure	bar	144.3	144.2	0.07
Take-off				
Mass flow	kg/s	1.140	1.138	0.14
Exhaust temperature	K	1350.0	1350.3	-0.02
Trapped FAR	-	0.030	0.030	-0.22
Power	kW	413.0	413.3	-0.05
Heat loss	kW	-172.0	-172.1	-0.05
Peak pressure	bar	250.0	250.1	-0.06
Cruise				
Mass flow	kg/s	0.394	0.394	-0.07
Exhaust temperature	K	1107.2	1107.0	0.02
Trapped FAR	-	0.025	0.025	-0.22
Power	kW	146.0	144.2	1.27
Heat loss	kW	-58.1	-58.0	0.04
Peak pressure	bar	123.2	123.0	0.11

Table A.10: Comparison of results of piston engine surrogate artificial neural network with simulation model of two-stroke CCE.

Parameter	**Unit**	**Neural Network**	**Simulation**	**Delta [%]**
Top of climb				
Mass flow	kg/s	0.985	0.985	-0.00
Exhaust temperature	K	1129.0	1129.1	-0.00
Trapped FAR	-	0.017	0.017	0.00
Power	kW	271.0	270.9	0.02
Heat loss	kW	-79.9	-79.9	0.02
Peak pressure	bar	250.0	249.9	0.02
Take-off				
Mass flow	kg/s	2.353	2.353	-0.01
Exhaust temperature	K	1350.0	1350.4	-0.03
Trapped FAR	-	0.020	0.020	-0.05
Power	kW	486.6	486.8	-0.04
Heat loss	kW	-141.7	-141.8	-0.04
Peak pressure	bar	250.0	249.9	0.06
Cruise				
Mass flow	kg/s	0.833	0.833	-0.00
Exhaust temperature	K	1115.7	1115.8	-0.00
Trapped FAR	-	0.018	0.018	0.00
Power	kW	222.0	222.0	0.01
Heat loss	kW	-65.3	-65.3	0.01
Peak pressure	bar	174.6	174.6	0.00

Table A.11: Comparison of results of piston engine surrogate artificial neural network with simulation model of intercooled two-stroke CCE.

Parameter	**Unit**	**Neural Network**	**Simulation**	**Delta [%]**
Top of climb				
Mass flow	kg/s	0.957	0.957	-0.01
Exhaust temperature	K	1031.8	1031.8	-0.00
Trapped FAR	-	0.022	0.022	0.00
Power	kW	345.6	345.5	0.00
Heat loss	kW	-93.6	-93.6	0.00
Peak pressure	bar	246.3	246.2	0.01
Take-off				
Mass flow	kg/s	2.297	2.297	-0.00
Exhaust temperature	K	1208.1	1208.1	0.00
Trapped FAR	-	0.025	0.025	0.01
Power	kW	642.0	641.9	0.01
Heat loss	kW	-155.0	-155.0	-0.00
Peak pressure	bar	250.0	249.9	0.03
Cruise				
Mass flow	kg/s	0.810	0.810	-0.00
Exhaust temperature	K	974.5	974.5	0.00
Trapped FAR	-	0.020	0.020	0.00
Power	kW	259.1	259.1	-0.03
Heat loss	kW	-68.1	-68.1	0.00
Peak pressure	bar	161.8	161.7	0.03

Table A.12: Comparison of results of piston engine surrogate artificial neural network with simulation model of free-piston CCE.

Parameter	**Unit**	**Neural Network**	**Simulation**	**Delta [%]**
Top of climb				
Mass flow	kg/s	1.108	1.108	-0.00
Exhaust temperature	K	1064.4	1064.4	-0.00
Trapped FAR	-	0.017	0.017	0.00
Power	kW	291.8	291.8	-0.00
Heat loss	kW	-52.4	-52.4	-0.00
Peak pressure	bar	156.5	156.5	-0.01
Take-off				
Mass flow	kg/s	2.543	2.543	-0.00
Exhaust temperature	K	1350.0	1350.0	0.00
Trapped FAR	-	0.024	0.024	0.01
Power	kW	764.4	764.4	-0.01
Heat loss	kW	-131.3	-131.3	0.01
Peak pressure	bar	250.0	250.0	-0.01
Cruise				
Mass flow	kg/s	0.945	0.945	-0.00
Exhaust temperature	K	1018.3	1018.4	-0.00
Trapped FAR	-	0.015	0.015	0.00
Power	kW	235.4	235.4	-0.01
Heat loss	kW	-36.1	-36.1	-0.02
Peak pressure	bar	124.6	124.6	0.01